



Two-mode dynamics and switching in quantum dot lasers.

Martin Virte

► To cite this version:

Martin Virte. Two-mode dynamics and switching in quantum dot lasers.. Other. Supélec; VRIJE UNIVERSITEIT BRUSSEL, 2014. English. NNT : 2014SUPL0020 . tel-01132177

HAL Id: tel-01132177

<https://theses.hal.science/tel-01132177>

Submitted on 16 Mar 2015

HAL is a multi-disciplinary open access archive for the deposit and dissemination of scientific research documents, whether they are published or not. The documents may come from teaching and research institutions in France or abroad, or from public or private research centers.

L'archive ouverte pluridisciplinaire **HAL**, est destinée au dépôt et à la diffusion de documents scientifiques de niveau recherche, publiés ou non, émanant des établissements d'enseignement et de recherche français ou étrangers, des laboratoires publics ou privés.



Brussels Photonics Team (B-PHOT),
Department of Applied Physics
and Photonics (TONA),
Vrije Universiteit Brussel
Belgium



OPTEL Research Group,
Laboratoire Matériaux Optiques,
Photonique et Systèmes (LMOPS),
Supélec
France

Two-mode dynamics and switching in quantum dot lasers

A PhD thesis submitted and defended publicly on October 20th 2014 by:

Martin Virte

The work described in this dissertation has been done in the frame of a joint PhD program between the Vrije Universiteit Brussel (Belgium) and Supélec (France)

Promotors:

Prof. Dr. Ir. Marc SCIAMANNA	Supélec, France
Prof. Dr. Krassimir PANAJOTOV	Vrije Universiteit Brussel, Belgique

2014



Vrije
Universiteit
Brussel

FACULTY OF ENGINEERING
Department of Applied Physics and Photonics

Two-mode dynamics and switching in quantum dot lasers

A thesis submitted in fulfilment of the requirements for the award
of the degree of Doctor in Engineering by

Martin Virte

October 2014

Promoters: Prof. Dr. Krassimir Panajotov
Prof. Ir. Marc Sciamanna

The work described in this thesis has been performed in the frame of a joint
PhD program with Supélec, France.



2014



Supélec

Numéro d'ordre: 2014-20-TH



SUPÉLEC

Ecole Doctorale EMMA

«Energie, Mécanique et Matériaux»

en cotutelle avec la **Vrije Universiteit Brussel**.

THÈSE DE DOCTORAT

Domaine: SPI

Spécialité: Photonics

Soutenue le **20 octobre 2014** par

Martin Virte

Two-mode dynamics and switching in quantum dot lasers

Directeurs de thèse:

Krassimir PANAJOTOV

Professeur, Vrije Universiteit Brussel, Belgique

Marc SCIAMANNA

Professeur, Supélec, France

Composition du Jury:

Président du jury:

Wolfgang ELSÄSSER

Professeur, Technische Universität Darmstadt, Allemagne

Rapporteurs:

Frederic GRILLOT

Maitre de conférences, HDR, Telecom ParisTech, France

Angel VALLE

Professeur, Universidad de Cantabria, Spain

Examineurs:

Sylvain BARBAY

Chargé de recherche, CNRS, France

Damien RONTANI

Docteur, Supélec, France

Hugo THIENPONT

Professeur, Vrije Universiteit Brussel, Belgique

Members of the Jury

Public Defense – October 20, 2014
In Supélec, Metz, France

Prof. Dr. Wolfgang Elsässer, President of the jury
Institute of Applied Physics,
Technische Universität Darmstadt, Germany

Prof. Dr. Frederic Grillot, reviewer
Laboratoire CNRS LTCI
Télécom Paris Tech, France

Prof. Dr. Angel Valle, reviewer
Instituto de Física de Cantabria,
Universidad de Cantabria, Spain

Dr. Sylvain Barbay, examiner
Laboratoire Photonique et Nanostructures
CNRS UPR20, France

Dr. Damien Rontani, examiner
Optel Research Group, Laboratoire MOPS,
Supélec, France

Prof. Dr. Ir. Hugo Thienpont, examiner
Department of Applied Physics and Photonics,
Vrije Universiteit Brussel, Belgium

Prof. Dr. Krassimir Panajotov, promoter
Department of Applied Physics and Photonics,
Vrije Universiteit Brussel, Belgium

Prof. Dr. Ir. Marc Sciamanna, promoter
Optel Research Group, Laboratoire MOPS,
Supélec, France

to my lovely Aurélie...

ABSTRACT

In this thesis, I study experimentally and theoretically the mode competition and the resulting nonlinear dynamics and switching in two-mode quantum dot laser systems.

First, I concentrate on the competition between polarization modes that takes place in quantum dot vertical-cavity surface-emitting lasers (VCSELs). It is well known that due to their circular geometry, VCSEL devices exhibit polarization instabilities that can lead to noise-induced mode hopping or switching between orthogonal linear polarizations. Although various dynamics accompanying these instabilities have been reported, a new peculiar random-like hopping between two non-orthogonal elliptically polarized states has been recently highlighted in QD VCSELs. This surprising behavior shows intriguing features which clearly call for a different interpretation than that of the other dynamics reported so far.

In this thesis, I show that the dynamical behavior reported experimentally can accurately be reproduced within the spin-flip model (SFM) framework. In particular, I demonstrate and confirm experimentally that the peculiar random-like hoppings are in fact deterministic low-dimensional chaotic fluctuations, i.e. “Polarization Chaos”. Moreover, I report in the same devices a new bistability between two self-pulsating dynamics of different frequencies and showing with different polarization orientations. Such dynamics can again be reproduced in the SFM framework when taking into account a slight misalignment of the cavity anisotropies. At last, I make a proof-of-concept demonstration of a high-speed random bit generator based on polarization chaos, hence demonstrating that the chaotic dynamics uncovered is relevant for optical chaos-based applications.

Secondly, I investigate the effects of an external optical feedback on quantum dot lasers emitting simultaneously from the ground and the excited states. I bring new light on the impact of optical feedback and the corresponding mechanisms and bifurcations. I highlight theoretically that optical feedback globally favors the ground state emission, but also that it can be used to switch from one mode to the other when changing the feedback rate and/or the time-delay. In addition, I experimentally report switching between the ground and excited states when varying the external cavity length at the micrometer scale, which supports the theoretical predictions.

RÉSUMÉ

Dans cette thèse, j'étudie théoriquement et expérimentalement la compétition de modes et la dynamique non linéaire résultant de cette compétition dans des systèmes lasers à boîtes quantiques et à deux modes.

Tout d'abord, je traiterais le cas de la compétition entre deux modes de polarisation apparaissant dans les diodes lasers nanostructurées à cavité vertical et émettant par la surface (VCSELs). A cause de leur géométrie circulaire, il est connu que les composants de type VCSEL ont une polarisation potentiellement instable qui peut conduire jusqu'à l'apparition de commutation et de sauts de modes stochastiques entre deux modes de polarisation linéaires. Bien que de nombreuses dynamiques accompagnant ces instabilités aient été rapportées, un surprenant saut de mode entre deux états polarisés elliptiquement a été récemment découvert dans les VCSELs à boîtes quantiques. Ce comportement montre des propriétés intrigantes qui nécessitent une interprétation alternative.

Dans cette thèse, je montre que ce comportement dynamique observé expérimentalement peut être reproduit en détail en utilisant le modèle spin-flip (SFM). En particulier, je démontre et confirme expérimentalement que les sauts de modes aléatoires sont en réalité des fluctuations chaotiques et déterministes de faible dimension: c'est à dire un chaos en polarisation. De plus, je décris dans les mêmes composants une nouvelle bistabilité entre plusieurs dynamiques auto-pulsées à différentes fréquences et montrant différents orientations de polarisation. Ces comportements peuvent eux aussi être reproduits avec le modèle SFM en considérant un léger désalignement des anisotropies de la cavité laser. Finalement, je démontre la pertinence de la dynamique chaotique observée pour les applications exploitant le chaos optique, en réalisant un générateur de nombres aléatoires à grande vitesse basé sur le chaos en polarisation.

Deuxièmement, j'étudie les effet d'une rétroaction optique à délai sur les lasers à boîtes quantiques émettant simultanément depuis l'état fondamental et le premier état excité. Je clarifie l'impact de cette rétroaction optique ainsi que les mécanismes et bifurcations correspondantes. Je montre théoriquement qu'une rétroaction optique favorise globalement l'émission par l'état fondamental, mais aussi qu'un tel montage peut être utilisé pour commuter entre ces deux modes d'émission lorsque l'on change le taux ou le délai de la rétroaction. Enfin, je confirme ces observations expérimentalement, en rapportant des commutations entre l'état fondamental et l'état excité lorsque la taille de la cavité externe est modifiée à l'échelle du micromètre.

SAMENVATTING

In mijn doctoraat onderzoek ik experimenteel en theoretisch de mode competitie in dubbele mode quantum dot laser systemen, en de daaruitvolgende niet-lineaire dynamica en switching.

Allereerst concentreer ik op de competitie tussen gepolariseerde modes die plaatsvindt in quantum dot (QD) vertical-cavity surface-emitting lasers (VCSELs). Het is gekend dat omwille van hun circulaire geometrie, VCSEL systemen polarisatie instabiliteiten bezitten die kunnen leiden tot ruis-geïnduceerde mode hopping of switching tussen orthogonale lineaire polarisaties. Er werd reeds gerapporteerd over verschillende dynamica die deze instabiliteiten beschrijven, maar recent onderzoek richt zich op het random-like hopping tussen niet-orthogonale elliptische polarisaties in QD VCSELs. Dit recent ontdekte fenomeen vertoont merkwaardige eigenschappen die niet verklaard kunnen worden aan de hand van reeds bestaande dynamica.

In deze thesis toon ik aan dat het dynamische gedrag dat experimenteel werd gemeten, gereproduceerd kan worden aan de hand van het spin-flip model (SFM). Meerbepaald toon ik aan en verifieer ik experimenteel dat de merkwaardige random-like hoppings in feite deterministisch laag-dimensionele chaotische fluctuaties zijn, ook wel gekend als “polarization chaos”. Bovendien toon ik in deze systemen een nieuwe bistabiliteit aan tussen twee zelf-pulserende dynamica van verschillende frequenties en met verschillende polarisatie richtingen. Dit fenomeen kan gereproduceerd worden in het SFM model wanneer een beperkte misalignatie van de cavity anisotropies in rekening gebracht worden. Vervolgens geef ik een proof-of-concept demonstratie van een hogesnelheid random bit generator, gebaseerd op polarisatie chaos. Hiermee toon ik aan dat de bestudeerde chaotische dynamica relevant is voor optische chaos-gebaseerde toepassingen.

Daarnaast onderzoek ik de effecten van externe optische feedback op quantum dot lasers die simultaan exciteren uit de grond en geëxciteerde toestanden. Ik geef een nieuwe kijk op de impact van optische feedback en de bijhorende mechanismes en bifurcaties. Ik toon theoretisch aan dat in het algemeen optische feedback een voorkeur heeft voor grondtoestand emissie, maar ook dat dit gebruikt kan worden om te switchen van de ene mode naar de andere door de feedback rate en/of tijdsvertraging te variëren. Bovendien toon ik experimenteel het switchen tussen de grond en geëxciteerde toestanden aan wanneer de externe caviteitslengte aangepast wordt op micrometer schaal, hetgene de theoretische voorspellingen staft.

*The fact that we live at the bottom of a deep gravity well,
on the surface of a gas covered planet going around a nuclear fireball
90 million miles away and think this to be normal is obviously
some indication of how skewed our perspective tends to be.*

— Douglas Adams,
The Salmon of Doubt:
Hitchhiking the Galaxy One Last Time

ACKNOWLEDGMENTS

Starting my PhD, it was quite obvious to me that you do not go through such journey alone and that, at some point, you need the support of other persons to reach the end. But I certainly never would have expected to rely so much on this support even in the peculiar frame of a joint PhD between France and Belgium. I was also lucky enough to meet/work/exchange with so much passionate and interesting people that I would definitely do it again.

So here we are, after three years, almost at the end of this adventure. Below is a bare attempt to make a non-exhaustive list of all the people who supported me in various ways during this time. Thank you.

First of all, I really need to acknowledge two persons who were literally behind all of this: my two promoters Marc Sciamanna and Krassimir Panajotov. I don't think anyone would contradict me if I say that Marc and Krassimir have very different styles of supervising students, but in my case, I probably could not have found any better promoter team. Of course, it was not three years of calm and steady progress, and I guess I was not always an easy student to supervise, but I definitely enjoyed a lot working, and learning so many things together with them.

I would also take the chance to acknowledge the support of Hugo Thienpont, head of the Department of Applied Physics and Photonics at VUB. Despite being one of the most busy men I ever met, he was always able to find time and solutions whenever needed. Especially, I really appreciated his unconditional support to solve any issues related to my peculiar situation.

Even though I had less interaction with him, I would also like to thank Serge Perrine the director of Supelec campus in Metz for his support.

Secondly, I wish to deeply thank all the members of the jury for their careful reading of this manuscript and for taking the time to evaluate the work I did during the last three years. In particular, I would like to emphasize the involvement of those who had to come once in Brussels and once in Metz for the private and public defense respectively; I thank them for accepting this additional burden.

A special thank should then go to the IT teams of both Supelec and B-Phot. My computer was definitely the keystone of all my work and I might have spend more time with it than with anyone else during these three years. Special thank to Gilles of Supelec for all the IT support even when I was not physically there (and for the jokes, your humor and the relax atmosphere of your office). Thanks also to Claudine and Patrick. In Brussels, a special thank should go to Marcin (and what I would like to call the VUB's polish connection) for providing me the extra screen. Thanks also to the rest of the IT team Raymundo and Tom. Thank you all for the amazing work you do so that we can have internet/storage/stuff all the time.

A second special thank should be for the secretary teams of Supelec and B-Phot. I believe that nothing would be possible anywhere without efficient secretaries, and I was lucky to meet skilled and very efficient persons at such position. Let me therefore thank Fabienne and Thérèse who I bothered quite a lot in Supelec, especially when I had to prepare my stay in Brussels while the procedure was everything but clear. Thanks also to Danielle, Laurence, Véronique and Dorothée also from Supelec. At B-Phot, Majorie deserves a special thanks as well for her support: she was the only one in Etterbeek all the time, so I annoyed her countless times for various little things and she always answered with a smile. Also coffee!! Thanks also to An for the crucial administrative support, and to Bernadette, Nadine and Nadia.

Next, I would like to acknowledge the mostly (but not exclusively) non work-related support of all my co-workers and fellow PhD students in Metz and in Brussels. For those in Metz and in no particular order, thanks to Damien, Nicolas, Delphine, Vianney, Andreas, Mathieu, Gilles (again), Noémie and all the staff of Supelec. Although I was not in Metz permanently, It was nice to be always welcomed back. In Brussels, I would like to mention in particular, Carlos, Etienne, Sanne (special thanks for the summary in dutch and for driving back and forth to my public defence), Marcin, Fabian, Tigran, Jacek, Mateusz, Simone, Ana and Camille for the coffee breaks, lunch breaks, and all the relaxing drinks we had together; I really enjoyed these moments. Thanks also to the SPIE student chapter: Lien, Diane, Evert, Iterio, Ben, Jens, Stefaan and the others for organizing nice events and thanks to all the people participating. Special thanks also to my office-mates Meiji, Tigran and Gebirie, for the relaxed ambiance in the office. In the end,

thanks to all the people at B-phot for their welcome and the good atmosphere in the lab. Furthermore, I would like to acknowledge the contribution of the two skilled interns I had the chance to supervise: Emeric and Elodie. I wish you both good luck for your PhD.

Besides all these very enjoyable and skilled persons I had the chance to meet in my professional environment, I was also supported by very important friends. Especially, I would like to deeply thank in no particular order, Thibaut, Cyrielle, Guillaume (Stesch), H  l  ne, Emmanuel (Manu), Olivier, Caroline, Damien and Thomas. I might not see you as much as I would like to, but knowing that you are here anytime is really important to me; so I take the chance of writing this down and of thanking all of you for being amazing and for supporting me during these three years. I would also like to thank everyone from Supelec, from Nancy, Grenoble and everywhere else, with whom I spend nice, friendly and relaxing moments in the last years; it really helped me to keep going and I owe you all for this.

Finally, I want to thank my family for supporting me in any ways from kindergarten to the end of my PhD. It was not always simple and easy, but I knew all the way that I would have had your unconditional support to back me up if needed. You taught me the value of hard work and more importantly of being passionate and proud of what you do, and that is something I deeply thank you for. We might have some disagreements (who doesn't?), and even though my ideas and my choices are not always in line with what you believe in, I know that you respect them.

Last, I could not finish these acknowledgments without taking the time to thank the most important person of these three years, my wife Aurélie. You have been supporting me from the beginning of this journey, helping me through the most challenging part, encouraging me when I was down, pushing me when I was losing some motivation and just being there when I needed you. Meeting you was probably one of the best thing that happened to me, and I am so lucky having you today by my side. Thank you for all your love and (almost) unlimited support.

Martin Virte
Brussels, October 22, 2014

LIST OF PUBLICATIONS

Some of the materials, ideas and figures in this dissertation have appeared previously in the following publications:

PUBLICATIONS IN PEER-REVIEWED JOURNALS

1. M. Virte, K. Panajotov, H. Thienpont, and M. Sciamanna, "Deterministic polarization chaos from a laser diode," *Nature Photon.* **7**, 60-65 (2013).
2. M. Virte, K. Panajotov, and M. Sciamanna, "Bifurcation to nonlinear polarization dynamics and chaos in vertical-cavity surface-emitting lasers," *Phys. Rev. A* **87**, 013834 (2013).
3. M. Virte, K. Panajotov, and M. Sciamanna, "Mode competition induced by optical feedback in two-color quantum dot lasers," *IEEE J. Quantum Electron.* **49**, 578 (2013).
4. M. Virte, M. Sciamanna, E. Mercier, and K. Panajotov, "Bistability of time-periodic polarization dynamics in a free-running VCSEL," *Opt. Express* **22**, 6772 (2014).
5. M. Virte, K. Panajotov, and M. Sciamanna, "Corrections to "mode competition induced by optical feedback in two-color quantum dot lasers" [jul 13 578-585], " *IEEE J. Quantum Electron.* **50**, 174 (2014).
6. M. Virte, E. Mercier, H. Thienpont, K. Panajotov and M. Sciamanna, "Physical random bit generation from chaotic solitary laser diode," *Opt. Express* **22**, 17271 (2014).
7. M. Virte, S. Breuer, M. Sciamanna and K. Panajotov, "Switching between ground and excited states by optical feedback in a quantum dot laser diode", *Appl. Phys. Lett.* **105**, 121109 (2014).

1. M. Virte, K. Panajotov, and M. Sciamanna, "Dynamics accompanying polarization switching in vertical-cavity surface-emitting lasers," in "Proc. SPIE, Semiconductor Laser and Laser Dynamics V, Eds K. Panajotov, M. Sciamanna, A. Valle and R. Michalzik," vol. 8432, pp. 84321E (2012).
2. M. Virte, M. Sciamanna, and K. Panajotov, "Bifurcation to chaotic polarization mode hopping in vertical-cavity surface-emitting lasers," in "Advanced Photonics Congress," (Optical Society of America), p. JTu5A.31 (2012).
3. M. Virte, K. Panajotov, and M. Sciamanna, "Impact of optical feedback on a quantum dot laser emitting simultaneously from the ground and excited states," in "Lasers and Electro-Optics Europe (CLEO EUROPE/IQEC), 2013 Conference on and International Quantum Electronics Conference," pp. 6801840 (2013).
4. M. Virte, K. Panajotov, H. Thienpont, and M. Sciamanna, "Polarization chaos from a free-running quantum dot laser diode," in "Lasers and Electro-Optics Europe (CLEO EUROPE/IQEC), 2013 Conference on and International Quantum Electronics Conference," pp. 6800709 (2013).
5. M. Virte, M. Sciamanna, E. Mercier, and K. Panajotov, "Experimental and theoretical analysis of limit cycle bistability in a free-running vcsel," in "Proc. SPIE, Semiconductor Laser and Laser Dynamics VI, Eds K. Panajotov, M. Sciamanna, A. Valle and R. Michalzik," vol. 9134, pp. 91340A (2014).
6. M. Virte, E. Mercier, H. Thienpont, K. Panajotov, and M. Sciamanna, "Random bit generation using polarization chaos from free-running laser diode," in "Proc. SPIE, Semiconductor Laser and Laser Dynamics VI, Eds K. Panajotov, M. Sciamanna, A. Valle and R. Michalzik," vol. 9134, pp. 913426 (2014).

CONTENTS

ABSTRACT	xi
ACKNOWLEDGMENTS	xv
LIST OF PUBLICATIONS	xix
CONTENTS	xxi
PREFACE: CONTEXT AND MOTIVATION	1
1 GENERAL INTRODUCTION	5
1.1 Semiconductor lasers	6
1.1.1 From stimulated emission to laser effect	6
1.1.2 Laser effect in semiconductor materials	7
1.2 Nonlinear dynamics of laser diodes	10
1.2.1 Brief history of chaos and lasers	10
1.2.2 Semiconductor lasers as damped nonlinear oscillators	11
1.2.3 Impact of time-delayed optical feedback	13
1.3 Polarization instabilities in vertical-cavity surface-emitting lasers	17
1.3.1 From edge-emitting lasers to VCSELs	17
1.3.2 Experimental observations of polarization instabilities in VCSELs	18
1.3.3 Theoretical interpretation of polarization instabilities	23
1.4 Quantum dot laser diodes	27
1.4.1 Quantum dots as a gain medium	28
1.4.2 Dynamical properties of quantum dot lasers	29
1.4.3 Simultaneous emission from the ground and the excited states	30
1.5 Outlines of the thesis	33
2 DETERMINISTIC POLARIZATION CHAOS	37
2.1 Description of the spin-flip model	38
2.1.1 SFM equations	38
2.1.2 Steady-states of the SFM	40
2.1.3 Key measurements	44

2.2	Bifurcations to polarization switching	46
2.2.1	Analysis of possible bifurcation scenarios	46
2.2.2	Scenario of type-II polarization switching	52
2.2.3	Self-pulsing dynamics without polarization switching	58
2.3	Deterministic polarization chaos in free-running VCSELs	64
2.3.1	Experimental characterization of quantum dot VCSELs	64
2.3.2	Route to polarization chaos	71
2.3.3	Statistics of the deterministic mode hopping	73
2.4	Experimental chaos identification	76
2.4.1	Estimation of the largest Lyapunov exponent	76
2.4.2	K_2 -entropy and correlation dimension	78
2.4.3	Statistical approach and discrimination of colored noise	81
2.5	Bistability of limit cycles	85
2.5.1	Experimental observations	85
2.5.2	Description of the asymmetric SFM	87
2.5.3	Impact of the asymmetry on the laser dynamics	89
2.6	Summary and perspectives	92
3	APPLICATION OF POLARIZATION CHAOS TO RANDOM BIT GENERATION	95
3.1	State of the art - optical chaos-based random bit generators	96
3.2	Experimental setup	100
3.3	System performances and influence of the post-processing	103
3.4	Entropy evolution and its link with polarization chaos	110
3.5	Summary and perspectives	115
4	TWO-MODE DYNAMICS IN QD LASERS WITH OPTICAL FEEDBACK	117
4.1	Background: two-color QD lasers subject to optical feedback	118
4.2	Mathematical modeling of the QD lasers	120
4.2.1	Rate equation with separated electron-hole dynamics	120
4.2.2	Analytical description of the steady-states	123
4.2.3	Stability analysis	125
4.3	Solitary QD laser behavior	127
4.4	Ground-excited state switching with optical feedback	130
4.4.1	Evolution at low injection currents	130
4.4.2	Evolution at medium injection currents	132
4.4.3	Evolution at large injection currents	135

4.5	Influence of the laser and feedback parameters	137
4.5.1	Impact of external cavity length variations	137
4.5.2	Impact of the electron escape rate	143
4.6	Experimental observation of switching for varying time-delays	146
4.6.1	Experimental setup	146
4.6.2	Behavior of the solitary laser diode	148
4.6.3	Impact of the optical feedback: experimental observations	149
4.7	Summary and perspectives	155
5	CONCLUSION AND PERSPECTIVES	159
5.1	Main achievements	160
5.2	Perspectives for future work	163
APPENDICES		
A	RÉSUMÉ EN FRANÇAIS	165
A.1	Introduction	166
A.2	Chaos en polarisation dans un laser VCSEL à boîte quantique	169
A.3	Génération de nombres aléatoires à partir du chaos en polarisation	175
A.4	rétroaction optique sur un laser à boîte quantique à deux couleurs	180
A.5	Conclusion	185
B	LINEARIZATION OF THE SFM	187
C	GRASSBERGER-PROCACCIA ALGORITHM IMPLEMENTATION	191
D	DDE-BIFTOOL DETAILS FOR LASERS WITH FEEDBACK	197
REFERENCES		201
LIST OF ACRONYMS		219
CURRICULUM VITAE		221

PREFACE: CONTEXT AND MOTIVATION

*The scientist does not study nature because it is useful to do so.
He studies it because he takes pleasure in it,
and he takes pleasure in it because it is beautiful.
If nature were not beautiful it would not be worth knowing,
and life would not be worth living.*

— Henri Poincaré, *Science and Method*

The science-fiction world helped propagating awfully wrong ideas about laser light such as laser guns or lightsabers, and, thanks to these inspired images, lasers are now commonly seen as fascinating, fancy science-looking pieces of technology. But at the same time, they are largely misunderstood. In real life, lasers are the spine of most photonic systems and are exploited as such in a tremendous range of applications: bloodless or eye surgery, forensic identification, 3D imagery, various metrology and military applications. Yet, the biggest life-changing use of laser technology has probably been its application in the field of telecommunications, where, combined with optical fibers, they opened the way toward long-distance high-speed communication schemes. Because of the astonishing performances of optical systems, electronic-based solutions are maintained only for cost-related reasons in particular for short distances - e.g. local/metropolitan area networks -, even though photonics is also taking over for extremely short distances. Indeed electronic computer interconnects start to become a hurdle, e.g. for the development of data-centers, especially in terms of heating and energy efficiency, while new on-chip optical interconnects based on silicon photonics demonstrate exciting performances. The common point for all distances however is that a laser is required to generate the light beam which will carry the information. Considering the strong requirements of these schemes - especially in terms of size, cost and efficiency -, semiconductor

lasers quickly appeared as the most convenient choice: they are electrically powered, extremely small, very efficient and relatively cheap devices. Yet, the irresistible growth of the amount of data shared over the internet pushes all the subsystems to their current limits, hence making upgrades of current solutions not only desirable, but necessary. It therefore motivates new studies to improve every parts of the system, obviously including laser diodes, for which a particular attention is required because of their dynamical complexity.

At first glance, lasers might appear as peculiar light bulbs, but the physical principle on which they rely - i.e. stimulated emission of radiation - intrinsically make them dynamical devices. Semiconductor lasers are generally expected to behave as damped nonlinear oscillators: when subject to a current step, they will oscillate toward a stable fixed point, i.e. toward a steady emission output power. However when subject to an external perturbation such as direct modulation, optical injection or feedback, laser diodes can rapidly be destabilized and exhibit a wide range of dynamics including self-pulsations and chaos. Considering these specific features, additional investigations using a dynamical viewpoint are therefore necessary.

The field of nonlinear dynamics - i.e. the analysis of dynamical systems - started from the study of the dynamics of astronomical and mechanical objects (such as pendulum or oscillators), and has attracted the interest of many scientists during ages. This field has however been dramatically transformed since 1963 and the discovery of deterministic chaos, i.e. an aperiodic deterministic dynamics of a nonlinear system with a high sensitivity to initial conditions. Chaos theory has then been a major paradigm-shift which significantly improved our understanding and our ability to predict and control complex dynamical systems, including cardiac arrhythmias or neuronal networks. Indeed, nonlinear dynamics is a very inter-disciplinary field with far reaching implications in all kinds of systems because the dynamical concepts and mechanisms such as chaos and bifurcations are generic.

In this context, the interest for investigating the nonlinear dynamics of semiconductor lasers is therefore three-fold: 1/ understanding the nonlinear mechanisms that drive the laser diode dynamics allows us to identify the essential features and intrinsic limitations of the devices. Considering the nonlinear dependencies of the laser behavior on its parameters, practical improvements - such as increasing the modulation bandwidth - are mostly a matter of trade-off between various parameters which therefore requires an in-depth analysis and understanding to be fully optimized. 2/ these studies allow to uncover new behaviors and dynamics, and thus to potentially pave the way toward new cutting-edge applications such as secure optical chaos communication or more recently ultrafast generation of random bits - e.g. for security applications and cryptography. In particular, analogies can be made with other systems and exciting applications

can be transposed and largely benefit from the fast internal time-scales of laser systems. 3/ As already stated above, the concepts of nonlinear dynamics are generic, laser systems therefore provide fast nonlinear sandboxes that are relatively easy to use and to analyze compared to other systems. For instance investigating peculiar dynamics such as excitability - a feature closely related to the behavior of a spiking neuron - is much easier in lasers than e.g. in real neurons. Studying the nonlinear dynamics of semiconductor lasers can therefore potentially provide essential inter-disciplinary insight on dynamical mechanisms.

Since the first demonstration of a laser diode in 1962, semiconductor lasers have benefited from many changes and improvements. One of the most important breakthrough in their development came from the introduction of quantum wells - i.e. a layer of semiconductor material thin enough to confine the electrons on 1-dimension - to act as the gain medium. This innovative solution has led to devices with a higher efficiency, a larger gain, a lower threshold and a reduced emission linewidth. It is then quite easy to believe that higher degrees of confinement could yield even better performances; and thus started the quest towards high-performance lasers based on quantum dots (QDs) - i.e. nanocrystals of semiconductor materials in which carriers are confined on all three dimensions. In theory, QD lasers were expected to exhibit astonishing features and to approach the perfect laser. Yet, production challenges and the complexity of real quantum dot structures revealed that these exciting expectations were actually too optimistic, hence slowing down - but not stopping - the progress of quantum dot lasers. Today, some of the production hurdles have been overcome and promising performances have been demonstrated, but, because of the additional complexity brought by the quantum dots, many characteristics and features remain to be clarified to fully benefit from these innovative devices.

In this thesis, we focus on the dynamics induced by a competition between two modes in quantum dot lasers. In particular, we investigate two different systems: 1/ a quantum dot vertical-cavity surface-emitting laser (VCSEL) in which two polarization modes can compete, and 2/ a quantum dot laser emitting simultaneously from the fundamental state (or ground state) and the first excited state subject to optical feedback.

On one hand, VCSELs are known to suffer from polarization instabilities: because of their circular geometry, the light polarization is selected only by the small anisotropies of the laser cavity, which are not strong enough to ensure a steady polarization. As a result, various polarization instabilities have been reported eventually accompanied by self-pulsing dynamics. Very recently however, surprising dynamical behaviors have been observed in QD VCSELs: the reported dynamical evolutions do not relate to any of the behaviors previously identified and some features even seem, at first glance, incompati-

ble. In particular, a peculiar random-like hopping dynamics between two non-orthogonal elliptically polarized modes has been observed, and shows statistical evolution opposed to the one reported so far for mode hopping dynamics in quantum well VCSELs. Such surprising observations obviously call for an in-depth investigation to bring new light on the underlying mechanisms and potential outcomes of these new dynamics.

On the other hand, multiple energy levels for the carriers can be confined in QD lasers, hence, under the proper conditions, the laser can emit from the fundamental energy level (ground state) or from other confined levels of higher energy, i.e. excited states. This situation can typically result in emissions at two distinct and largely separated optical frequencies. Because of this specific feature, this system raised interest especially for terahertz generation and all-optical processing. However the control of the two-mode emission is challenging, and thus many investigations have been conducted using two-section QD lasers or optical injection schemes. On the other hand, although promising results have been demonstrated, only few studies considered the impact of a time-delayed optical feedback: no in-depth theoretical and experimental investigation of such scheme has been conducted. Additional work is therefore required to clarify the impact of optical feedback on such two-color quantum dot lasers.

To sum up, the purpose of this thesis is to highlight and to understand the mode competition mechanisms and their effects on quantum dot laser systems. Because these behaviors can have a dramatic impact if not prevented, but also because they could be efficiently controlled to conceive new paradigm-shifting applications, laser dynamics is an essential field of study to both ensure reliability of current applications and to provide new innovative ways of exploiting the resources of semiconductor lasers.

1

GENERAL INTRODUCTION

*Progress isn't made by early risers.
It's made by lazy men trying to find easier
ways to do something.*

— Robert Heinlein

The goal of this general introduction is, of course, to present the context of the work described in this thesis, but is also to present the essential concepts of both nonlinear dynamics and semiconductor lasers. Obviously some scientific background is required but I hope this introduction will allow even the less experienced readers to follow the main ideas and results of the work I present in this thesis.

This chapter is organized as follows. First, in section 1.1, I will briefly explain what a laser is, and describe the basics of semiconductor lasers. In section 1.2, I will discuss the nonlinear dynamics of lasers and laser diodes; in particular, I will emphasize the long-time relationship between chaos and lasers. Then in section 1.3, I will focus on a major breakthrough in the development of laser diodes: the vertical-cavity surface-emitting laser (VCSEL) structure, and discuss in detail its major drawback: polarization instabilities. In section 1.4, we focus on another ground breaking evolution for laser diodes: the introduction of quantum confined materials as gain medium - e.g. quantum wells, quantum wires and quantum dots - which enabled significant improvements of semiconductor laser devices. This innovation also appeared to be a source of exciting new physics especially from the viewpoint of nonlinear dynamics. Finally, in section 1.5, I will describe the contribution of the work presented and will present the outlines of this thesis.

1.1 SEMICONDUCTOR LASERS

Before getting into the specifics of the devices investigated in this work, I will start with a basic question specifically aimed at non-specialists: “what is a laser?”. Then, considering the countless studies and investigations about lasers in general, since their first experimental demonstration more than 50 years ago, I will quickly focus on a much more narrow field of study: the case of semiconductor lasers, or laser diodes.

1.1.1 *From stimulated emission to laser effect*

The LASER acronym stands for “Light Amplification by Stimulated Emission of Radiation”, which directly relates to the fundamental principle of the stimulated emission of radiation theoretically predicted by A. Einstein in 1916. In a nutshell, an atom or molecule, considered as a two level system, can interact with a photon in three different ways, as depicted in Fig. 1.1. If the atom is on the lower energy level, an incoming photon can be absorbed and the atom can be excited: the atom goes on the upper energy level, as in Fig. 1.1(a). Once excited the atom can emit a photon when returning to the lower energy level, and this event can happen in two different ways: 1/ the atom goes down to the lower energy level spontaneously, i.e. without external perturbations; this is called spontaneous emission, see Fig. 1.1(b) or 2/ the fall back toward a lower energy level is stimulated by an external photon, and thus the newly created photon is a perfect replica of the first one, including phase and frequency characteristics, see Fig. 1.1(c). Put in a different way, the initial radiation is amplified by means of the stimulated emission. Cascading this stimulated process would therefore create a highly coherent flow of identical photons with the same phase and same frequency: a *laser beam*.

Theoretically it can be demonstrated that stimulated emission becomes the dominant process if we have more atoms in the upper level than in the lower energy level: a so-called *population inversion*. The excitation of the atoms inside the *gain medium* - i.e. the medium in which the stimulated emission will take place and therefore provide a gain to the optical beam - is typically obtained through electrical or optical *pumping*. In both cases, if the pump is strong enough there will be more atoms on the upper energy level than on the lower level, hence creating the required population inversion. Once such situation is achieved, the stimulated emission becomes the dominant process and light amplification can be obtained.

The final step to get a laser beam is to ensure coherence of the light beam: to that end, the *gain medium* is placed inside a *resonator* in which selective amplification occurs. In

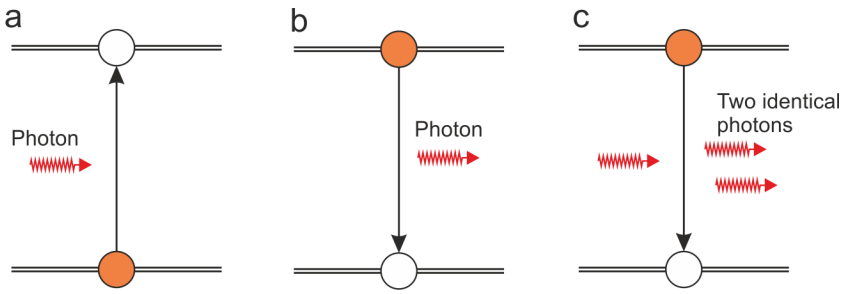


Figure 1.1 – **Absorption, spontaneous and stimulated emission of radiation in a two-level system.** (a) Radiation absorption scheme: if the energy of the incoming photon is high enough, it can be absorbed by an atom on the lower energy level which then moves to the upper level. (b) Spontaneous emission scheme: after some time, an atom on the upper level can spontaneously fall back to the lower energy level and emit a photon without any external perturbation. (c) Stimulated emission: an incoming photon can stimulate the fall of an excited atom to the lower energy level, hence stimulating the emission of a second strictly identical photon.

practice, the resonator is as simple as a pair of mirrors forming a cavity around the gain medium. The laser beam can then be obtained when the gain overcomes all the losses of the cavity such as *internal losses* - e.g. radiation absorption - and *emission losses*, when photons finally exit the gain medium, and hence do not contribute further to the stimulated emission process. Interestingly, the emission losses can be strongly reduced by increasing the reflectivity of the mirrors forming the cavity, which therefore lower the gain requirements. Finally, the point at which the gain equals the losses is the so-called *laser threshold*.

To sum up, three ingredients are required to build a laser: 1/ a *gain medium*, 2/ a *pump* and 3/ a *resonator*. Based on these three essential bricks, numerous types of laser systems have been developed: ranging from the optically pumped ruby solid-state laser - like the first laser demonstrated by T. H. Mainman in 1960 [1] -, to gas or fiber lasers. Despite such a variety of devices, the most common type of lasers nowadays is the semiconductor laser or laser diode. Indeed, because they are cheap, small, handy, reliable and efficient, these components quickly became the best choice for a wide range of applications: from CD/blu-ray technology to optical telecommunications.

1.1.2 Laser effect in semiconductor materials

Because of their specific properties - they are neither conductors nor insulators -, semiconductors are the keystone of today's electronics. In this kind of material, we do not find well-defined energy levels as pictured in Fig. 1.1, but instead we have two energy

bands separated by a *band-gap*: the upper band is called the *conduction band* while the lower band is referred to as the *valence band*. At zero temperature, all the electrons occupy the valence band. But at room temperature, some electrons have enough energy to reach the conduction band and create empty states - holes - in the valence band. In the rest of this dissertation, electrons and holes will be called *carriers*.

To obtain a *population inversion* by electrical pumping in a semiconductor structure, we need to tune the conductivity of the material by introducing a controlled level of impurities that will give it additional electrons (n-type doping) or holes (p-type doping); such process is called *doping*. Thus, by making a junction between p-type and n-type doped regions in the same semiconductor material, a so-called p-n homojunction, as displayed in Fig. 1.2(a), we can obtain a small region, around the junction, where population inversion can be achieved with a sufficiently strong injection current. This structure was the first demonstration of a laser diode made in 1962 by two competing groups led by R. Hall and M. Nathan respectively [2,3].

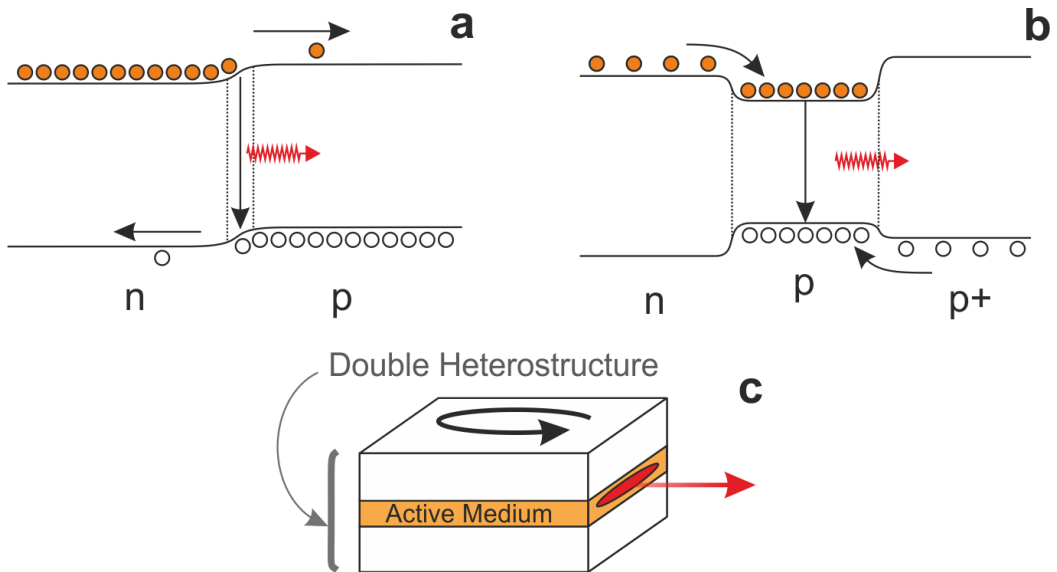


Figure 1.2 – **Scheme of p-n homojunction and n-p-p+ double heterostructure.** (a) Typical p-n homojunction, the lack of confinement structure leads to a very weak population inversion. (b) n-p-p+ double heterostructure showing three different band gaps, hence improving the confinement of the carriers in the central p doped region. (c) Scheme of a typical edge-emitting laser with a double heterostructure.

Although the basic structure presented above is sufficient to create a laser beam, it requires very high currents, hence making continuous wave emission at room temperature operation impossible. To overcome this hurdle, H. Kroemers suggested in 1963 to form

a double heterostructure - i.e. use a material with relatively small band-gap in the active layer sandwiched by two layers of different semiconductor materials with larger band-gaps - in order to enhance the population inversion in the active region [4]. As depicted in Fig. 1.2(b), such structure creates a well of potential where the carriers can be easily trapped, which therefore makes the *population inversion* much easier to achieve. Based on this idea, room-temperature laser diodes were successfully demonstrated experimentally by Z. Alferov in 1970 [5]. At this time, the common semiconductor laser structure was the so-called edge-emitting laser (EEL) - where the light is emitted from the edge of the structure, as depicted in Fig. 1.2(c) - which could be easily achieved through regular epitaxial growth processes of the different materials.

For such ground-breaking advance that led to the wide spreading of lasers and photonics in our everyday life, H. Kroemers and Z. Alferov were awarded the nobel prize in physics in 2000 [6,7].

The last 50 years clearly saw an intensive development and improvement of semiconductor lasers with an increasing amount of applications. But beyond the common performances of laser diodes - such as narrow linewidth, low consumption or high efficiency - the interest in these devices was also motivated by their exciting dynamical properties.

1.2 NONLINEAR DYNAMICS OF LASER DIODES

For most of us, lasers seem to behave like regular light bulbs: you can switch them on or off and no dynamics is really expected. Nevertheless, they are intrinsically dynamical devices, and although they are not all showing self-pulsations or chaotic behaviors, as we will see in this section, small external perturbations can be sufficient to unlock a tremendous amount of dynamical evolution [8,9]. Several applications based on the nonlinear dynamics and optical-chaos generated in lasers and especially in laser diodes have been demonstrated, including e.g. displacement measurement or Doppler velocimetry [9], but the two most significant applications so far have been secured chaos communication [10], and high-speed random bit generation [11].

1.2.1 *Brief history of chaos and lasers*

Although the concept of complex dynamics emerged as early as the 1900s, including the major contribution of H. Poincaré, modern studies of nonlinear dynamics really begun with the observation of deterministic, complex and irregular fluctuations in simulated time-series by E. Lorenz in 1963 [12]. Such *deterministic nonperiodic flow* - as coined by E. Lorenz - is directly linked with the nonlinearities of the relatively simple 3-equation system used in [12]:

$$X' = -\sigma X + \sigma Y \quad (1.1)$$

$$Y' = -XZ + rX - Y \quad (1.2)$$

$$Z' = XY - \beta Z \quad (1.3)$$

with σ , r and β the parameters of the system. The prime denotes the time-derivative and the equations are normalized in time.

This peculiar - deterministic but irregular - behavior was later called *chaos* and is typically characterized by its extreme sensitivity to initial conditions: two systems starting at slightly different situations - potentially indistinguishable from each other at the beginning - will exhibit completely different evolutions after a certain time. As an example, we plotted in Fig. 1.3 the divergent evolutions of simulated time-series based on Lorenz's equations with slightly different initial conditions (the distance between the two points is $\delta = 10^{-6}$). At first, the two time-series seem to follow exactly the same trajectory until $t > 9$ where small differences arise. Finally, the gap between the two time-series increases until they differ completely for $t > 17$.

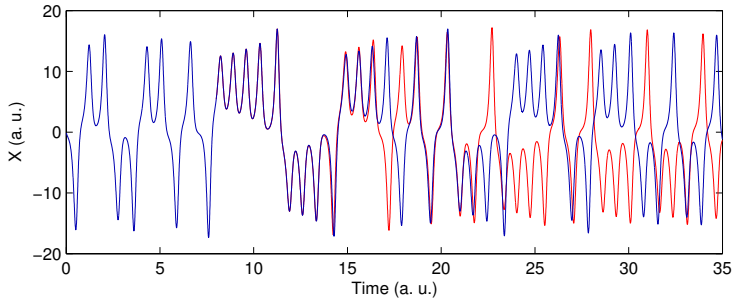


Figure 1.3 – **Divergent time-series of Lorenz chaos starting at slightly different initial conditions.** We plot the evolution of the X variable of Lorenz equations with the following parameters: $\sigma = 10$, $r = 28$ and $\beta = 8/3$. The two initial conditions for (X, Y, Z) differ by $\delta = 10^{-6}$ measured as the euclidian distance between the two points.

The set of three equations used by E. Lorenz were initially designed to model the atmospheric flow, but a couple of years later H. Haken theoretically demonstrated the strong analogies with laser systems [13]. In particular, he showed that Lorenz's equations are the same - after some changes of variables and normalization - than the Maxwell-Bloch equations for a two-level homogeneously broadened single-mode laser. In this frame, (X, Y, Z) variables relate to the electric field, polarization and carrier population in the laser respectively. The r parameter interestingly plays the same role as the pump while the two other parameters relate to typical time-scales of the dynamics; see the next subsection for details.

Because such analogy clearly suggests that chaotic dynamics could be generated in lasers, several investigations have been conducted to uncover chaos in laser systems [14–17] and in particular Lorenz-Haken chaos [18, 19]. In these studies it quickly appeared however that all kind of lasers - depending on their intrinsic properties - are not suited for chaos generation in a free-running configuration, i.e. without an additional external degree of freedom.

1.2.2 Semiconductor lasers as damped nonlinear oscillators

In Lorenz equations, all variables have comparable relaxation time-scales, i.e. all time constant parameters have roughly the same order of magnitude. In laser systems, however, this is not the case and some variables can evolve much faster than others. Because chaos requires at least three degrees of freedom [20], the fast relaxation of one variable, which can then be eliminated adiabatically, will prevent the emergence of chaotic dynamics. Three time constants can be identified in the Lorenz-Haken equations for lasers:

the photon lifetime T_p , the polarization relaxation time T_{pol} and the carrier lifetime or population inversion relaxation time T_e . Thus, in 1984, a simple classification of laser systems dependent on these time constants was suggested [9, 16]:

- Class C: when all the time-constants are of the same order of magnitude $T_p \sim T_{pol} \sim T_e$, the lasers are defined as class C. Single-mode class C lasers will, *à priori*, be described by the full set of Lorenz-Haken equations and are therefore candidates for chaos generation if all conditions are met. Class C lasers are typically NH_3 or $Ne - Xe$ lasers.
- Class B: when the polarization relaxes much faster than the other variables, i.e. $T_{pol} \ll (T_p, T_e)$, the corresponding equation can be adiabatically eliminated. The lasers are then defined as class B and can be modeled by two equations. A large range of devices are classified in this group, including semiconductor lasers, for which we typically find $T_p \approx 3$ ps and $T_e \approx 1$ ns, fiber laser or CO_2 lasers.
- Class A: when the photon lifetime largely exceeds the one of the polarization and of the population inversion, i.e. $T_p \gg (T_{pol}, T_e)$, only the field equation remains and we obtain class A lasers whose evolution can be described by a single equation. Visible $He - Ne$ lasers and dye lasers are classified in this category.

Although such classification is an obvious over-simplification, it gives useful insight on the dynamical behavior of the lasers. While Class C lasers are supposed to be the most complex ones, potentially chaotic, lasers of classes A & B are expected to be intrinsically stable as one or two variables relax much faster than the others. Thus, lasers of classes A & B will need additional degrees of freedom to generate complex dynamics and/or chaos.

With only two degrees of freedom, semiconductor lasers are generally expected to behave like under-damped oscillators - while class A lasers will be closer to over-damped oscillators - and can be modeled with two equations for the complex electrical field E and the carrier population N that can be written as follows in a fully normalized form [9]:

$$\frac{dE}{dt} = (1 - i\alpha)NE \quad (1.4)$$

$$T \frac{dN}{dt} = P - N - (2N + 1)|E|^2 \quad (1.5)$$

With P the normalized pump parameter, $T = T_e/T_{ph}$ the normalized carrier lifetime and α the linewidth enhancement factor (or α -factor) - which models the carrier-induced variations of the gain and of the refractive index. These equations are dimensionless and, in particular, normalized by the photon lifetime. Despite its apparent simplicity, this set of equations takes into account the main nonlinearities of laser diodes.

When subject to a current step, laser diodes will typically exhibit - as can be expected from under-damped oscillators - damped relaxation oscillations toward a stationary fixed point, and the frequency of these oscillations scales as a square-root of the injection current. With the theoretical model above, considering that the carrier lifetime is relatively large compared to the photon lifetime (typ. $T \approx 500 - 1000$), we can then approximate the pulsation of the relaxation oscillations to: $\omega_{RO} = \sqrt{\frac{2P}{T}}$. In real devices, the frequency of these oscillations is generally around 1-10 GHz. This intrinsic frequency is an essential feature as it generally gives the upper frequency limit that can be achieved through direct modulation of the injection current.

Because semiconductor lasers are driven by two nonlinear equations, only one additional degree of freedom is potentially sufficient to induce much more complex dynamical behavior. In practice this degree of freedom can take various forms such as direct modulation of the injection current, optical injection or time-delayed feedback. Interestingly, laser diodes appear to be quite sensitive to these external perturbations and can be easily destabilized toward self-pulsating dynamics or chaos.

1.2.3 Impact of time-delayed optical feedback

The effect of an optical feedback on the dynamics of a laser diode has been studied as early as the 1970s [21]. In fact, this study started as a very practical issue: when coupling the output of a semiconductor laser into an optical fiber, a small amount of the light could be fed back into the laser cavity hence inducing unexpected and undesired dynamical behaviors.

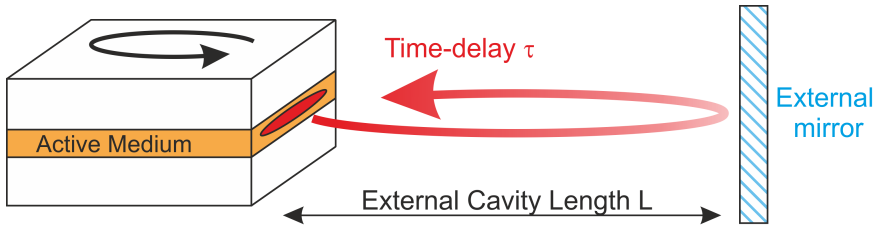


Figure 1.4 – **Scheme of a laser diode with external time-delayed optical feedback.** The output of the laser is reflected by an external mirror placed at a distance L , inducing a delay $\tau = 2L/c$, with c the celerity of light in the air. A small amount of the light - depending on the external mirror and the laser front facet reflectivities - is then fed back inside the laser diode cavity.

A simple scheme of the situation is depicted in Fig. 1.4 where we show an edge-emitting laser with an external cavity formed by an additional mirror. In the case of an unfiltered conventional feedback, the external cavity can be typically characterized by its length and the external mirror reflectivity. It is however important to remark that the amount of light being effectively fed back inside the laser cavity cannot be measured directly but requires indirect measurement such as threshold reduction. In practice, however, the reflectivity of the external mirror already provides a valuable insight.

Empirically, the dynamical behavior of semiconductor lasers when subject to optical feedback can be grossly classified in five different regimes as described in [9, 22] and pictured in Fig. 1.5. The feedback levels are indicated as the feedback ratio inside the cavity, that is the power effectively being fed back in the cavity, over the output power of the laser:

- Regime 1 - very small feedback (less than 0.001 %): small effects. Depending on the feedback phase, the linewidth becomes broader or narrower than the one of the solitary laser.
- Regime 2 - small feedback levels (less than 0.01 %): appearance of external cavity modes - stationary states whose frequency is shifted by a multiple of the external cavity frequency, i.e. $k \frac{c}{2L}$ with k an integer, L the cavity length and c the celerity of light - and the fast hopping between these modes produces a splitting of the optical frequency peaks.
- Regime 3 - narrow region for weak feedbacks (around $\sim 0.01\%$): restabilization of the laser and reduction of the laser linewidth.
- Regime 4 - moderate feedback levels (between 0.1 and 10%): undamped relaxation oscillations and large broadening of the emission line. Chaotic behaviors appear and might evolve up to the coherence collapse regime [23].
- Regime 5 - strong feedback regime (larger than 10 %): extended cavity regime where the external and internal cavities play the same role. This regime generally requires anti-reflective coating of the laser facet.

Although this classification is not detailed enough to account for the richness of the laser dynamics, it provides a fair description of the expected behavior of the laser. In particular, it shows that only a very small perturbation - as low as 0.1% - is sufficient to induce dynamical behaviors. Although this level is estimated as the feedback ratio inside the cavity, it can largely be achieved in practice and an isolation of about 40 dB is usually recommended to avoid any potential feedback effects [9].

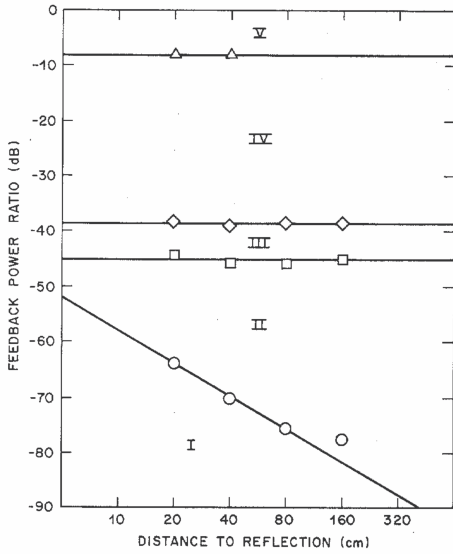


Figure 1.5 – Identification of the 5 different regimes for semiconductor lasers with optical time-delayed feedback. The different operating states are identified in the feedback power ratio versus external cavity length plane. Taken from [22].

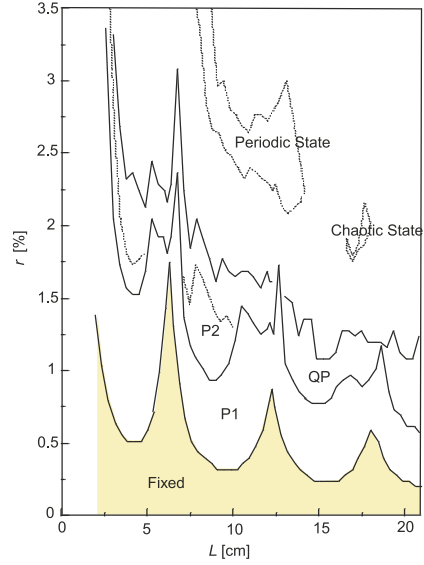


Figure 1.6 – Experimental periodic stabilization enhancement. Different regimes are identified in the reflectivity versus cavity length plane. Fixed: stationary state, P1 & P2: period 1 & 2 oscillations resp. and QP: quasi-periodic oscillations. Taken from [9].

In Fig. 1.5, only the first regime strongly depends on the external cavity length, but this simplified classification neglects in particular a periodicity related to the relaxation oscillation frequency. As shown in Fig. 1.6, when the external cavity frequency is in tune with the relaxation oscillation frequency, the laser exhibits a largely enhanced stability [9]; in particular the mirror reflectivity required to destabilize the stationary solution is largely increased. For larger external cavities however, this enhanced stability is much less pronounced as can be seen in Fig. 1.6. As a reminder, since the relaxation oscillation frequency depends on the injection current of the laser, this effect will depend on it as well.

So far, most of the studies focused on the so-called long cavity regime - i.e. when the time-delay is larger than the period of the relaxation oscillations. In the short cavity regime, the laser appears to behave quite differently, with enhanced stability and peculiar dynamics [9, 24]. A clear distinction between the two cases should therefore be considered.

Theoretically, one of the keystone has been the introduction of a relatively simple rate equation model, by Lang and Kobayashi in 1980, which appeared to accurately predict a large part of the dynamics uncovered [25]. In the context of the normalized model described previously, the model of Lang and Kobayashi includes one additional term accounting for the time-delayed optical feedback. As a result, the field equation now reads:

$$\frac{dE}{dt} = (1 - i\alpha)NE + \kappa e^{-i\omega_0\tau}E(t - \tau) \quad (1.6)$$

with τ the external round-trip time normalized by the photon lifetime, ω_0 the dimensionless frequency of the laser and κ the normalized feedback strength. The carrier equation is left unchanged. In this frame and as can be seen in the equation above, the feedback term takes into account a single round-trip in the external cavity and depends only on two parameters: 1/ the time-delay τ , i.e. the length of the external cavity and 2/ the feedback rate κ which relates to the amount of light being fed back in the laser cavity. This parameter directly depends on the reflectivity of the laser front facet and of the external mirror, but as mentioned above, in the experiment only the latter can be easily measured and tuned.

The feedback phase shift $e^{-i\omega_0\tau}$ which depends on the laser optical frequency generally has a limited impact on the dynamics - in the classification above, its effect mainly appears in regimes I to III - and in some theoretical studies the term is simply neglected or set to an arbitrary value, see e.g. [26]. In real life, it is quite obvious however that the phase-shift will induce a periodic dependence of the dynamics with respect to the external cavity length at the scale of a half-wavelength, i.e. typically below the micrometer scale. The factor 2 appears because the light makes a complete round trip of $2L$ in the external cavity before being fed back to the laser.

Finally, it should be mentioned that the α -factor also strongly influences the dynamics of the laser diode. To make it short, the smaller the α parameter is, the more stable the laser will be [27]. For typical semiconductor lasers, α ranges from 3 to 7 while gas lasers have an α -factor close to 0 [9]. Yet, we will see, in section 1.4, that these values are not valid anymore in the case of quantum dot laser diodes.

To conclude, typical laser diodes are expected to behave as under-damped oscillators, but external perturbations, such as time-delayed optical feedback, can easily destabilize them and induce various dynamical behaviors as they bring additional degrees of freedom to the system. In the next section, we will however see that internal/geometrical effects can also provide such additional degree of freedom and can be sufficient to induce various instabilities in laser diodes.

1.3 POLARIZATION INSTABILITIES IN VERTICAL-CAVITY SURFACE-EMITTING LASERS

Semiconductor lasers have seen many improvements since the early 70's, and their performances have been largely upgraded. In this process, one of the most important step has been the introduction of the Vertical-Cavity Surface-Emitting Laser (VCSEL). The interest for surface-emitting devices arose with the idea of heavy parallelization for e.g. computer optical interconnects. That motivated the development of high-density 2-dimensional arrays of laser devices, and obviously, because of their small size, high efficiency and convenient electrical pumping, semiconductor lasers were carefully considered. Yet the creation of 2D arrays is quite challenging if the devices are not emitting from the surface, i.e. in the direction normal with respect to the wafer surface. Thus, few designs were suggested - e.g. with an integrated mirror or grating - but the VCSEL structure was quickly demonstrated to be the most effective solution. However, its physics also uncovered a relatively unstable polarization which represents a severe drawback.

1.3.1 *From edge-emitting lasers to VCSELs*

The VCSEL structure has been first introduced and demonstrated in 1979 by Soda *et al.* [28]. As pictured in Fig. 1.7, EELs emit from the edge of the structure while VCSELs emit in the direction perpendicular to the active layer. The smaller active region potentially allows for lower threshold - in smaller active medium, the same current densities can be achieved with a lower total injection current - but the net gain is also severely reduced and therefore lower losses are required to achieve laser operation. Because of insufficient mirror reflectivities, the first VCSEL was only lasing at low temperature (77 K) and under large current densities requiring pulsed operation to avoid damages. An essential improvement then came from the introduction of Distributed Bragg Reflectors (DBRs) which allow for reflectivities of the order of 99.9 % - to be compared with the 98 % reflectivity of gold mirrors as used in [28]. Thanks to these new reflectors combined with quantum well technology, VCSELs finally reached continuous wave operation at room temperature in 1989 with a current threshold of only few milliamps [29].

Today, VCSELs are extremely common lasers and are used intensively, in particular for optical telecommunications. In addition to their low threshold and therefore low consumption, VCSELs also generally exhibit larger modulation bandwidth which makes them even more suited for telecommunication purposes. Their surface emission layout also greatly simplifies their production as it allows for on-chip testing and creation of 2D arrays. Finally, the typical circular geometry of VCSEL produces a circular beam which

can be better coupled into optical fibers. In summary, VCSELs exhibit almost all features required for optical communication, but they also exhibit a major drawback: polarization instabilities.

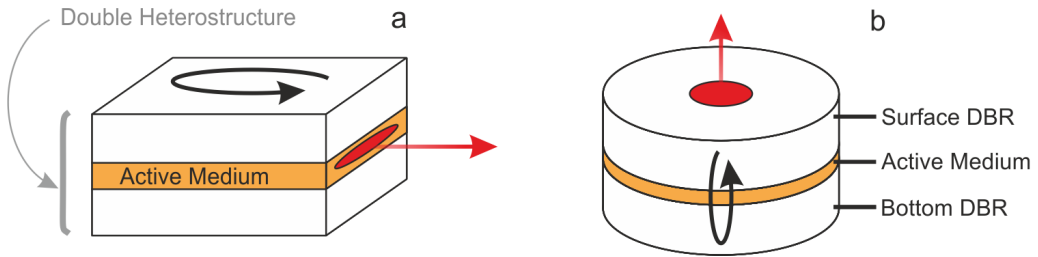


Figure 1.7 – **Schemes of typical edge-emitting laser and VCSEL structures.** (a) Scheme of an EEL structure with the active medium in between the two other layers forming the double heterostructure. The emission takes place on the side of the structure. (b) Scheme of a VCSEL with the cavity placed vertically between two DBRs and the output beam on the vertical axis.

1.3.2 Experimental observations of polarization instabilities in VCSELs

In EELs, the vertical linear polarization of the output beam is constrained by the geometry of the device. In contrast, as shown in Fig. 1.7, VCSELs typically exhibit a circular geometry that does not yield any rule for polarization selection. Nonetheless, a VCSEL will generally emit linearly polarized light at threshold due to the small anisotropies of the laser cavity, but they cannot fully compensate for the lack of geometrical selection. As a result, variations of the injection current, device temperature or strain can give rise to polarization instabilities.

As we will see here, such instabilities represent a severe drawback of the VCSEL structure as they dramatically alter the properties of the devices and can be especially harmful for polarization sensitive applications. For a recent and detailed review about these instabilities, see e.g. [30].

A solitary VCSEL usually exhibits two preferred orthogonal linearly polarized (LP) modes slightly separated in frequency - typically $\Delta f = 1 - 15$ GHz - due to the birefringence of the cavity [32]. At threshold, the laser generally emits linearly polarized light with a direction related to the crystallographic axes of the structure [33–35]. Increasing the current or changing the temperature can however lead to various polarization instabilities among which the most striking phenomenon is polarization switching (PS): the first LP mode, otherwise stable since threshold, is destabilized and, after some eventual

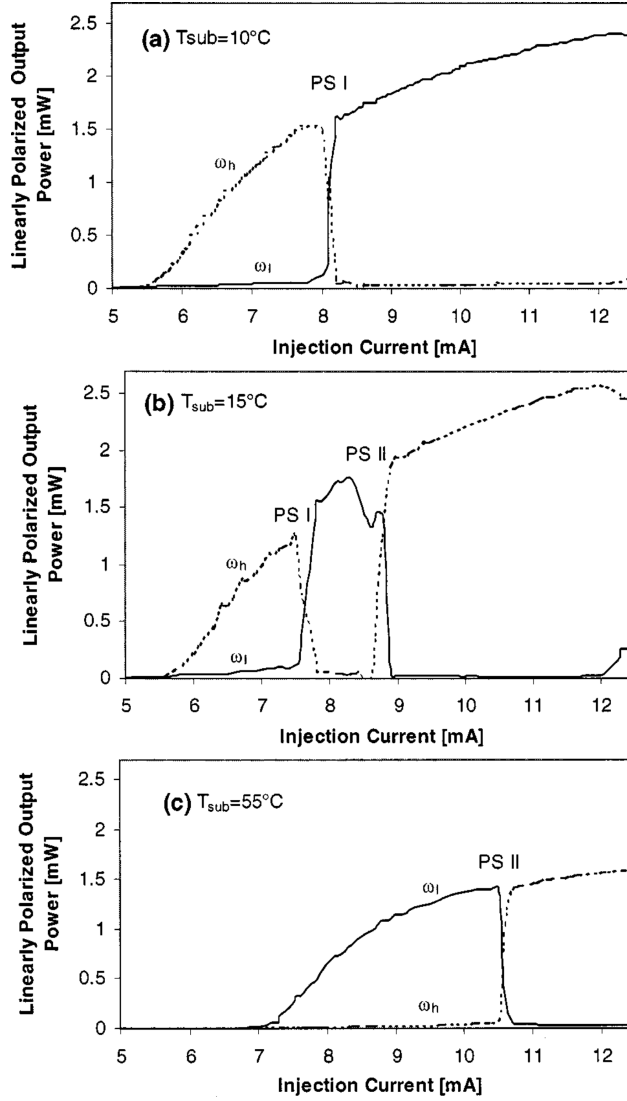


Figure 1.8 – **Details of the different types of polarization switchings.** Polarization-resolved optical output power versus DC injection current at three different substrate temperatures: (a) $T = 10^\circ\text{C}$ gives a PS of type I, (b) $T = 15^\circ\text{C}$ gives a double PS: type I then type II, (c) $T = 55^\circ\text{C}$ gives a PS of type II. HF (LF) is plotted in dashed (solid) line. Taken from [31].

complex dynamical transitions, the laser settles on the orthogonal LP mode. During the last twenty years, this astonishing dynamics has been largely studied and several different kinds of events, characteristics and features have been reported.

Polarization switching is typically reported for variations of the injection current or the substrate temperature - mainly because these are two parameters that can be easily modified -, but some experimental investigations also highlighted the crucial role of the strain applied to the device. Depending on the orientation and the strength of the applied strain, the anisotropies of the cavity will be altered hence changing the polarization instabilities. To that end, the creation of a hot-spot on the VCSEL outside the metal contact using an external beam has been proved to be efficient [35–37]. The orientation of the strain is determined by the position of the output beam and the temperature rise - measured by the spectral red-shift of the laser spectrum - controls the strength of the modification. Alternatively, one can also use mechanical techniques: when putting a small steel rod behind the wafer, the pressure applied by the laser holder induces some strain in the device. The strain orientation is then set by the rod orientation while its strength is controlled by the pressure applied through the laser holder [38,39].

Because the two orthogonal LP modes are detuned due to the linear birefringence of the cavity, we refer to them as the low-frequency (LF) and the high-frequency (HF) modes respectively. We can then identify two different types of polarization switchings: a switching from HF to LF mode is defined as type I while a switching from LF to HF mode will be identified as type II. A combination of these events have also been reported as a double PS: at first a type I switching occurs then followed by a PS of type II, see e.g. [31,40]. The different types of PSs have been summarized in Fig. 1.8 where the polarization resolved output power are plotted for three different situations: interestingly, as described in [31], in the investigated device the three PS types can appear just by changing the substrate temperature.

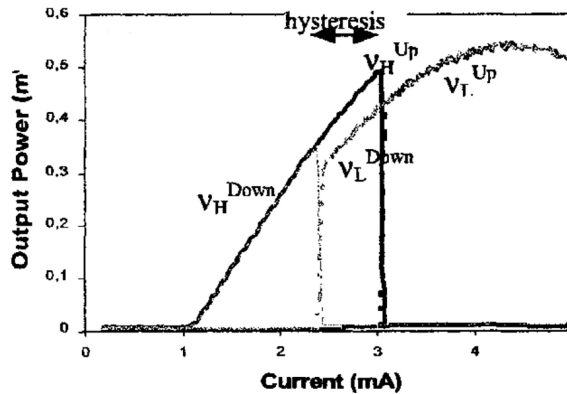


Figure 1.9 – Typical polarization switching of type I showing an hysteresis between the two LP modes. Polarization resolved output power evolution versus increasing (solid line) and decreasing (dashed line) injection currents. Taken from [39].

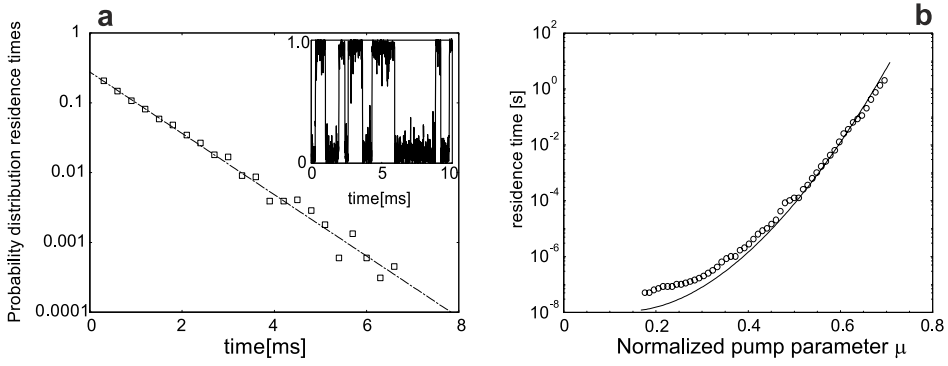


Figure 1.10 – **Characterization of the noise-induced hopping between orthogonal LP modes accompanying type I PS.** (a) Distribution of the dwell-time or residence time for a fixed injection current. The inset shows a typical part of the mode-hopping time-series. (b) Evolution of the average dwell-time for increasing injection currents. Taken from [41].

For a PS of type I, the VCSEL typically experiences an abrupt switching between the two orthogonal LP modes [31, 32, 40, 42–45], see Fig. 1.9. An overlap between the stability regions of the two modes can also appear, and typically leads to an hysteresis cycle unveiled when scanning this range of current back and forth. Such effect is also pictured in Fig. 1.9. In this region of bistability, and because the noise itself can be sufficient to push the laser from one mode to the other, a mode hopping dynamics can appear where the system continuously hops in time between the two orthogonal LP modes [41, 44–47]. In this context, some studies showed that the dynamics projected on the two polarization eigen-axes - i.e. the two preferred axes of polarization - are clearly anti-correlated [46, 47]. To characterize such noise-induced hopping dynamics, the statistical features of the residence time or dwell-time - i.e. the time between two successive jumps - have been considered. As shown in Fig. 1.10, the dwell-time exhibits an exponential distribution (a) and its mean value increases exponentially with the injection current (b), from hundreds of nanoseconds to seconds. This situation has been demonstrated to be accurately modeled as a 1D Kramer's hopping problem [41]: the laser system behaves like a particle in a double well of potential separated by a barrier of potential. The height of the barrier increases along with the injection current, thus explaining the rise of the average dwell-time shown in Fig. 1.10(b). This result confirms in particular the stochastic (noise-induced) origin of the mode hopping between the two orthogonal LP states that can be observed in the frame of a type I PS.

It should be noted that the bistability between the two LP modes cannot always be unveiled by scanning the injection current, i.e. the hysteresis cycle does not necessarily appear. Indeed, in the peculiar situation reported in [48], an injected pulse is required to switch to the other orthogonal polarization state. The underlying mechanism behind

this configuration has been identified as a pitchfork bifurcation; further details can be found in [49].

In Fig. 1.9, we also observe that the output power of the second mode is lower than that of the first one. This feature indicates that the system switches to the gain disfavored mode [50], which therefore suggests that the switching does not take place only because of a gain switching to the gain favored mode.

Finally, it is interesting to mention that type I PS can degenerate to two-mode emission near threshold at high temperatures [40]. In this case, the laser emits from both LF and HF modes at threshold, i.e. from both orthogonal LP modes at the same time. Although the polarization resolved time-series appear to be partially anti-correlated, the coexistence of the two modes is not the result of a mode-hopping as can be found in the vicinity of the switching point in type I PSs [40].

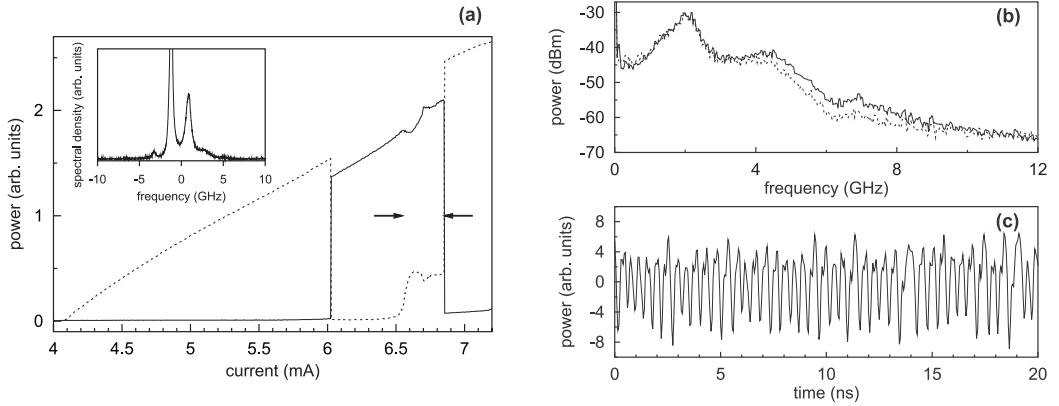


Figure 1.11 – **Dynamics accompanying a type II polarization switching.** (a) Polarization resolved LI curve showing the double PS scenario experienced by the laser; the two arrows indicate the region of nonlinear dynamics. The inset shows the optical spectrum inside this region for a current of 6.6 mA and after projection onto a linear polarization. (b) Radio-frequency spectrum recorded during another run of the experiment after projection onto the linear polarizations with maximum (solid) and minimum (dashed) DC-output. (c) Time-series of the dynamics after projection onto the linear polarization with maximum DC-output. Taken from [51].

PSs of type II, on the other hand, exhibit different features. Although they have been observed less often than type I PSs, they seem to typically exhibit a transition through elliptically polarized (EP) states and self-pulsing solutions before reaching the orthogonal LP mode at high currents [38, 51, 52]. As can be observed in Fig. 1.11(a), after the first type I PS, a strong increase of the extinct mode output power starting at 6.5 mA is observed. The polarization ellipticity strongly increases and the laser starts exhibiting self-pulsing dynamics, see Fig. 1.11(b) for the radio-frequency spectrum and (c) for a typi-

cal time-series. We clearly observe a strong peak in the radio-frequency spectrum around 2.1 GHz which relates to the splitting frequency between the two orthogonal modes - i.e. to the birefringence. Although it could not be entirely confirmed in this experiment, the pulsing-dynamics on orthogonal LP modes appears to be anti-correlated [51]. Finally, mode-hopping dynamics have also been uncovered in the case of Type II PS, but no further investigations have been conducted [52].

To a certain extent, the recent experimental reports of Olejniczak *et al.* [53, 54] can be assimilated as an incomplete type II polarization switching. Indeed in these two experimental studies, the authors report on a peculiar evolution in a quantum dot VCSEL: at threshold the laser emits linearly polarized light, but increasing the injection current leads to the emergence of an EP state, and then a large transition of self-pulsing dynamics including mode hopping. Although no final switching toward the orthogonal LP mode appears in a reasonable range of currents - the laser ends up on a two-mode emission - and the characteristic frequency of the dynamics relates to the relaxation oscillation frequency of the laser - instead of the birefringence frequency as in [51] -, this bifurcation scenario clearly shows some similarities with the specific features described for type II PSs. What is more surprising however is that the mode hopping dynamics reported in [53, 54] takes place between two non-orthogonal elliptically polarized modes with main axes being symmetrical with respect to the axis of linear polarization at threshold. On top of that, the evolution of the dwell-time is opposed to the one of the noise-induced hopping dynamics observed in type I PS: the average dwell-time **dramatically decreases** from seconds to nanoseconds time-scales for increasing injection currents whereas **an exponential increase** is observed for the stochastic mode hopping between orthogonal LP modes reported for type I PSs. Thus, even though the experimental observations unveiled some of the specific features of a type II PS, the surprising characteristics of the mode hopping dynamics between non-orthogonal EP states call for an alternative interpretation than that of a noise-induced hopping.

1.3.3 Theoretical interpretation of polarization instabilities

Since the first reports on polarization instabilities, several theoretical approaches have been considered to model and understand the experimental observations described above. In the mechanisms suggested to describe the phenomenon of PSs we distinguish two distinct approaches: 1/ “Static” mechanisms - not time-dependent - where the switchings are induced by different evolutions of the gain spectrum or the modal gains of the two orthogonal LP modes, e.g. because of the stress or the temperature. 2/ “dynamical” - time dependent - mechanisms where the switchings are the result of the system inter-

nal dynamics. Obviously, dynamical models are required to obtain self-pulsations and mode-hopping dynamics, but “static” approaches provide essential information on different key underlying mechanisms for PSs.

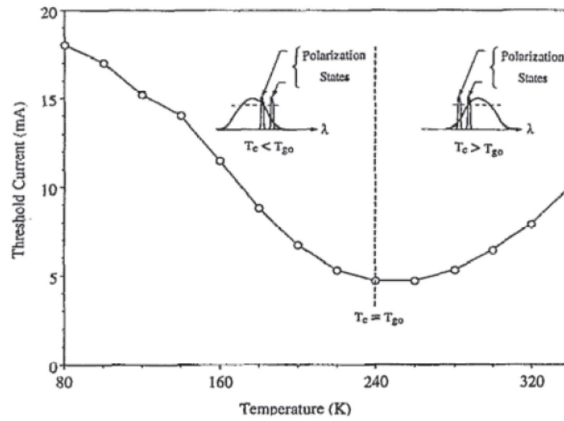


Figure 1.12 – **Impact of the spectral red-shift of the gain.** Threshold current versus substrate temperature; the minimum threshold appears at $T_{g0} = 240$ K and the inset shows the corresponding evolution of the gain curve with respect to the two polarization modes. Taken from [32].

The first “static” mechanism which has been suggested is of thermal origin and is linked to the current induced self-heating in the laser cavity. Increasing the current induces a rise of temperature in the laser cavity, hence a spectral red-shift of the gain [32,34]. Because of their slight detuning the two polarization modes do not experience the same gain, and therefore one mode experiences a higher gain than the other. As a result, a sufficiently large shift of the gain frequency would invert the situation hence inducing a switching between the two modes, see Fig. 1.12. This mechanism alone can only explain a type I switching, but including the evolution of the losses, as in [31], can explain all the reported kinds of switchings, including double switching scenarios.

Alternatively, another mechanism based on current induced self-heating, so-called thermal lensing, has been proposed [43]. In this case, it is expected that the current heating will change the transverse refractive index and create a thermal lens. This waveguide then modifies the confinement factor of the modes, and a PS can appear due to different evolutions of the modal gains for the two LP modes. This effect however only explains type I switching.

The last “static” mechanism we will discuss here is spatial hole burning which can play a significant role in multi-transverse mode devices [55,56]. Basically, the lasing mode will locally consume almost all carriers hence diminishing the available local gain: it creates

a spatial gain hole. This effect can then induce a polarization switching if the modal gain of another transverse mode with orthogonal polarization finally exceeds the modal gain of the fundamental mode.

Although thermal effects are supported by some experimental observations - in particular the limited frequency response of the switching dynamics [53, 57, 58] - some others clearly highlighted that polarization switchings could also occur without any evolution of the active region temperature [59] or in such wide range of temperatures that thermal evolution should probably be ruled out [50].

In contrast to the “static” mechanisms, the “dynamical” interpretations do not rely on a single mechanism but consider the dynamical and interdependent evolution of the different variables of the system; the latter being modeled by a set of time-dependent nonlinear equations. At first, analogies were made with EELs hence introducing a two polarization-mode model with a single carrier population [49]. This relatively raw description was mainly used to model the effects of gain nonlinearities that would lead to PS dynamics. In this framework, several PS features have been accurately reproduced, such as polarization hopping between orthogonal LP modes [44, 45], PS frequency response evolution [58], and effects of the nonlinear gain [60].

Yet, a more comprehensive model relevant for quantum well VCSELs has quickly been introduced: the Spin-Flip Model (SFM) presented in 1995 by San Miguel, Feng and Moloney [61]. The paradigm-shift of this approach is that it takes into account the spin-flip relaxation processes of the carriers - see Refs. [30, 61] and references therein for details - which makes it relevant to quantum well devices. Some made the hypothesis that the time-scale of the spin-flip processes was small enough for adiabatically eliminating them from the equations [62], and have demonstrated that essential features were still accurately reproduced [41, 47, 63, 64]. However a wide range of spin-flip times were experimentally reported using time-resolved pump-probe measurements: from few tens of picoseconds [65, 66], to few hundreds of picoseconds [67, 68]. In the latter case, the spin-flip dynamics can no longer be eliminated as its time-scale cannot be neglected when compared to the carrier lifetime which is typically of the order of a few nanoseconds. A different reduction of the SFM model to only two variables has also been proposed using asymptotic methods and similarly strong approximations [69].

With no anisotropies in the laser cavity - i.e. for a fully isotropic VCSEL - the SFM model predicts that a laser will emit linearly polarized light [70]. However when considering anisotropies in the cavity [71, 72], type I and type II switchings can be easily highlighted [70, 73]; double PS however can only be reproduced when taking into account gain saturation [74]. The scenario of type II PSs with a transition through EP states and dynamics at the birefringence frequency is also accurately reproduced [51, 70], as is the two-mode emission near threshold [40, 70]. Other features, such as a cascade of

three Hopf bifurcations for large birefringence and stochastic hopping between LP and EP states, have also been unveiled theoretically but remain to be confirmed experimentally [75]. Interestingly a frequency shift in the noise spectrum has also been theoretically uncovered and linked to saturation effects and spin-flip time-scales [76]. Finally, the SFM model has also been completed to take into account additional phenomenons such as gain-saturation [74], anisotropy misalignment [77], or stress and thermal effects [78–80]. In the end, “dynamical” interpretations have been demonstrated to accurately reproduce the essential dynamical features observed in experiments: in particular the stochastic hopping between the two orthogonal LPs or the dynamical scenario of type II PSs. However, the importance of considering the spin-flip processes has not been fully confirmed. Indeed no specific feature predicted only by the complete SFM model - such as the three Hopf bifurcation cascade [75] - has been unveiled so far; therefore the role of the spin-flip time on the polarization instabilities of VCSELs still remains to be clarified.

1.4 QUANTUM DOT LASER DIODES

In the previous section, we briefly stated that the introduction of Quantum Wells (QWs) - i.e. an active layer thin enough to confine the carriers to its 2-dimensional plane - as the active region of VCSELs allowed to reach continuous emission at room temperature [29]. As pictured in Fig. 1.13, confining a material reduces the available energy levels and thus can largely increase the amount of available carriers at a given level. Using QWs as the active region in laser diodes has clearly been one of the major step forward in semiconductor laser technology - with the introduction of the VCSEL structure - which dramatically improved the performances of devices and is now largely considered as standard. But, considering that one-dimension confinement already greatly improves the devices, it is quite straightforward to think that 2 or 3-dimension confinement - leading to quantum wires and quantum dots (QDs) respectively with the corresponding band structures displayed in Fig. 1.13 - might push the performances even further.

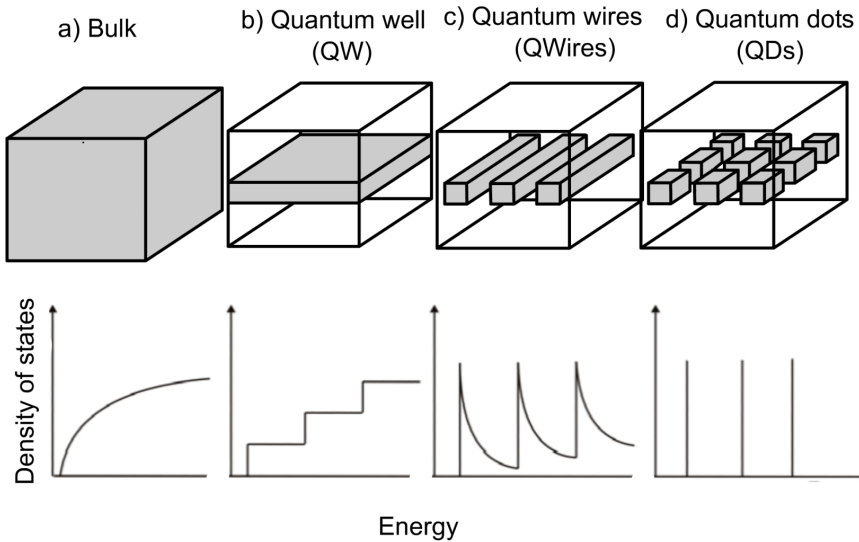


Figure 1.13 – **Impact of the confinement on the material band structure.** For the bulk material (a), the density of states evolves continuously. Confining the material in one direction to a quantum well (b) creates a step distribution. A confinement in two dimension makes the distribution shrinks (c), up to a discrete distribution for a three dimension confinement, i.e. for quantum dots (d).

1.4.1 *Quantum dots as a gain medium*

Because the energy levels of quantum dots are discrete - similarly to single atoms - their use as active regions in lasers were theoretically shown to exhibit extremely high differential gain, ultra-low threshold, perfect temperature stability and large modulation bandwidth; in a nutshell, they could be the perfect laser diodes [81]. These conclusions were however obtained using extremely strong assumptions - such as identical dots or single energy levels - that were rapidly disproved in real devices [82].

Whereas the quality of QW lasers benefited from the large development of epitaxial processes, the manufacturing of quantum dot devices appeared to be much more challenging. As mentioned in [82,83], an important breakthrough was the discovery of the self-organization effect: taking advantage of the strain induced by lattice-mismatch, a precise deposition process can lead to the formation of three-dimensional islands created by the relaxation of the accumulated strain. For lasers in the 0.8-1.3 μm wavelength range, two procedures are typically considered: 1/ The Stranski-Krastanov method that leads to the formation of a so-called wetting layer - i.e. a thin 2-dimensional layer formed before the accumulated strain is sufficient to induce the formation of 3-dimensional islands [84] -, and 2/ the so-called submonolayer deposition where the wetting-layer formation is avoided by a non-uniform deposition [85].

Self-organized processes typically result in random positions and sizes of the quantum dots, and relatively large distributions have been reported, see e.g. Fig. 1 in [86]. Because different dot sizes imply different energy gaps (and therefore different emission frequencies), such distribution induces inhomogeneous broadening which deteriorates the performances of the lasers. At this point, it is worth noting that, although great progress has been made to improve the uniformity of the dots, some alternative techniques have been developed to prevent this effect by creating patterned quantum dot structures [84]. Additional complexity also arises from other factors such as the need to consider one or more excited states [82], or the small confinement factor [83].

In terms of performances, the last 10 years saw a great improvement for QD lasers [82]. In particular we can mention low threshold current densities - down to only 13 A/cm² [87] - and large modulation bandwidths - more than 20 GHz at 1 μm [88], and 12 GHz in the 1.3 μm telecommunication band [89]. However, despite these improvements, the best laser performances today are still obtained using quantum well laser structures. Nevertheless, quantum dot laser diodes also attracted a huge interest because of their specific dynamical properties. In particular, the complex capture and escape processes in the dot structure seem to induce new features and behaviors. As a result, the nonlinear dynamics community has quickly considered these devices as a source of new physics.

1.4.2 *Dynamical properties of quantum dot lasers*

From a dynamical viewpoint, the main difference distinguishing QD lasers from their QW counterpart is the description of the carrier dynamics. Whereas in QW devices a single equation for the carriers was sufficient, a proper description of QD devices requires to take into account the different dynamics of electrons and holes but also the contribution of the excited state(s) and the eventual wetting layer as additional energy levels [90–92].

Experimentally, it appeared that QD lasers tend to exhibit highly damped relaxation oscillations compared to regular semiconductor lasers [93], see e.g. Fig. 1.14(a). This high-damping has been linked to the presence of multiple energy levels for carriers and its impact on the carrier dynamics [90, 94]: simulated time-series using the detailed model described in [90] are plotted in Fig. 1.14(b) and clearly show a good agreement with experimental results in (a). At the same time, the large damping suggests that QD laser devices might actually be somewhere between class A and class B lasers. As mentioned earlier, class B lasers are expected to behave like under-damped oscillators while class A lasers would be over-damped oscillators: typically class-B lasers will oscillate toward a stable steady-state whereas class-A lasers will approach it exponentially. Moreover class-A like behaviors of QD devices have been reported both theoretically and experimentally in optically injected devices [95, 96], hence suggesting that despite the increased internal complexity of QD lasers a single equation might be sufficient to describe their evolution.

In terms of stability, the use of QDs instead of QWs has also been expected to make devices with an almost zero α -factor possible. As already mentioned, a smaller α -factor would yield more stable and more robust devices, especially against external perturbations such as optical feedback. In practice, a large range of α -factor values have been reported - from close to 0 [97, 98], to almost 60 [99] - and it appeared that different operating conditions would lead to largely different values, hence explaining the observed discrepancy [100]. Interestingly, a very recent report also suggests that the same conclusion hold for regular semiconductor lasers but with much smaller variations [101]. On the other hand, theoretical investigations showed that a fixed value for the linewidth enhancement factor is, in fact, not accurate enough to describe the carrier induce refractive index changes in QD devices [102]. Even though differences arise only for the most complex dynamics and/or chaotic behaviors, a more detailed and comprehensive model seems to be required in order to obtain a precise modeling of these dynamics.

Nevertheless, in agreement with the expectations of small α devices, enhanced robustness against optical feedback has been demonstrated in QD lasers [103–105], as an example the emergence of coherence collapse has been reported for feedback levels as high

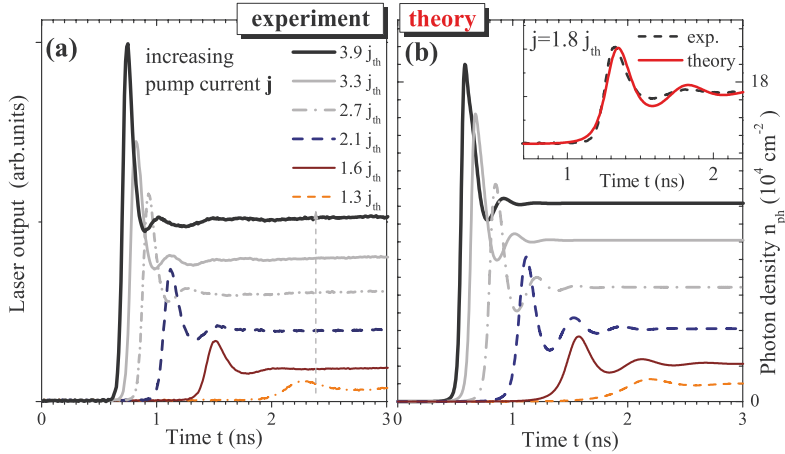


Figure 1.14 – **Turn-on dynamics of a QD laser showing strongly damped relaxation oscillations.** (a) Experimental measurements and (b) simulated data for various injection currents from 1.3 to 3.9 times the current threshold j_{th} . The inset shows the detail of the turn-on at $1.8j_{th}$ for both experimental (dashed black) and simulated (solid red) time-series. Taken from [90].

as -8 dB [103], to be compared to -20/-30 dB feedback levels that are generally expected for quantum well lasers. Interestingly, the reduced sensitivity to feedback has also been linked to the high-damping observed in QD lasers [104].

1.4.3 Simultaneous emission from the ground and the excited states

Although some QD lasers might exhibit class-A like behaviors, which suggests that they could be described by a single equation, the importance of the excited states on laser dynamics should not be neglected. Indeed, it represents one additional energy level for the carriers before reaching the ground state and the intraband relaxation time can therefore influence the lasing process. For instance, it has been demonstrated that in an optical injection scheme, this relaxation time can increase or decrease the size of the locking region, hence modifying the excitability characteristics of the system [107]. Yet the most striking feature is that, because of this additional level, QD lasers can also emit simultaneously from the ground (GS) and the excited states (ES), i.e. simultaneously at two distinct and largely separated optical frequencies [106,108]. This property attracted a relatively large attention especially as it opens the way toward several applications such as THz generation [109–111], or two-color mode locking [112,113].

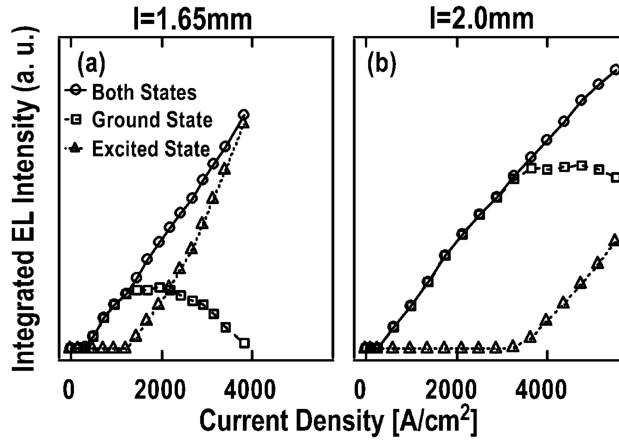


Figure 1.15 – State resolved LI curve of a QD laser emitting from the GS and ES simultaneously. Evolution of the emission for two devices with different cavity lengths - 1.65 mm (a) and 2.0 mm (b) - versus current density. At threshold, the laser only emits from the GS, but an increase of the current leads to a saturation of the GS and the emergence of ES emission. In (a), larger injection currents lead to a decrease of the GS emission, until it completely vanishes and the laser only emits from the ES. Taken from [106].

In Fig. 1.15, we show the state resolved LI curve of a QD laser showing simultaneous GS-ES emission. At low injection currents, close to the threshold, the laser only emits in the GS. When the injection current is increased, the GS emission saturates and, because the carriers cannot relax toward the GS anymore, they are accumulated on the ES which starts lasing. Then, for higher injection currents, the ES becomes the dominant mode, consuming all the carriers, making the GS emission to vanish: this effect has been referred to as *GS quenching*.

Using standard rate equations, the saturation of the GS and the emergence of the ES-emission has been successfully demonstrated, see e.g. Fig. 1 of Ref. [114], but the GS quenching does not appear and the output power of the GS emission remains constant at high currents. To reproduce accurately this behavior, separate electron and hole dynamics - and in particular different escape rates - need to be considered [115]. It should also be mentioned that, in this context, it has been shown that the evolution of the relaxation oscillation frequency with the current is largely impacted by the emergence of the ES emission [116]; so far these results have however not been confirmed experimentally.

Recently, a more complete model also taking into account separated electron and hole dynamics has been introduced [117]. Although this study essentially confirms and complete the work described in [115], it also brings new light on the turn-on dynamics of the GS-ES simultaneous emission. As plotted in Fig. 1.16, at first the laser looks like it

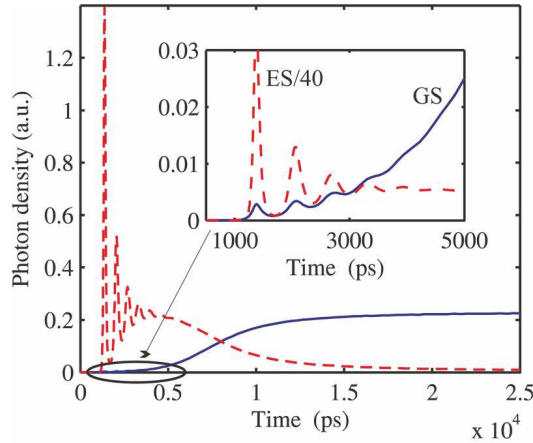


Figure 1.16 – **Turn on dynamics of QD laser emitting from GS and ES simultaneously.** The GS evolution is displayed as a blue solid line while ES evolution is shown as a red dashed line. The inset presents a detail of the GS turn-on dynamics with the ES time-series divided by a factor 40 to help the comparison. Taken from [117].

only emits from the ES, and strongly oscillates toward an unstable steady-state. In fact, the two modes start lasing at the same time - see inset of Fig. 1.14 -, but since the ES has a larger differential gain and that it collects the carriers first, the ES emission dominates. Then, after about 5 nanoseconds, a switching between GS and ES emission occurs; the GS emission consumes the carrier faster as its output power increases, and thus starts depleting the ES level. At last, the emission from the ES completely vanishes as the carriers are fully sucked out by the GS emission and the system reaches the stable steady-state. Similar transient behaviors, showing a good agreement with the theoretical results, have been experimentally reported [118,119].

In the end, QD lasers are exciting and surprising new devices showing increased complexity and at the same time, a more stable behavior closer to class A lasers than any other semiconductor lasers. In addition, their ability to emit simultaneously from the ground and excited state is an exclusive and astonishing feature, with a large range of potential applications. Yet the underlying mechanisms and dynamical properties of this feature still remain to be clarified. Interesting behaviors have been reported in QD laser emitting simultaneously from the GS and ES with optical injection schemes; both in theory [107], and in experiment [120]. But very few studies were conducted to analyze the impact of optical feedback on such lasers [110,121,122], especially, and in contrast with the case of optical injection, no in-depth investigation of the dynamical evolution has been made so far.

1.5 OUTLINES OF THE THESIS

The work in this thesis is devoted to two distinct topics sharing a strong focus on the nonlinear dynamics of quantum dot devices. On one side, we investigate the dynamics of free-running quantum dot VCSELs. In particular, we perform both theoretical and experimental work in order to provide a clear viewpoint and to explain the peculiar dynamics recently reported by Olejniczak *et al.* [53, 54]. On the other side, we make an in-depth analysis of the impact of a time-delayed optical feedback on the dynamics of a quantum dot laser emitting simultaneously from the ground and the excited state. This thesis will therefore be organized as follows.

In chapter 2, we study the nonlinear dynamics of free-running QD VCSELs induced by polarization instabilities. First, we provide a detailed description of the SFM model including its steady-states, main bifurcations and we present the figures of merit we will use in the rest of the chapter. Second, we perform an in-depth analysis of the dynamics predicted in the frame of the SFM model. Even though it was designed to model quantum well devices and not quantum dot ones, we successfully reproduce the dynamics and the bifurcation scenario reported experimentally in the QD devices [54]. At the same time, we unveil a different scenario matching all the dynamical features accompanying the type II switching in a QW laser described in [51]. We therefore demonstrate that the SFM model provides a unifying framework to describe the dynamics accompanying polarization instabilities and switchings in VCSELs. Third, we propose a deterministic interpretation of the random-like hopping dynamics reported in [54]. We show that the chaotic dynamics predicted by the SFM model yield a double-scroll attractor with the two scrolls oscillating around unstable EP states. Thus, this chaotic (deterministic) dynamics can be interpreted as a random-like hopping between two EP states. We demonstrate that all the features reported experimentally are reproduced - in particular the statistical evolution of the dwell-time - and report a bifurcation scenario in perfect agreement with the experimental reports. Fourth, we confirm the deterministic nature of the experimental dynamics. Using several algorithms, we unambiguously prove that the laser diode produces chaotic polarization fluctuations, hence providing the first demonstration of a free-running single-mode laser diode turning into temporal chaos without the need for external perturbation or forcing. Fifth, in the same devices, we unveil a bistability of limit cycles oscillating around different EP states. We demonstrate that this result implies some symmetry-breaking in the laser cavity. We then obtain theoretically

a good qualitative agreement by considering a small misalignment between the phase and amplitude anisotropy. This result therefore confirms again the validity of the SFM in reproducing the details of the reported polarization dynamics.

Following the discovery of polarization chaos in a free-running laser diode, we investigate the potential applications of the dynamics in chapter 3 and make a proof of concept of a polarization chaos based random bit generator (RBG). Considering the specificity of this field, we first provide a brief state of the art of optical chaos-based RBG. In particular, we present the empirical requirements reported to obtain random bits at high-speed and argue about the potential interest of exploiting the chaos from a free-running laser. Then, we present in detail our experimental setup and point out the main issues with the proposed scheme. Especially, we highlight the fact that polarization chaos dynamics is clearly not optimal according to the empirical requirements. Nevertheless, in the following section, we report on a successful generation of random sequences at high-speed (> 100 Gbps) and describe the impact of the post-processing on the randomness of the output sequences. Finally, we perform a theoretical investigation to explain the surprisingly good performances obtained. Thus we demonstrate that the low-pass filtering induced by the limited bandwidth of the acquisition electronics plays a significant role in achieving the generation of random sequences at high-speed.

In chapter 4, we investigate the impact of a time-delayed optical feedback on a quantum dot laser emitting simultaneously from the ground and the excited states. First, we provide a brief state-of-the-art on this topic. Although only few studies focused on the effect of an optical feedback on such system, we remind the results uncovered so far. Second, we present the theoretical model we will use along with the approximations made. We describe analytically the four steady-states of the model and bring new light on their stability. Third, we describe the behavior of the solitary laser diode and demonstrate a good agreement with experimental reports. Especially, we complete other experimental and theoretical works by identifying the bifurcations connecting the different steady-states involved. Fourth, we show that the optical feedback can induce a switching from the ground to the excited state emission. Although on a global scale, the feedback favors the ground state emission, a fine tuning of the feedback strength allows to select the output emission state. In addition, we highlight external cavity modes of the ground state and unveil large bistability regions with the fundamental mode of the excited state emission. Fifth, we study the impact of various parameters on the switching dynamics uncovered previously. We focus on the impact of external cavity length and electron escape rate. We highlight periodic evolution of the dynamics - with a period related to the laser wavelength - with respect to the external cavity length. We demonstrate that this effect is directly induced by an interplay between the different feedback phase

evolution for the ground and excited state emission. We also show that, when changing the electron escape rate so that the laser emits from the excited state directly at threshold, the switching dynamics is not significantly altered even though the selection of the two modes at threshold is inverted. Sixth, we perform an experimental analysis of the effect of optical feedback on quantum dot lasers emitting from the ground and the excited states simultaneously. For starter, we describe the experiment that has been set up at TU Darmstadt. Then, we report interesting experimental observations that confirms the switching dynamics theoretically predicted in this chapter. In particular, we report an incomplete periodical switching obtained using piezo-electric actuators: the periodicity of the dynamics relates to the wavelength of the modes, hence supporting the features uncovered theoretically.

Finally, we conclude in chapter 5. We summarize the main results and achievements of the work presented in this manuscript along with the perspectives for future investigations.

2

DETERMINISTIC POLARIZATION CHAOS

*The most exciting phrase to hear in science,
the one that heralds the most discoveries,
is not “Eureka!” but “That’s funny...”*

— Isaac Asimov

In this chapter, we focus on the dynamical behavior of free-running quantum dot VCSELs. We report new dynamics such as polarization chaos and bistability of self-pulsating dynamics. We also provide new evidence of the validity of the spin-flip model (SFM) framework. The chapter will therefore be organized as follows: in section 2.1 we describe in details the SFM and the essential underlying mechanisms that it considers. Then in section 2.2, we demonstrate that this theoretical framework predicts a large number of possible bifurcation scenarios and shows qualitative agreement with experimental reports of dynamics accompanying polarization switchings. In section 2.3, we focus on the random-like hopping between elliptically polarized states reported by Olejniczak *et al.* [54]: we confirm that this dynamics cannot be explained as a noise-induced hopping and provide a chaotic interpretation in the SFM framework that matches all the experimental features. Based on experimentally recorded time-series, we then unambiguously demonstrate in section 2.4 that this mode-hopping dynamics is indeed chaos, hence demonstrating the first temporal chaotic output from a free-running laser diode, i.e. without any external perturbation or forcing. In section 2.5, we report a bistability of limit cycles in the chaotic devices and demonstrate that such phenomenon can be accurately described by taking into account a small misalignment between cavity anisotropies. Finally, we sum up, discuss the results and the perspectives of this work in section 2.6.

Some of the materials presented in this chapter have been already published in [123–129].

2.1 DESCRIPTION OF THE SPIN-FLIP MODEL

As already discussed in section 1.3, the main drawback of VCSELs is the polarization instabilities that arise due to their typical circular geometry. Yet, they generally emit linearly polarized (LP) light at threshold, but when varying the injection current or the temperature, the stable LP mode at threshold can be destabilized and the laser will switch to the orthogonal polarization mode: a so-called Polarization Switching (PS). The two preferred orthogonal LP modes typically exhibit a slight detuning due to the birefringence of the laser cavity, and are therefore referred to as the “low frequency” (LF) and “high-frequency” (HF) modes respectively. As discussed in section 1.3, the PSs can then be classified in two different categories that exhibit very distinct features [31]: type I/ the laser switches from HF to LF mode and type II/ the laser switches from LF to HF mode.

To describe and explain these instabilities, several theoretical approaches - considering various physical mechanisms - have been suggested. In the work presented in this thesis, we focus on the dynamical instabilities accompanying polarization switching events and we therefore choose a comprehensive time-dependent description of VCSEL dynamics: the spin-flip model (SFM). Introduced by San Miguel, Feng and Moloney in 1995, this model has been shown to efficiently describe several essential dynamical features of VCSELs [61,70].

2.1.1 SFM equations

The essential idea behind the SFM is to consider separately the photon generated by the recombination of spin up (\uparrow) and spin down (\downarrow) electrons and holes, i.e. the generation of right (+) and left (-) circularly polarized light. Two carrier reservoirs are defined, for spin up (\uparrow) and spin down (\downarrow) carriers respectively, coupled by a single decay rate that models the complex microscopic spin-flip relaxation processes equilibrating the carrier population, see e.g. [61]. We obtain a four level model as pictured in Fig. 2.1, and the four-equation model then writes as follows, in terms of the slowly varying mean electric field amplitude E_{\pm} [70]:

$$\frac{dE_{\pm}}{dt} = \kappa(1 + i\alpha)(N \pm n - 1)E_{\pm} - (i\gamma_p + \gamma_a)E_{\mp} \quad (2.1)$$

$$\frac{dN}{dt} = -\gamma \left(N - \mu + (N + n)|E_+|^2 + (N - n)|E_-|^2 \right) \quad (2.2)$$

$$\frac{dn}{dt} = -\gamma_s n - \gamma \left((N + n)|E_+|^2 - (N - n)|E_-|^2 \right) \quad (2.3)$$

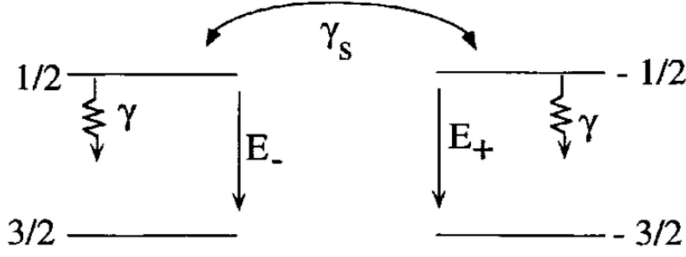


Figure 2.1 – **Four-level description of the SFM model.** The two separated carrier reservoirs for spin up and spin down electrons and holes are only connected through the spin-flip relaxation processes γ_s . Taken from [70].

The carrier populations of the two reservoirs, D_+ and D_- respectively, are described by two variables: $N = D_+ + D_-$ the normalized total carrier population and $n = D_+ - D_-$ the normalized carrier population difference. κ is the decay rate of the electric field in the cavity, α is the linewidth enhancement factor, and μ is the normalized injection current. The decay rate of the total carrier population is γ while γ_s is the decay rate modeling the spin-flip relaxation processes. The linear phase and amplitude anisotropies are modeled by γ_p and γ_a respectively. In eqs. (2.1)-(2.3), we also applied an additional frequency shift of $\omega_0 = \kappa\alpha$ which leads to a zero emission frequency at threshold for E_{\pm} when no anisotropy is considered, i.e. for $\gamma_a = 0$ and $\gamma_p = 0$.

In terms of real variables, the SFM is a set of six equations, but only the phase difference between the right and left circularly polarized fields is essential. Hence, using a phase-amplitude decomposition of the field terms $E_{\pm} = R_{\pm}e^{i\Psi_{\pm}}$ as in [69], we can describe the VCSEL evolution with only 5 inter-dependent equations considering only the phase difference $\Phi = \Psi_+ - \Psi_-$:

$$\frac{dR_+}{dt} = \kappa(N + n - 1)R_+ - (\gamma_a \cos(\Phi) + \gamma_p \sin(\Phi)) R_- \quad (2.4)$$

$$\frac{dR_-}{dt} = \kappa(N - n - 1)R_- - (\gamma_a \cos(\Phi) - \gamma_p \sin(\Phi)) R_+ \quad (2.5)$$

$$\frac{d\Phi}{dt} = 2\kappa\alpha n - \left(\frac{R_-}{R_+} - \frac{R_+}{R_-}\right) \gamma_p \cos(\Phi) + \left(\frac{R_-}{R_+} + \frac{R_+}{R_-}\right) \gamma_a \sin(\Phi) \quad (2.6)$$

$$\frac{dN}{dt} = -\gamma \left(N - \mu + (N + n)R_+^2 + (N - n)R_-^2 \right) \quad (2.7)$$

$$\frac{dn}{dt} = -\gamma_s n - \gamma \left((N + n)R_+^2 - (N - n)R_-^2 \right) \quad (2.8)$$

It should be noted however that to obtain reliable optical spectra from numerical integration, one of the discarded phase must be considered for the evolution of the field variable. Indeed, the phase term evolution gives the optical frequency of the system - with respect to $\omega_0 = \kappa\alpha$.

On a more practical side, it is important to note that the circular polarizations E_+ and E_- relate to the horizontal E_x and vertical E_y polarizations with the following relationships:

$$E_x = \frac{E_+ + E_-}{\sqrt{2}} \quad \text{and} \quad E_y = -i \frac{E_+ - E_-}{\sqrt{2}} \quad (2.9)$$

Equations (2.4)-(2.8) can then be expressed in terms of the linearly instead of the circularly polarized light components. The corresponding equations can be found e.g. in [70].

Finally, in the description above the injection current is normalized but time-related parameters - such as γ_a , γ_p , or γ_s - are not. A time normalization can be easily performed by removing the carrier lifetime parameter: γ . With this minimal change, the SFM parameters become all normalized in time by the carrier lifetime. In practice, the parameters of the normalized and un-normalized equations are identical when expressed in ns^{-1} and for $\gamma = 1 \text{ ns}^{-1}$.

In this dissertation, we will mainly use the un-normalized set of equations and always with $\gamma = 1 \text{ ns}^{-1}$. In section 2.5, however, we will use a fully normalized version of the SFM. But, as explained above, the same parameters can be used in both systems.

2.1.2 Steady-states of the SFM

The equations are symmetric with respect to the right and left circularly polarized light emissions and to the anisotropy term ($i\gamma_p + \gamma_a$). Changing the sign of the latter will therefore simply exchange the role of the two linearly polarized light components, i.e. reverse the X and Y axis. We can therefore limit our analysis to $\gamma_p > 0$; the results can then be transposed to $\gamma_p < 0$ by changing the sign of the amplitude anisotropy term γ_a . From eqs. (2.4)-(2.8), we can deduce the four following steady-states for the SFM:

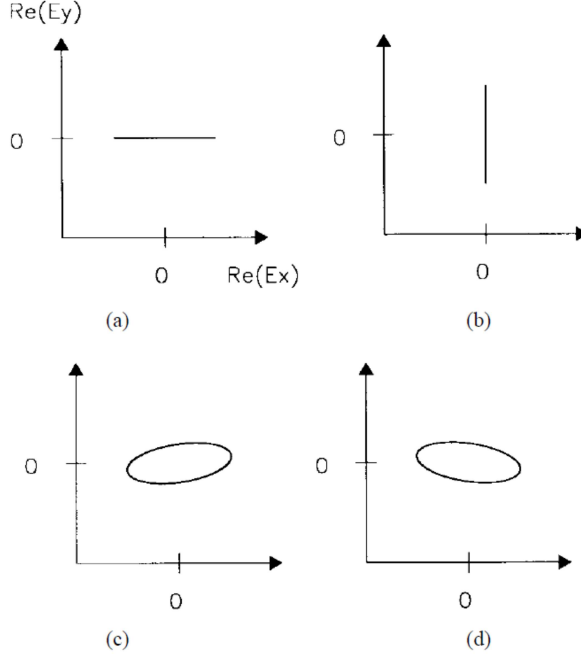


Figure 2.2 – **Representation of the four steady-states of the SFM model.** We represent the steady-states of the SFM model in the $(\text{Re}(E_x), \text{Re}(E_y))$ plane: at the top are the two linearly polarized states X-LP (left) and Y-LP (right), while the two symmetric elliptically polarized states are given at the bottom. Taken from [70].

- (A) the X-LP steady-state is the low frequency LP with a frequency $\omega_X = -\gamma_p + \gamma_a \alpha$ and is given by

$$R_{\pm} = \sqrt{\frac{\mu - N_0}{2N_0}}, \quad \Phi = 0, \quad N_0 = 1 + \frac{\gamma_a}{\kappa}, \quad n_0 = 0 \quad (2.10)$$

Physically, this steady-state only exists when the injection current exceeds its threshold. For $\gamma_a = 0$, the X-LP is stable from threshold $\mu_{x,th} = N_0 = 1$ up to a current μ_x where a pitchfork bifurcation occurs creating two elliptically polarized states - see CASE (B). The expression of this upper stability boundary μ_x is:

$$\mu_x = 1 + \frac{\gamma_s \gamma_p}{\gamma(\kappa \alpha - \gamma_p)} \quad (2.11)$$

The expressions of these boundaries become however much more complex when $\gamma_a \neq 0$. The upper limit can still be expressed in a relatively short way:

$$\mu_x = \left(1 + \frac{\gamma_a}{\kappa}\right) \left(1 + \frac{\gamma_s}{\gamma} \frac{(\gamma_p^2 + \gamma_a^2)}{(\kappa\alpha - \gamma_p)\gamma_p + (\kappa + \alpha\gamma_p)\gamma_a}\right) \quad (2.12)$$

The expression of $\mu_{x,th}$ becomes much more complex but, in practice, $\mu_{x,th} \approx N_0$ remains a sufficiently accurate approximation. Nonetheless the reader can find valuable additional details in the following references: [70,71,75]. In addition, it is worth noting that the pitchfork bifurcation destabilizing this steady-state is supercritical for most parameter sets used, but it has been demonstrated that this bifurcation can become subcritical for low values of α . The critical value can be approximated by $\alpha_c \approx 1 + \gamma_p/\kappa - 2\gamma_a/\gamma_p$. In that case, noise-induced switchings between linear and elliptical polarizations can appear [75].

- (B) The X-LP steady-state is destabilized by a pitchfork bifurcation which creates two elliptically polarized (EP) states with main axes symmetrically oriented with respect to the X axis. There is no direct analytical expression for these steady-states, but finding them numerically is relatively straightforward as described in detail in [75]. First, we can easily express the phase and amplitude variables, along with the frequency, as a function of carrier population variables:

$$R_{\pm}^2 = \frac{\mu - N \mp n\gamma_s}{2(N \pm n)} \quad (2.13)$$

$$\tan(\Phi) = \frac{N - 1}{\alpha n} \quad (2.14)$$

$$\omega_{el} = \frac{\kappa^2 \alpha ((N - 1)^2 - n^2) - \gamma_a \gamma_p}{\kappa(N - 1)} \quad (2.15)$$

We can then obtain an equation for n^2 only depending on N and on the system parameters:

$$n^2 = \frac{(N - 1)N(N - \mu)\alpha\gamma_p + \gamma_a A(N)}{\gamma_a \gamma_s (N - 1) + \alpha\gamma_p (N - \mu - \gamma_s)} \quad (2.16)$$

with

$$\begin{aligned} A(N) = & (N - 1)^3 \gamma_s + (N - 1)^2 (1 + \gamma_s) + (\mu + \gamma_s - 1) \frac{\gamma_p^2}{\kappa^2} \\ & + (N - 1) \left(\frac{(\gamma_s - 1)\gamma_p^2}{\kappa^2} - (\mu - 1) \right) \end{aligned} \quad (2.17)$$

Equations (2.13)–(2.17) can then be inserted in the steady-state solution of equations (2.7)–(2.8):

$$\begin{aligned} & \alpha^2 \kappa^4 n^4 + \kappa^2 (\kappa^2 (N-1)^2 (1-\alpha^2) + 2\alpha\gamma_a\gamma_p) n^2 - \kappa^4 (N-1)^4 \\ & + \kappa^2 (N-1)^2 (\gamma_a^2 - \gamma_p^2) + \gamma_a^2 \gamma_p^2 = 0 \end{aligned} \quad (2.18)$$

We then obtain an equation depending only on N , and which can be easily solved numerically. In the case where the pitchfork bifurcation creating the EP states is supercritical, they are stable from their creation and, for larger currents, are destabilized by Hopf bifurcations which lead the system toward self-pulsating solutions, nonlinear dynamics and chaos.

- (C) The Y-LP is the high frequency LP with a frequency of $\omega_Y = \gamma_p - \gamma_a \alpha$ and is obtained by

$$R_{\pm} = \sqrt{\frac{\mu - N_0}{2N_0}}, \quad \Phi = \pi, \quad N_0 = 1 - \frac{\gamma_a}{\kappa}, \quad n_0 = 0 \quad (2.19)$$

Again this state only exists when the injection current exceeds its threshold. For $\gamma_a = 0$, the Y-LP threshold is $\mu_{y,th} = N_0 = 1$, hence for $\mu > 1$ the Y-LP steady-state physically exists. It is stable when the normalized current is above $\mu > \mu_y$. At the limit $\mu = \mu_y$, we find a Hopf bifurcation - most often subcritical - destabilizing the Y-LP steady-state. The expression of μ_y is:

$$\mu_y = 1 - \frac{\gamma_s}{\gamma} + 2\alpha \frac{\gamma_p}{\gamma} \quad (2.20)$$

When a non-zero amplitude anisotropy is considered - $\gamma_a \neq 0$ -, the corresponding expressions become much more complex, but for large injection current the previous equation provides a valid approximation. Near threshold, the amplitude anisotropy has a large impact that can be summarized in two cases: 1/ for $\gamma_a < 0$, the Y-LP is stable at threshold and the Hopf bifurcation is an upper bound of its stability region, 2/ for $\gamma_a > 0$, the Y-LP is not stable at threshold and the Hopf bifurcation becomes a lower bound of the Y-LP stability area. Similarly to X-LP, the Y-LP threshold expression is complex when non-zero amplitude anisotropy is considered, but again the approximation $\mu_{y,th} \approx N_0$ remains sufficient in practice.

2.1.3 Key measurements

To obtain reliable and relevant information on the dynamical evolution of the laser emission, we cannot only rely on the core variables presented previously. Indeed a different viewpoint can often be valuable to understand the physical mechanisms. We therefore present here the key measurements that will be exploited in this thesis.

Considering the four-level model described, we can easily get two characteristic frequencies of the system: the birefringence-induced frequency or splitting frequency F_{split} - i.e. the difference of frequency between the two linearly polarized steady-states - and the relaxation oscillation frequency F_{RO} . They are calculated as follows:

$$2\pi F_{\text{split}} = |\omega_X - \omega_Y| = |2\gamma_p - 2\alpha\gamma_a| \quad (2.21)$$

$$2\pi F_{\text{RO}} = \sqrt{2\kappa\gamma(\mu - 1)} \quad (2.22)$$

The averaged output power of the two linear polarizations $\langle |E_X|^2 \rangle$ and $\langle |E_Y|^2 \rangle$, with $\langle \cdot \rangle$ meaning time average, are not sufficient to provide a reliable picture of the emitted light polarization and polarization dynamics. An essential tool is therefore the four Stokes parameters s_0 , s_1 , s_2 and s_3 , which are time-dependent variables and are defined as follows [70]:

$$s_0(t) = |E_+|^2 + |E_-|^2 = \rho^2 \quad (2.23)$$

$$s_1(t) = 2\text{Re}(E_+ \cdot E_-^*) = \rho^2 \cos(2\chi) \cos(2\phi) \quad (2.24)$$

$$s_2(t) = 2\text{Im}(E_+ \cdot E_-^*) = \rho^2 \cos(2\chi) \sin(2\phi) \quad (2.25)$$

$$s_3(t) = |E_+|^2 - |E_-|^2 = \rho^2 \sin(2\chi) \quad (2.26)$$

with ρ the total intensity, χ the instantaneous ellipticity and ϕ the angle of the main axis of the polarization ellipse. Although the time-dependent Stokes parameters always satisfy the identity $s_0^2 = s_1^2 + s_2^2 + s_3^2$, this is no longer true for time-averaged variables and we observe that $\langle s_0 \rangle^2 > \langle s_1 \rangle^2 + \langle s_2 \rangle^2 + \langle s_3 \rangle^2$. In particular, this property allows us to define the fractional polarization (FP) - that can be viewed as a measure of the amount of light being polarized - which ranges from $\text{FP} = 0$ for unpolarized light to $\text{FP} = 1$ for completely polarized light:

$$\text{FP} = \frac{\langle s_1 \rangle^2 + \langle s_2 \rangle^2 + \langle s_3 \rangle^2}{\langle s_0 \rangle^2} \quad (2.27)$$

In practice, we will also use the averaged instantaneous ellipticity - that we will refer to as averaged ellipticity in the rest of the manuscript - calculated as follows:

$$\chi = \left\langle \frac{1}{2} \arcsin \left(\frac{s_3}{s_0} \right) \right\rangle \quad (2.28)$$

For the purpose of continuation of bifurcations (as described in the following), it appears handy to use the following variable:

$$A = \frac{R_+^2}{\mu - 1} \quad (2.29)$$

In the case of $\gamma_a = 0$, we obtain $A = 1/2$ for linearly polarized states and elliptically polarized states appear symmetrically with respect to the $A = 1/2$ value. In practice, for small values of γ_a , these equalities are not valid anymore but remain good approximations.

Finally, we simulate the system evolution through direct numerical integration of the equations - with a standard 4th order Runge-Kutta algorithm -, including the 5 interdependent equations and an additional phase term to obtain the optical frequency of the system. We also complement these simulations by using continuation techniques with the DDE-BIFTOOL package [130]: instead of describing the system evolution in time by integrating the equations, we start from a known solution and numerically follows its evolution step by step for small changes of the parameters. Such technique therefore allows us to uncover both stable or unstable states and identify the bifurcations of the system through a numerical analysis of the system eigenvalues. Although we can easily follow steady-states and periodic solutions, continuation techniques cannot be used on quasi-periodic solutions or chaotic attractors.

2.2 BIFURCATIONS TO POLARIZATION SWITCHING

In this section, we use direct numerical integration combined with continuation techniques to identify the bifurcations leading to PSs and to analyze how they are modified when varying the laser parameters.

First, we unveil several PS bifurcation scenarios predicted by the SFM for different values of the birefringence and amplitude anisotropy, including type I and type II PSs with various features. In particular, we highlight that the frequency of the dynamics accompanying PSs does not necessarily relate to F_{split} , i.e. the birefringence frequency; in fact the frequency is defined by a bifurcation problem and can therefore take a large range of different values that does not necessarily relate to the characteristic frequencies of the system. Secondly, we make a detailed investigation of two specific cases: 1/ a type II PS scenario showing a good agreement with the experimental report of Sondermann *et al.* [51] - including a transition through EP states and anticorrelated self-pulsing dynamics at the birefringence frequency - and 2/ an incomplete switching scenario matching the experimental observations of Olejniczak *et al.* [53, 54] - including self-pulsations at the relaxation oscillation frequency, two-mode emission for large injection currents and mode-hopping dynamics between non-orthogonal EP states. Thus, we confirm the relevance of the SFM to model the dynamics of VCSELs and motivate new experiments.

2.2.1 Analysis of possible bifurcation scenarios

First, we focus on the evolution of the bifurcations limiting the stability of the three steady-states described previously. Of particular interest is the Hopf bifurcations destabilizing the two EP states which lead to self-pulsating solutions at a frequency close to the Hopf frequency - related to the imaginary part of the complex eigenvalues at the bifurcation point. In this section, unless stated otherwise, we will use the following parameter values: $\gamma_a = \{-0.7, 0.7\} \text{ ns}^{-1}$, $\gamma_s = 100 \text{ ns}^{-1}$, $\gamma = 1 \text{ ns}^{-1}$, $\gamma_p \in [0, 100] \text{ ns}^{-1}$, $\kappa = 600 \text{ ns}^{-1}$, $\alpha = 3$ and $\mu \in [1, 10]$.

The stability map for the steady-states is depicted in Fig. 2.3 for $\gamma_a = -0.7 \text{ ns}^{-1}$ and Fig. 2.4 for $\gamma_a = +0.7 \text{ ns}^{-1}$. Because the sign of γ_a has a major influence on the system evolution, we need to display the two cases separately. On both figures, the (a)-panel summarizes the parameter regions where the different polarization states are stable in the plane of injection current versus phase anisotropy. The evolution of the Hopf bifurcation frequencies - i.e. the frequency of the self-pulsing dynamics created close to the bifurcation point - are given in panel (b), along with the splitting F_{split} frequency or

birefringence frequency. And in panel (c), we show the evolution of the same frequencies but normalized by the relaxation oscillation frequency F_{RO} which varies as a square root of the injection current as described by eq. (2.22). Finally, this overview is completed by a couple of bifurcation diagrams for increasing and decreasing injection currents in order to clarify the dynamical evolution of the system.

The thresholds of the two LPs is not displayed in Figs. 2.3 and 2.4 for simplicity, but the difference between a positive and negative amplitude anisotropy can be simply described as follows: 1/ for $\gamma_a < 0$, a good approximation gives $\mu_{x,th} = 1 + \gamma_a/\kappa$ and $\mu_{y,th} = 1 - \gamma_a/\kappa$. The threshold of X-LP is lower than the one of Y-LP and therefore the laser starts emitting on this state. 2/ for $\gamma_a > 0$ the two approximations remain valid but the situation is reversed: the threshold of Y-LP is lower and X-LP is unstable, hence the laser starts emitting on Y-LP.

From Figs. 2.3 and 2.4, we can identify as much as nine different bifurcation scenarios - delimited by different colors and identified by numbers. For scenarios 1 to 4, i.e. for $\gamma_a < 0$, the laser starts emitting on X-LP and we observe the following evolution:

- **CASE 1** - blue area of Fig. 2.3 and bifurcation diagram of panel (d): the laser starts on the X-LP mode and as the injection current is increased a pitchfork bifurcation occurs (black dashed line) which creates the two symmetric EP states described earlier. Then the Hopf bifurcations destabilizing the two EP states appear (blue line) leading the system to a stable periodic solution. The frequency of this dynamical state is either close to F_{split} for small γ_p values or to F_{RO} for higher values of γ_p (see Fig. 2.3-(b) and (c)). If the injection current is increased further, the system experiences a transition through complex dynamical states and chaos until it reaches suddenly the Y-LP stable state as shown in Fig. 2.3(d). Therefore this case corresponds to a type II PS with a large dynamical transition.

For decreasing injection currents, the laser remains on the Y-LP state until it is destabilized by a subcritical Hopf bifurcation (dash-dotted red line). Then, the laser eventually experiences a short dynamical transition before switching back to X-LP or EP steady-states depending on the parameter values.

- **CASE 2** - red area of Fig. 2.3 and bifurcation diagram of panel (e): is similar to CASE 1, except that the system never reaches the Y-LP steady-state for larger injection current as it never becomes stable. Thus, the laser starts emitting on the X-LP steady-state at threshold which is then destabilized by a pitchfork bifurcation (black dashed line) creating two symmetrical EP steady-states. These two states are however quickly destabilized by symmetrical Hopf bifurcations (blue line) that lead the system toward self-pulsing dynamics at a frequency close to F_{RO} as shown in

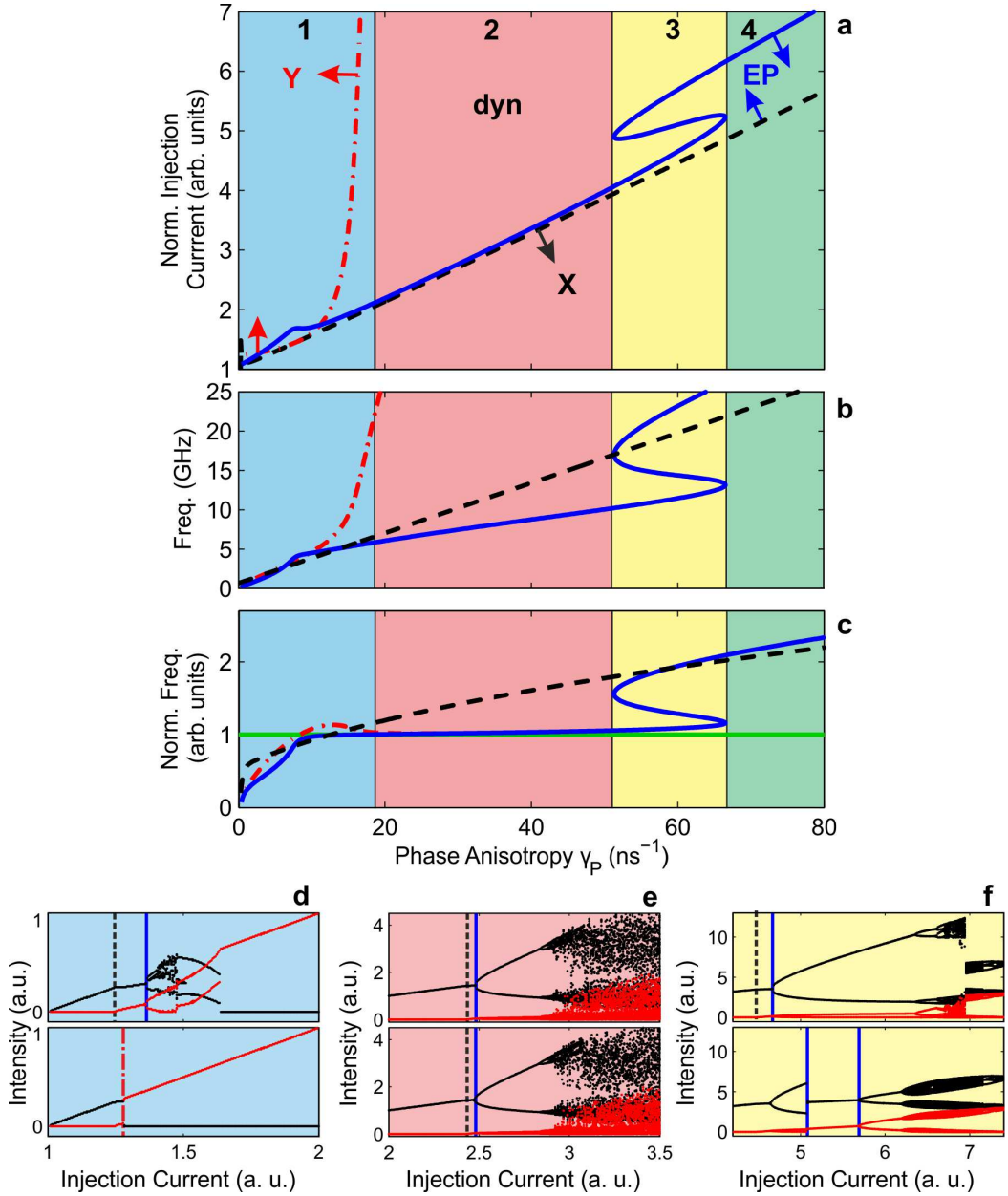


Figure 2.3 – **Steady-state stability diagram for a negative amplitude anisotropy.** (a) Stability diagram, in the injection current versus phase anisotropy plane, of the linearly and elliptically polarized steady-states with $\gamma_a = -0.7$. The red dash-dotted curve is the Y-LP Hopf bifurcation, the black dashed curve is the X-LP pitchfork bifurcation and the blue solid curve is the EP Hopf bifurcation. (b) Frequencies associated with the Hopf bifurcations, the legend is identical to (a) except for the dashed black curve which gives the birefringence induced frequency splitting. (c) is the same as (b) but normalized by the relaxation oscillation frequency given by the green horizontal solid line. Panels (d, e, f) give the simulated bifurcation diagrams for increasing (top) and decreasing injection currents (bottom) for $\gamma_p = 4, 25, 60$ respectively. The vertical lines identify the bifurcations with the same type and color than in (a).

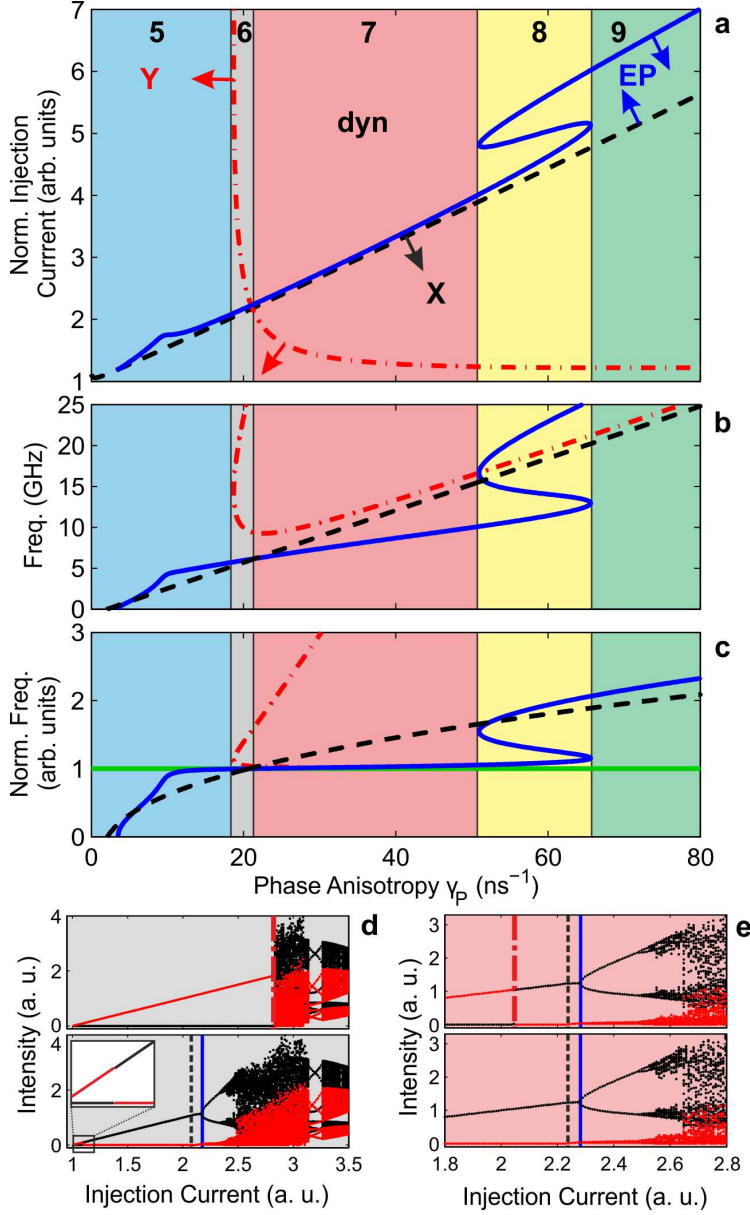


Figure 2.4 – **Steady-state stability diagram for positive amplitude anisotropy.** (a) Stability diagram, in the injection current versus phase anisotropy plane, of the linearly and elliptically polarized steady-states with $\gamma_a = +0.7$. The red dash-dotted curve is the Y-LP Hopf bifurcation, the black dashed curve is the X-LP pitchfork bifurcation and the blue solid curve is the EP Hopf bifurcation. (b) Frequencies associated with the Hopf bifurcations, the legend is identical to (a) except for the dashed black curve which gives the birefringence induced frequency splitting. (c) is the same as (b) but normalized by the relaxation oscillation frequency given by the green horizontal solid line. Panels (d) and (e) give the simulated bifurcation diagrams for increasing (top) and decreasing injection currents (bottom) for $\gamma_p = 20, 22$ respectively. The vertical lines identify the bifurcations with the same type and color than in (a).

Fig. 2.3(c). Next, multiple bifurcations occur for increasing injection currents and lead the system towards a much more complex dynamical state, see Fig. 2.3(e).

- **CASE 3** - yellow area of Fig. 2.3 and bifurcation diagram of panel (f): is identical to **CASE 2** except that three Hopf bifurcations (blue lines) occur on the EP state branch, creating a bistability region between periodic solutions and EP steady-states. This particular hysteresis phenomenon, a bistability between steady-states and self-pulsating solutions, has already been described by Prati *et al.* [75], and is displayed in Fig. 2.3(f). We can note that the first bifurcation is supercritical and leads the system to a stable periodic solution at a frequency close to the relaxation oscillation frequency; the second bifurcation is subcritical and the third one is also supercritical but with a frequency much closer to F_{split} . For higher currents a sequence of bifurcations leads the system to a much more complex dynamical state.
- **CASE 4** - green area of Fig. 2.3: is similar to **CASE 2**, but the stability region of the EP states is much bigger and the periodic solution frequency created by the Hopf bifurcation does not relate either to F_{split} nor to F_{RO} .

In **CASES 2** and **4**, for decreasing injection currents the laser simply follows backward the scenario described. No hysteresis or bistability is highlighted in these cases. For a negative amplitude anisotropy, $\gamma_a = +0.7$, the main change with respect to the previous situation concerns the Y-LP steady-state. The Y-LP solution is now stable at threshold for all values of the birefringence, but for $\gamma_p > 20$ a Hopf bifurcation quickly destabilizes it. Therefore the scenarios for high phase anisotropy resemble previous cases but with an additional type I PS at low injection currents:

- **CASE 5** - blue area of Fig. 2.4: the laser emits on the Y-LP at threshold and this steady-state is always stable; hence the laser only emits on the Y-LP. Yet for low injection currents the X-LP steady-state is also stable and it has been suggested that a jump from the Y-LP to the X-LP could be possible with sufficient noise [51]. In that case the laser would experience a first noise-induced type I PS and then a scenario similar to **CASE 1**.
- **CASE 6** - gray area of Fig. 2.4 and bifurcation diagram of panel (d): the laser starts on the Y-LP from threshold until a Hopf bifurcation (red dash-dotted line) destabilizes it. Beyond this bifurcation no stable states are available; thus for higher injection currents, the laser experiences complex pulsing dynamics similar to those described in **CASE 2**, see Fig. 2.4(d). For decreasing injection currents the X-LP

steady-state is also stable, hence the laser does not switch back to the Y-LP steady-state directly when it becomes stable again. Instead the laser keeps exhibiting a scenario similar to CASE 2 until the X-LP is destabilized close to threshold. We therefore observe a very large region of bistability between the stable Y-LP and scenario of CASE 2, as shown in Fig. 2.4(d).

- CASE 7 - red area of Fig. 2.4 and bifurcation diagram of panel (e): the laser starts on the Y-LP until it is destabilized by a subcritical Hopf bifurcation (red dash-dotted line): a type I switching occurs without any dynamical transition. As a result, for increasing injection currents, the laser then follows a scenario identical to CASE 2 including a transition through EP states, periodic solutions at the relaxation frequency F_{RO} and complex dynamical behaviors for higher injection currents.
- CASE 8 - yellow area of Fig. 2.4: similarly to the previous case, the laser experiences a first type I PS at relatively low injection currents. Then the system exhibits a scenario very similar to CASE 3 including the sequence of three Hopf bifurcations creating a peculiar hysteresis phenomenon described in [75].
- CASE 9 - green area of Fig. 2.4: identical to CASE 7 but with a pitchfork bifurcation occurring at a very large injection currents and also a large area of stability for the EP states. The frequency of the periodic solution created by the Hopf bifurcation does not relate clearly to any characteristic frequency of the laser.

In CASES 7 to 9, we can find a region of bistability between Y-LP and X-LP at low injection currents. For increasing currents, the laser starts emitting on the Y-LP because its threshold is lower. As described above however, the laser switches to the X-LP steady-state when Y-LP is destabilized. Thus for decreasing currents, the laser stays on the X-LP until it is destabilized close to threshold as pictured in the inset of Fig. 2.4(d). Between the X-LP threshold and the Hopf bifurcation point, we therefore observe a bistability region between the two linearly polarized steady-states.

In CASES 6 and 7, the laser experiences a restabilization of the Y-LP steady-state for very high, quite unrealistic injection current values. Indeed for currents typically over three times the threshold, VCSELs can give rise to higher order transverse modes that are not accounted for in this single-mode VCSEL model. Also very high currents might damage the devices and are therefore out of reach. According to [74] however, taking into account the gain saturation might increase the curvature radius of the red curve; thus the stabilization of Y-LP could occur at realistic values of the injection current. CASE 7 would then become a double PS scenario.

The two stability diagrams and the frequencies of the Hopf bifurcations in figure 2.3 and 2.4 show that the dynamics accompanying PSs and predicted by the SFM cannot be linked directly to the beating frequency of the two linearly polarized modes or to the relaxation oscillation frequency. The dynamics of the system is, in fact, a bifurcation problem and cannot be reduced to competing effects leading to oscillations at either F_{RO} or F_{split} . However, in the next sections, we demonstrate the importance of the periodic solutions created by the Hopf bifurcations appearing on Y-LP and EP branches as they influence the whole dynamical behavior of the system.

2.2.2 Scenario of type-II polarization switching

Here, we analyze in detail the type-II switching scenario identified as CASE 1 in the previous section for which we observe strong similarities with the experimental results reported in [51]: in particular, the frequency of the dynamics accompanying the PS is close to the birefringence induced frequency F_{split} and anticorrelated self-pulsations can be observed.

In this subsection, we use $\gamma_a = -0.7 \text{ ns}^{-1}$ and $\gamma_p = 4 \text{ ns}^{-1}$, and as previewed in Fig. 2.3, we observe a clear type-II PS for an increasing injection current $\mu \in [1, 2]$. To describe the dynamical evolution of the system and the underlying mechanisms, we combine several viewpoints that are summarized in Figs. 2.5, 2.6 and 2.7. We show the evolution of the fractional polarization, the average ellipticity and the average polarization resolved output power as a function of the injection current in Figs. 2.5(a), (b) and (c) respectively. In Figs. 2.5(d–e), we present the polarization resolved bifurcation diagrams, i.e. the extrema of the simulated time-series, after projection onto the X and Y linear polarization axes for increasing (d) and decreasing (e) injection currents. We highlight several dynamical states which are then detailed in Fig. 2.6 where we give the Fast Fourier Transform (FFT) of the complex electrical field (left), the output polarization (middle) and the corresponding time-series (right). Finally, we detail continuation results and bifurcation identification in Fig. 2.7 with the evolution of the steady-states and periodic solutions in the (A, μ) plane (a) and the evolution of the time-periodic solution frequency versus current in (b). In this figure, we also plot the evolution of the relaxation oscillation frequency F_{RO} and the splitting frequency $F_{split} = 1.94 \text{ GHz}$ for the parameters used in this section.

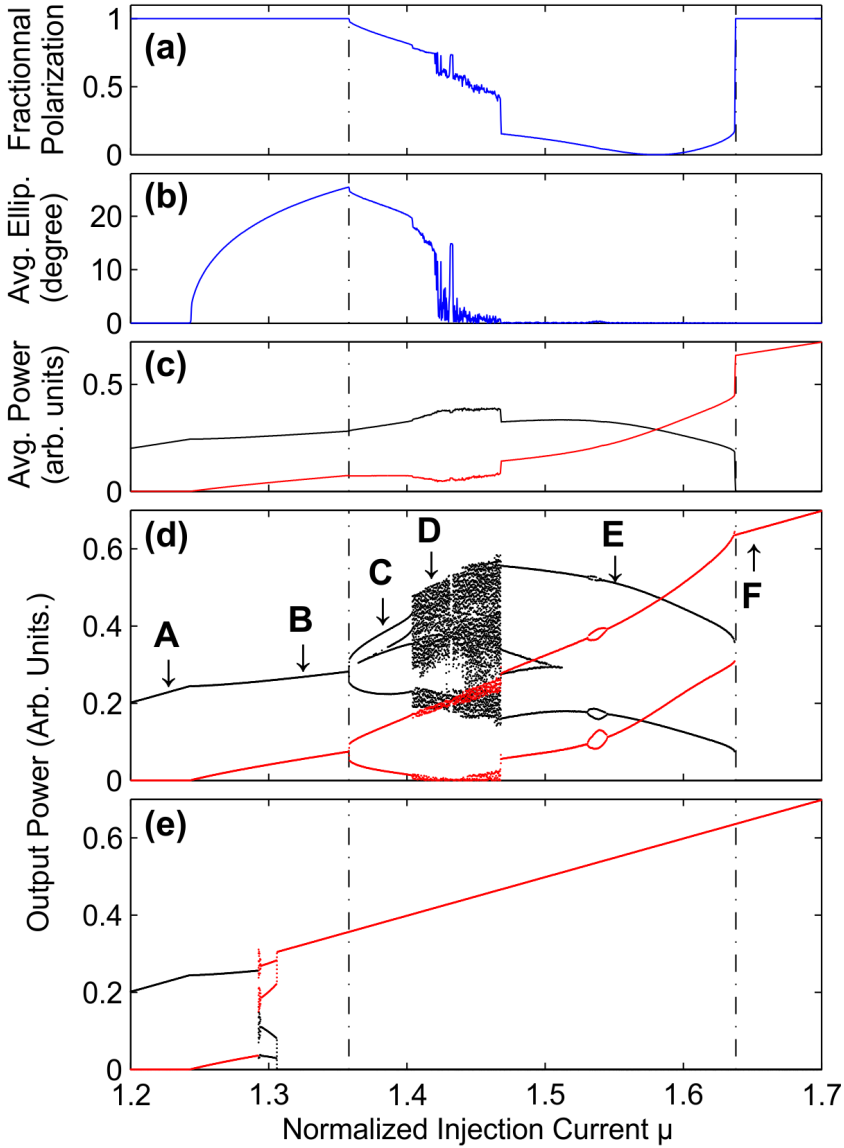


Figure 2.5 – **Simulated bifurcation diagram for a type II polarization switching.** Direct numerical simulation of CASE 1, with $\gamma_p = 4 \text{ ns}^{-1}$, described in sec. 2.2.1: (a) fractional polarization, (b) averaged ellipticity, (c) average output power after projection on the X (black) and Y (red) polarization axes. Data are averaged over hundreds of nanoseconds. (d-e) bifurcation diagrams of the output power after projection on the X (black) and Y (red) polarization axes, i.e. extrema of the corresponding time-series, for increasing and decreasing injection currents respectively. The two vertical dashed lines indicate the current range where the laser shows nonlinear polarization dynamics. The labeled arrows point to the position of the time-series detailed in figure 2.6.

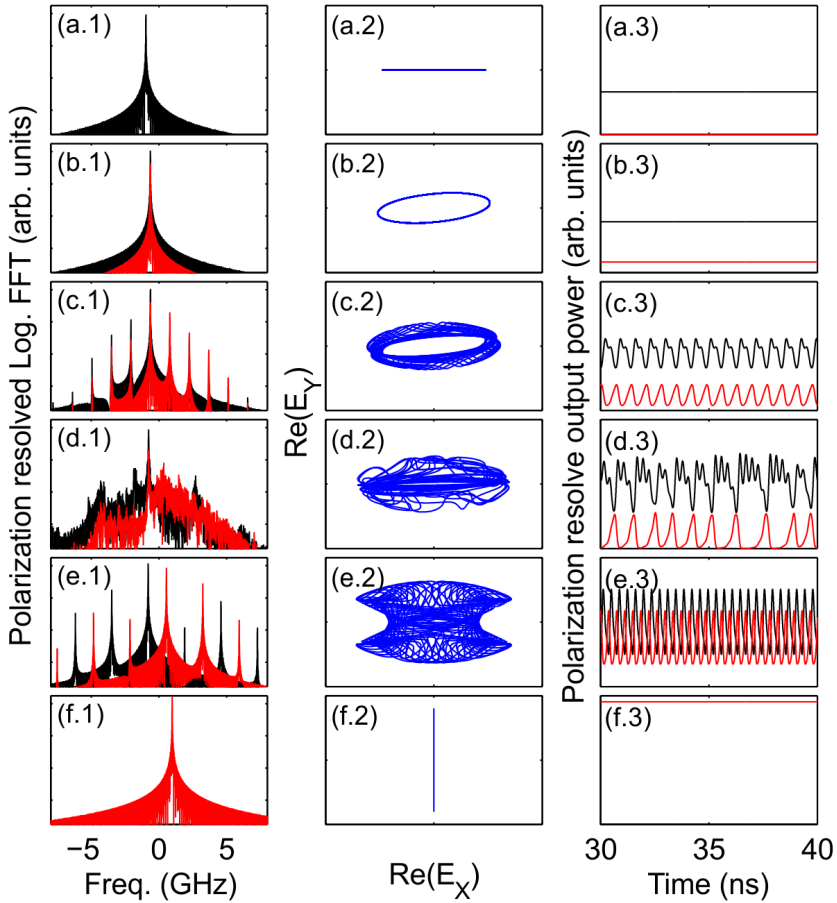


Figure 2.6 – **Detailed characteristics of the different dynamics obtained in a type-II PS scenario.**

Injection currents are (a) $\mu = 1.223$, (b) $\mu = 1.323$, (c) $\mu = 1.381$, (d) $\mu = 1.416$, (e) $\mu = 1.549$ and (f) $\mu = 1.650$. The first column (left) gives a logarithmic plot of the complex field FFT versus frequency, the second one (middle) is a representation of the output polarization given by the system trajectory in the $(\text{Re}(E_X), \text{Re}(E_Y))$ plane and the third (right) gives the time traces observed for the dynamical states. Both the FFT and the time traces are polarization resolved, hence red and black plots are for the projection on the X and Y polarization axes respectively.

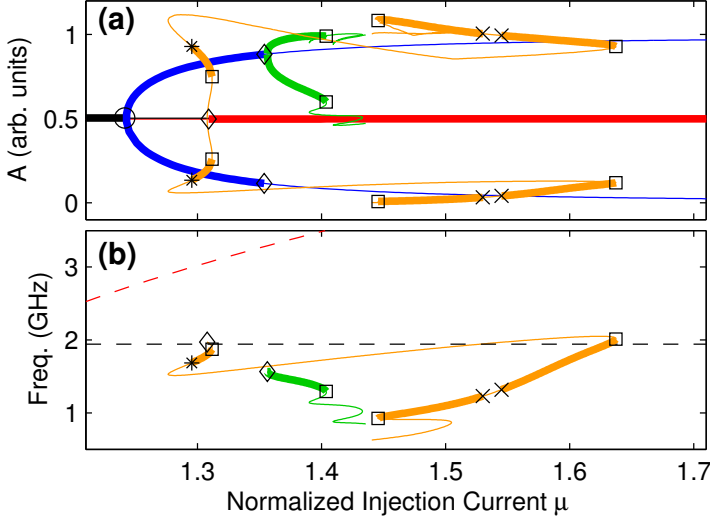


Figure 2.7 – **Bifurcation diagram for a type II PS obtained with continuation techniques.** This is CASE 1, with $\gamma_p = 4 \text{ ns}^{-1}$, as described in sec. 2.2.1: the stable (unstable) part of the branches are in thick (thin) lines. (a) Maximum and minimum of $A = R_+^2/(\mu - 1)$ versus normalized injection current. The X and Y-LPs are in black and red respectively and the EP states are in blue. The periodic solution created on the EP state is in green (a similar branch is created on the other Hopf bifurcation but not represented). The solution created on the Y-LP state is in orange and is a peculiar two-mode period-2 solution, the highlighted frequency is therefore the detuning between the two modes (see details in the text). Diamonds are Hopf, squares are saddle-node, stars are torus and crosses are period doubling bifurcations. On diagram (b) the black dashed line gives F_{split} and the red one shows F_{RO} as a function of the current μ .

We consider a negative amplitude anisotropy, hence the laser starts emitting on the X-LP state, i.e. with $E_y = 0$. As shown in Fig. 2.6(a.1) the optical frequency is slightly lower than the reference frequency ω_0 as expected for the X-LP state ($\omega_X = -\gamma_p + \gamma_a \alpha$). At $\mu = 1.24$, this steady-state is destabilized by a pitchfork bifurcation creating the two EP states, which can be clearly identified in Fig. 2.7. In practice these two states are strictly equivalent and the system settles randomly on one of them. We observe in Fig. 2.6(b.1) that the optical frequencies of the two LP modes are still locked to the same value.

A further increase of the injection current leads to the destabilization of the EP states by Hopf bifurcations at $\mu = 1.36$. Interestingly, because the two EP states are equivalent, identical Hopf bifurcations occur on both branches hence creating symmetric limit cycles. The bifurcations being supercritical the system starts exhibiting time-periodic self-pulsing dynamics with, as seen in Fig. 2.7(b), a frequency close to $F_{\text{split}} = 1.94 \text{ GHz}$

and apparently not related to F_{RO} (≈ 3 GHz at this current range). Despite these self-pulsations, the system still exhibits a polarization close to the unstable EP as can be seen in Fig. 2.5(a, b) and 2.6(c.2). In terms of frequency, we clearly see in Fig. 2.6(c.1) that the optical frequency remains at ω_x and numerous sidebands appear at the harmonics of the fundamental frequency $\sim F_{split}$. The polarization resolved time-series in Fig. 2.6(c.3) show anti-correlated dynamics between the X and Y LP modes, similar to what has been observed experimentally in [51].

This time-periodic solution is then destabilized by a saddle-node bifurcation at $\mu = 1.404$ and the system enters a small region of chaotic dynamics. Indeed, although the Y-LP steady-state is stable at this range of current, the laser never reaches it and evolves chaotically. Despite the chaotic nature of the dynamics, the emitted light is still partially polarized, but the ellipticity quickly drops down for increasing currents. The analysis of the chaotic behavior falls out of the scope of this section, but further details about these chaotic fluctuations and their experimental confirmation can be found in section 2.3. At $\mu = 1.45$ a new periodic solution is stabilized by a saddle-node bifurcation - orange curve in Fig. 2.7 - but it is only for $\mu = 1.47$ that the laser reaches it hence ending the chaotic region.

This new dynamics created by the Hopf bifurcation destabilizing the Y-LP steady-state is however very peculiar: it is a period-1 solution for the right and left circular polarizations, while it is a two-mode period-2 solution for the projections on the X and Y LP as can be seen in Fig. 2.6(e). First, the amplitude evolution of the circularly polarized modes R_{\pm} are anti-phased, hence it induces a period-2 evolution of the LP modes (we have $E_x = (E_+ + E_-)/\sqrt{2}$ and $E_y = -i(E_+ - E_-)/\sqrt{2}$). Secondly, due to the phase difference evolution combined with the anti-phased dynamics of R_{\pm} , the Y LP mode is bounded in phase while the X LP is centered around the origin of the complex plane, hence the two modes exhibit different optical frequencies. As a result of this peculiar evolution, the frequency identified by continuation techniques in Fig. 2.7(b) is the detuning F_{detune} between the two modes and not the frequency of the oscillations. This is confirmed by the FFT and the corresponding time-series plotted in Fig. 2.6(e.3) and (e.1) respectively. The main peaks of the optical spectra for X-LP and Y-LP are separated by the frequency F_{detune} highlighted by continuation techniques ranging from about 1 GHz - roughly at half the splitting frequency F_{split} - up to 2 GHz ($\approx F_{split}$). For each mode, we observe a frequency comb with sidebands at even multiples of the detuning - which correspond to the period-2 dynamics for the LP modes - and the two frequency combs for X-LP and Y-LP are interleaved. In the meantime, the time-series show anti-correlated self-pulsations at two times the detuning. Considering that the detuning F_{detune} is between 1 and 2 GHz, the frequency of the oscillation equals $2F_{detune}$ and therefore roughly relates to the splitting frequency $F_{split} \approx 1.94$. As a result of this two-mode dynamics, the frac-

tional polarization reaches very low values with a minimum when the average output power on both modes is equal - around $\mu = 1.58$, see Fig. 2.5. At last, this dynamical state is destabilized by another saddle-node bifurcation at $\mu = 1.638$ and the system finally reaches the Y-LP steady-state.

Decreasing the injection current unveils a large region of bistability between the whole dynamical scenario described so far and the Y-LP emission as can be seen in Fig. 2.5(e). The Y-LP steady-state gets destabilized by a subcritical Hopf bifurcation at an injection current as low as $\mu = 1.306$. The unstable periodic solution created by this bifurcation is however quickly stabilized by a saddle-node bifurcation at $\mu = 1.312$ and then it becomes unstable again as a torus bifurcation occurs at $\mu = 1.295$. Considering the stability of all the states involved, we report a tiny region of tri-stability between EP, Y-LP and this new self-pulsing dynamics for $1.306 < \mu < 1.312$. Finally, if the current is decreased further, the system settles back on one of the EP states and then on the initial X-LP steady-state which is stable at threshold.

At this point it is worth noting that, if one cannot resolve all the dynamical evolution of the system or only looks at the average polarization resolved output power as in Fig. 2.5(c), almost none of the specific features reported here can be detected.

In the end, this bifurcation scenario definitively shows the essential features described in the experimental report of Sondermann *et al.* [51]. Indeed, we successfully reproduce a type II PS with a transition through elliptically polarized states followed by anti-correlated self-pulsations with a frequency related to the birefringence frequency. The optical spectrum of the two-mode dynamics displayed in Fig. 2.5(e.1) matches qualitatively well the spectrum highlighted in [51] and the multiple peak spectrum shown in [52]. However, these experimental reports do not provide the optical spectra for the projection onto the orthogonal direction of polarization, hence cannot confirm if the two spectra are effectively interleaved. In addition, we shall remark that in [51], the authors identify the “effective” birefringence from the frequency of the self-pulsing oscillations. The work described here however demonstrates that such link cannot be made; although the frequency of the dynamics can be close to the birefringence dynamics, it can also relate to the relaxation oscillation frequency or to none of the above, as seen in Figs. 2.3 and 2.7(b). Nevertheless, as no scaling of the self-pulsation frequency with the injection current is provided in [51], we do not have enough information to unambiguously identify the origin of the dynamics.

2.2.3 Self-pulsing dynamics without polarization switching

We successfully demonstrated that the SFM shows a good qualitative agreement with experimental observations of a type-II PS, showing a clear transition through EP states and anticorrelated dynamics at a frequency close to the birefringence frequency. However, other experimental investigations on quantum dot VCSELs uncovered different features that seem, *à priori*, incompatible [53, 54]: indeed these reports highlight self-pulsation dynamics at the relaxation oscillation frequency and a final state that is not the LP steady-state orthogonal to the one stable at threshold, but a simultaneous emission of the two orthogonal LP modes. The detuning between the modes is measured around 5 GHz and sidebands at the relaxation oscillation frequency also appear in the polarization resolved optical spectrum, see Fig. 6 in [54]. In addition, Olejniczak *et al.* uncovered a random-like hopping dynamics between two non-orthogonal EP states with a scaling of the dwell-time - i.e. the time between two successive jumps - opposed to the one reported for the noise-induced hopping between LP modes reported for type I PSs as discussed in section 1.3. Here we demonstrate that all these features can, in fact, be accurately described in the SFM framework: we provide a detailed analysis of the bifurcation scenario identified as CASE 2 and demonstrate that it agrees qualitatively well with the experimental results described in [53, 54].

We set the anisotropy parameters at $\gamma_a = -0.7 \text{ ns}^{-1}$ and $\gamma_p = 25 \text{ ns}^{-1}$ respectively, and use the same kind of representation than in the previous subsection: they are given in Figs. 2.8 and 2.9 for direct numerical integration results and in Fig. 2.10 for continuation results. As mentioned earlier, with this set of parameters the laser does not exhibit a complete type-II switching but only a destabilization of the low frequency LP toward complex nonlinear dynamics. We provide an in-depth investigation of the complete bifurcation scenario and discuss in detail the qualitative agreement obtained with the experimental observations described in [53, 54]

Similarly to the case described in the previous section, the laser starts emitting on the low-frequency X-LP until a pitchfork bifurcation occurs and creates the two symmetrical EP states at $\mu = 2.43$. However, this time the EP states are only stable in a narrow range of current as they are destabilized at $\mu = 2.49$ by supercritical Hopf bifurcations. The system then starts exhibiting self-pulsating dynamics but, in contrast to the previous case, as can be seen in Figs. 2.10 and 2.9(a.1), the frequency of the time-periodic solution is close to F_{RO} and not F_{split} , and therefore matches the experimental observations of [54]. Moreover, we can remark that if one considers the time-averaged output power, the first periodic solution can be easily mistaken as an EP state, hence explaining the relatively large region of stable EP state reported in [54], to be compared with the small region

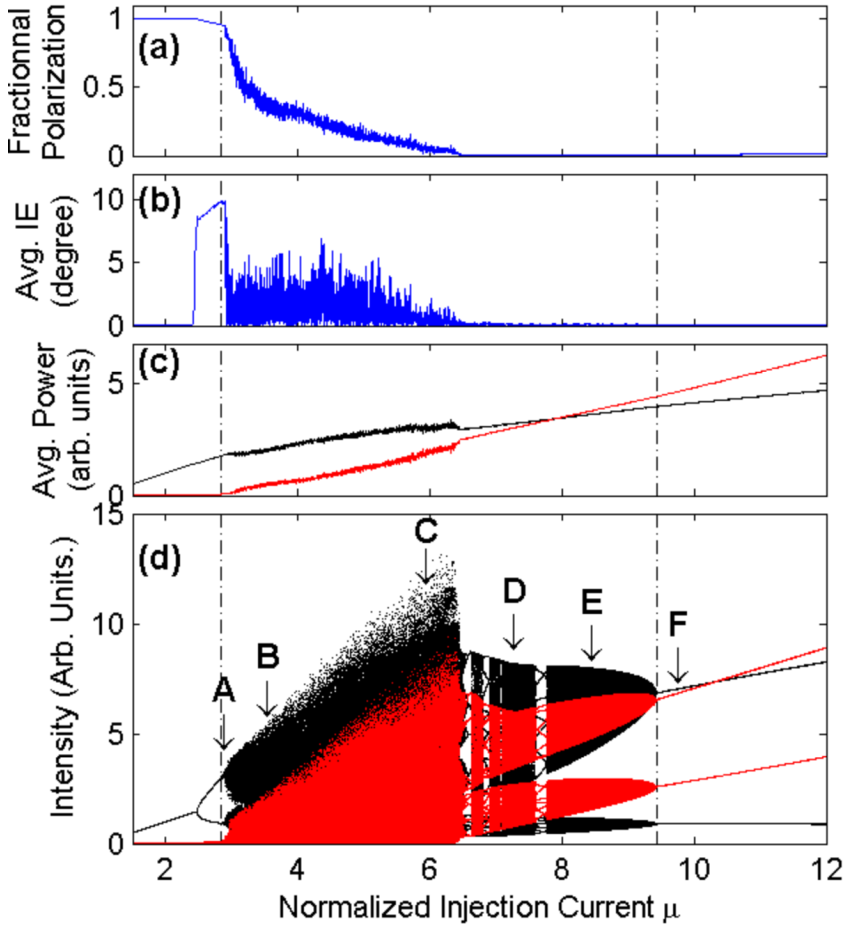


Figure 2.8 – **Simulated bifurcation diagram for a transition to self-pulsing dynamics without switching.** Direct numerical simulation of a transition to a complex dynamical state without switching corresponding to CASE 2, with $\gamma_p = 25 \text{ ns}^{-1}$, described in sec. 2.2.1: (a) fractional polarization, (b) averaged ellipticity, (c) average output power after projection onto the X (black) and Y (red) axes of polarization. Data are averaged over hundreds of nanoseconds. (d) bifurcation diagram of the output power after projection onto the X (black) and Y (red) axes of polarization, i.e extrema of the corresponding time-series. The dashed lines indicate the current range where the laser shows complex dynamics such as chaos and quasiperiodic dynamics.

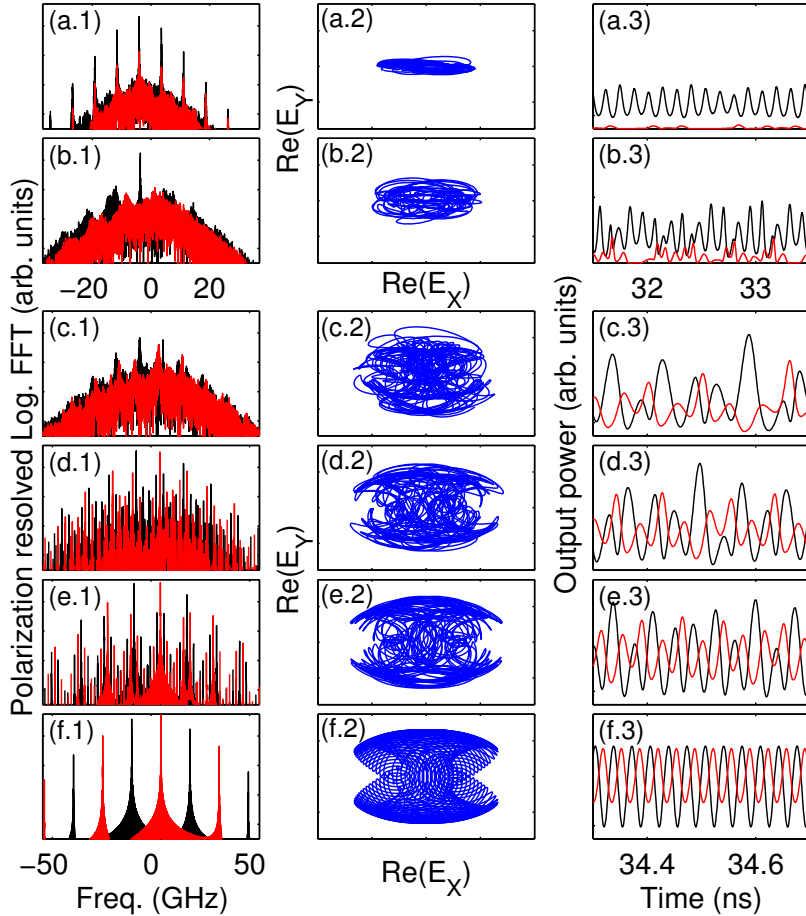


Figure 2.9 – **Detailed characteristics of the different dynamical states obtained for a transition to self-pulsing dynamics without switching** Injection currents are (a) $\mu = 2.910$, (b) $\mu = 3.552$, (c) $\mu = 5.960$, (d) $\mu = 7.298$, (e) $\mu = 8.475$, (f) $\mu = 9.786$. The first column (left) gives a logarithmic plot of the complex field FFT versus frequency, the second one (middle) is a representation of the output polarization given by the system trajectory in the $(\text{Re}(E_X), \text{Re}(E_Y))$ plane and the third (right) gives the time traces observed for the dynamical states. Both the FFT and the time traces are polarization resolved, hence red and black plots are for the projection on the X and Y polarization axes respectively.

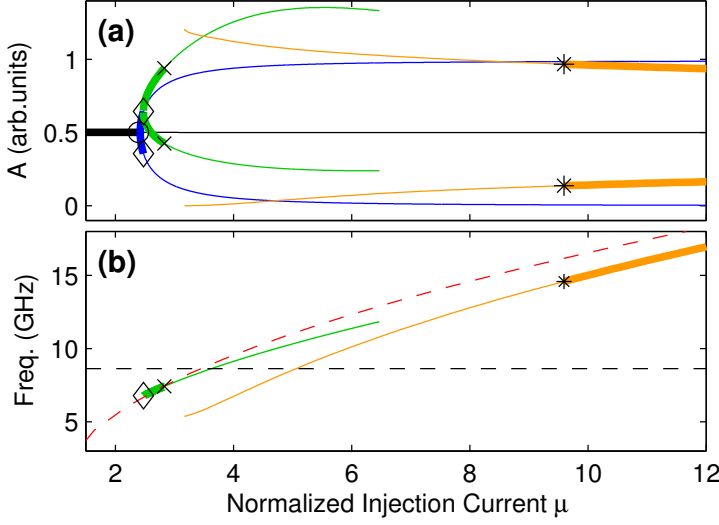


Figure 2.10 – **Bifurcation diagram obtained with continuation techniques for a transition to self-pulsing dynamics without switching.** This is CASE 2, with $\gamma_p = 25 \text{ ns}^{-1}$, as described in sec. 2.2.1: the stable (unstable) part of the branches are in thick (thin) lines. (a) Maximum and minimum of $A = R_+^2/(\mu - 1)$ versus normalized injection current, (b) Frequency of the periodic solutions versus normalized injection current. The X and Y-LPs are in black and red respectively and the EP states are in blue. The periodic solution created on the EP state is in green (a similar branch is created on the other Hopf bifurcation but not represented). The solution created on the Y-LP state is in orange and is a peculiar two-mode period-2 solution, the highlighted frequency is therefore the detuning between the two modes (see details in the text). Diamonds are Hopf, squares are saddle-node, crosses are period doubling and stars are torus bifurcations. In panel (b) the black dashed line gives F_{split} and the red one F_{RO} .

observed theoretically. For increasing injection currents, the stable limit cycle oscillating around the unstable EP state is then destabilized by a sequence of period doubling bifurcations leading the system toward a chaotic dynamics with anticorrelated fluctuations of the polarization. Interestingly, this chaotic dynamics can be, at first sight, confused with a mode hopping between two non-orthogonal EP states matching the dynamics reported in [54]. The distinction between chaos and mode hopping dynamics will be the focus of section 2.3.

For $2.84 < \mu < 6.42$, no stable state (neither steady nor time-periodic) is available. The laser evolves chaotically, but we still observe a qualitative change of the optical spectrum when the current is increased. Comparing Fig. 2.9(b.1) and (c.1), we remark the emergence of a new peak in the Y LP mode and multiple sidebands at the relaxation oscillation frequency for both the X and Y LP modes. We therefore report strong simi-

larities between the optical spectra of Fig. 2.9(c.1) and the one uncovered experimentally in Fig. 6 of [54]: the two detuned orthogonal LP modes emit simultaneously, and both optical spectra exhibit sidebands at the relaxation oscillation frequency $F_{RO} \approx 12$ GHz. Although no higher injection current is considered in the experimental report of Olejniczak *et al.* [54], it is interesting to describe the further evolution of the dynamics as we find some elements explaining the origin of the two-mode emission observed.

At $\mu = 6.42$, based on the bifurcation diagram in Fig. 2.8(d) and optical spectra in Figs. 2.9(c.1)–(d.1), we clearly observe a sudden change of the dynamics: the system goes from a chaotic behavior to a more ordered quasi-periodic dynamics and smoothly evolves toward a periodic solution with two modes similar to the one described in the previous case. In fact, in the optical spectra of Figs. 2.9(c.1) to (f.1), we observe the slow rise of a new peak on the Y polarization axis. This peak is at the frequency of the high-frequency LP ($\omega_Y = \gamma_p - \gamma_a \alpha$) and gradually becomes the dominant one for $\mu > 8$. Although the time-series seem unaltered by this qualitative evolution - compare Figs. 2.9(c.3) and (d.3) before and after $\mu = 6.42$ respectively -, the numerous, well-defined peaks in the spectra of Fig. 2.9(d.1) confirm this evolution. As the current is increased further, the optical spectrum gets simplified as in Figs. 2.9(e.1)–(f.1), hence allowing us to trace back the quasi-periodic dynamics to the dynamics from which it originates.

Using continuation techniques, we identify this final state as the peculiar two-mode period-2 solution created by the Hopf bifurcation destabilizing the Y-LP steady-state already highlighted in the previous case, see orange line in Fig. 2.10. Here the Hopf bifurcation occurs at extremely (and unrealistic) injection currents about $\mu \approx 50$, but the dynamical solution is similar to the one observed in the previous subsection for $\gamma_p = 4 \text{ ns}^{-1}$. As already described before, it is a period-1 solution for the left and right circular polarizations E_{\pm} but, because of the phase difference evolution and anti-phase dynamics of R_{\pm} , it becomes a two-mode period-2 solution when considering the X and Y-LPs. We remind that, as a result of this peculiar dynamics, the frequency obtained by continuation techniques is the frequency detuning F_{detune} between the two linearly polarized modes and not the frequency of the output power oscillations. The two spectra are plotted in Fig. 2.9(f.1) and we observe again two interleaved spectra for X-LP and Y-LP with sidebands at even multiples of the detuning frequency between the two modes. The frequency of the sidebands is confirmed by the time-series of panel (f.3) showing anti-correlated self-pulsations at two times the detuning frequency. With the parameters considered here, this means that the oscillations appear at a frequency close to 30 GHz, i.e. about two times F_{RO} .

Following the scenario backward then allows us to identify the different frequency contributions. The two-mode solution is destabilized by a torus bifurcation at $\mu \approx 9.5$. We see that one additional frequency appears, creating additional sidebands with multiple

harmonics around every peaks of the optical spectra, see Fig. 2.9(e.1). Interestingly, we can identify frequency components at the relaxation oscillation frequency $F_{RO} \approx 15$ GHz. Next, the quasi-periodic solution is further altered as more and more harmonics appear and we finally obtain the complex spectra plotted in Fig. 2.9(d.1). The detuning between the main peaks of the two LP modes is however still matching the frequency of the unstable periodic solution uncovered by continuation techniques. Thus, we remark that the detuning between the two-modes is already fixed at the frequency F_{detune} of the unstable two-mode solution even before the appearance of the quasi-periodic dynamics. In Fig. 2.9(c.1), despite the chaotic behavior, the detuning between the two modes is already matching the frequency given by the thin orange line in Fig. 2.10(b): $F_{\text{detune}} \approx 9.8$ GHz. This result has therefore a striking conclusion: in the case of a two-mode emission from both orthogonal LP modes, the detuning is not defined by the birefringence frequency but is again a bifurcation problem.

For decreasing currents, the laser follows the same - but, of course, reversed - bifurcation sequence and we do not find any bistability in this case.

Finally, the scenario described above agrees well with the experimental observations reported in [53, 54]: it includes the transition through EP states, the emergence of self-pulsing dynamics at the relaxation oscillation frequency and we will show in the next section that it also exhibits a random-like hopping dynamics between two non-orthogonal EP states. Moreover, we also accurately reproduce the two-mode emission reported in [54] with the additional sidebands at the relaxation oscillation frequency. More importantly however, we highlight that, in contrast with commonly accepted interpretations, the detuning between the two orthogonal LP modes does not relate to the birefringence of the cavity in this situation. In fact, we show that, similarly to the conclusions drawn for the previous scenario, this is a bifurcation problem: the frequency is determined by the solution created by the Hopf bifurcation destabilizing the Y-LP mode even though this event might take place at unreachable injection currents.

The most important conclusion of this section would therefore be that the birefringence or “effective” birefringence cannot be unambiguously uncovered by dynamical measurements: not by measuring the frequency of the self-pulsing dynamics accompanying PSs nor by measuring the detuning between the two orthogonal LP modes. Although it can be close to either the birefringence frequency or the relaxation oscillation frequency, absolutely no conclusion can be made from this measurement without additional details, e.g. scaling of the dynamics with the injection current as in [54] to identify the contribution of the relaxation oscillation frequency. Based on this new insight, we can conclude that the estimation of the “effective” birefringence provided in [51] and [54] are not completely reliable and should be considered with caution.

2.3 DETERMINISTIC POLARIZATION CHAOS IN FREE-RUNNING VCSELS

In the frame of the SFM, the bifurcation scenarios predicted accurately reproduce the essential features of the self-pulsing dynamics accompanying PSs. Especially, we showed in the previous section a good agreement with both the type II PS scenario described in [51] and the transition toward nonlinear self-pulsing dynamics without switching reported in [53, 54]. In both cases however, we highlighted that the frequency of the dynamics or the detuning between the two LP modes cannot, in general, be linked to the characteristic frequencies of the system, i.e. the birefringence frequency F_{split} or the relaxation oscillation frequency F_{RO} . Indeed, the oscillation frequency or the detuning can actually take a wide range of values which cannot be traced back to the characteristic frequencies mentioned above. In particular, the value of the birefringence cannot be measured through dynamical measurements such as the frequency of the self-pulsing dynamics as in [51], or the detuning between the two orthogonal LP modes as in [54]. Nevertheless, we showed that all the dynamical features observed experimentally can be reproduced in the frame of the SFM with frequencies close to those claimed in the reports above. One peculiar feature however remains to be discussed: the random-like hopping between two non-orthogonal elliptically polarized states observed in a quantum dot VCSEL [54].

In this section, we perform a more in-depth investigation of the reported mode-hopping dynamics and show that it clearly calls for a different interpretation than any noise-induced hopping already reported in VCSELS. We provide a new deterministic interpretation of this dynamics based on the SFM framework: we obtain a convincing agreement with all the statistical features of the dynamics and demonstrate some similarities with Lorenz chaos [12]. Several indicators retrieved from the experimental time-series lead to the conclusion that the random-like hopping dynamics is indeed chaotic.

2.3.1 *Experimental characterization of quantum dot VCSELS*

We investigate submonolayer InGaAs quantum dot VCSELS with high-speed layout grown at the Technical University of Berlin. The details of the devices can be found in [85]. As shown in table 2.1, the wafer contains 4 groups of 36 devices with different mesa diameters ranging from 26 to 36 μm . While larger mesa sizes (typ. $> 31 \mu\text{m}$) generally lead to multimode emission, most of the lasers appear to exhibit a single longitudinal mode. On the other hand, the lasers with the smaller mesa sizes (25 and 26 μm) appear to be not working. The lasers showing strong multimode behaviors were left aside as their analysis fall out of the scope of this work.

In practice, to power the quantum dot VCSELS on the wafer, we need to use probes carefully positioned using a microscope and micrometer actuators. Although it increases the complexity of the setup, it also allows us to easily investigate all the devices on the wafer without removing any mechanical pieces. To easily use the two 3-direction micrometer actuators that move the probes, the wafer has to be placed on the table horizontally. On Fig. 2.11(a), we can also observe that the wafer is placed on a Peltier element which, combined with a calibrated resistive sensor - connected to the two small blue wires - and a temperature controller - not shown here -, allows to control the device temperature with a 0.01°C resolution. Because the collimation lens must be set very close to the laser, we place it directly over the wafer and then use a mirror at 45° to redirect the beam horizontally, see Fig. 2.11(b). The rest of the optical elements can then be placed normally on the optical table using regular optical posts.

31	30	31	30	31	30
32	29	32	29	32	29
33	28	33	28	33	28
34	27	34	27	34	27
35	26	35	26	35	26
36	25	36	25	36	25

31	30	31	30	31	30
32	29	32	29	32	29
33	28	33	28	33	28
34	27	34	27	34	27
35	26	35	26	35	26
36	25	36	25	36	25

31	30	31	30	31	30
32	29	32	29	32	29
33	28	33	28	33	28
34	27	34	27	34	27
35	26	35	26	35	26
36	25	36	25	36	25

31	30	31	30	31	30
32	29	32	29	32	29
33	28	33	28	33	28
34	27	34	27	34	27
35	26	35	26	35	26
36	25	36	25	36	25

Table 2.1 – **Mapping of the InGaAs quantum dot VCSEL wafer used in the experiment.** The wafer is composed of 4 groups of 36 devices. The numbers indicate the mesa size of each device while the cell color shows whether the laser is not working (gray), exhibiting random-like hopping (green), or exhibiting no dynamical behavior (white). As can be seen on this map, the wafer contains at least seven devices exhibiting random-like hoppings between elliptically polarized states.

The dynamics of the devices is intrinsically linked to their polarization properties, the experiment therefore needs to focus on these specific aspects. The setup is similar to the one described in [53, 54]: the scheme is displayed in Fig. 2.11. The temperature of the device is measured by a calibrated sensor and stabilized by a temperature controller combined with a Peltier module. For the sake of clarity, these elements are not pictured in the scheme. To send the optical beam to the measurement equipment, we need to cou-

ple it into a fiber. Therefore to avoid unwanted reflections from the fiber front-facet, we place an optical isolator before the coupler. For simplicity, the polarizers of the isolator are fixed and we use a half-wave plate to perform polarization resolved measurements. In this chapter, we take for reference the axis along which the light is linearly polarized at threshold, i.e. we define the polarization at 0° as the orientation of the linear polarization at threshold.

In this section, we use the following equipment. The temperature/current controller is a Profile LDC 1000 controller. For polarization LI-curve measurements, we use a Newport 2832-C power meter. To record time-series, we use an oscilloscope Tektronix CSA7404 (4GHz bandwidth - 20 GSamples/s) with its built-in photodiode (700-1650nm - 2.4 GHz bandwidth). For radio-frequency (RF) spectrum measurements, we use an Anritsu MS2667c RF spectrum analyzer (7 kHz - 30GHz bandwidth) and a fast NewFocus 1554-B photo-detector (10kHz - 12GHz bandwidth) combined with a NewFocus 1422-LF RF amplifier (20 GHz bandwidth).

We demonstrated in the previous section 2.2 that the scenario experimentally reported by Olejniczak *et al.* [53, 54] in the devices presented here can be accurately predicted in the frame of the SFM model. Especially, we reproduce the dynamics at the relaxation oscillation frequency and the two-mode dynamics observed for large currents. On the other hand, this experimental report also highlighted a peculiar mode-hopping dynamics between two non-orthogonal elliptically polarized states with their main axes being symmetrical with respect to the axis of the linear polarization at threshold; a typical time-series is displayed in Fig. 2.12(b) inset. This hopping can be observed in a very large range of injection currents - between $I_S \approx 1.95$ mA and $I_R \approx 3.55$ mA as defined in Fig. 2.12(a) - and shows, as already discussed in section 1.3, a statistical evolution opposed to the one reported for noise-induced hopping dynamics [41]. Indeed, as displayed in Fig. 2.12(b), the average dwell-time - i.e. the time between two successive jumps - shows a dramatic decrease for increasing currents, instead of an exponential increase as seen for the noise-induced dynamics. Because none of the reported features relates to the noise-induced hopping between LP states, that has already been reported and explained as a Kramer's hopping problem, such observation clearly calls for a different interpretation.

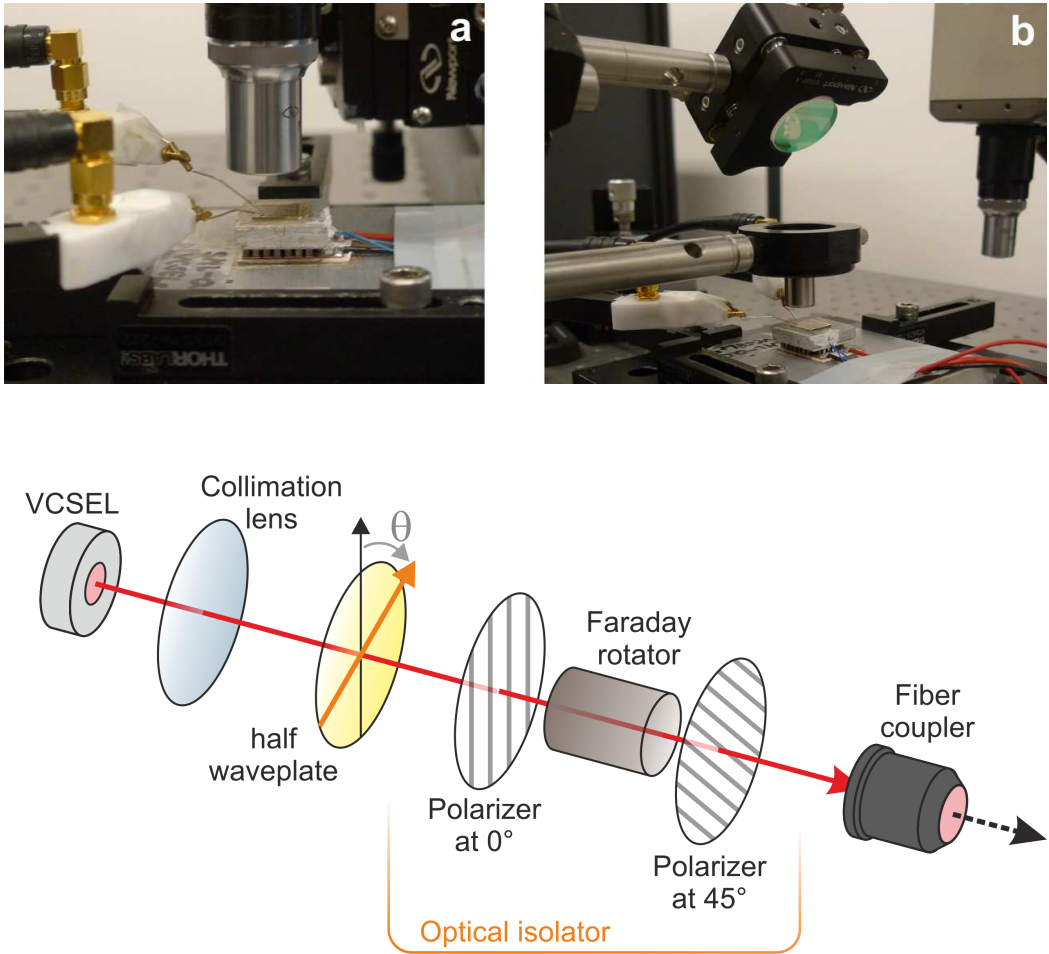


Figure 2.11 – **Scheme of the experimental setup.** (a) shows the wafer on the Peltier element during the electrical probe placement. (b) shows the setup in the characterization configuration where one device is connected; the light is collimated by a lens, and a mirror at 45° is used to direct the beam horizontally. Finally, the bottom part of the figure shows a scheme of the experimental setup, but for clarity the mirror is not represented. The laser is collimated, then goes through a rotatable half-waveplate - used to change the analyzed polarization orientation - and finally a optical isolator to prevent undesired reflections from the fiber fact. The beam is then coupled into a fiber and directed towards measurement equipments.

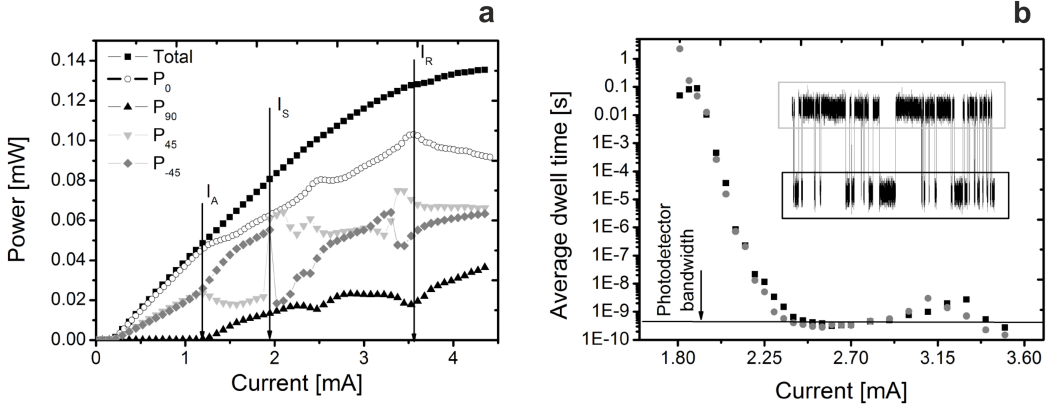


Figure 2.12 – **Polarization resolved LI-curves for increasing currents and statistics of the mode hopping dynamics.** (a) Polarization resolved-LI curve showing the evolution of the system for increasing injection currents. From threshold to I_A the laser emits on a LP state, and then on an EP state for $I_A < I < I_S$. Between $I_S < I < I_R$ a random-like hopping dynamics between two EP states is observed, and finally for $I > I_R$ the laser emits in a two mode emission. (b) Evolution of the average dwell-time - i.e. the time between two successive jumps - for the mode-hopping dynamics. The inset shows a typical time-series of the random-like hopping projected at 45° of the linear polarization at threshold. Taken from [54].

In this section we provide additional experimental details in order to identify essential features that would support our interpretation of polarization mode-hopping in QD VCSELs. In particular, we make a comprehensive investigation of the devices integrated in the wafer presented earlier at various temperatures. Thus, as shown in table 2.1, we found 7 devices exhibiting the reported mode hopping dynamics out of the 144 total number of devices on the wafer. It therefore seems to us that the mode-hopping dynamics is a quite reproducible feature even though it can take place at various temperatures. In our case, the experiments being performed in normal laboratory conditions, we did not investigate temperatures below 18° to avoid condensation which could damage the whole wafer and, considering the large number of devices and that such comprehensive investigation is time-consuming, we limited ourselves to temperatures below 26° for the moment.

This comprehensive analysis of almost all the devices on the wafer allowed us to identify the common features of the bifurcation scenario leading to the mode-hopping dynamics. First, the switching from one EP orientation to the symmetric one, as observed at I_S in Fig. 2.12(a), seems to be a marker of the mode-hopping dynamics. Indeed, this switching appears to be quite systematic before the emergence of the hopping dynamics; it even disappears when the temperature is sufficiently changed for the mode-hopping dynamics to vanish. At this point, it is worth noting that this switching relates to the

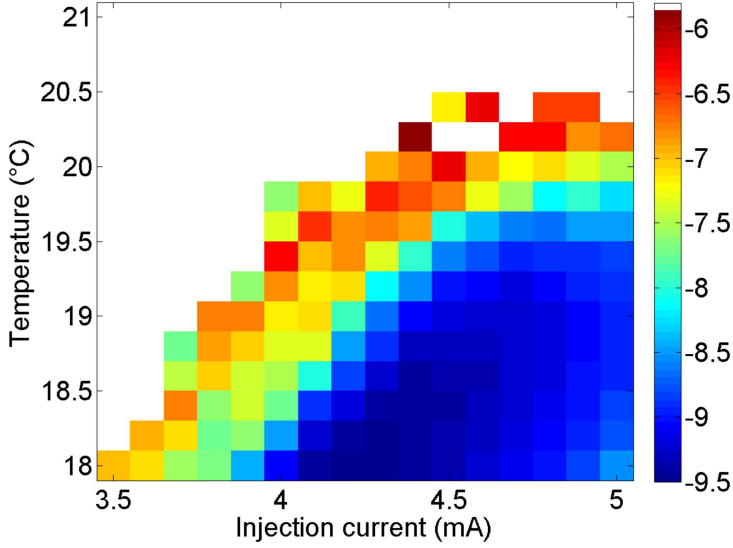


Figure 2.13 – **Evolution of the average dwell-time with respect to the temperature and the injection current.** The value of the average dwell-time is indicated by the colormap on the right side of the figure in a logarithmic scale. White regions indicate that no mode hopping could be found. Because of the limited length of the recorded time-series used for this measurement, the maximum dwell-time that could be measured was limited to $1\ \mu\text{s}$; The statistical significance of large averaged dwell-times should therefore be considered carefully.

bistability of limit cycles that will be discussed in section 2.5 of this chapter. Secondly, we observe a strong dependence of the polarization dynamics on the temperature. In Fig. 2.13, we plot a map showing the evolution of the average dwell-time in the temperature versus injection current plane. When the temperature is increased, the average dwell-time increases dramatically and fast hopping dynamics is pushed toward larger currents. Thus, changing the temperature by just a couple of degrees is therefore sufficient to suppress the reported dynamics.

Finally, we report surprising RF spectra which also confirm that an alternative interpretation is required to explain this peculiar hopping dynamics. First, we observe that before the mode hopping region, the laser is not in an EP steady-state: instead, we see in Fig. 2.14(a) that it exhibits a self-pulsing solution oscillating around the EP state. Then, for larger currents, the mode-hopping dynamics emerges, destroying this self-pulsating solution and any specific features of the RF spectrum. On few other spectra, we also observed the appearance of a second peak at half the limit cycle frequency, hence providing evidence of a period doubling bifurcation. Thus, for a current of $3.94\ \text{mA}$, we observe a

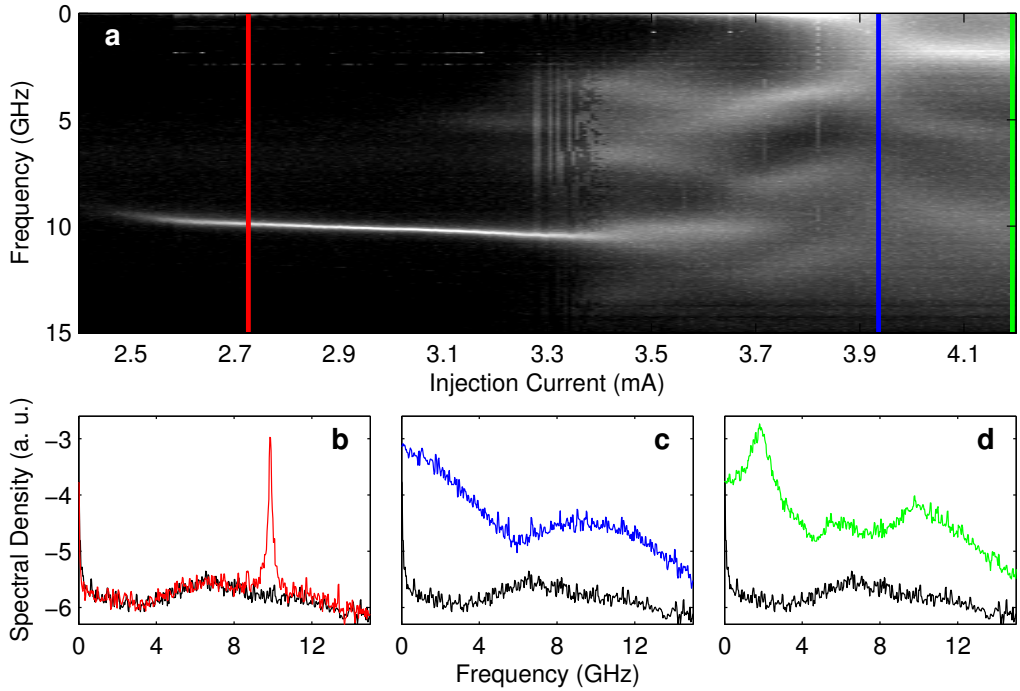


Figure 2.14 – **Experimental radio-frequency spectra of the dynamics.** (a) shows the evolution of the RF spectrum for increasing injection currents. The three detailed spectra have been taken at three different injection currents highlighted by the colored vertical lines: (b) red line, before the mode hopping region at 2.73 mA, (c) blue line, in the middle of the mode hopping region at 3.94 mA and (d) green line, for a very fast hopping at 4.19 mA. The spectrum plotted in black on all three panels gives the noise floor. All the spectra considered here have been recorded for a polarizer oriented at $+45^\circ$ with respect to the linear polarization at threshold.

peculiar RF spectrum with a large “low-frequency” contribution and just a small bump at the frequency of the previous periodic solution, as shown in Fig. 2.14(b). Finally, in Fig. 2.14(c), we report a strong peak at low frequency - which matches the average dwell-time time scale - and another wide but smaller peak around 10GHz which seems to relate to the frequency of the first self-pulsing solution. In the end, the evolution of the spectrum seems quite complex with many details and specific features that cannot be explained in the frame of a stochastic mode-hopping, see e.g. Fig. 7 in [64].

The experimental work described in this section has been performed with the participation of Emeric Mercier during his internship at the VUB. I therefore gladly acknowledge his contribution to the experimental results obtained.

2.3.2 Route to polarization chaos

We present here a chaotic interpretation - i.e. deterministic and hence opposed to the common stochastic viewpoint - of the random-like polarization mode hopping reported in the previous subsection. Interestingly, the route to chaos described here appears in a very wide range of birefringence values. We therefore use the same set of parameters as in section 2.2, and in particular we choose $\gamma_a = -0.7 \text{ ns}^{-1}$ and $\gamma_p = 4 \text{ ns}^{-1}$ because the bifurcation scenario appears to be clearer in this case. It should be remarked however that we also observe a similar scenario for $\gamma_p = 25 \text{ ns}^{-1}$, hence demonstrating a complete agreement with the experimental scenario reported in quantum dot VCSELs [53,54].

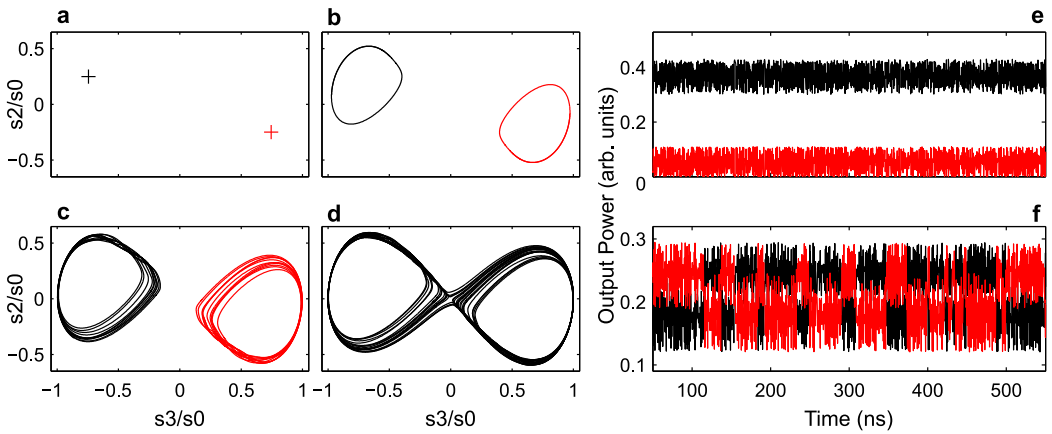


Figure 2.15 – **Route to polarization chaos in the SFM framework.** Bifurcation sequence in the Stokes parameter ($s_2/s_0, s_3/s_0$) plane for an increasing injection current μ . (a) For $\mu = 1.34$, there are two symmetric non-orthogonal elliptically polarized states. (b) For $\mu = 1.39$, the two EP states are simultaneously destabilized by two Hopf bifurcations, hence creating two limit cycles that oscillate around the now unstable elliptically polarized states. (c) For $\mu = 1.41$, cascades of period doubling bifurcations lead to the emergence of two single-scroll chaotic attractors. (d) For $\mu = 1.425$, the two attractors finally merged into a single double-scroll attractor with the two “wings” oscillating around the unstable EP states. (e, f) Time-series of the polarization resolved output power at $\mu = 1.425$: projections at 0° (black) and 90° (red) (e) and projections at 45° (black) and -45° (red) (f).

Here we use a different viewpoint based on a projection of the system trajectory in the Stokes parameter ($s_3/s_0, s_2/s_0$) phase-space. At threshold the laser emits linearly polarized light and, as already detailed in the previous section, this steady-state is destabilized by a supercritical pitchfork bifurcation which creates two symmetric elliptically polarized steady-states, see black and red crosses in Fig. 2.15(a). We plot the evolution of the ellipticity and the orientation of the ellipses main axes with respect to the linear polarization at threshold for increasing injection currents in Fig. 2.16. We observe that

both characteristics strongly increases just after the pitchfork bifurcation, but then the evolution is relatively smooth: the maxima are reached for both features around $\mu = 1.35$ when the EP steady-states are destabilized. We observe that the maximal ellipticity is about 25° while the maximal angle between the main axes of the ellipses and the linear polarization at threshold is about 22° . Considering that both EP steady-states are symmetrical with respect to the LP at threshold, the maximum angle between the two main axes of the ellipses is about 45° . As a result, the two polarizations are never orthogonal at any injection current. A similar evolution has been observed for a wide range of birefringence.

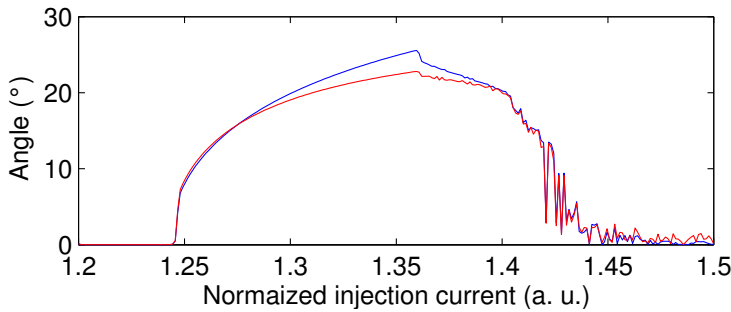


Figure 2.16 – **Evolution of elliptically polarized steady-state characteristics with the injection current.** We show the evolution of the ellipticity in blue and the orientation of the ellipse main axis with respect to the linear polarization at threshold in red for increasing injection currents. Since the two EP steady-states are symmetric, the orientation of the ellipses main axes is identical and the plotted evolution is valid for both states. Both values are given with the same scale in degrees.

For larger currents, the two EP states get destabilized by two Hopf bifurcations, hence creating two symmetrical limit cycles displayed in black and red in Fig. 2.15(b). Next, cascades of period doubling bifurcations destabilize the two limit cycles and create two single-scroll chaotic attractors. As can be seen in Fig. 2.15(c), the chaotic trajectories keep oscillating around the unstable EP steady-states. Interestingly, the size of the two attractors grow when the current is increased. As a result, beyond a critical value of the injection current the two single-scroll attractors merge to form a double-scroll “butterfly” attractor, see Fig. 2.15(d). Of course, this attractor shape clearly reminds the first discovery of chaotic motion and the chaotic attractor of Lorenz [12].

For a more practical viewpoint, we also plot the chaotic evolution of the system for polarization resolved output power in Figs. 2.15(e,f). We use an injection current of $\mu = 1.425$ and average the time-series over 0.5 ns to simulate a slower photodetector response to match the results of [54]. In Fig. 2.15(e) we plot the output power projected

at 0° and 90° in black and red respectively, i.e. the polarization at threshold and the orthogonal one. Although the signal seems very noisy - despite the absence of noise in the simulations - , we could easily conclude that the laser just emits elliptically polarized light as no evidence of switching can be found. This is not true anymore when looking at the projection at 45° and -45° shown in black and red respectively in Fig. 2.15(f): indeed in these projections we clearly observe irregular random-like anticorrelated hops between two different states exactly as reported experimentally.

In the rest of this thesis, considering that the chaotic behavior only appears through polarization fluctuations, we will refer to this dynamics as “Polarization Chaos”.

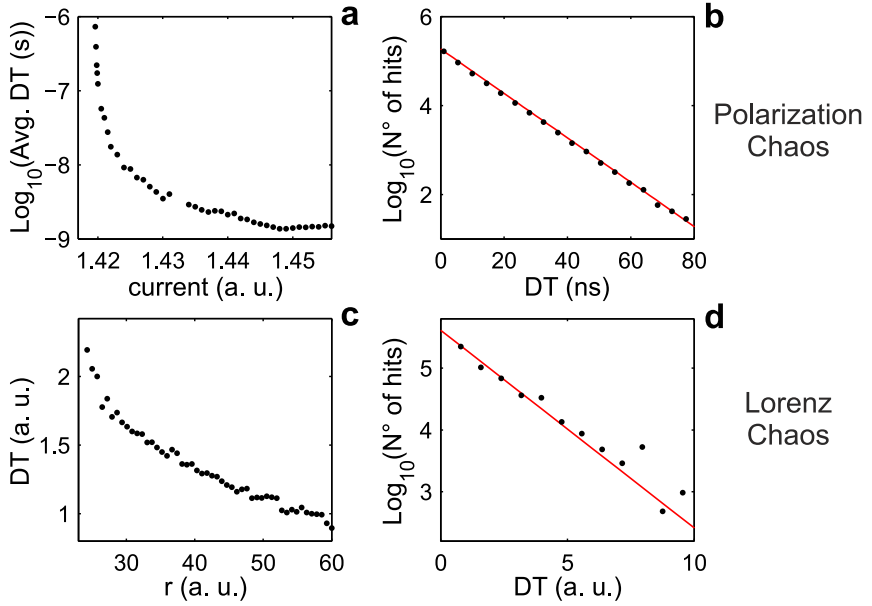


Figure 2.17 – **Statistical properties of mode dwell time and comparison between polarization and Lorenz chaos.** Dwell time statistics for simulated polarization chaos in a laser diode (a,b) and for Lorenz chaos (c,d). (a) Semi-logarithmic plot of the average dwell time for polarization chaos versus injection current. (b) Distribution of the dwell time for polarization chaos at $\mu = 1.425$. (c) Average dwell time evolution for Lorenz chaos versus r parameter. (d) Distribution of the dwell time of Lorenz chaos for $r = 27$.

2.3.3 Statistics of the deterministic mode hopping

One of the key feature that distinctly called for a different viewpoint than the noise-induced Kramer’s hopping interpretation is the statistical features of the polarization mode-hopping observed in QD VCSELS [54]. Indeed, as opposed to the stochastic switchings observed between two orthogonal linearly polarized states [41], the dwell-time of the

dynamics - i.e. the time between two successive jumps - exponentially decreases along with increasing injection currents [54]. To prove a qualitative agreement with our theoretical interpretation we therefore need to perform a detailed statistical analysis of the dwell-time for the chaotic dynamics obtained theoretically. Considering the similarities of the chaotic attractor unveiled and Lorenz chaos, as seen in Fig. 2.18, we also perform a similar analysis on the latter. Indeed, following the Lorenz-Haken analogy [13], briefly described in section 1.2, the r parameter of Lorenz's equations plays the same role as the injection current in Maxwell-Bloch equations for lasers. The results of this statistical analysis is given in Fig. 2.17 where we show the evolution of the average dwell-time (a and c, respectively) and its distribution for $\mu = 1.425$ and $r = 27$ (b and d, respectively).

In Fig. 2.17(a), we show for polarization chaos a significant decrease - from microseconds to nanoseconds - of the average dwell-time when the current is increased. The dwell-time distribution follows an exponential decay law as shown in Fig. 2.17(b). These statistical features are in good agreement with the experimental observations. In practice, these features can easily be explained: the size of the two "wings" of the attractor keep growing for increasing currents, hence making it easier for the system to jump from one side to the other. Interestingly we also observe similar features for Lorenz chaos. In particular in Fig. 2.17(c), we observe a decrease of the average dwell-time when increasing the r parameter, which plays the same role as the injection current. We also report an exponential distribution of the dwell-time as displayed in Fig. 2.17(d). Nevertheless, we remark that the observed decrease of the dwell-time is much smaller for Lorenz chaos than for polarization chaos. Indeed, the average dwell-time is only divided by 2 for Lorenz chaos while few orders of magnitude of difference appear in the SFM framework.

The statistical analysis brings the interesting conclusion that, although the random-like hopping of both Lorenz and polarization chaos show an exponential distribution - which at first sight might be interpreted as the result of a noise driven Kramer's hopping problem -, the scaling of the dwell-time with the r parameter or the current suggests an interpretation based on a bifurcation scenario to chaos rather than on stochastic Kramer's hopping in a bistable system.

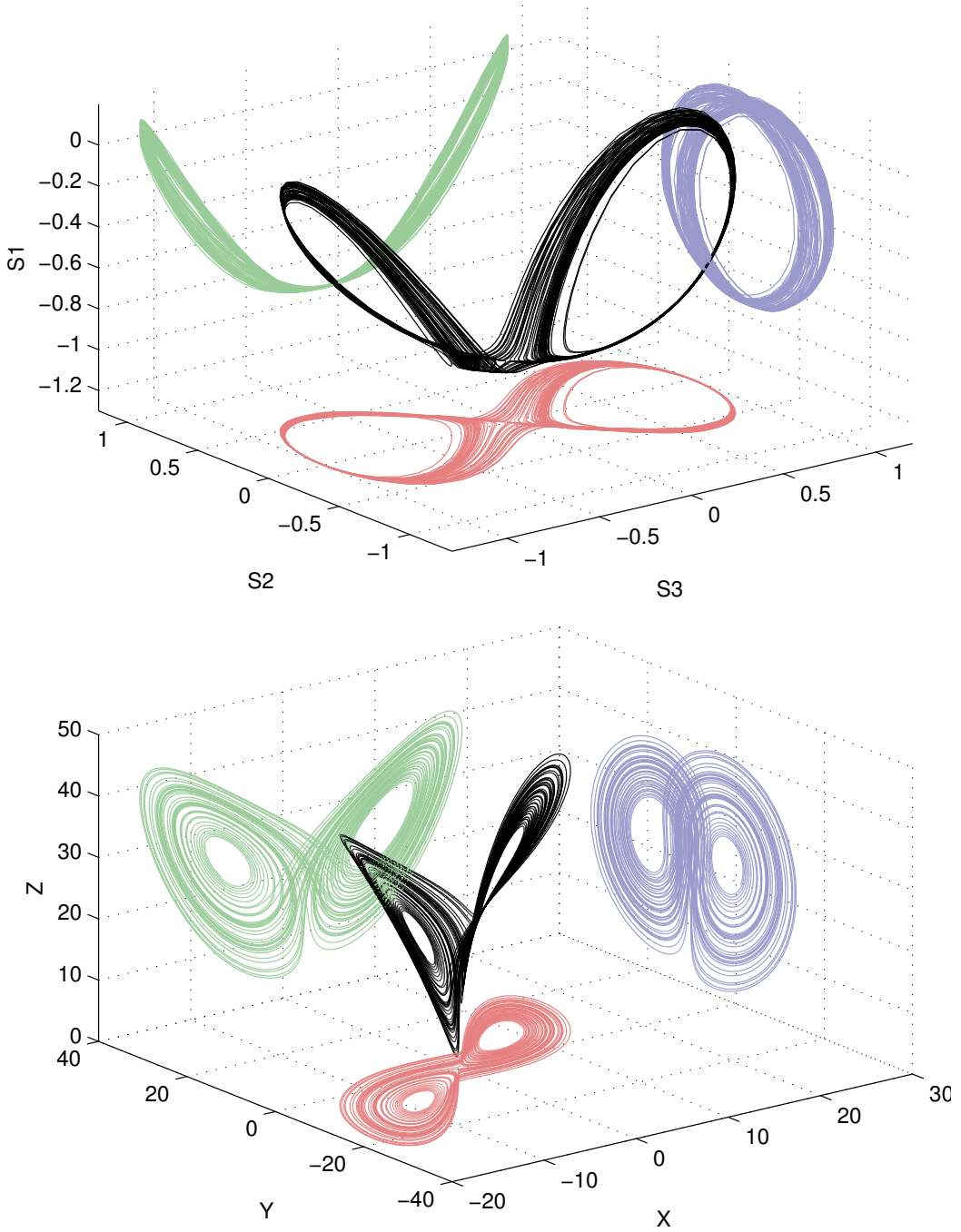


Figure 2.18 – **Attractors of polarization chaos and Lorenz chaos.** (top) representation of the chaotic attractor of polarization chaos in the normalized Stokes parameter phase space for $\mu = 1.43$ and $\gamma_p = 4 \text{ ns}^{-1}$. (Bottom) representation of Lorenz chaos in its three dimensional phase-space for $\sigma = 10$, $r = 28$ and $\beta = 8/3$

2.4 EXPERIMENTAL CHAOS IDENTIFICATION

The theoretical predictions of the SFM model successfully reproduce all the reported experimental features, hence justifying our chaotic interpretation for the random-like polarization dynamics observed. Yet, the fact that a free-running laser diode does not behave like a damped oscillator and can turn into chaos without the need of external forcing or perturbation is not a straightforward assumption. We therefore need to unambiguously confirm the chaotic nature of the experimental time-series to fully validate the suggested interpretation.

In this section, we therefore exploit experimental time-series of the mode-hopping dynamics and we apply several algorithms which provide essential indications. In particular, we evaluate the largest Lyapunov exponent, along with the Kolmogorov entropy and the correlation dimension of the chaotic attractor. Finally, we make sure that the chaos identification is not the result of a colored noise which could, in principle, influence the results of the algorithms we used.

2.4.1 Estimation of the largest Lyapunov exponent

By definition, a chaotic dynamics will exhibit a high sensitivity to initial conditions: thus two identical systems starting at similar but not identical initial positions will show completely different evolution after a certain time. This feature is directly linked with the existence of a positive Lyapunov exponent. Demonstrating that the system exhibits at least one positive exponent is therefore sufficient to demonstrate the chaotic nature of a dynamics.

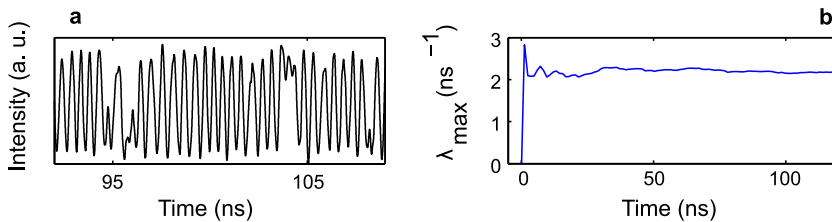


Figure 2.19 – **Estimation of the largest Lyapunov exponent from experimental time-series.** (Left) Typical time-series recorded experimentally at $+45^\circ$ of the LP at threshold, and exploited for the evaluation of the largest Lyapunov exponent using Wolf's algorithm. (Right) Evolution of the Lyapunov exponent estimation versus the position in the time-series during its scanning.

In practice we cannot control the initial condition of the system. Nevertheless, we can overcome this hurdle by exploiting long time-series as in Wolf's algorithm [131]. The basic idea behind this algorithm is that a chaotic dynamics follows an attractor: although the system will never be twice in the exact same state, it will go through very similar states repeatedly. We can then see the points where the system exhibits similar evolution as near neighbors and we can evaluate the rate at which their corresponding system trajectories diverge from each other, i.e. estimate the largest Lyapunov exponent which quantifies this divergence. When two trajectories cannot be considered as near neighbors anymore, we select surrogates within the time-series. This step is however more complicated than the above description might suggest as we need to maintain the orientation of the vector separating the near neighbors to ensure a reliable estimate.

Here we perform this algorithm on the time-series partially displayed in Fig. 2.19(a). Following the notation of [131], we use an embedding dimension around $M = 10$ and a time-step of $\tau = 100$ ps. The maximal distance allowed between near neighbors before changing surrogate appeared to be not too crucial, but the orientation conservation during this step appeared to be more challenging. The estimation of the Lyapunov exponent is displayed in Fig. 2.19(b). We also checked that for different embedding dimension and time-steps we still obtain a similar estimate. Thus we measure a largest Lyapunov exponent roughly around $\lambda_{\max} \approx 2 \text{ ns}^{-1}$ (overall we obtained $1.2 < \lambda_{\max} < 2.5 \text{ ns}^{-1}$).

As explained earlier, measuring from the experimental time-series a largely positive maximum Lyapunov exponent ($\lambda_{\max} \approx 2 \text{ ns}^{-1}$) could be sufficient to confirm the chaotic nature of the dynamics. Here, however, the main issue is to determine whether the hopping dynamics is deterministic or noise-induced: hence the noise would not have to be necessarily the dominant process. As a result, in the case of a noise-induced hopping, we can imagine that we could obtain a positive Lyapunov estimation while the dynamics is only a combination of deterministic but non-chaotic and stochastic processes. To dissipate any further doubt, we therefore perform additional verifications that will provide altogether a clear and unambiguous discrimination of the chaotic origin of the polarization mode-hopping dynamics reported.

2.4.2 K_2 -entropy and correlation dimension

In this subsection, we use the Grassberger-Procaccia (GP) algorithm [132–134] which estimates the K_2 -entropy, i.e. Kolmogorov entropy - where $K_2 = 0$ for periodic or quasi-periodic systems, positive for chaos and $K_2 = \infty$ for purely stochastic processes - and provides an estimation of the attractor correlation dimension D_2 for the mode-hopping dynamics recorded experimentally.

Description of the GP algorithm

Starting with a sequence X of N points, we divide it into $N - D$ vectors of size D and we compute the correlation integral $C_D(r)$ for this new sequence, that is, the average number of vectors that can be found in a sphere of radius r around a single vector. Mathematically, $C_D(r)$ is given by the following equation:

$$C_D(r) = \lim_{N \rightarrow \infty} \frac{1}{N^2} \left[\sum_{n,m} (d(X_n, X_m) < r) \right] \quad (2.30)$$

Then according to Grassberger and Procaccia [132], in the case of a chaotic dynamics, the correlation integral would behave as: $C_D(r) \approx r^\nu \exp(-\tau D \kappa)$ where τ is the time-series time-step, ν the correlation dimension and κ the Kolmogorov entropy. Hence we can deduce an estimation of the K_2 -entropy and correlation dimension D_2 using the following:

$$K_2 = \lim_{\substack{D \rightarrow \infty \\ r \rightarrow 0}} \frac{1}{\tau} \ln \left(\frac{C_D(r)}{C_{D+1}(r)} \right) \quad (2.31)$$

$$\text{and } D_2 = \lim_{\substack{D \rightarrow \infty \\ r \rightarrow 0}} \frac{d \ln(C_D(r))}{d \ln(r)} \quad (2.32)$$

For a very small radius r , the K_2 -entropy will diverge anyway because of limited numerical precision or additional noise in the time-series. We therefore look for the convergence of the Kolmogorov entropy in the radius range where the slope of the correlation integral converges.

In practice, we obviously do not have access to an unlimited amount of data and the time-step is limited by the oscilloscope sampling rate. However the latter is not crucial as we only need the dynamics to be sufficiently resolved - the time-series exploited for the analysis are sampled at 20 GSamples/s while the time-scale of the hopping dynamics is around the nanosecond -, and previous studies relied on sequences of a few tens of

thousands of points which are largely accessible nowadays [132, 135]. However the application of the GP algorithm is numerically demanding and we found that using a larger number of points is time-consuming and not always necessary: here we use time-series of 20,000 points. Finally, unlike in mathematical simulation, we have to consider intrinsic noises of the system and measurement tools which are not part of the chaotic dynamics. To improve the efficiency of the GP algorithm on such noisy dataset, we therefore use an extra re-embedding procedure based on singular-value analysis [136, 137].

Embedding based on singular-value analysis

The idea behind this re-embedding procedure is to keep only the dominant part of the dynamics hence suppressing the noisy part of the data which could disturb the GP algorithm. Although it could be done by filtering or processing the data in other ways, the singular-value decomposition has been demonstrated to make the optimal choice of linear transformation [137].

We start by defining a time-window M , then we divide the recorded time-series X of N points into $N - M$ vectors of size M : $Y(n) = \{X(n), X(n+1), \dots, X(n+M-1)\}$, with the size of Y being $(N - M) \times M$. Then we compute the covariance matrix of Y : $A = Y^T Y$, along with its eigenvalues λ and eigenvector matrix V . As a result, we obtain the following identity:

$$\Theta V = A V = Y^T Y V \quad (2.33)$$

With Θ the diagonal matrix formed with the eigenvalues $\lambda_{i \in [1, M]}$ - also called singular-values of A - they are generally sorted by order of magnitude for simplicity. By definition, V forms an orthogonal basis and therefore the projection of Y onto this basis would provide M linearly independent variables:

$$P = YV = \{P_1(n), \dots, P_m(n)\} \quad (2.34)$$

These independent variables are usually called “Principal Components”, and the variance of each component is equal to its corresponding eigenvalue. The main features of the dynamics are therefore represented by the components related to the largest eigenvalues, and discarding the components related to the smallest ones would, in theory, dismiss the contribution of the noise part. We can then apply the Grassberger-Procaccia algorithm using the first components as in a multi-variate approach. Considering this additional re-embedding procedure, we must however discard vectors which are not sufficiently separated in time, i.e. use the additional condition $|n - m| > M$ in eq. (2.30).

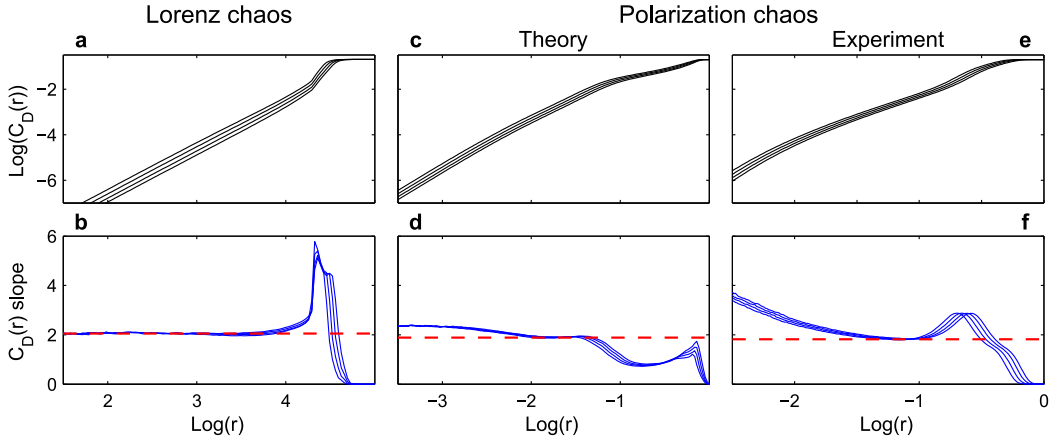


Figure 2.20 – **Chaos identification based on the Grassberger-Procaccia algorithm.** Results of the GP algorithm for Lorenz chaos (a,b), theoretical polarization chaos (c,d), and experimental time-series (e,f) showing logarithmic plots of correlation integral $C_D(r)$ versus sphere radius r (a,c,e) and the slope of the correlation integral versus sphere radius r (b,d,f). In all three cases, the GP algorithm converges, creating a plateau on the slope of the correlation integral. The red dashed lines give estimate of the correlation dimension in all three cases: Lorenz chaos $D_2 \approx 2.05$, theoretical polarization chaos $D_2 \approx 1.89$ and experimental time-series $D_2 \approx 1.82$.

Application of the algorithm

In practice, we use a time-window of $M = 0.6 \text{ ns}$ for the re-embedding procedure and keep the 5 most significant principal components of the singular-value analysis. The other components exhibit variances more than 1000 times smaller, i.e. $\lambda_{i>5} < \lambda_1 \cdot 10^{-3}$. For comparison, we also compute the K_2 -entropy and the correlation dimension of Lorenz chaos and Polarization chaos based on simulated time-series without any re-embedding. For Lorenz chaos, we use the following parameters: $\sigma = 10$, $r = 28$ and $\beta = 8/3$. For the simulation, we use a time-step of 0.004 but we downsample the data by a factor 20 for the GP-algorithm. For polarization chaos, we use the same parameters as in the previous section with an injection current of $\mu = 1.43$. The simulation time-step is 0.001 and the downsampling factor is 20, i.e. we take one out of each 20 sample points. For the application of the GP-algorithm, we only exploit the output power projected at 45° of the linear polarization at threshold to mimic experimental data.

The evolution of the correlation integral curves for increasing vector size D is given in Fig. 2.20 for Lorenz chaos (a,b), for direct numerical simulation of the chaotic dynamics with the SFM model (c,d) and for the experimental time-series (e,f). Only values of $D \in [12, 15]$ are displayed for clarity. In all three cases, we obtain a clear convergence of the correlation integral slope around $C_D \approx 2$: for each time-series, a well-resolved

plateau can be seen in the bottom plots in Fig. 2.20. Thus we obtain the following values for the K_2 -entropy: $K_2 \approx 1.65$ for Lorenz chaos, $K_2 \approx 2.5 \text{ ns}^{-1}$ for the simulated polarization chaos and $K_2 \approx 7.1 \text{ ns}^{-1}$ for the experimental time-series. At last, we also verified that no convergence appears in the case of stochastic polarization mode hopping simulated in a similar way as in [44]. Indeed, as expected, the correlation integral never converges for increasing D , which would then lead to an infinite value of K_2 .

2.4.3 Statistical approach and discrimination of colored noise

As already stated before, GP or Wolf's algorithm are not flawless and some peculiar stochastic dynamics could potentially exhibit results similar to those observed in the previous section. To fully confirm the chaotic nature of the dynamics, we first try to model the random-like hopping dynamics as a Hidden Markov Process - hence analyzing whether the jumps between elliptically polarized states are influenced by hidden additional variables or any external perturbation. Then, we consider the tests suggested in [138] designed to discriminate low-dimensional dynamics from peculiar colored noises which can exhibit finite non-zero K_2 -entropy values. Although the experimental time-series successfully pass all the suggested tests, we describe here only the most significant one.

M			N		
	0	1		0	1
0	0.8292	0.1708	0	1.0000	0
1	0.1369	0.8631	1	0	1.0000

Table 2.2 – **Results of the Baum and Welch algorithm for simulated Polarization chaos.** The transition Markov matrix M is displayed on the left while the hidden-related transition matrix N is given on the right. The two colored cells show that the off-diagonal elements of matrix N are 0 hence indicating that simulated polarization chaos can be seen as a purely Markovian process. No spontaneous emission noise is considered here.

Hidden Markov models (HMMs) are used in a variety of fields, including speech/gesture recognition or bio-informatics. But HMMs can also be exploited for the analysis of chaotic signals [139]. Here we focus on a recent development of such modeling to identify noise or external perturbation effects on physical systems [140]. Especially, in the context of a two-mode system, this approach provides valuable insight in the origin of the hopping dynamics between two modes.

We first convert the recorded mode-hopping time-series into a bit sequence corresponding to the system state - e.g. 1 for the upper state and 0 for the lower state. Then, we apply the Baum and Welch algorithm - or forward-backward procedure - to retrieve two 2×2 matrices [140, 141]: the transition Markov Matrix (M) and the hidden related transition Matrix (N). M shows the characteristics for the purely Markovian part of the dynamics while the N matrix indicates hidden processes contribution. As a result, for a purely Markovian process the N matrix will be diagonal, hence the off-diagonal values of the N matrix will confirm if the time-series can be considered as generated by a purely Markovian process or if we need to include the contribution of hidden processes.

To have a baseline, we first perform this modeling on simulated time traces using the SFM model and the same parameters as for the GP algorithm (in particular, we use $\mu = 1.43$). Applying the Baum and Welch algorithm, we find the matrices M and N displayed in table 2.2; thus we observe that the off-diagonal elements of N are 0. We can therefore conclude that the mode hopping dynamics between the two wings of the double-scroll attractor simulated by the SFM model can be modeled by a purely Markovian process. Moreover, adding some intrinsic noise to the system - i.e. a spontaneous emission noise β_{sp} - has little effect on the algorithm and the N matrix obtained: for $\beta_{sp} < 10^{-6} \text{ ns}^{-1}$ the off-diagonal elements of N possibly differs from 0 but remain negligible with values below $< 10^{-20}$. However, for larger levels of noise $10^{-6} < \beta_{sp} < 10^{-4} \text{ ns}^{-1}$, the off-diagonal elements of N become significant, with values of the order of 0.01. As a result, we can conclude that the simulated polarization chaos dynamics can be modeled as a purely Markovian process for low levels of noise; however, for strong noise levels, the modeling of the dynamics would require hidden markov processes. Although not displayed here, similar results have been obtained for Lorenz chaos.

Similarly, we perform this test for the time-series recorded experimentally. Hence, based on the raw data - we use neither re-embedding nor downsampling for this analysis -, the application of the algorithm give us the M and N matrices displayed in table 2.3. Unlike with simulated time-series, we do not find the off-diagonal elements of N to be zero, but they appear to be extremely small (below 10^{-12}). Considering the potential perturbations from the experimental setup, these values appear quite negligible and we conclude that the dynamics can be seen as a purely Markovian Process. Which means that the random-like jumps are not the result of noise, but of the internal system dynamics. In addition, this result suggests that the level of spontaneous emission noise in the device is low enough to have only little impact on the dynamics: in particular, it suggests that the noise itself might not be sufficient to induce a jump between the two wings of the attractor.

M			N		
	0	1		0	1
0	0.3125	0.1009	0	0.9999	$2.2e^{-12}$
1	0.6875	0.8991	1	$2.3e^{-19}$	0.9999

Table 2.3 – **Results of the Baum and Welch algorithm for experimental time-series.** The transition Markov matrix M is displayed on the left while the hidden-related transition matrix N is given on the right. The two colored cells highlight the extremely small off-diagonal elements of matrix N indicating that no hidden process needs to be considered in the modeling of the recorded dynamics.

At last, we present here one of the tests suggested in [138] to discriminate low-dimensional dynamics from colored noise exhibiting finite non-zero K_2 -entropy. In the case of a fully stochastic process, two points of a time-series will be correlated only if they are close in time, as opposed to chaotic processes where a larger correlation exists between points. Indeed for a system driven by a low-dimensional attractor some order can be found in the deterministic random-like dynamics. The main defect of the GP algorithm is that it does not consider the time separation between points hence allowing some noises to exhibit a finite K_2 -entropy. To verify that the recorded dynamics does not fall into this case, we can perform the following test:

Based on a sequence X of length N , we define a time-window M and divide the sequence into $N - M$ vectors of size M . Then, for each value of separation in time $\Delta t = |n - m|$, we choose randomly a large number of pairs of points and consider the distribution of their separation in space $d(X_n, X_m)$. We therefore analyze the evolution of the distribution of the separation in space for increasing separation in time. For clarity, it is easier to consider the contour plot of this evolution.

Here we use a time-window of $M = 0.6 \text{ ns}$ as for the GP algorithm. In Fig. 2.21, we display the evolution of the separation in space for increasing time-separation for 500 pairs of points chosen randomly in the sequence. As described in [138], a noise-induced process will only exhibit a transient behavior as no correlation appears for larger time separation. Here, however, we find several sharp dropouts in the distribution: they are manifold, irregularly distributed and appear in the whole range of time-shift considered, i.e. several tens of nanoseconds. Especially, we find strong oscillations of the distribution for separation as large as 84 ns which could definitely not be observed for a random process. Such result therefore confirms that the recorded dynamics shows some correlation at large time-scales and therefore cannot be interpreted as a noise-induced process.

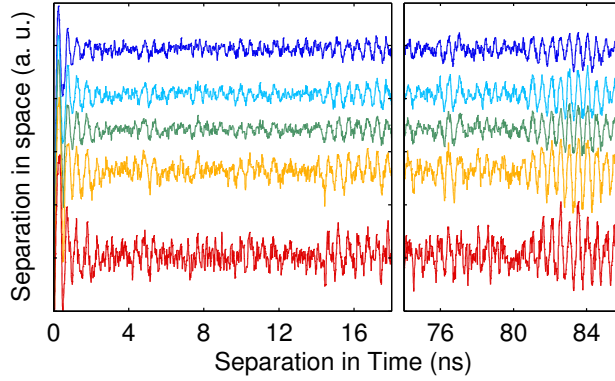


Figure 2.21 – **Discrimination between chaos and colored noise.** Plot of a space-time separation contour map for the experimental time-series. Different curves correspond to different fractions of the distribution: above the blue line represents 10%, then from blue to red the fractions are 30%, 50%, 70% and 90% of points above the red curve. The dropouts indicate a particular proximity in space between pairs of points for a given time-shift. Such dropouts can be found in the whole range of time-shift we consider, that is, several tens of nanoseconds, demonstrating some intrinsic order inside the random-like dynamics.

Finally, considering all the evidence gathered in this section: Wolf's algorithm, GP algorithm, HMM modeling and the additional tests described in [138], and in addition to the good agreement obtained on the bifurcation scenario presented in the previous section, we can safely state that the dynamics previously unveiled is indeed chaos. We therefore report, for the first time, chaotic fluctuations in a single-mode laser diode without the need for external perturbation or forcing, hence highlighting one more time the richness of VCSEL polarization dynamics.

2.5 BISTABILITY OF LIMIT CYCLES

So far in this chapter, we have shown that the EP states that can appear in a VCSEL play a key role in the dynamical evolution and polarization properties of these lasers. However, the mechanism selecting the EP state is still obscure, and therefore remains to be clarified.

In the theoretical framework described so far, the two EP states appear symmetrically with respect to the linear polarization at threshold. From the expression of these two states it is obvious that, apart from their different orientations, the two EPs are strictly equivalent. In fact, the complete bifurcation sequence is identical for both EP as can be observed in Fig. 2.7: identical bifurcations occur at exactly the same injection current and create equivalent solutions that only differ by their polarization orientation. However, experimental observations cast some doubts about such symmetry as the polarization ellipse always exhibits the same orientation after the destabilization of the LP stable at threshold.

Here we report on a peculiar phenomenon calling for a deeper analysis: we observe a bistability between two limit cycles (LCs) oscillating around two EPs with main axis symmetrically oriented with respect to the axis of the LP at threshold. In addition, the two LCs exhibit different oscillation amplitudes and slightly different frequencies. As briefly explained above, such asymmetry between the two elliptical polarization cannot be predicted in the SFM framework. However, we demonstrate in this section that taking into account a small misalignment between the phase and amplitude anisotropies is a sufficient perturbation to break the system symmetry. With this seemingly minor change, we can in fact accurately reproduce the behavior unveiled experimentally.

2.5.1 *Experimental observations*

The experimental setup is the same as the one described in section 2.3. The axis of the linear polarization at threshold is again taken as the reference for the polarization orientation, and is identified as the polarization at 0° . To record the time-series we use a fast photodetector (NewFocus 1554-B, 10 kHz - 12 GHz bandwidth), an electronic amplifier (NewFocus 1422LF, 20 GHz) but here the oscilloscope that we use is different from the previous section (Agilent DSOX92504A, 25 GHz, 80 GS/s). The RF spectra of the measured time-series are then obtained through a FFT of the recorded time traces.

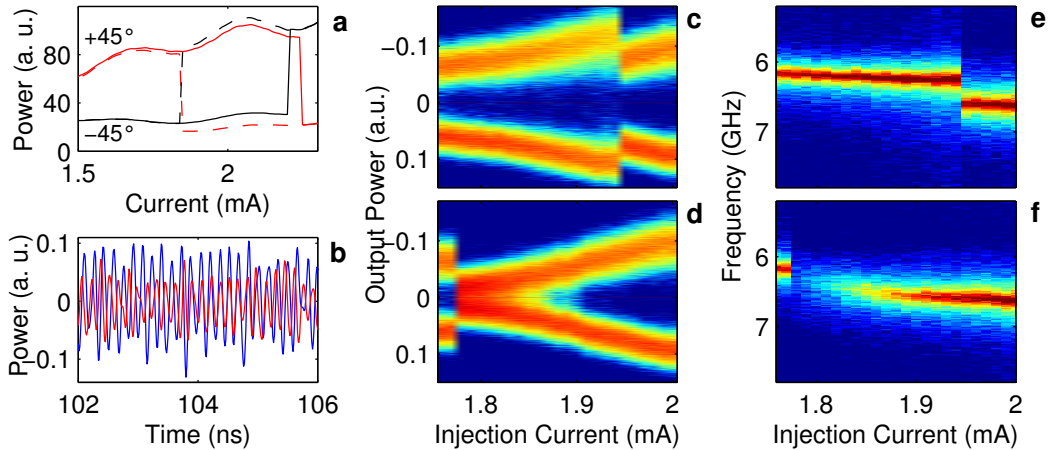


Figure 2.22 – **Experimental observations of the limit cycle bistability.** (a) Polarization resolved LI curve at $+45^\circ$ and -45° with respect to the LP at threshold: in red and black for increasing (solid) and decreasing (dashed) injection currents respectively. (b) Time-series recorded at a current of 1.85 mA for increasing (blue) and decreasing (red) currents. (c)–(d) Plot of the time-series extrema versus increasing (top, c) and decreasing currents (bottom, d). (e)–(f) FFT of the time-series versus increasing (top, e) and decreasing currents (bottom, f). Time series considered for panels b to f are recorded at 0° with DC removed.

The device temperature is set at 22°C and, in this case, the laser becomes chaotic at high injection currents following the bifurcation sequence described in the previous section. The EP states are quickly destabilized and a limit cycle (LC) oscillating around an unstable EP polarization appears with a frequency of about 6.25 GHz, see the time-series in Fig. 2.22(b). As can be observed in Fig. 2.22(c,e), the amplitude of the LC increases with the current, until $J = 1.95$ mA where the LC is destabilized and a new dynamics appears with a different oscillation amplitude and a slightly higher frequency of 6.55 GHz. More importantly, we find that the new self-pulsing dynamics oscillates around the other symmetrical EP state, see the inversion of the black and red curves for the projections at $+45^\circ$ and -45° in Fig. 2.22(a). From this point, decreasing the injection current unveils a region of bistability between the two LCs - see Fig. 2.22(a,d,f) - until the laser finally settles back on the first LC for currents below $J = 1.77$ mA. It is also worth noting that, before this last switching, the cycle fades out toward an EP steady-state as can be seen from the decreasing amplitude in Fig. 2.22(d) and the vanishing peak in Fig. 2.22(f). Due to a high sensitivity of the device to experimental conditions, such as the stress from the probes, the range of currents at which the bistability appears can change for different measurements. In particular, the switchings occur at different current values in Fig. 2.22(a) and panels (c–f).

The experimental work described in this section has been performed with the participation of Emeric Mercier during his internship at the VUB. I therefore gladly acknowledge his contribution to the experimental results obtained.

2.5.2 Description of the asymmetric SFM

The emergence of a limit cycle bistability is in itself an interesting development, showing once again the richness of the laser nonlinear dynamics, but it also raises essential questions. Especially, such reproducible hysteresis between two limit cycles oscillating around different elliptically polarized states confirms that the two EP states are not equivalent. Yet, as described in sec. 2.1, in the SFM framework the two EP states are strictly equivalent as their definition is completely symmetric. In this context, only noise-induced switchings might appear but they would not be reproducible as are the experimental observations described above. In addition, the different characteristics - both amplitude and frequency of the bistable limit cycles are different - cannot be explained from a symmetrical viewpoint.

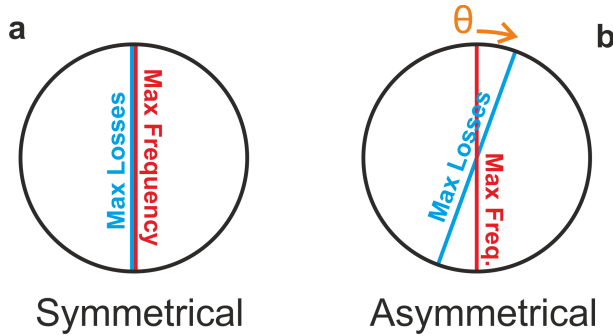


Figure 2.23 – **Symmetry breaking from anisotropy misalignment.** The anisotropy configuration of the SFM model used so far is displayed in (a) where we easily observe two axes of symmetry (vertical and horizontal). These symmetries can however be easily broken simply by considering a small angle θ between the two anisotropy axes as in (b). Thus no axis of symmetry exists anymore in the cavity and the elliptical polarizations will experience different parameters depending on their orientation.

To solve this situation we break the symmetry of the cavity anisotropies. In the model described in sec 2.1, the situation is the one of Fig. 2.23(a): the two anisotropy axes are aligned, hence we clearly observe two orthogonal axes of symmetry in the cavity. But introducing a small angle between the phase and amplitude anisotropies breaks the symmetry, and we clearly observe that one elliptical mode will always experience higher losses than the other. Thus, to describe the behavior of the investigated VCSEL, we use

a modified version of the SFM model, described in [77] which writes as follows in its dimensionless time-normalized form:

$$\frac{dE_{\pm}}{dt} = \kappa(1 + i\alpha)(N \pm n - 1)E_{\pm} - (i\gamma_p + (\cos(2\theta) \mp i\sin(2\theta))\gamma_a)E_{\mp} \quad (2.35)$$

$$\frac{dN}{dt} = \mu - N - (N + n)|E_+|^2 - (N - n)|E_-|^2 \quad (2.36)$$

$$\frac{dn}{dt} = -\gamma_s n - (N + n)|E_+|^2 + (N - n)|E_-|^2 \quad (2.37)$$

All the notations of section 2.1 have been kept for simplicity. θ is defined as the angle between the axis of maximum frequency and the axis of maximum losses. At this point it is convenient to define effective anisotropies:

$$\overline{\gamma_p^{\pm}} = \gamma_p \mp \sin(2\theta)\gamma_a \quad (2.38)$$

$$\text{and } \overline{\gamma_a} = \cos(2\theta)\gamma_a \quad (2.39)$$

Interestingly, the effective amplitude anisotropy is the same for both the right and left circular polarizations and only the phase amplitude or birefringence differs. Then, similarly to what is done in [69], we can transform eq. (2.35) into three real equations for the amplitude of the two circular polarizations R_{\pm} and their phase difference ϕ :

$$\frac{dR_+}{dt} = \kappa(N + n - 1)R_+ - \overline{\gamma_a}R_- \cos(\phi) - \overline{\gamma_p^+}R_- \sin(\phi) \quad (2.40)$$

$$\frac{dR_-}{dt} = \kappa(N - n - 1)R_- - \overline{\gamma_a}R_+ \cos(\phi) + \overline{\gamma_p^-}R_+ \sin(\phi) \quad (2.41)$$

$$\frac{d\phi}{dt} = 2\kappa\alpha n + \overline{\gamma_a}\sin(\phi)\left(\frac{R_-}{R_+} + \frac{R_+}{R_-}\right) + \left(\overline{\gamma_p^-}\frac{R_+}{R_-} - \overline{\gamma_p^+}\frac{R_-}{R_+}\right)\cos(\phi) \quad (2.42)$$

The last two equations remain unchanged. In the next sections, unless stated otherwise, we use the following dimensionless parameters: $\kappa = 600$, $\alpha = 3$, $\gamma_p = 35$, $\gamma_a = -10$ and $\gamma_s = 100$. Although the equations described here are dimensionless unlike those presented in section 2.1, as already highlighted in the same section, all the parameters remain entirely compatible with the parameter sets used previously as we always kept a carrier decay rate of $\gamma = 1 \text{ ns}^{-1}$.

2.5.3 Impact of the asymmetry on the laser dynamics

With the given set of parameters and without asymmetry, i.e. $\theta = 0$, we obtain the dynamical evolution given in Fig. 2.24. The bifurcation scenario is very similar to the one described in section 2.2.3, and shows the same sequence to polarization chaos as described in the previous section. We observe a pitchfork bifurcation, at $\mu = 3.4$, destabilizing the linear polarization at threshold and leading the system to an EP steady-state. Then a limit cycle oscillating around this EP state appears at $\mu = 3.5$, its amplitude increases with the current until it is destabilized by a cascade of period doubling bifurcations toward chaotic fluctuations for $\mu > 5$. In addition, we observe that the EP state orientation can change to the symmetrical EP state without any qualitative change of the scenario and a decreasing current does not unveil any kind of bistability.

As described earlier, in this case the two EP orientations are strictly equivalent - they experience identical bifurcations and dynamical characteristics - thus the two scenarios can only be distinguished by the different orientation of the main polarization axis. In this frame we therefore cannot explain the limit cycle bistability reported experimentally as we need asymmetric EP states in order to obtain different stability information, limit cycle amplitudes and frequencies for the observed EP states.

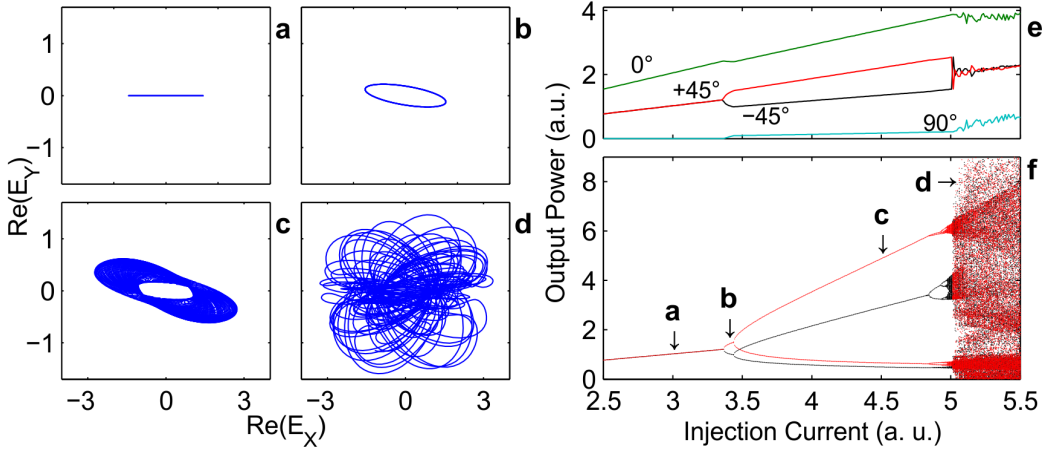


Figure 2.24 – Evolution of the dynamics without asymmetry, i.e. with aligned phase and amplitude anisotropies. (a)–(d) Polarization of the emitted light given by the trajectory of the system in the $(\text{Re}(E_X), \text{Re}(E_Y))$ phase plane in the 4 cases identified in (f). (e) Polarization resolved LI curve for -45° , 0° , $+45^\circ$ and 90° with respect to the polarization at threshold in black, green, red and blue respectively. (f) Extrema of the polarization resolved output power time-series at $+45^\circ$ and -45° in red and black respectively.

Introducing a small misalignment between the phase and amplitude anisotropies, i.e. considering a small additional asymmetry in the SFM model, we observe dramatic changes in the bifurcation scenario. In Fig. 2.25, we plot the simulated polarization resolved LI-curves, bifurcation diagrams and RF spectra obtained for a misalignment of only $\theta = -0.023$. This very specific angle has been chosen in order to provide a good match with the reported experimental features. For simplicity, we call EP_+ (EP_-) the EP state exhibiting a dominant emission at $+45^\circ$ (-45°); we also name the two limit cycles oscillating around these two states “ LC_+ ” and “ LC_- ”.

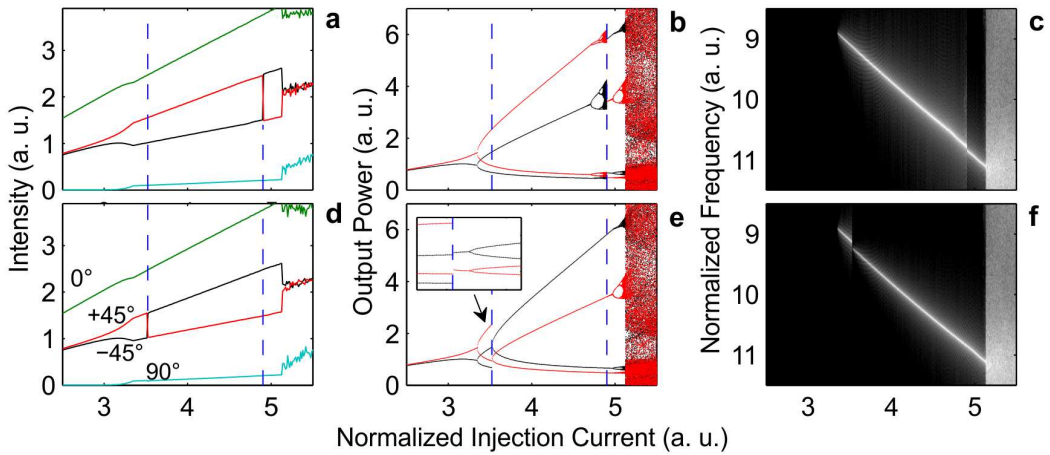


Figure 2.25 – **Impact of the asymmetry on the VCSEL dynamics.** (a)–(d) Polarization resolved LI curves for -45° , 0° , $+45^\circ$ and 90° with respect to the polarization at threshold in black, green, red and blue, respectively. (b)–(e) Extrema of the polarization resolved output power time-series at $+45^\circ$ and -45° in red and black respectively. The blue dashed vertical lines show the limits of the bistability region. The inset in (e) shows a zoom of the transition between the two limit cycles. (c)–(f) Normalized radio-frequency spectra of the polarization resolved time-series at $+45^\circ$. Those results are given for increasing (top) and decreasing (bottom) normalized injection currents.

First, we observe that the newly introduced asymmetry removes the pitchfork bifurcation. Thus at threshold the polarization is not exactly linearly polarized anymore but slightly EP_+ elliptical. Then for levels of current where the pitchfork bifurcation occurred - i.e. $\mu \sim 3.4$ -, the system now experiences a smooth transition toward an EP_+ steady-state with increasing ellipticity. This therefore confirms that the two EP states are not equivalent anymore as the new asymmetry obviously favors the EP_+ orientation. It is noteworthy that the sign of the misalignment angle selects the EP_\pm orientation, and we did not uncovered any other differences on the system dynamics for the selected angle values.

Secondly, we report an hysteresis cycle - and therefore a bistability - similar to the one reported experimentally. As can be seen in Figs. 2.25(a,d) and (b,e), we unveil a bistability between LC_+ and LC_- limit cycles. Indeed, the introduced misalignment seems to have no impact on the Hopf bifurcation at $\mu = 3.5$ that destabilizes the EP_+ steady-state and creates LC_+ . The amplitude of the cycle largely increases along with the injection current until it gets destabilized by a sequence of period-doubling bifurcation. With no misalignment, the laser would then enter a large region of polarization chaos, but here we find a polarization switching towards a second limit cycle which appears to be LC_- . The FFT of the simulated time-series in Fig. 2.25(c) shows a slight frequency shift, about 0.07 between the two cycles - i.e. about 70 MHz for a carrier lifetime of 1 ns. From this point, decreasing the current unveils a region of bistability between the two periodic solutions, delimited by the two vertical dashed lines in Figs. 2.25(a,b) and (d,e). The amplitude of LC_- decreases until the system reaches a steady EP_- emission around $\mu = 3.5$ (see inset in Fig. 2.25(e)). The transition is also visible in the FFT spectrum evolution in Fig. 2.25(f) where we can clearly see the main peak vanishing close to the switching point. The EP_- is however only stable in a tiny region and the system quickly settles back on LC_+ . At this point we observe that the frequency shift is slightly larger at 0.1 - about 100 MHz for a carrier lifetime of 1 ns - which matches the order of magnitude observed experimentally.

Finally, it should be emphasized that a misalignment angle between the phase and amplitude anisotropies as small as $\theta = -0.023$ - which makes the effective birefringence parameters differ by less than 3% - induces dramatic dynamical changes in the SFM polarization dynamics compared to the case of aligned anisotropies, and brings very good agreement with experimental results.

2.6 SUMMARY AND PERSPECTIVES

To sum up, in this chapter we focus on polarization dynamics of free-running VCSELs i.e. the behavior of surface-emitting lasers without external forcing or perturbation.

From a dynamical viewpoint, we first demonstrate that the frequency of the dynamics accompanying polarization switchings is a bifurcation problem and cannot be reduced to a competition between the two characteristic time-scales of the system - the birefringence frequency and the relaxation oscillation frequency. Indeed, depending on e.g. the birefringence of the laser cavity, the laser can experience different types of bifurcation scenarios and self-pulsing dynamics, that can exhibit various frequencies. In particular, it means that the characteristic frequencies of the system cannot be recovered from dynamical measurements: although the frequencies of the self-pulsations can be close to one of the characteristic frequencies of the system, they are not directly related.

In this frame, we also provide a dynamical interpretation of the peculiar random-like hopping dynamics between two non-orthogonal elliptically polarized states reported by Olejniczak *et al.* [53,54]. We successfully obtain an outstanding qualitative agreement with simulations of the SFM, hence suggesting that the reported polarization fluctuations are in fact chaotic, i.e. fully deterministic features, as opposed to typical noise-induced Kramer's hopping interpretation, that could be applied to the mode-hopping dynamics in QW VCSELs reported so far. Based on experimental data, we then unambiguously confirm the chaotic nature of the recorded dynamics, by using several algorithms and tools to discriminate chaos from stochastic processes. We therefore report, for the first time, a temporal chaotic behavior in free-running single-mode laser diodes.

Finally, in the same devices, we experimentally observe a new and intriguing bistability, between two limit cycles oscillating around two non-orthogonal elliptically polarized states. We show that this reproducible feature could not be explained in the theoretical framework considered so far. Furthermore, these experimental observations confirm that the two elliptically polarized states are not equivalent in real devices, and that the model should therefore be asymmetrical with respect to elliptically polarized states. Then, we demonstrate that considering a small misalignment between the phase and amplitude anisotropies is sufficient to reproduce the reported bistability with a good qualitative agreement. In addition, we show that a small misalignment already has a dramatic impact on the polarization dynamics of the VCSEL.

From a more theoretical point of view, we provide several new indications that prove the validity of the SFM for VCSEL dynamics. Indeed, we show that the SFM can be considered as a unifying framework, as it accurately reproduces most of the dynamical features of VCSEL polarization behavior reported so far, including the dynamics accompanying polarization switchings and the chaotic polarization fluctuations. In the last part of this chapter, we also show that the SFM also provides an accurate description of new self-pulsating polarization dynamics observed experimentally.

The perspectives of the work described in this chapter are, to my opinion, three fold:

- First, we show that, although it has been largely studied already, there are still experimental findings that were unknown about VCSEL dynamics. The new behaviors reported in this document are an additional demonstration of the dynamical richness of VCSELs. Also the demonstration that such relatively simple model like the SFM can be a unifying dynamical framework shows that we are far from having completely figured VCSEL dynamics out. Such result of course motivates theoretical and experimental investigations in order to fully understand and grasp all the details of polarization instabilities in VCSELs.
- Secondly, we show experimentally that quantum dot VCSELs can generate chaotic polarization output. The model used to reproduce this behavior does not consider any specific features of quantum dots. This point raises important questions: is it possible to design quantum-well VCSEL showing the same features? And what would be the essential mechanisms/structures leading to polarization chaos? Considering speed issues, we could then consider spin-polarized VCSELs to generate polarization chaos at extremely high-speed that would definitely benefit to optical chaos-based applications.
- Third, we found a new simple and very efficient way of generating chaos without the need for either complex designs, setups or forcing schemes. But can we use this new chaotic dynamics directly and replace other schemes? Although we give some answers about this in the next section - where we use polarization chaos to generate random bit sequences -, the chaotic dynamics reported in this chapter shows very different characteristics compared to e.g. chaos originating from time-delayed laser systems, and therefore different schemes might need to be considered.

3

APPLICATION OF POLARIZATION CHAOS TO RANDOM BIT GENERATION

*The generation of random numbers
is too important to be left to chance*

— Robert R. Coveyou

Our discovery of polarization chaos in a free-running laser diode provides a simple way of generating optical chaos without the need for external perturbation or forcing. Although it clearly opens new ways for optical chaos-based applications, the low-dimension of the dynamics might cast some doubts about its direct use. In this chapter, we counter these doubts and demonstrate that polarization chaos can be directly and efficiently exploited for physical random bit generation at high-speed. We achieve highly competitive bitrates (> 100 Gbps) and demonstrate that these striking results can be attributed to the “butterfly” shape of the chaotic attractor and the large growth rate of the dynamical entropy.

Part of the work presented in this chapter has been published in [142, 143].

3.1 STATE OF THE ART - OPTICAL CHAOS-BASED RANDOM BIT GENERATORS

Randomness, and consequently sequences of random numbers, have an extremely wide range of applications going from scientific interest - including e.g. monte carlo simulation - to cryptography, games - e.g. to shuffle cards or for online gambling - or even art and politics [144]. Obviously for art or games, random-like or pseudo-random sequences might be sufficient, but more sensitive topics (e.g. cryptography) bring stronger requirements and true random number sequences are highly desirable. As a result, the most demanding applications both in terms of quality of the randomness and amount of data remain security applications where random numbers are exploited to ensure confidentiality or integrity. Because of today's increasing needs for security, faster and safer - i.e. high-quality - Random Number Generators or Random Bit Generators (RBGs) are required, hence motivating a renewed interest. Generating a large amount of pseudo-random numbers from computations is quite easy. However they are only *pseudo random* as they are generated by a fully deterministic process. Moreover, once the seed - i.e. the starting point of the algorithm - is known the exact same sequence can easily be recomputed. Generating *true random numbers* based on physical systems is also quite feasible, but the speed of these system is generally quite limited. For instance, commercially available devices provide bitrates up to only tens of Mbps [145, 146], even though few hundreds of Mbps can also be achieved using several RBG channels [147]. To overcome these hurdles, many studies have been conducted, and thus numerous concepts of RBGs have been suggested such as entangled systems [148], quantum fluctuations [149–152], boolean networks [153], weakly coupled super-lattices [154] or amplified spontaneous emission in super-luminescent diodes [155–157]. Of these concepts however, the RBGs based on optical chaos have so far shown the most promising performances especially in terms of speed, with bitrates up to tens [158–160], and even hundreds of Gbps [157, 161–165].

By definition, chaos is not random, but when generated physically its sensitivity to initial conditions amplifies the intrinsic noises of the system [166–168]. This means that if two identical systems start from the same initial condition, after a sufficiently long time, they will evolve differently because of different intrinsic noises. Hence some studies were conducted in electronic systems to extract random bit sequences from chaotic dynamics and bitrates of few Mbps have been demonstrated [169–171]. However, in 2008, Uchida *et al.* successfully demonstrated bitrates up to 1.7 Gbps based on optical chaos from laser diodes with time-delayed optical feedback [11]. Such breakthrough was made possible by taking advantage of the time-scale and large bandwidth (up to 10 GHz) of optical chaos. This pioneering performance however requires quite a complex setup including:

1/ two lasers pushed into chaos by external optical feedback loops with incommensurate time-delays, 2/ two 1-bit analog-to-digital converters (ADCs) with a carefully set threshold to perfectly balance the ratio of 0 and 1, 3/ combining the two bit streams from both lasers using an XOR gate. Nevertheless, two exciting ways of improvement have been identified and investigated since then: optimizing the dynamics and its acquisition, and developing new randomness extraction techniques, i.e. post-processing methods.

The possibilities of improving the dynamics were already mentioned by Uchida *et al.* as they briefly stated that bitrates up to 6.2 Gbps have been demonstrated when increasing the chaos bandwidth through optical injection. Following this idea, different schemes have been suggested and interesting results have been demonstrated in laser diodes with polarization-rotated feedback [164, 172], photonic integrated circuits [161], extremely short optical feedback cavities [173, 174] or optical injection schemes [158, 163]. But a dramatic improvement has also been reported when very special care is taken to optimize the acquisition of the chaotic dynamics: especially optimization of the sampling rate and of the recorded chaotic time-series histogram appear to be essential issues [164]. On the other hand, the method chosen to extract random bits from the chaotic dynamics also appeared to be an essential step with exciting possible outcome. Soon after the first demonstration of chaos-based optical RBG, the use of multibit acquisition schemes combined with the computation of high-order derivatives has been shown to lead to bitrates of hundreds of Gbps [160, 162]. Although this method was later criticized as the final bitrate can exceed the information theoretic limit and the origin of the randomness cannot be traced back to the chaotic dynamics [175], this result motivated numerous studies and new methods of extraction have been suggested. Especially, different multibit extraction techniques have been introduced - using 8 or 16-bits ADCs as opposed to the 1-bit ADC used in [11] - in which only the least significant bits (LSBs) are finally kept to form the output bit sequence [161, 164, 172]. In addition, this method has also inspired the use of delayed comparisons where the chaotic waveform is then compared with a time-shifted version of itself [160], or combined using a bitwise xor [158, 163] or reversed XOR [157]. At this point, after discussing the development of an optical chaos-based random number generator, it is also important to consider the complexity of the processing in terms of real-time applications. Although the first breakthrough of Uchida *et al.* has been obtained in real-time [11], performances of hundreds of Gbps have all been achieved using off-line processing. However, when considering complex processing techniques, such as the high-order derivative computation proposed in [162], for which samples with an increasing number of bits are compared at rates of tens of GHz, it is necessary to address how these operations could potentially be achieved in real-time. Although handling a continuous bistream above ten Gbps is a challenging task, some interesting directions should be considered: 1/ The sampling rate at which the data are recorded can of course be reduced in order to obtain a more reasonable output. This would of course let some room of im-

provement in terms of performances on a more longer term. 2/ most of the processing techniques suggested so far could probably be parallelized and optimized in order to reduce the speed at which a single bitstream need to be processed. 3/ the next generation of field-programmable gate-arrays promise transceivers with performances above 50 Gbps which could therefore provide a versatile platform to implement the randomness extraction stage. Finally, the performances demonstrated by the optical chaos-based random bit generators are obviously at the limit of the capability of the electronics, but considering the dramatic and continuous improvement in this field, this challenge will probably be efficiently tackled in the next years.

As evident from the above discussion, various solutions for both the physical generation of the chaotic dynamics and the random bit extraction technique have been proposed. Surprisingly, only few studies focused on the theoretical basis and the link between the characteristics of the chaos and the potential bitrate that could be achieved. Nevertheless, a couple of paper investigated the link between the achievable bitrate for random sequences and the entropy growth rate for laser diodes with time-delayed optical feedback [173,176]. These studies interestingly underline that the growth rate of the entropy and the resulting memory time - i.e. the time after which the system loses its memory about its previous state - are directly linked to the largest Lyapunov exponent of the chaotic dynamics [176]. In addition, they report memory times as short as 1 ns for very short external cavities [173], hence justifying performances of few Gbps obtained with a 1-bit ADC. Finally, it is worth noting that an experimental analysis of the noise amplification by the chaotic dynamics has been successfully performed in a semiconductor laser with integrated external cavity [174].

From all these studies, a set of common requirements on the dynamics necessary to obtain random bit sequences at high-speed emerged. Even though fulfilling these requirements does not imply that random sequences at a large bitrate will be obtained, they somehow summarize the basic needs that appeared empirically. The requirements are as follows:

- Broad and flat power spectrum [11, 164, 172, 177, 178]. This requirement is mainly motivated by the need to mimic white noise, and is supported by several experiments where a larger bandwidth led to a strong increase of the final bitrate [11, 178].
- Fast autocorrelation decay [164, 172]. Obviously correlation is opposed to the goal of randomness, hence the faster the autocorrelation reaches zero, the faster new samples can be used. In particular, the width of the central autocorrelation peak can be linked to the optimal sampling rate which can be achieved with a given system [164].

- Rapid growth of the entropy [173, 174, 176]. As demonstrated in [176], the entropy growth defines the memory time of the system. Thus, faster growth will lead to smaller memory times, hence to a less predictable system and therefore to more random schemes.
- Large positive finite-time Lyapunov exponents [160]. The idea behind this requirement is that a chaotic dynamics can be locally non-random, i.e. be completely predictable for a relatively short time. Positive finite-time Lyapunov exponents are required to avoid these local events and therefore to improve the final randomness of the system.

To conclude, all these requirements motivate the use of large bandwidth high-dimensional complex dynamics exhibiting several positive Lyapunov exponents. Consequently, it motivates the use of a rather strong optical feedback [172], which typically lead to hyper-chaos [135, 179], i.e. chaos with several positive Lyapunov exponents.

Nevertheless, we demonstrate in the following that generation of random sequences at high-speed can be achieved using the polarization chaos dynamics from a free-running laser diode. Despite a low dimension of the dynamics, a small number of positive Lyapunov exponents and small bandwidth, we successfully obtain competitive performances compared to other schemes - with chaotic dynamics being a much better match to the requirements above -, hence bringing new light into the conditions leading to randomness at high-speed from chaos.

3.2 EXPERIMENTAL SETUP

The key element in the scheme we propose in this section, is a VCSEL device able to generate polarization chaos (see section 2.3). A detailed description of the device we used in the experiments can be found in [54, 85]. The chaotic dynamics can be seen as a random-like hopping dynamics between the two “wings” of the chaotic attractor which oscillate around two unstable EP states, represented by the red and blue ellipses in Fig. 3.1. A detailed approach of polarization chaos can be found in section 2.3. To convert these chaotic fluctuations of polarization in chaotic intensity fluctuations, that we can easily record, we simply use a polarizer. We orient it at 45° with respect to the linear polarization at threshold in order to maximize the mode-hopping amplitude, as already stated in [54].

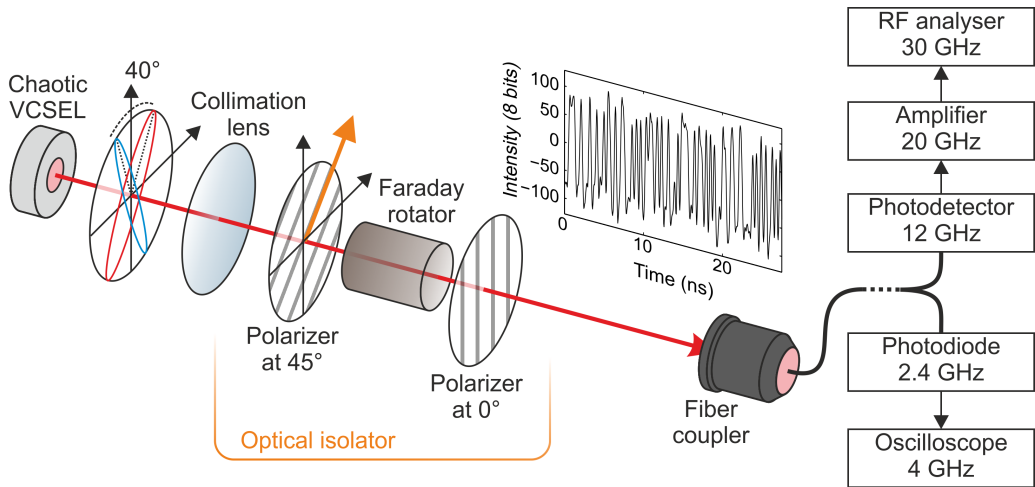


Figure 3.1 – **Experimental setup: from polarization chaos to chaotic time series.** The VCSEL generates polarization chaos: using a polarizer at 45° with respect to the LP direction at threshold, polarization chaos can be transformed into chaotic intensity fluctuations. This polarizer combined with a rotator and a second polarizer forms an optical isolator which prevents reflections from the fiber front facet. RF spectra are acquired with a fast photo detector, an electronic amplifier and a RF spectrum analyzer, whereas time-series are recorded with the small-bandwidth photodiode of the oscilloscope optical channel. Electronic bandwidths are indicated for each device.

The output beam is then coupled into a fiber plugged into two different measurement branches: one for the time-series acquisition using the built-in small-bandwidth photodiode (2.4 GHz bandwidth) of the oscilloscope (Tektronix CSA7404, 4 GHz, 20 GS/s) and the second for RF spectrum acquisition using a large bandwidth photodiode (NewFocus 1554-B, 12 GHz), a RF amplifier (NewFocus 1422-LF, 20 GHz) and a RF spectrum ana-

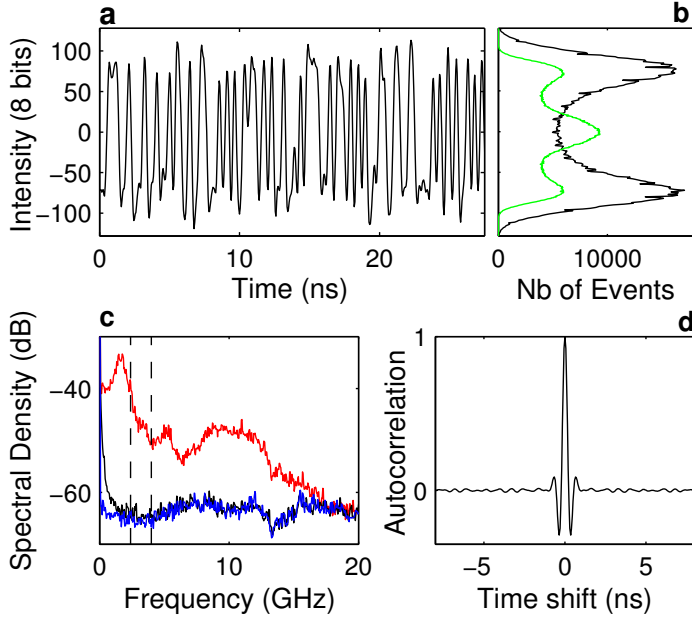


Figure 3.2 – **Characterization of polarization chaos time-series.** (a) Typical intensity fluctuations recorded by the oscilloscope 8-bit ADC and the small-bandwidth photodiode with the corresponding distribution given by the black curve in (b); the green curve shows the resulting histogram after a comparison of the time-series with a time-shifted (250 ps) version of itself. (c) RF spectra of the chaotic fluctuations, laser noise and amplification noise in red, black and blue respectively. Vertical dotted lines give the electronic bandwidth of the small-bandwidth photodiode of the oscilloscope optical channel and of the oscilloscope (2.4 and 4 GHz resp.). (d) Autocorrelation of the time-series.

lyzer (Anritsu MS2667c, 7 kHz - 30 GHz). We then add a Faraday rotator and a second polarizer to form an optical isolator that prevents undesired reflections from the fiber front-facet. Finally, using a variable neutral density filter - not pictured - we adjust the optical power received by the small-bandwidth photodiode in order to fully use the 8-bit range of the scope ADC, we typically target a ratio of saturated points between 10^{-4} and $10^{-1}\%$ estimated over 2 million points. The injection current is also tuned in order to obtain a fast hopping dynamics, typically a dwell-time - i.e. the time between two successive jumps - below 1 ns.

The characteristics of the recorded time-series are given in Fig. 3.1. Considering the double-scroll attractor, resembling the one of Lorenz, we can easily identify two different time-scales in the dynamics: 1/ the fast oscillations around an unstable EP state - corresponding to the wings of the butterfly attractor -, and 2/ the slower jumps between the two EP orientations - corresponding to the hops between the two wings of the attrac-

tor. Because of the limited bandwidth of the oscilloscope optical channel, the recorded time-series can only catch the slow part of the dynamics hence we typically obtain time-series as plotted in Fig. 3.2(a). In addition, this mode-hopping also leads to a two-peak histogram as in Fig. 3.2(b). Here, we measure an average dwell-time of about 0.06 ns. Both parts of the dynamics can easily be spotted on the RF spectra in Fig. 3.2(c): low-frequencies correspond to the slow mode-hopping with a relatively broad peak around 1.7 GHz - which matches the averaged dwell-time measured from the time-series - while the top-hat-shaped peak around 10 GHz is induced by the fast oscillations around the unstable EP states. Finally, the autocorrelation of the time-series exhibits a single-oscillation with quite limited side-peaks. The width of the central peak is about 0.7 ns, i.e. about two times larger than those reported in RBG systems based on time-delayed feedback [11,164]. Quite importantly, because no time-delay is involved in the suggested scheme, no correlation appears for time-shifts beyond 1 ns. Finally, to confirm the low dimension of the chaotic attractor and observe if any changes might have appeared compared to the previous section, we re-computed the correlation dimension of the dynamics using the GP algorithm combined with the singular-value re-embedding procedure, as described in sec. 2.4. We obtain a dimension of $D_2 \approx 2.3$ which appears to be slightly higher than the one computed previously, but the low-dimension of the dynamics is confirmed again.

To conclude, it is clear that polarization chaos is less optimal than the chaotic dynamics exploited in other optical chaos-based RBG schemes, with respect to the dynamical requirement described earlier. Yet, in the next section, we show that, despite non-optimal features, we achieve generation of random sequences with highly competitive performance.

3.3 SYSTEM PERFORMANCES AND INFLUENCE OF THE POST-PROCESSING

In the context of RBGs, the goal is to generate uncorrelated and unbiased bit sequences with uniform distribution, i.e. for each bit the probability of having 0 or 1 should be exactly 50 % and entirely independent of previous occurrences. To evaluate the performances of a system as a RBG, we typically use two standard batteries of tests: the NIST statistical test suite [180], and the DieHard test suite [181]. Based on statistical measurements, these tests check whether the hypothesis “the submitted bit sequences have been generated by a perfect RBG” can or cannot be rejected. In our case, we would then consider the tests as successful if the hypothesis cannot be rejected; indeed this would mean that our system can generate bit sequences that can be considered as statistically random. In practice, the results are typically presented via a set of $p_values \in [0, 1]$ which quantify the probability of having the statistical features of the generated bit sequences assuming that the perfect RBG hypothesis is true. The 15 tests of the NIST suite are performed with 1000 sequences of a million bits, and the results are presented via the proportion of sequences that successfully passed each test and the uniformity of the p_values - that we will refer to as the P-value. With a typical significance level of 0.01 (i.e. a sequence passes the test if the $p_value > 0.01$), the uniformity of the p_values , the P-value, must be larger than 0.0001 and the proportion in the range 0.99 ± 0.0094392 . The 18 tests of the DieHard suite are performed with a sequence of 80 millions of bits, and the tests are successful if the p_values are between 0.01 and 0.99.

Comparing the dynamical characteristics and the random sequence requirements detailed earlier, it is quite clear that the recorded time-series cannot be considered random as such. As described in the state of the art though, this is common and all previous experimental realizations of chaos-based RBGs needed to set a suitable post-processing method to extract the randomness of the time-series. In particular, this additional stage must be implemented to remove the bias in the sequence of zeros and ones, and secondly to possibly increase the achievable bitrate. As already reported [11], using a single threshold to generate random bits is a challenging task as it needs to be precisely set and readjusted to avoid long-term bias. To reduce experimental constraints, the use of multibit generation scheme combined with bit truncation methods has been demonstrated to be efficient [157,160,172]. However, using such method with the recorded polarization chaos time-series always results in a strongly biased sequence even considering only the least significant bit: typically we obtained 50.1% of 1 versus 49.9% of 0 for sequences of 2 million bits - i.e. a $p_value \sim 4.10^{-12}$ largely below the typical significance level of 0.01. To compensate for such imperfections, we compare the original 8-bit waveform with a time-shifted version of itself as in [160] but with an extra time-shift, as described in Fig. 3.3.

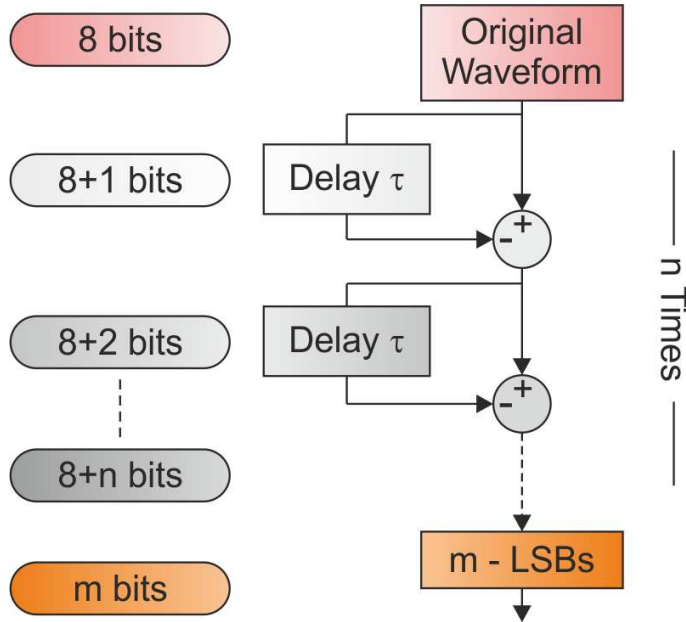


Figure 3.3 – **General scheme of the post-processing method.** We compare n times the original waveform with a time-shifted - by a delay τ - version of itself. This processing artificially increases the number of bit necessary to describe the temporal evolution of the time-series. Finally, we extract the m least significant bits for each data point of the processed sequence.

Here we set the time-shift at 250 ps which corresponds to the time for the decay of the autocorrelation. This extra time-shift is therefore large enough to avoid correlated dynamics but is also small enough to keep the details of the chaotic dynamics. Especially, this processing allows to keep the details of the mode hopping dynamics that occurs, on average, at a 0.6 ns time-scale. In particular, this is confirmed by the appearance of a three-peak histogram of the waveform after comparison, as displayed in Fig.3.2(b). Statistically, the processing also improves the symmetry of the distribution and therefore helps producing unbiased sequence of random bits. From a more general viewpoint, we consider the post-processing method described in Fig. 3.3. At first, we will use a single comparison ($n=1$), but we also consider having a larger number of comparison stages similarly to the high-order derivative technique described in [160, 162]. Especially, each comparison will virtually add one bit to each data point, somehow “expanding” the randomness on a larger number of bits. In the end, it allow us to keep more bits at the end of the process and therefore obtain a larger bitrate. However, as already mention earlier, this technique should also be considered carefully as the final bitrate might exceed the information theoretic limit [164, 175].

Using the experimental scheme described in Fig. 3.1 and the post-processing described in Fig. 3.3, we successfully generate bit sequences that pass all the statistical tests by retaining 5 LSBs ($m = 5$) for a waveform recorded at 20 GS/s and with a single comparison ($n = 1$) and a time-shift of $\tau = 250$ ps - see case 1 in table 3.1 and 3.2 placed at the end of this section in pages 108 and 109 respectively. Hence we confirm that despite its low-dimension and, at first glance, not ideal characteristics for random bit generation, polarization chaos can be efficiently exploited to produce random bit sequences at highly competitive bitrates - 5 bits \times 20 GS/s = 100 Gbps - without unconventional and/or complex post-processing methods.

Additionally, we have also checked that a much higher bitrate can be achieved by increasing the number of comparisons between the time-shifted waveforms, hence allowing us to keep more bits for each data point [160, 162, 165]. As precised in [164, 165], although this method shows very appealing performances, the output sequence exceeds the fundamental information-theoretic limit which therefore makes the sequence pseudo-random as discussed in e.g. [164]. Nevertheless, using numerous comparisons we successfully retained up to 28 bits ($m = 28$) for 23 comparisons ($n = 23$) with the same time-shift of $\tau = 250$ ps generating bit sequences that pass all the statistical tests, see case 2 in table 3.1 and 3.2.

Finally, to have more insight about the time-shift impact on the post-processing and on the randomness of the final sequence, we try the same approach for different time-shifts and observe the results of the NIST statistical test suite. In Fig. 3.4, we sum up the evolution of the output sequence randomness versus the time-shift used in the post-processing. Because we apply this comparison numerically - i.e. after the sampling of the time-series - we can only change the time-shift by a 50 ps time-step which corresponds to the 20 GS/s sampling rate used for the acquisition.

When keeping 5 LSBs ($m = 5$) after a single comparison ($n = 1$), we obtain the evolution described in Fig. 3.4(a). We observe that the threshold for the output sequence to be considered as random is only achieved for one value of the time-shift: $\tau = 250$ ps. Moreover we observe a strong variance of the results and, in most cases, the worst P-value (uniformity of P_values) shows very low values that fall below the scope of the graph. Nevertheless, increasing the number of comparisons - e.g. to $n = 2$ as in Fig. 3.4(b) - strongly improves the overall results. Hence we observe that 6 configurations produce sequences that can statistically be considered as random. Also, unlike (a), for all configurations the results remain in the vicinity of the threshold: indeed no proportion or P-value falls outside of the graph scale. In addition, we observe that two of them only fail the "Random Excursion" or "Random Excursion Variant" tests. This is quite important as they are the only two tests that cannot be systematically applied to all the sequences submitted. Indeed for statistical relevance, they need the tested sequences to exhibit a

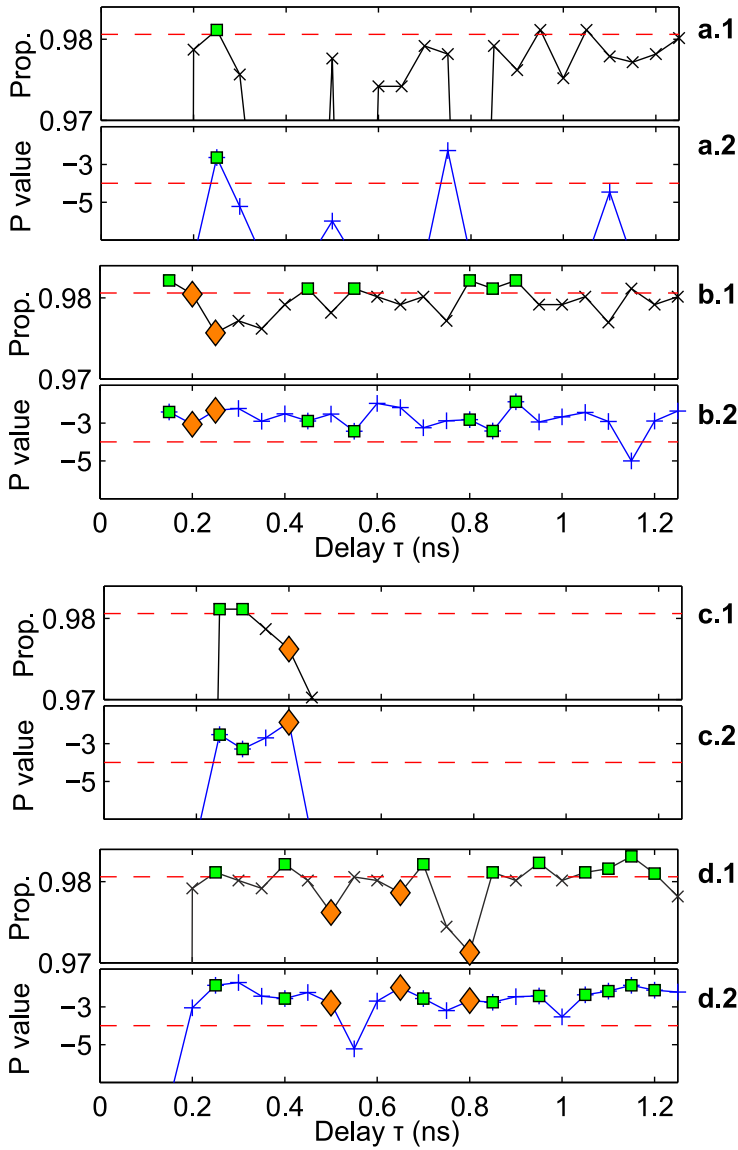


Figure 3.4 – Evolution of the output sequence randomness for a processing time-shift variation.

To evaluate the randomness, we indicate the worst proportion (1, top) and P-value - uniformity of the p_values - (2, bottom) across all the NIST test results. Horizontal dashed red lines indicate the threshold above which the output sequence can be considered as random. Green squares indicate time-shift values where both proportion and P-value are above this threshold. Orange diamonds indicate cases where only the "Random Excursion" or "Random excursion Variant" tests failed, see details in the text. The processing parameters - number of comparisons n and number of bits retained m - are: (a) $n = 1$, $m = 5$, (b) $n = 2$, $m = 5$, (c) $n = 23$, $m = 28$, (d) $n = 23$, $m = 27$.

large number (> 500) of “random walk” cycles, see [180] for details. If this requirement is not fulfilled the sequence is discarded from the test. As a result, the number of tested sequences varies and the proportion threshold - defined by $p \pm 3 \frac{p(1-p)}{m}$ with p the probability goal set at $p = 0.99$ and m the number of sequences - should vary as well. As a result, the orange diamond could therefore be considered as configurations generating a “potentially” random output.

In Fig. 3.4(c), we consider the fastest generator without consideration of the information theoretic limit: we perform $n = 23$ comparisons and keep $m = 28$ LSBs. Thus we observe that two configurations pass the statistical tests for $\tau = 250$ and $\tau = 300$ ps, and one more is considered a “potential” solution. However for $\tau > 450$ ps the results dramatically falls down and are clearly far from being random. When decreasing the number of considered bits however, we observe a large improvement, see Fig. 3.4(d). We report 9 good configurations along with 3 “potential” solutions. Also all the results remain again in the vicinity of the threshold indicating the statistical limit for the sequences to be considered as random.

To conclude, we successfully generate random sequences based on polarization-chaos, and achieve competitive bitrates (> 100 Gbps) without complex and/or unusual post-processing techniques. In addition, we see that to achieve the best performances for generation of random sequences the time-shift of the post-processing need to be set carefully. Although we did not investigate the underlying mechanism inducing those variations in the randomness of the output sequences, we clearly highlight that the valid range of time-shifts can be widely increased by selecting less LSBs or by increasing the number of comparisons.

Statistical Tests	Case 1		Case 2	
	P-Value	Prop.	P-value	Prop.
Frequency	0.0127	0.9861	0.0170	0.9881
Block-Frequency	0.5687	0.9851	0.0160	0.9921
Cumulative Sum	0.0023	0.9831	0.0954	0.9881
Runs	0.7116	0.9821	0.7637	0.9891
Longest Run	0.4172	0.9871	0.2034	0.9891
Rank	0.9819	0.9881	0.0127	0.9921
FFT	0.8360	0.9901	0.2284	0.9812
Non Overlap. Templates	0.0061	0.9812	0.0029	0.9812
Overlapping Templates	0.1007	0.9901	0.8920	0.9901
Universal	0.2480	0.9851	0.0661	0.9911
Approximate Entropy	0.0037	0.9861	0.6475	0.9921
Random Excursions	0.0354	0.9832	0.2858	0.9873
Random Excursions Var.	0.2162	0.9866	0.0038	0.9825
Serial	0.0767	0.9861	0.3161	0.9931
Linear Complexity	0.6579	0.9901	0.3283	0.9891

Table 3.1 – **Results of the NIST Statistical Tests.** The tests are performed with 1000 sequences of 1 million bits each. We use a significance level of $\alpha = 0.01$, hence the tests are successful if the P-values (here, uniformity of the p_values) is larger than 0.0001 and the proportion is in the range 0.99 ± 0.0094392 . For tests generating multiple outputs we give the worst case. In case 1, we use a single comparison and keep the 5 LSBs of the waveform. In case 2, we perform 23 comparisons and keep 23 LSBs of the waveform. In both cases the time-shift is 250 ps.

Statistical Tests	Case 1		Case 2	
	P-Value	Success	P-value	Success
Birthday Spacing [KS]	0.956792	success	0.389664	success
Overlapping 5-permutation	0.186900	success	0.128625	success
Binary Rank for 31x31 matrices	0.872671	success	0.912627	success
Binary Rank for 32x32 matrices	0.327389	success	0.382529	success
Binary Rank for 6x8 matrices [KS]	0.618094	success	0.538768	success
Bistream	0.08572	success	0.11933	success
OPSO	0.0112	success	0.0468	success
OQSO	0.0462	success	0.0254	success
DNA	0.0831	success	0.0854	success
Count the 1s on a stream of bytes	0.360770	success	0.722437	success
Count the 1s for specific bytes	0.040344	success	0.022000	success
Parking lot [KS]	0.850322	success	0.784046	success
Minimum Distance [KS]	0.266732	success	0.179058	success
3D spheres [KS]	0.175171	success	0.690888	success
Squeeze	0.825330	success	0.332211	success
Overlapping Sums [KS]	0.161946	success	0.036895	success
Runs [KS]	0.172702	success	0.134305	success
Craps	0.303552	success	0.429254	success

Table 3.2 – **Results of the Diehard Statistical Tests.** The tests are performed with a sequence of 80 millions bits. For tests with multiple p_values, the worst case is selected. The tests are considered successful if the p_values are between 0.01 and 0.99. [KS] indicates that the single p_value is obtained through a Kolmogorov-Smirnov test. Description of case 1 and 2 is similar to the one given for Table 3.1.

3.4 ENTROPY EVOLUTION AND ITS LINK WITH POLARIZATION CHAOS

Against all odds and despite unfitted characteristics - including a low-dimension and a limited bandwidth - we successfully obtain a highly competitive RBG. To explain these unexpected results, we theoretically investigate the entropy growth rate of the system as suggested in [176]. Indeed the randomness in chaos-based RBGs originates from the amplification of intrinsic microscopic noises of the system by the chaotic dynamics. The averaged entropy growth rate therefore provides a good theoretical estimate of these amplification properties, hence of the time after which the system is expected to become unpredictable. As a result, such investigation can provide an estimate of the highest sampling rate for which two adjacent acquisitions can be supposed to be totally uncorrelated. Unless in very specific cases [174], such analysis is however not possible experimentally as we cannot bring the system back to the exact same initial condition.

To perform this analysis, the first step is to generate simulated time-series of the chaotic laser dynamics. Then, we set a threshold that will transform the time-series into a 1-bit sequence, i.e. 1 or 0 depending if the output value is above or below the threshold. This limit has to be set very carefully as the long-time average ratio of 0 and 1 must be as close as possible to 50% - considering long time-series we need to have the same number of 1s and 0s to provide a reliable picture of the entropy growth. Starting from the same initial condition at $t = 0$, we simulate 1000 time-series with different noise sequences. Hence we can compute the probability $P_{0,1}(t)$ of 0s and 1s at time t over all the 1000 different noise sequences considered, and therefore evaluate the time-dependent entropy $H(t)$ defined by the following equation:

$$H(t) = - \sum_{i=0}^1 P_i(t) \cdot \log_2 (P_i(t)) \quad (3.1)$$

Especially, the time-dependent entropy is $H(t) = 0$ if at time t all time-series exhibit the same value 0 or 1, and $H(t) = 1$ if we have exactly $P_0(t) = P_1(t) = 0.5$, i.e. the system exhibits value 1 or 0 exactly for 50% of the simulations. The main hypothesis is to consider that an entropy of 1 is equivalent to a complete unpredictability of the system. Considering the noise amplification properties of the system, different noise sequences will lead, after a sufficient time, to uncorrelated output. We therefore know that on average $H(t)$ will increase and will reach a steady value of 1 at some point. However, as precised in [176], its evolution also strongly depends on the initial condition: indeed it can be easily understood that different initial positions on the chaotic attractor will obviously lead to different outcomes. To overcome this hurdle, we average the time-dependent entropy over 1000 different initial conditions $\langle H(t) \rangle$, i.e. we generate 1000

simulated time-series with different noise sequences for 1000 different initial conditions. Finally, we define the *memory time* of the system T_m as the time when the averaged time-dependent entropy exceeds 0.995: $\langle H(t) \rangle > 0.995$. This value has been chosen because it corresponds to the pass criteria of the frequency test or 0/1 ratio test of the NIST statistical test suite [176]. Empirically, this memory time has been shown to depend linearly on the noise strength in dB:

$$T_m = T_0 + L(10 \cdot \log_{10}(S_n)) \quad (3.2)$$

with T_0 the reference time, equal to the virtual memory time for a noise strength of 0 dB, S_n the noise strength and L the slope of the curve, which depends on the system and is closely related to the chaos characteristics. Intuitively, the memory time will decrease for an increase of the noise strength, hence L will be negative. However the evolution of this curve does not depend on the definition of the memory time: using a threshold of 0.9 will lead to the same linear dependence. So a rate independent of the noise level, called the entropy rate, can be defined:

$$R_e = -\frac{\Delta \log_e(S_n)}{\Delta T_m} = \frac{1}{10 \log_{10}(e)} \cdot \frac{1}{|L|} \quad (3.3)$$

The entropy rate appears to be very close to the maximum Lyapunov exponent of the dynamics [176]. In practice, the memory time will give the expected largest sampling rate that could be used for random bit generation, but the entropy rate - independent from the noise strength - provides a valuable insight on the dynamics characteristics and also a good figure of merit to compare different schemes.

Here, we simulate the time-series based on the SFM model described by eqs. (2.4)–(2.8) in section 2.1. We use a simulation time-step of 1 ps but downsample the obtained time-series by a factor 10 to avoid having an excessive amount of data. As in [176], we define the noise strength as the ratio of the peak power of the center frequency to the noise floor level in the FFT of the time-series. Thus we obtain noise strengths of -30, -40, -50 and -60 dB for spontaneous emission rates β_{sp} of 10^{-4} , 10^{-6} , 10^{-8} and 10^{-10} ns^{-1} respectively. In section 2.3, we demonstrate that the chaotic polarization fluctuations are qualitatively well reproduced using the spin-flip rate equation model. Here we use the same set of parameters as in section 2.3, but we take an injection current of $\mu = 2.963$ and a birefringence of $\gamma_p = 25 \text{ ns}^{-1}$ for which polarization chaos is observed with fast oscillations at a frequency of around 8 GHz and with an average dwell-time of 0.6 ns. The equipment limited bandwidth is modeled by a low-pass first-order filter with cut-off frequency at 2.4 GHz.

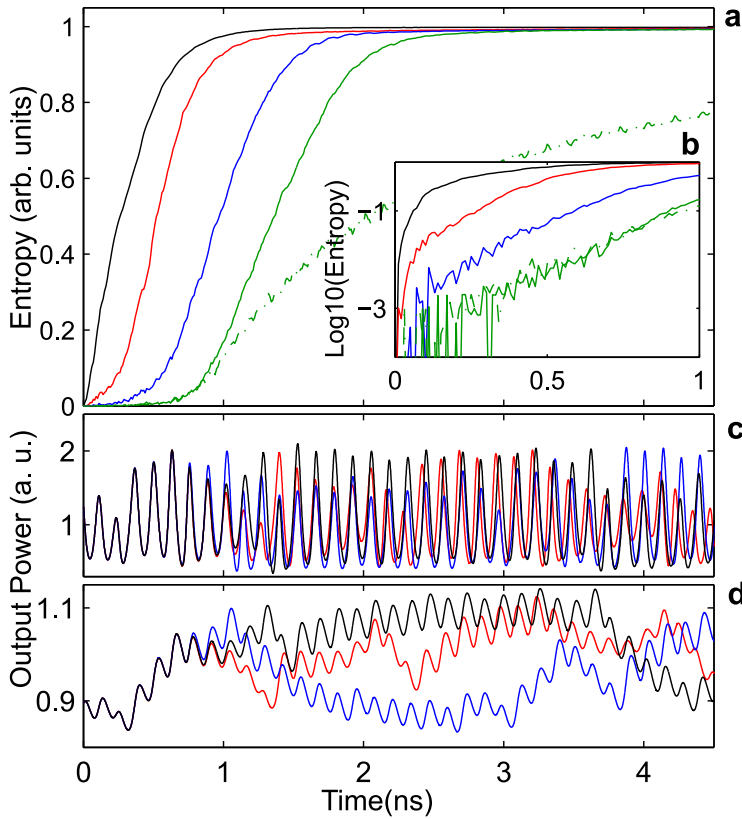


Figure 3.5 – **Entropy evolution for polarization chaos with different noise levels.** (a) Black, red, blue and green lines give the entropy evolution for noise levels of -30, -40, -50 and -60 dB respectively. Dash-dotted and solid lines give the evolution for unfiltered and filtered cases respectively. (b) is the same plot as (a) but in logarithmic scale for the entropy. (c) and (d) give an example of the separation between 3 different chaotic time-series for a noise level of -60 dB with unfiltered and filtered output power respectively.

In Fig. 3.5, we give the time-evolution of the dynamical entropy for different noise strengths and show the impact of the low-pass filtering. The measured entropy evolution for filtered data is shown as a solid line while the unfiltered case is given as a dash-dotted line. We clearly observe a significant effect of the filtering on the measured entropy that is also confirmed in Figs. 3.5(b,c) where we plot the trajectories of the output power for three different noise sequences, for the unfiltered and filtered cases respectively. Without the filter, we see strongly dominant correlated oscillations at relatively high frequency, which makes it quite hard to distinguish the different trajectories. On the other hand, when these oscillations are filtered out, we quickly discriminate the different evolutions. Thus we can conclude that the most random part of the dynamics is the slow mode-

hopping - the slow jumps between the two wings of the attractor -, and that filtering out the fast part - the fast oscillations around the unstable EP states - therefore leads to a first efficient and easy stage of randomness extraction.

As suggested in [176], we define the memory time as the time when the entropy reaches the value of 0.995, i.e. the time after which we can consider that all information about the initial state has been lost. In Fig. 3.5, we report for the filtered dynamics memory times up to eight times smaller than the one reported with time-delayed feedback in [176]: around 1.5 ns versus more than 13 ns respectively at a -30 dB noise level. However it should be noted that memory times below 1 ns have also been reported in time-delayed optical feedback systems with short external cavities and spontaneous emission rates of 10^{-3} ns^{-1} [173]. The short memory time for polarization chaos is also explained by the large value, around 7 ns^{-1} , of the largest Lyapunov exponent theoretically determined using Shimada's algorithm [182]. In particular the Lyapunov exponent corresponds to the slope of the entropy growth versus time when short time separations are considered: this is clear in Fig. 3.5(b). At last, we estimate the entropy rate, i.e. the memory time evolution with respect to the noise level: we find a value of 4.8 ns^{-1} to be compared with the 1.7 ns^{-1} reported in [176]. Considering these theoretical results, we could expect to obtain random sequences using a single threshold and a sampling time larger than 1.5 ns, i.e. a sampling rate up to 660 MS/s.

Finally, we implement the multibit post-processing described in the previous subsection to observe its impact on the entropy growth rate. We try to match the experimental conditions by setting the maximal and minimal threshold to reach the same amount of saturation for the filtered time-series as in experimental acquisitions, i.e. a ratio of saturated points between 10^{-4} and 10^{-1} %. Then, we encode the filtered simulated time-series on 8 bits to match the ADC of the oscilloscope used in the setup. Next, we perform a single comparison between the waveform and a time-shifted version of itself with a time-shift $\tau = 250 \text{ ps}$. Last, we extract only the least significant bit of the processed waveform and perform the previous 1-bit entropy analysis on this extracted bit. The results are displayed in Fig. 3.6, where we observe a further decrease of the memory time. Indeed, including this post-processing stage we reach memory-times largely below the nanosecond time-scale. For a noise level of -30dB we report a memory time even below 50 ps, which appear to be in good agreement with the sampling rate of 20 GS/s used for the experimental demonstration. Although, we do not consider all the 5 LSBs retained for the proof-of-concept demonstration, this result demonstrates that a significant increase of RBG performances can be expected from proper post-processing methods.

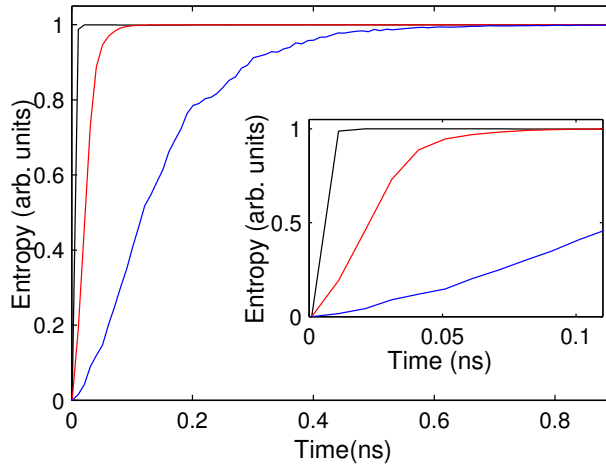


Figure 3.6 – **Entropy evolution for polarization chaos with the post-processing stage.** Black, red and blue curves give the evolution of the entropy for noise levels of -30, -40 and -50 dB respectively. The inset shows a zoom of the same plot to highlight that memory times below 100 ps can be achieved for noise levels of -40 dB, and below 50 ps for a -30 dB noise level.

We therefore demonstrate that the low-pass filtering due to the limited bandwidth of the acquisition electronics is an essential step for the generation of random sequences at high speed based on the low-dimensional polarization chaos described in the previous chapter. It is important to remark however that this property is only valid for the dynamics described and exploited here. Furthermore, we linked this effect to the double-scroll structure of the chaotic attractor of the polarization chaos dynamics. Our results therefore bring new light on the relationship between chaos and the generation of random sequences at high-speed.

3.5 SUMMARY AND PERSPECTIVES

To conclude, we demonstrate in this chapter that polarization chaos can efficiently be used for chaos-based random number generation at high speed.

We make a proof-of-concept demonstration of a highly simplified scheme for random bit generation. We take advantage of the chaotic fluctuations from a free-running laser diode, demonstrated in chapter 2, to get rid of any additional forcing or perturbation - such as time-delayed feedback or optical injection - that was needed, so far, to turn the laser diode into chaos. Despite dynamical characteristics - i.e. small radio-frequency bandwidth and low dimension of the chaotic attractor - that might appear, at first glance, detrimental for random bit generation at high-speed, we successfully report a bitrate of 100 Gbps without the need for unusual or complex post-processing techniques. When increasing the complexity of the processing, we also show that we can achieve bitrates up to 560 Gbps, generating sequences passing all the statistical tests. Finally, we convincingly link the reported performances to the properties of the chaotic attractor. Based on the analysis of the 1-bit entropy evolution, we show that filtering the time-series at a relatively low frequency is, in fact, an essential stage to achieve randomness at high-speed based on polarization chaos. This filtering, combined with a large Lyapunov exponent, therefore explains the good performances of the proposed scheme, although the post-processing method also appears to be a critical stage.

Considering these interesting results, this study also opens the way toward exciting perspectives and opportunities:

- First, the underlying mechanism allowing to achieve such performances based on polarization chaos still needs to be identified. We demonstrate that the time-series filtering is essential - as it discards the correlated fast oscillations on the wings of the attractor -, but its theoretical relationship with the dynamical process, such as the finite-time Lyapunov exponents, still remain to be clarified. This step would then allow us to optimize the RBG process by underlining the key parameters.
- Secondly, the simple suggested scheme shows extremely strong potential for on-chip, low-consumption and low-cost random bit generator. Indeed, the proposed setup benefits from the advantages of VCSELs and from the increased simplicity of the scheme. The possibilities to form VCSEL matrices also suggests that the solution described in this chapter is suited for massive on-chip parallelization, hence paving the way toward on-chip Tbps random bit generation.

- Third, although the low dimension and dynamical properties of polarization chaos casted some doubts about its applicability for chaos-based applications, we clearly dissipate those doubts in the work reported in this section. Hence, an obvious perspective is the utilization of polarization chaos in other applications such as chaos communication.

4

TWO-MODE DYNAMICS IN QD LASERS WITH OPTICAL FEEDBACK

No, our science is no illusion. But an illusion it would be to suppose that what science cannot give us we can get elsewhere.

— Sigmund Freud, *The Future of an Illusion*

In this chapter, we investigate theoretically and experimentally the impact of a time-delayed optical feedback on a QD laser emitting simultaneously from the ground and the excited states. We first provide a brief summary of the state-of-the-art on this topic in section 4.1. Then, in section 4.2, we describe the theoretical framework that we use to model the behavior of QD lasers with optical feedback. In section 4.3, we present the properties of the solitary laser diode and, in particular, the impact of carrier capture and escape rates on its emission. In section 4.4, we report that an optical feedback can induce GS-ES switching and show that the optical feedback favors the GS emission. In section 4.5, we describe the impact of the laser and feedback parameters on the switching dynamics. In particular, we focus on the impact of the external cavity length and of the electron escape rate on the dynamics of the QD laser. Finally, we present in section 4.6 the first experimental results obtained in collaboration with TU Darmstadt where we highlight incomplete GS-ES switchings for varying external cavity length which supports the theoretical results.

Part of the work presented in this chapter has been published in [183–185].

4.1 BACKGROUND: TWO-COLOR QD LASERS SUBJECT TO OPTICAL FEEDBACK

Although simultaneous GS-ES emission has been reported for more than 10 years, and, since then, numerous investigations of the dynamics of QD lasers have been performed, only few studies so far considered the impact of an optical feedback on such two-color QD lasers.

On one hand, optical feedback has been used to stabilize and enhance specific features of QD devices. As pictured in Fig. 4.1, a weak optical feedback has been shown to efficiently trigger the ground state emission in a two-section QD laser diode emitting from the excited state only in solitary configuration [110]. Interestingly, the same configuration was also used to stabilize two distinct modes of the excited state [111]. With the same goal of improving the dynamical properties of QD lasers, theoretical investigations demonstrated that, with the proper parameters, an optical feedback could also enhance the laser modulation bandwidth [122].

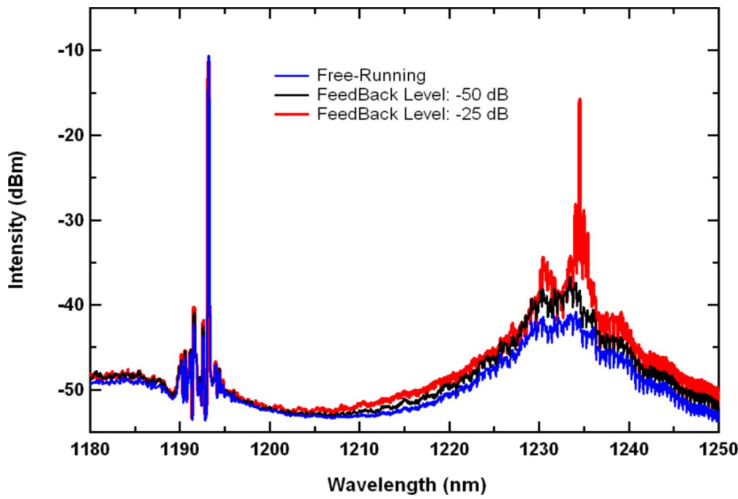


Figure 4.1 – **Triggering the ground state emission using optical feedback.** The spectrum of the free-running laser is in blue while spectra with feedback levels of -50 and -25 dB are in red and black respectively. Taken from [110].

On the other hand, as mentioned in section 1.4, QD lasers are also very interesting devices because of their complex carrier dynamics. Of course, simultaneous GS-ES emission is a consequence of this dynamics and a time-delayed optical feedback on such peculiar two-mode system - where the two modes are only coupled through the carrier dynamics between the ground and the excited levels - may bring additional dynamics from mode competition. Indeed, for a strong optical feedback, as pictured in Fig. 4.2, anti-phase low-frequency fluctuations between the ground and the excited state emissions

have been reported [121]. Despite such severe mode competition, the total output power remains almost constant hence showing that the two modes almost perfectly compensate for each other. This behavior clearly reminds observations made in multimode quantum well laser diodes [26, 186], where similar anti-phase dynamics has been reported. Finally, it should be noted that, even though the system dynamics is completely different, the optical feedback impact on GS-ES emission has also been considered in quantum dot mode-locked lasers [187].

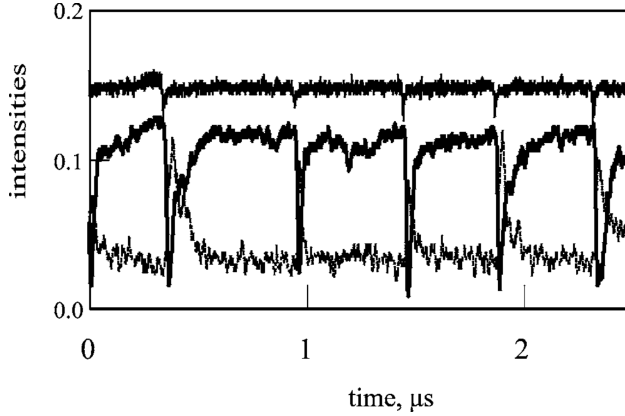


Figure 4.2 – **Antiphase low-frequency fluctuations recorded experimentally.** The bottom, middle and top curves correspond to the ES, GS and total intensity respectively. Despite the strong oscillations reported for the ground and the excited state emissions, the total output power remains almost constant. Taken from [121].

In spite of these earlier work, no in-depth investigation of the mode competition induced by optical feedback for QD laser emitting simultaneously from the ground and excited states has been conducted. In particular, the bifurcation scenarios and underlying physical mechanisms explaining the two mode dynamics remain to be clarified.

4.2 MATHEMATICAL MODELING OF THE QD LASERS

4.2.1 Rate equation with separated electron-hole dynamics

We model our QD laser diode as described by Viktorov *et al.* [115, 121]. The model considers the ground and the excited states with separated dynamics for electrons and holes without wetting layer - the carriers are directly injected to the excited state. The coupling of the different states is only considered through the carrier capture/escape rates; see a scheme of the model presented in Fig. 4.3. After normalization by the photon lifetime τ_p , the four equations for the carriers read as:

$$\dot{n}_e^e = \eta(J(1 - n_e^e) - Bn_e^e(1 - n_h^g) + C_en_h^g(1 - n_e^e) - n_e^e - (n_e^e + n_h^e - 1)|E_e|^2) \quad (4.1)$$

$$\dot{n}_h^e = \eta(J(1 - n_h^e) - Bn_h^e(1 - n_h^g) + C_hn_h^g(1 - n_h^e) - n_h^e - (n_e^e + n_h^e - 1)|E_e|^2) \quad (4.2)$$

$$\dot{n}_e^g = \eta(2Bn_e^e(1 - n_e^g) - 2C_en_e^g(1 - n_e^e) - n_e^g - (n_e^g + n_h^g - 1)|E_g|^2) \quad (4.3)$$

$$\dot{n}_h^g = \eta(2Bn_h^e(1 - n_h^g) - 2C_hn_h^g(1 - n_h^e) - n_h^g - (n_e^g + n_h^g - 1)|E_g|^2) \quad (4.4)$$

Here $n_{e,h}^{g,e}$ are the electron and hole populations and $E_{e,g}$ the slowly varying electrical fields for the excited and the ground states respectively. J is the injection current and $\eta = \tau_p/\tau_c$ is the nonradiative carrier decay rate $1/\tau_c$ normalized in time. We also consider that the capture rate from the ES to the GS is identical for both electrons and holes $B_e = B_h = B$. The asymmetry between the dynamics of electrons and holes therefore only comes from the escape rate $C_{e,h}$ from the GS to the ES [115].

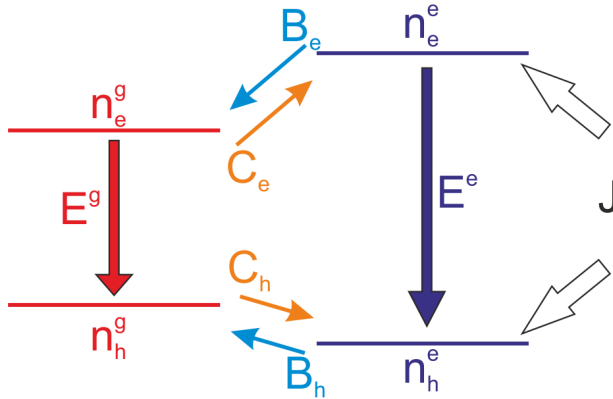


Figure 4.3 – **Scheme of the theoretical model of a QD laser.** The GS (ES) related parameters are in red (blue) respectively. Capture rates (from ES to GS) are in light blue while escape rate (from GS to ES) are in orange. In black is the injection current. The notations are the same than in the text.

Physically, as described in [115], the escape rate for the electrons is relatively small compared to the carrier capture rate ($C_e \ll B$), while the escape rate for the holes has a comparable value ($C_h \approx B$). Thus, for simplicity we can make the following approximations: $C_e = 0$ and $C_h = B$. With these approximations, some simplifications of the equations are then possible and lead to:

$$\dot{n}_e^e = \eta(J(1 - n_e^e) - Bn_e^e(1 - n_h^g) - n_e^e - (n_e^e + n_h^e - 1)|E_e|^2) \quad (4.5)$$

$$\dot{n}_h^e = \eta(J(1 - n_h^e) - B(n_h^e - n_h^g) - n_h^e - (n_e^e + n_h^e - 1)|E_e|^2) \quad (4.6)$$

$$\dot{n}_e^g = \eta(2Bn_e^e(1 - n_e^g) - n_e^g - (n_e^g + n_h^g - 1)|E_g|^2) \quad (4.7)$$

$$\dot{n}_h^g = \eta(2B(n_h^e - n_h^g) - n_h^g - (n_e^g + n_h^g - 1)|E_g|^2) \quad (4.8)$$

Unless stated otherwise, we will use the four equations above for the mathematical development presented in the next section. However, it should be noted that, with $C_e = 0$ and $C_h = B$, it is not possible to model a QD laser emitting only from the ES. Hence, at some point, we will consider small but non-zero electron escape rates, in particular in sections 4.3 and 4.5. Taking $C_e \neq 0$ does not discard the mathematical development presented here, but increases the complexity of the solutions obtained: it changes order-2 polynomial equations in order-3 equations which are less easy to manipulate.

For the electrical field, as detailed below, only the contribution of the resonant carriers is taken into account and the optical feedback is introduced as two additional delayed terms [121]. We obtain two equations which, after normalization by the photon lifetime τ_p , read as:

$$\dot{E}_{e,g} = \frac{1}{2}(g_{e,g}(n_e^{e,g} + n_h^{e,g} - 1) - 1)E_{e,g} - i\frac{a_{e,g}}{2}(n_e^{e,g} + n_h^{e,g})E_{e,g} + \kappa E_{e,g}(t - \tau) \quad (4.9)$$

Considering the ground and the excited states as respectively two-fold and four-fold degenerated, we have $g_e = 4g_0$ and $g_g = 2g_0$, with g_0 the effective gain factor per state scaled to the losses. The second term on the right-hand side of eq. 4.9 accounts for the carrier-induced change of frequency [121]. Similarly to [121], we only consider the contribution of the resonant carriers. This term reads as: $\delta\omega_{e,g} = a_{e,g}(n_e^{e,g} + n_h^{e,g})$. For simplicity, we also assume that $a = a_g = a_e$. The optical feedback is modeled by the term: $\kappa E_{e,g}(t - \tau)$ where κ is the normalized feedback rate, and τ is the time-delay. It should be noted that, at first, κ is taken as a real quantity, i.e. we do not consider any feedback phase. In section 4.5, we will however further discuss the impact of the feedback phase, when describing the impact of time-delay variations on the laser dynamics.

In this contribution, we use the following parameters: $J \in [1, 12]$, $\eta = 0.02$, $B = 150$, $\alpha = 5$, $g_0 = 0.75$, $\kappa \in [0, 0.1]$ and $\tau = 100$. Based on the approximated expression of the relaxation oscillation frequency developed in [116], the laser is in the long external cavity regime for $J > 3.8$, i.e. the time-delay is larger than the period of the relaxation oscillations. In practice, these parameters typically correspond to an external cavity of about 6 centimeters and a power reflectivity of the external mirror of less than 2%. The numerical integration scheme considers a fixed time step of 0.2 ps.

The coefficient α is related to the linewidth enhancement factor: $\alpha = \alpha/g_0 \approx 6.67$. Such high value for the α -factor has been reported experimentally in [99]. Furthermore, in [121], the authors demonstrate a good agreement between theory and experiment using $\alpha = 5$ (i.e. $\alpha \approx 6.67$). Nevertheless, as already mentioned in the general introduction, a recent theoretical study also suggests that a constant α -factor is not adequate to fully describe in details the complexity of quantum dot laser dynamics [102], however such approach, using a fixed value of the α -factor, allows us to describe the overall dynamics that can be expected in our system in a relative simple way, as well as to identify the underlying mode competition mechanisms and bifurcations.

Finally, in this chapter, we focus a lot on the balance between GS and ES emission. We therefore set up a figure of merit so that we can easily observe the respective evolution of the two-modes, thus we use the following measure:

$$R = \tanh \left(\left(\frac{P_{ES}}{P_{GS}} - \frac{P_{GS}}{P_{ES}} \right) \frac{1}{10} \right) \quad (4.10)$$

with $P_{GS,ES}$ the GS and ES emission output power respectively. As a result, R is a symmetric and bounded variable ranging from -1 when the laser only emits from the ground state to $+1$ when the laser only emits from the excited state. When the output power is identical for both modes, we obviously obtain $R = 0$. Moreover, we put an additional $1/10$ constant inside the hyperbolic tangent to expand the linear part of the function, so that we can discriminate power differences over a factor 10 between the two modes. For instance, for $P_{ES} = 5P_{GS}$ we obtain $R \approx 0.45$, and for $P_{ES} = 10P_{GS}$ we have $R \approx 0.76$. This measure will be of particular interest to create maps of the evolution of the QD laser emission, and will be mainly exploited in section 4.5.

4.2.2 Analytical description of the steady-states

Similarly to single-mode lasers subject to conventional optical feedback, the solutions of our set of equations have a phase indeterminacy that can be exploited [188]. We use two additional parameters $\Delta_{e,g}$ which describe frequency shifts of the electric fields for the ES and the GS respectively:

$$\begin{aligned} \dot{E}_{e,g} = & \frac{1}{2}(g_{e,g}(n_e^{e,g} + n_h^{e,g} - 1) - 1)E_{e,g} \\ & - i\frac{a}{2}(n_e^{e,g} + n_h^{e,g})E_{e,g} + i\Delta_{e,g}E_{e,g} + \kappa E_{e,g}(t - \tau). \end{aligned} \quad (4.11)$$

With these additional Δ parameters we can get rid of the phase indeterminacy by forcing $E_{e,g}$ to be real. Hence, for $E_{e,g} \neq 0$, we have two additional conditions for the system steady-states:

$$\Delta_{e,g} = -\kappa \left(\frac{a}{g_{e,g}} \cos(\Delta_{e,g}\tau) + \sin(\Delta_{e,g}\tau) \right) + \frac{a}{2} \left(\frac{1}{g_{e,g}} + 1 \right), \quad (4.12)$$

$$n_e^{e,g} + n_h^{e,g} = 1 + \frac{1}{g_{e,g}} - 2\frac{\kappa}{g_{e,g}} \cos(\Delta_{e,g}\tau). \quad (4.13)$$

Equation 4.12 is similar to the equation of the frequency shift for the external cavity modes in the well-known Lang-Kobayashi model [188]. Clearly eq. 4.12 is nonlinear and cannot be solved analytically, but since the equation is independent, we can express every other variables as a function of $\Delta_{e,g}$. We can then consider separately the four different cases listed below:

1. No lasing, $E_{e,g} = 0$:

This gives us independent electron and hole populations. For the hole population it comes that:

$$n_h^e = \frac{J}{(J + B + 1) - 2B^2/(2B + 1)}, \quad (4.14)$$

$$\text{and } n_h^g = \frac{2Bn_h^e}{2B + 1}. \quad (4.15)$$

Then, we need to solve the following second order polynomial equation for the GS electron population n_e^g :

$$B.n_e^{g2} + (-(J + B + 1) - 2BJ)n_e^g + 2BJ = 0, \quad (4.16)$$

$$\text{then } n_e^e = \frac{J}{(J + B + 1) - Bn_e^g}. \quad (4.17)$$

2. GS lasing only, $E_e = 0$, $E_g \neq 0$:

For this case, we have $E_e = 0$ and from eqs. 4.5-4.6 we obtain the following relationships:

$$n_e^e = \frac{J}{(J+B+1) - Bn_h^g}, \quad (4.18)$$

$$\text{and } n_h^e = \frac{J + Bn_h^g}{J+B+1}. \quad (4.19)$$

Also eq. 4.13 gives us:

$$n_h^g = 1 + \frac{1}{g_g} - 2\frac{\kappa}{g_g} \cos(\Delta_g \tau) - n_e^g. \quad (4.20)$$

These relations allow us to find a second-order equation for n_e^g by combining equations 4.7 and 4.8:

$$(Y-2)Bn_e^{g^2} + (2BJ - XB - (Y-2)(J+B+1))n_e^g + (X(J+B+1) - 2BJ) = 0, \quad (4.21)$$

$$\text{with } X = \frac{2BJ}{J+B+1} + (Y-1)\Sigma_g, \quad (4.22)$$

$$Y = \frac{2B^2}{J+B+1} - 2B. \quad (4.23)$$

3. ES lasing only, $E_e \neq 0$, $E_g = 0$:

The derivation here is similar to the previous case. The useful relations write as follows:

$$n_e^g = \frac{2Bn_e^e}{2Bn_e^e + 1}, \quad \text{and} \quad n_h^g = \frac{2Bn_h^e}{2B+1} \quad (4.24)$$

Finally, we obtain the following equation for n_e^e :

$$(2B^2 - 2BX)n_e^{e^2} + (2BY - X)n_e^e + Y = 0 \quad (4.25)$$

$$\text{with } X = 2(J+B+1) - \frac{2B^2}{2B+1} \quad (4.26)$$

$$Y = ((J+B+1) - \frac{2B^2}{2B+1})\Sigma_e \quad (4.27)$$

4. GS and ES simultaneous lasing, $E_{e,g} \neq 0$:

This case is a bit more complex as we cannot use exactly the same method. Eq. 4.13 can be used for both lasing modes: we can get rid of the hole population variables in all equations. Then by combining eqs. 4.5-4.7 and 4.6-4.8 respectively, we find two expressions for n_e^g :

$$n_e^g = \left((J+1)\Sigma_e + \frac{\Sigma_g}{2} \right) - 2(J+1)n_e^e, \quad (4.28)$$

$$n_e^g = \frac{((2B+1)\Sigma_g - 2B\Sigma_e) + 4Bn_e^e}{2Bn_e^e + 2B + 2}, \quad (4.29)$$

with $\Sigma_{g,e}$ the total carrier (electrons + holes) populations given by eq.4.13. Finally by combining these expressions we can find a second-order equation for n_e^e :

$$\begin{aligned} 2B(J+1)n_e^{e2} + (2B + (2B+2)(J+1))n_e^e - \left(B \left((J+1)\Sigma_e + \frac{\Sigma_g}{2} \right) \right) n_e^e \\ + \left(\frac{B\Sigma_g}{2} - (B + (B+1)(J+1))\Sigma_e \right) = 0. \end{aligned} \quad (4.30)$$

This analytical approach is exploited in the next sections to efficiently provide starting points for the application of continuation techniques on branches of stable and unstable steady-state solutions.

 4.2.3 *Stability analysis*

The stability of these steady-states is determined by an 8x8 evolution matrix from the linearized perturbation equation. In the case of a GS or an ES single-mode emission, previously described as cases 2 and 3, this matrix can be separated into two independent submatrices. Stability information from the extinct mode carrier population can then be extracted and calculated separately. This appears to be very useful as our continuation software DDE-BIFTOOL [130] uses a numerical approach to find the system eigenvalues and can therefore miss some, especially those being far from 0.

The stability analysis is performed by solving the following characteristic equation:

$$\det \left(M - \lambda I_2 + M_{\text{delay}} e^{-\lambda \tau} \right) = 0, \quad (4.31)$$

where λ corresponds to the unknown eigenvalues of the system, I_2 is the 2x2 identity matrix, M and M_{delay} are the contributions of the ordinary and delayed parts of the equation respectively. These two matrices are:

$$M = \begin{pmatrix} \frac{1}{2} (g(n_e + n_h - 1) - 1) & \Delta - \frac{g}{2} (n_e + n_h) \\ -(\Delta - \frac{g}{2} (n_e + n_h)) & \frac{1}{2} (g(n_e + n_h - 1) - 1) \end{pmatrix} \quad (4.32)$$

$$M_{\text{delay}} = \kappa \begin{pmatrix} \cos(\Delta \tau) & \sin(\Delta \tau) \\ -\sin(\Delta \tau) & \cos(\Delta \tau) \end{pmatrix} \quad (4.33)$$

For simplicity we do not write the subscripts further on. It should however be understood that for a lasing GS, we consider here the variables for the excited state: n_e^e , n_h^e , Δ_e , g_e , and so on. For a lasing ES, the situation is obviously reversed. Developing eq. 4.31 and separating the real and imaginary parts give the following system:

$$(A^2 + B^2) - 2Ax + (x^2 - y^2) + 2\kappa ((A - x)\cos(y\tau) - y\sin(y\tau)) e^{-x\tau} + \kappa^2 \cos(2y\tau) e^{-2x\tau} = 0 \quad (4.34)$$

$$2Ay + 2xy + 2\kappa ((A - x)\sin(y\tau) + y\cos(y\tau)) e^{-x\tau} + \kappa^2 \sin(2y\tau) e^{-2x\tau} = 0 \quad (4.35)$$

with $\lambda = x + iy$, $A = \frac{1}{2} (g(n_e + n_h - 1) - 1)$ and $B = -\Delta + \frac{g}{2} (n_e + n_h)$. The problem then reduces to solving this highly nonlinear set of equations. Although several methods are available, we choose the classic Newton-Raphson method which appears to be efficient enough in our case. As will be detailed in the next sections, the stability eqs. 4.34 and 4.35 give the system eigenvalues whose evolution can be linked to transcritical bifurcations connecting the GS or ES single-mode emission to the simultaneous GS-ES emission steady-states.

4.3 SOLITARY QD LASER BEHAVIOR

Based on the analytical description presented in the previous section, we plot in Fig. 4.4 the evolution of the branches of steady-state solutions for increasing injection currents in the case of the free-running laser diode, i.e. $\kappa = 0$. The stability information is directly provided by the stability analysis performed in the previous section for single-mode emission steady-states, and complemented by a numerical approach using the DDE-BIFTOOL package [130]. As can be seen in Fig. 4.4, with our set of parameters we find simultaneous emission in free-running configuration, i.e. when no optical feedback is applied.

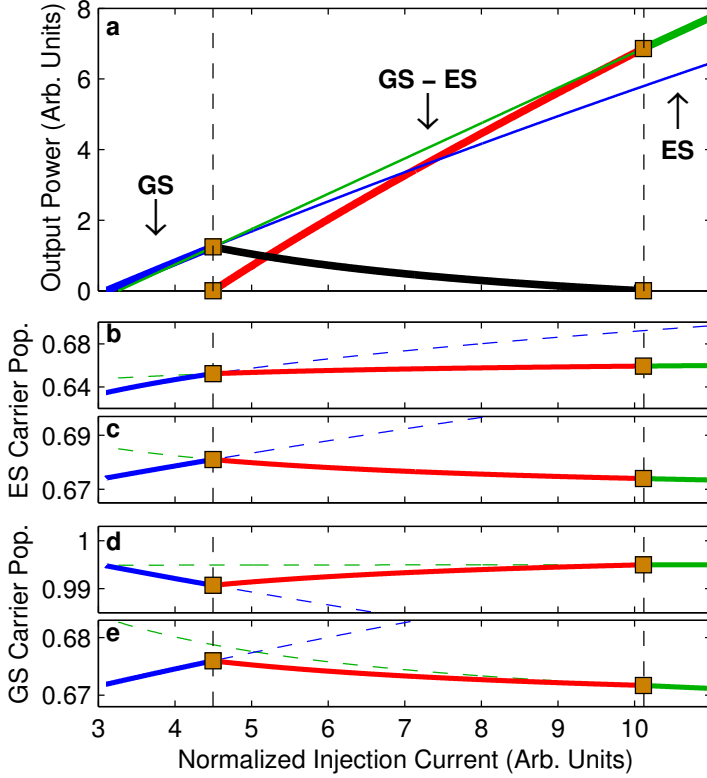


Figure 4.4 – **Analytical LI curve of the transition from GS to ES emission.** (a) Analytical L-I curve without feedback. The output power of each mode is plotted against the injection current for the three lasing steady-states of the system. The carrier population evolution is given in panels (b) to (e): electrons (b) and holes (c) for the ES, electrons (d) and holes (e) for the GS. In all panels, blue (Green) lines are for GS (ES) single-mode solutions whereas black (red) lines are for the GS (ES) emission in the case of GS-ES simultaneous emission solutions. Thick (thin) lines stand for stable (unstable) steady-states. Transcritical bifurcations are identified as orange squares.

Similarly to previous experimental and theoretical reports [106,115,189], the laser emits only from the GS at threshold and the simultaneous GS-ES emission steady-state only appears when the injection current is increased, here above $J > 4.5$, when the new steady-state is stabilized by a transcritical bifurcation. For larger currents, the GS output power decreases while the ES output power increases, and quickly the latter becomes the dominant emission process for currents above $J \approx 5$. For $J > 10.2$, the GS emission completely disappears as a transcritical bifurcation connects the GS-ES emission steady-state to the ES only steady-state. As expected from the previous analysis, we indeed observe three competing steady-states linked together by transcritical bifurcations. Moreover, we find that the eigenvalues corresponding to the transcritical bifurcations are obtained from the submatrix identified in section 4.2.3. Hence, in this theoretical framework, the destabilization of the GS (ES) single-mode emission directly comes from the ES (GS) carrier population, i.e. the carrier population of the extinct mode. Furthermore, it is worth noting that, for the lasing modes, the carrier populations are not clamped as can be seen in Fig. 4.4(b-e), but only the carrier population sum (electron + hole) has a fixed value, as indicated in eq. (4.13).

The GS-ES resolved LI-curve in Fig. 4.4 is very similar to the one reported in [190,191], although obtained with a different modeling. Yet, the analytical expressions of the steady-states and the identification of the primary bifurcations bring a new insight into the mode competition.

To go further, we consider the impact of the escape rates of electrons and holes on the emission of the solitary laser. In Fig. 4.5, we present the evolution of the system LI-curve for increasing electron escape rates: $0 < C_e < 4$. We observe that the region of GS emission, starting at threshold, quickly shrinks and vanishes for $C_e > 3$. The region of simultaneous emission follows the same evolution, and the ES emission quickly becomes stable directly at threshold for $C_e > 3$.

If we extend our analysis to the whole electron/hole escape rate map, i.e. we consider also the case $C_h < B$, we can identify three different behaviors of the laser when the injection current is increased, as pictured in Fig. 4.5(b): 1/ GS emission only (GS): the laser only emits from the ground state in the whole range of injection current considered, 2/ simultaneous GS-ES emission (SIM): the laser emits from the GS at threshold, but for larger injection currents, the ES emission appears, and 3/ ES emission only (ES): the laser only emits from the excited state in the whole range of current considered. These three cases are defined for a reasonable range of current, i.e. for $J \in [0, 13]$. As a result, if simultaneous emission appears for $J > 13$, it will therefore not be considered in the map displayed. Moreover, as explained earlier, the escape rate is lower for the electrons than for the holes. We therefore consider that the case $C_e < C_h$ is physically impossible, and do not investigate it. This is the gray area displayed in Fig. 4.5(b).

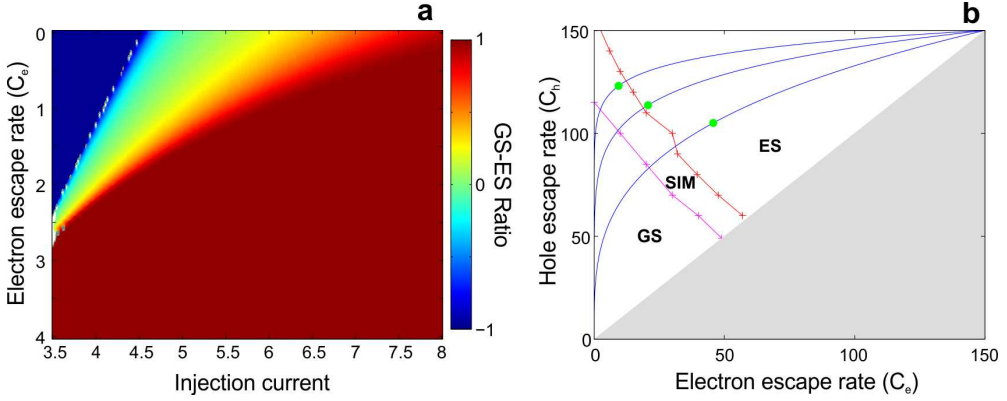


Figure 4.5 – **Impact of electron/hole escape rates on the solitary laser emission.** (a) Simulated evolution of the solitary laser LI-curve for increasing electron escape rates versus injection current. GS (ES) emission is in blue (red) and intermediate colors indicate the GS/ES emission ratio R . (b) Mapping of GS, simultaneous and ES emission in the hole versus electron escape rate plan. The pink line separates GS and simultaneous GS-ES emission areas, while the red line separates the latter and the region of ES emission. The gray area corresponds to $C_e > C_h$ and is considered as non-physical. The three blue lines give the trajectory of three different system for increasing temperatures, with room temperature identified as the green dot.

We complement this figure by showing the trajectories of three different systems in this plane for increasing temperatures; these are the three blue curves in Fig. 4.5(b). According to [115], the escape rates can be calculated as: $C_{e,h} = B_{e,h} \exp(-\Delta E_{e,h}/k_b T)$, with $\Delta E_{e,h}$ the energy gap between the ground and the excited states for the electrons and holes respectively, k_b the Boltzman constant and T the temperature. Here we use the three following pairs of energy gaps: $\Delta E_e = \{30, 50, 70\}$ meV and $\Delta E_h = \{9, 7, 5\}$ meV for the bottom, middle and top curves respectively. The green dot indicates the position of the system at room-temperature. Based on the results displayed in Fig. 4.5(b), it is clear that the system will always go through the simultaneous emission region. At low temperatures, the laser will only emit from the ground state while at high temperatures, only the excited state will be lasing. The temperature at which the simultaneous GS-ES emission occurs will then depend on the energy gap structure for electrons and holes. Finally, it should be noted that the current range for which the laser emits simultaneously from the GS and the ES - i.e. the range of current between the ES emission threshold and the quenching of the GS: $[4.5, 10.1]$ in Fig. 4.4 - strongly depends on the asymmetry between electron and hole escape rates. The stronger the asymmetry is the smaller the simultaneous emission current range will be. In the extreme case, for e.g. $C_e = C_h = 57$, we observed no GS quenching at all, similarly to the evolution obtained when no distinction is made between electron and hole dynamics as in Fig. 1 of [107].

4.4 GROUND-EXCITED STATE SWITCHING WITH OPTICAL FEEDBACK

Although GS-ES simultaneous emission can occur directly in the solitary laser diode, we expect a strong modification of the GS-ES competition when the laser is subject to optical feedback. In this section, we will limit our investigations to the following escape rate parameters: $C_e = 0$ and $C_h = B$.

Considering the behavior of the laser in a free-running configuration, we can easily identify three cases in terms of injection currents: 1/ low currents: the laser emits only from the ground state, e.g. $J = 4$, 2/ medium currents: the laser emits simultaneously from the ground and excited states, e.g. $J = 5$, and 3/ large currents: the laser only emits from the excited state, e.g. for $J = 11$.

4.4.1 Evolution at low injection currents

Using the analytical approach described previously along with continuation techniques and direct numerical integrations, we unveil the evolution of the system for increasing feedback rates at a fixed injection current of $J = 4$. The continuation results are given in Fig. 4.6 where we plot the output power against the feedback rate for the three competing steady-states, while bifurcation diagrams obtained from direct numerical integrations are given in Fig. 4.7.

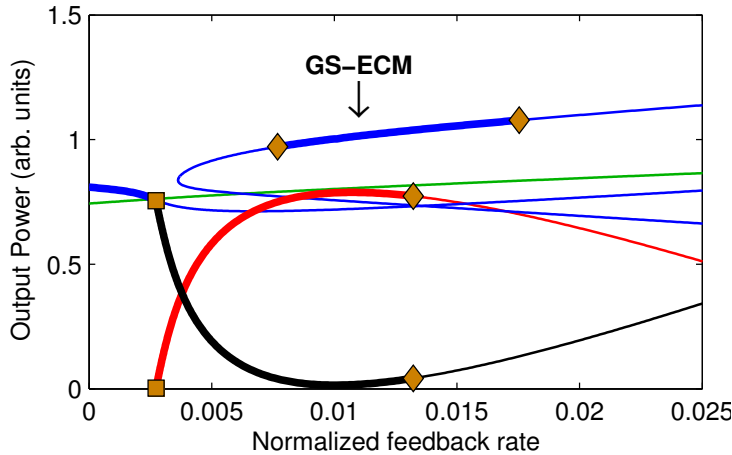


Figure 4.6 – **Bifurcation diagram for $J = 4$ obtained by continuation techniques: output power versus feedback rate.** Blue (green) lines represent GS (ES) single-mode solutions while black (red) lines represent the GS (ES) emission in the case of simultaneous GS-ES solutions. Thick (thin) lines indicate stable (unstable) steady-states. Transcritical (Hopf) bifurcations are identified as orange squares (diamond).

At first, we observe in Fig. 4.6 that the GS emission is quickly destabilized by a transcritical bifurcation, around $\kappa \sim 0.003$, which leads the system toward a simultaneous GS-ES emission steady-state. Then the ES emission quickly becomes the dominant mode as the feedback rate is increased. The branch of the simultaneous GS-ES emission steady-state is finally destabilized by a Hopf bifurcation at $\kappa \sim 0.012$. These results also show that the first external cavity mode of the GS emission (GS-ECM) appears around $\kappa \sim 0.004$ from a saddle-node bifurcation. It is stabilized by a Hopf bifurcation at higher feedback rates around $\kappa \sim 0.008$, hence unveiling a large region of bistability between the GS-ECM and the simultaneous GS-ES emission steady-state for $0.008 < \kappa < 0.012$. For stronger feedbacks, the GS-ECM gets destabilized by a Hopf bifurcation at $\kappa \sim 0.017$.

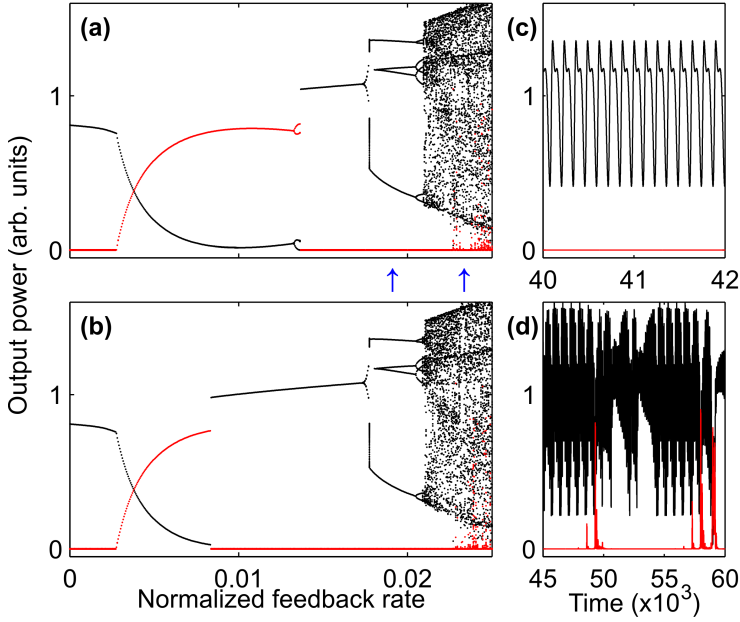


Figure 4.7 – **Bifurcation diagram for $J = 4$ obtained by direct numerical integrations.** (a-b) Bifurcation diagram: extrema of the output power versus increasing (a) and decreasing (b) feedback rates for an injection current of $J = 4$. Black (red) dots represent GS (ES) emissions. (c-d) Output power time-traces for normalized feedback rates of $\kappa = 0.019$ (c) and $\kappa = 0.023$ (d). The two blue arrows indicate the position of these two time-traces in the bifurcation diagram.

In Fig. 4.7, we plot the extrema of the GS (black) and ES (red) output power simulated time-series for increasing (a) and decreasing (b) feedback rates. These results complement the continuation analysis displayed on Fig. 4.6 by showing the secondary bifurcations leading to self-pulsing dynamics and further to chaos. Thus, we can see that around $\kappa \approx 0.013$, the simultaneous GS-ES emission steady-state is destabilized by a supercritical Hopf bifurcation creating a stable limit cycle, but the emerging periodic solution is quickly destabilized and the system ends up on the first GS-ECM. Hence we observe an hysteresis phenomenon where the laser switches between GS emission (first GS-ECM) and simultaneous GS-ES emission with a strongly dominant ES emission. For larger injection currents, as already indicated in Fig. 4.6, the GS-ECM is destabilized at $\kappa \approx 0.018$ by a subcritical Hopf bifurcation and the laser experiences a bifurcation scenario leading to complex chaotic behaviors. At first, the self-pulsating dynamics are found only in the GS and not in the ES, see Fig. 4.7(c); the period of these oscillations is about 110 which is close to the time-delay $\tau = 100$, hence suggesting that the two time-scales might be related. Next a bifurcation cascade occurs and this solution is destabilized toward a more complex dynamical regime with emission from both GS and ES. As shown in Fig. 4.7(d), the laser exhibits a strongly dominant GS chaotic emission with irregular sudden bursts of ES emission, which are anticorrelated with GS output power oscillations.

To sum up, at low injection currents, we observe an interesting bistability between a simultaneous GS-ES emission (with a strongly dominant ES emission) and a stable GS emission steady-state (the first GS-ECM). Varying the feedback rate, we can easily switch from one state to the other and we therefore demonstrate that the optical feedback can efficiently be used to control the laser output. Finally, for a stronger feedback, the system experiences a bifurcation scenario toward more complex dynamical behaviors, but always with a strongly dominant GS-emission.

4.4.2 *Evolution at medium injection currents*

We now discuss the case of moderate injection current levels, for which the solitary QD laser emits simultaneously from the ground and the excited states.

In Fig. 4.8, we plot the analytical and continuation results obtained for an injection current of $J = 5$. Although without optical feedback the laser emits simultaneously from the GS and ES with a dominant GS emission, an increase of the feedback strength quickly leads to an increase of the ES emission output power. As opposed to the previous case however, the simultaneous GS-ES emission branch reaches the ES-only steady-state

through a transcritical bifurcation around $\kappa \approx 0.004$. Thus the ES emission branch is stabilized and remains stable up to $\kappa \approx 0.01$ where a Hopf bifurcation occurs. In the meantime, we observe that the first GS-ECM branch is also stable for a relatively large range of feedback rates $0.005 < \kappa < 0.022$. Thus we unveil a large region of bistability, but, unlike the previous case, between GS and ES single-mode solutions, i.e. with no simultaneous emission involved. For decreasing feedback rates, we see that the GS-ECM stability is limited by a transcritical bifurcation around $\kappa \approx 0.005$ that unveils a new simultaneous GS-ES steady-state. This new solution is however quickly destabilized by a saddle-node bifurcation around $\kappa \approx 0.004$. In addition, we can observe that multiple ECMs appear at larger feedback rates for both GS and ES emissions, however none of them appear to be stable. Finally, it is worth noting that the eigenvalues corresponding to the transcritical bifurcations are again obtained from the sub-matrices detailed in section 4.2.3, i.e. the eigenvalues relate to the extinct mode.

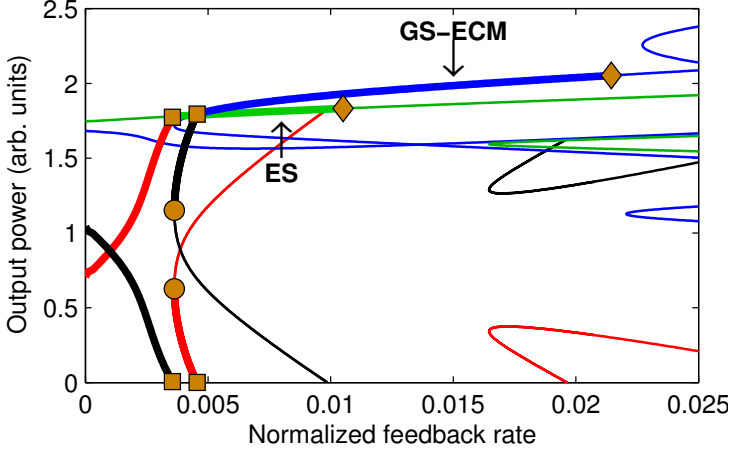


Figure 4.8 – **Bifurcation diagram for $J = 5$ obtained by continuation techniques: output power versus feedback rate.** Blue (Green) lines represent GS (ES) single-mode solutions while black (red) lines represent GS (ES) emission in the case of simultaneous GS-ES solutions. Thick (thin) lines indicate stable (unstable) steady-states. Transcritical, Hopf and saddle-node bifurcations are identified as orange squares, diamonds and circles respectively.

Results of direct numerical integrations are displayed in Fig. 4.9(a,b) for increasing and decreasing feedback rates respectively. Again the simulated results match the continuation results and complement them by showing secondary bifurcations and the evolution toward complex dynamics. We observe that the Hopf bifurcation destabilizing the ES-only steady-state is subcritical, hence making the transition toward the GS-ECM more sudden. Again we observe an hysteresis cycle but, in contrast to the previous case and

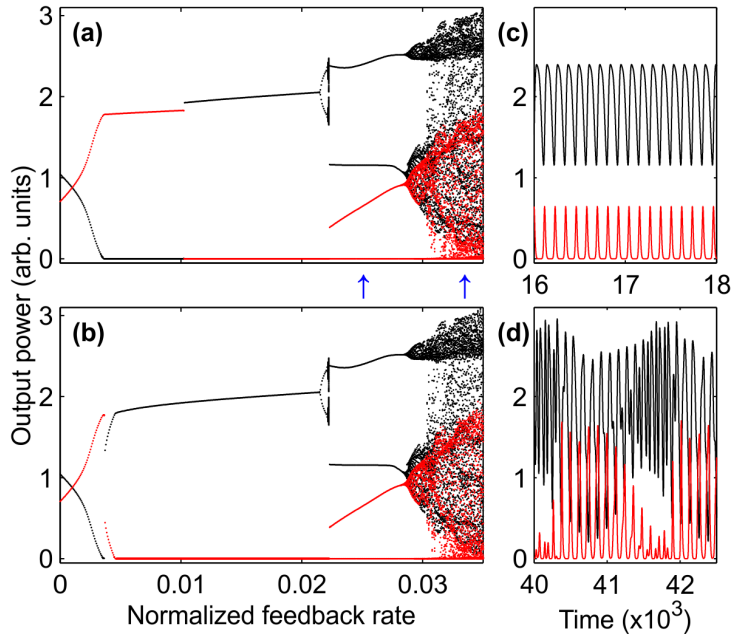


Figure 4.9 – **Bifurcation diagram for $J = 5$ obtained by direct numerical integration.** (a-b) Bifurcation diagram: extrema of the output power versus increasing (a) and decreasing (b) feedback rates for an injection current of $J = 5$. Black (red) dots represent the GS (ES) emission. (c-d) Output power time-traces for normalized feedback rates of $\kappa = 0.025$ (c) and $\kappa = 0.033$ (d). The two blue arrows indicate the position of these two time-traces in the bifurcation diagram.

as expected from continuation results, with a bistability between stable GS and ES emission steady-states with a complete extinction of the other mode. For decreasing currents, we highlight a transition through a new GS-ES simultaneous emission steady-state already uncovered by continuation techniques.

For stronger feedback levels, we observe that the Hopf bifurcation destabilizing the first GS-ECM is now supercritical. Yet the created limit cycle gets quickly destabilized and the system settles on a two-mode self-pulsing dynamics, see Fig. 4.9(c). The GS and ES output power oscillations are anti-correlated and exhibit a periodicity of about 120 which is again close to the time-delay. In Fig. 4.9(d), we see that increasing the current further leads the system toward anti-phase chaotic dynamics but still with a dominant GS emission as in the previous case. We still observe oscillations with a period of 120, but we can also identify a larger time-scale at a period of about 1580. The dynamics could therefore be interpreted as a quasi-periodic dynamics, that bifurcates to chaotic anti-phase low-frequency fluctuations similar to the report of [121].

In the end, the bifurcation scenario obtained at $J = 5$ appears to be very similar to the one described for $J = 4$. However, we observe an interesting evolution with a simultaneous GS-ES emission that connects to and stabilizes the ES-emission steady-state. In practice, it means that the bistability uncovered is now between two single-mode steady-states: we can switch between GS and ES emission with a complete extinction of the other mode and with similar output powers for both modes.

4.4.3 Evolution at large injection currents

Finally, for large currents where the laser only emits from the ES without optical feedback, the bifurcation scenario for increasing feedback rates is much more complex. Nevertheless, using direct numerical integrations, we can still get some valuable insight on the evolution of the dynamics.

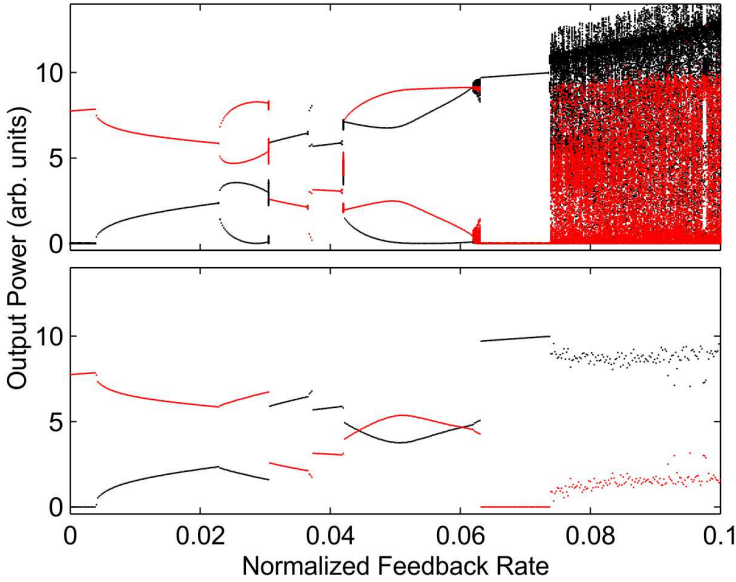


Figure 4.10 – **Bifurcation diagram for $J = 11$ obtained by direct numerical integrations.** We plot the extrema of the output power (top) and averaged output power (bottom) for increasing feedback rates. Black and red dots represent GS and ES emission respectively.

In Fig. 4.10, we give both the bifurcation diagrams for GS and ES emission for increasing feedback rates and the evolution of their respective averaged output power. For small feedback rates, we can identify a first transcritical bifurcation leading to simultaneous GS-ES emission, but for $\kappa > 0.02$, as already stated, the laser starts experiencing a much more complex bifurcation scenario involving several switchings and dynamical solutions. Nevertheless, if we consider the time-averaged output power evolution, we distinguish a clear trend: increasing the injection current leads, on average, to a switching from ES to GS emission. Although the evolution is not regular, we can still observe an increase of GS emission for increasing feedback rates. The system even reaches a GS only steady-state around $\kappa \sim 0.07$, and it remains the dominant mode for stronger feedbacks. This trend is also supported by the previous observations at lower injection currents: at high feedback rates, the laser always exhibited a dynamical state with a strongly dominant GS emission. Such result is also supported by recent experiments in which optical feedback is used to trigger the GS emission in a two section QD laser [110].

To conclude, we showed that optical feedback can induce a bistability between GS and ES emission and that a fine tuning of the feedback strength allows to control the output mode with potentially a complete extinction of the other mode. In addition, we report that an optical feedback, overall, favors the ground state emission in a two-color QD laser: no matter what is the solitary behavior of the laser, a strong enough feedback will trigger the ground state emission and will eventually make it the dominant mode.

4.5 INFLUENCE OF THE LASER AND FEEDBACK PARAMETERS

In the last section, we demonstrated that both the injection current in the free-running operation and the optical feedback influence the mode competition in QD laser diodes. It is therefore interesting to analyze in more details the impact of the system parameters, especially we focus on the effects of the external cavity length - i.e. the time-delay - and the electron escape rate both of which can severely alter the solitary laser behavior.

4.5.1 *Impact of external cavity length variations*

Using the same set of parameters as in the previous section - in particular, we take $C_e = 0$, we investigate the impact of the time-delay on the GS-ES switching dynamics of the QD laser diode. In Fig. 4.11, we present a map of the steady-states in the normalized time-delay τ versus normalized feedback rate κ plane. We clearly observe a strong impact of the time-delay on the switching behavior, and we identify three distinct *bubbles* - i.e. three ranges of time-delay - where a GS to ES switching takes place. In between, the laser only emits from the ground state until the steady-state is destabilized and the system evolves toward self-pulsing dynamics.

Inside the bubbles, we observe a smooth evolution from larger time-delays - where the ES emission is triggered but does not take over - to smaller time-delays - where the laser completely switches from the GS to the ES emission with a complete extinction of the ground state. The latter situation is however not always reached as can be seen from the bubble around $\tau = 101.5$ in Fig. 4.11, where no complete switching appears.

Although the scope of such mapping is fairly limited as it requires intensive time-consuming simulations, the repetition of those bubbles suggests that some kind of recurrence of the observed dynamics exists when varying the feedback time-delay.

To uncover the mechanism responsible for such evolution, let us have a closer look in the analytical expressions of the steady-states as described in section 4.2. Interestingly, the only link with the feedback terms - for all steady-states described - comes from the total carrier population terms (electron + hole populations):

$$\Sigma_{e,g} = n_e^{e,g} + n_h^{e,g} = 1 + \frac{1}{g_{e,g}} - 2 \frac{\kappa}{g_{e,g}} \cos(\Delta_{e,g} \tau) \quad (4.36)$$

The equation above clearly shows that the time-delay only appears through the last term. We can therefore define $\Psi_{e,g} = \Delta_{e,g} \tau [2\pi]$ and analyze in details the evolution of the steady-states in the (Ψ_g, Ψ_e) plane, which can then be complemented by an analysis of the system trajectory in the same plane.

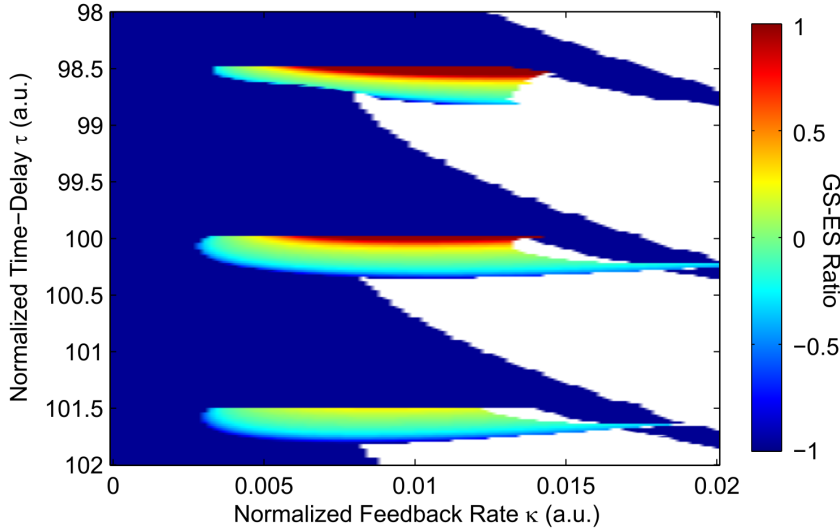


Figure 4.11 – **Impact of the time-delay on the GS-ES switching dynamics.** GS (ES) emission is in blue (red) and intermediate colors indicate the ratio between GS/ES emission. The white regions indicate dynamical evolution.

In all the cases described so far, the simultaneous GS-ES steady-state is the solution that bifurcates from the ground to the excited state emission - connecting the two other steady-states through transcritical bifurcations and effectively inducing switchings from the GS to the ES emission. We therefore only focus on this GS-ES solution. We plot its evolution for increasing feedback rates in Fig. 4.12.

The color code of Fig. 4.12 indicates the ratio between the ground and the excited state emissions. As shown in the previous section, the simultaneous GS-ES emission connects through transcritical bifurcations to GS or ES emission steady-states. We can therefore assume that the white regions connected to blue (red) areas correspond to GS-emission (ES-emission). Without feedback, the laser only emits from the ground state. The simultaneous GS-ES emission steady-state only appears around $\kappa > 0.003$ and is centered around $(\Psi_g, \Psi_e) = (\pi, 0)$. Then, for increasing feedback rates, the area where the simultaneous emission steady-state emerges expands and we observe a switching starting at the center of this area, see Figs. 4.12(a) to (c). For $\kappa \geq 0.006$, the steady-state disappears as it connects with the ES steady-state around the same point $(\Psi_g, \Psi_e) = (\pi, 0)$ as shown in Fig. 4.12(d). Finally, the simultaneous emission connects with the ES emission for almost all values of Ψ_e and we obtain in Fig. 4.12(f) a clear separation between two areas separated by thin bands of simultaneous emission: 1/ GS emission for $\Psi_g = 0$ or 2π and 2/ ES emission around $\Psi_g = \pi$. A complete switching can therefore only be achieved

if the system reaches the central area of the plot, roughly around $\Psi_g = \pi$ and $\Psi_e = 0$ for feedback rates larger than $\kappa > 0.005$. On the other hand, for $\Psi_g \approx 2\pi$ or $\Psi_g \approx 0$ the simultaneous GS-ES emission steady-state simply does not exist at all even at a relatively high feedback rate of $\kappa = 0.009$, see Fig. 4.12(f). Interestingly, the most important phase variable appears to be the one related to the ground state Ψ_g , while the other Ψ_e - related to the excited state - has a much smaller impact especially at larger feedback rates.

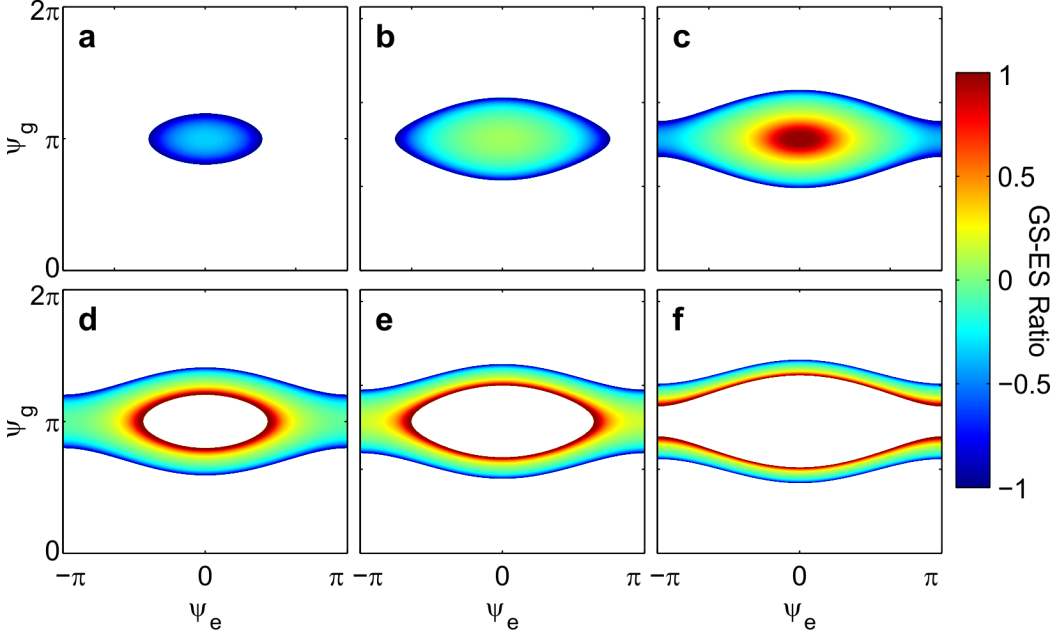


Figure 4.12 – **Evolution of the GS-ES simultaneous emission steady-state in the (Ψ_g, Ψ_e) phase map.** We consider the following feedback rates: (a) $\kappa = 0.003$, (b) $\kappa = 0.004$, (c) $\kappa = 0.005$, (d) $\kappa = 0.006$, (e) $\kappa = 0.007$ and (f) $\kappa = 0.009$. GS (ES) emission is in blue (red) and intermediate colors indicate the ratio between GS/ES emission. The white regions indicate that the simultaneous emission steady-state does not physically exist in these areas.

Although such mapping clarifies the dependence of the simultaneous GS-ES steady-state on the frequency-shift and the time-delay, the essential data are the system position in this plane and, even more importantly, its trajectory when varying the time-delay. At this point, it is however crucial to remind that so far we neglected the feedback phase-shift - we used $\kappa E(t - \tau)$ for the feedback term - whereas a more comprehensive model would consider the following term: $\kappa \exp(-i\omega_0^{e,g}\tau) E(t - \tau)$, with $\omega_0^{e,g}$ the frequency of the excited and the ground state emissions respectively. In this case, because of the

feedback phase: $\exp(-i\omega_0^{e,g}\tau)$, the two equations for the frequency shifts $\Delta_{e,g}$ get an additional term inside the sine and cosine functions:

$$\Delta_{e,g} = \frac{a}{2} \left(\frac{1}{g_{e,g}} + 1 \right) - \kappa \left(\frac{a}{g_{e,g}} \cos(\Delta_{e,g}\tau - \omega_0^{e,g}\tau) + \sin(\Delta_{e,g}\tau - \omega_0^{e,g}\tau) \right) \quad (4.37)$$

The optical frequency generally has a limited impact on the overall dynamics of the system because, in common multimode devices, the frequencies are roughly the same for all modes. Here, the GS and ES emissions are largely separated in terms of frequency: for instance, in [113], the authors report $\lambda_{GS} = 1275 \text{ nm}$ and $\lambda_{ES} = 1207 \text{ nm}$. In the context of the model used and with a photon lifetime around 2 ps , we would then obtain $\omega_0^e = 3120$ and $\omega_0^g = 2960$. This difference of about 5% confirms that largely different evolutions for Δ_e and Δ_g should be expected, hence the effect of the feedback phase cannot be neglected.

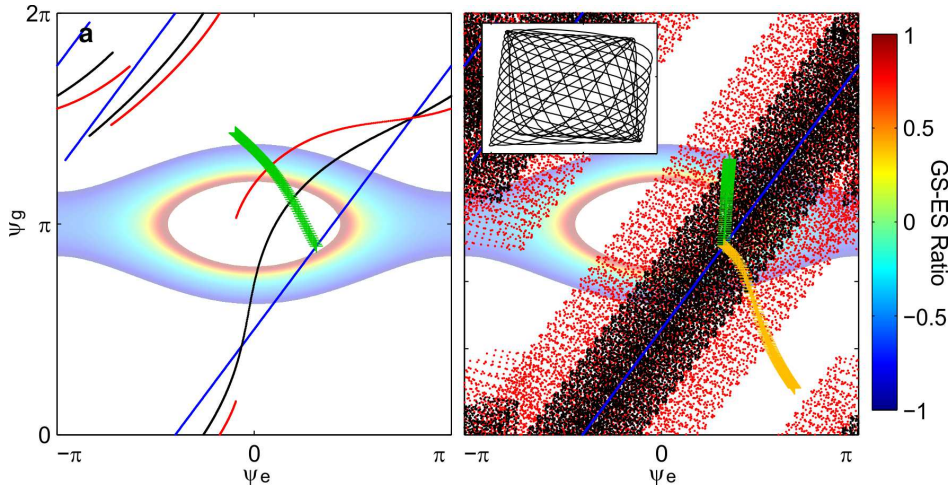


Figure 4.13 – **System trajectory in the (Ψ_g, Ψ_e) phase map without (a) and with the feedback phase (b).** We consider time-delays in $\tau \in [99, 101]$ for three different feedback rates: $\kappa = 0$ in blue, $\kappa = 2.10^{-3}$ in black and $\kappa = 4.10^{-3}$ in red. For the sake of clarity and because of the erratic trajectory when considering the feedback phase in (b), we only plot a dot at the calculated point without a connecting line. The inset of (b) shows a detail of the trajectory for $\kappa = 2.10^{-3}$. The system trajectories for fixed time-delays and increasing feedback rates $\kappa \in [0, 0.1]$ are shown in green for $\tau = 100.2$ (in (a) and (b)), and in yellow for $\tau = 100.2015$ (only in (b)). To help the reader compare the system trajectory with the evolution of the simultaneous GS-ES emission steady-state, the evolution of the latter for $\kappa = 0.006$ is shown in the background.

In Fig. 4.13, we plot the trajectory of the system for time-delays $\tau \in [99, 101]$ without (a) and with feedback phase (b). We observe that the system position in the (Ψ_e, Ψ_g) phase map dramatically changes with respect to both the time-delay and the feedback rate. In

Fig. 4.13(a), the evolution is relatively smooth and the system goes through both the switching and non-switching areas. In fact, we can roughly estimate the limits between the switching bubble around $\tau = 100$, displayed in Fig. 4.11 - see, in particular, the trajectory at $\tau = 100.2$ displayed in Fig. 4.13(a) -, and the stable GS emission when the system is outside of the switching area. On the other hand, when the feedback phase is considered, the trajectories are way more complex, see Fig. 4.13(b). As presented in the inset of this figure, the system trajectory follows a well-defined pattern due to the combined effect of both GS and ES feedback phase variations with the time-delay. But the system runs through this trajectory very quickly with respect to the variations of the time-delay: in Fig. 4.13(b), the time-delay only varies between 99 and 101. Moreover, the trajectory pattern expands in the (Ψ_e, Ψ_g) phase map when the feedback rate is increased, and, as a result, the whole space can be quickly filled - i.e. for small variations of the time-delay, the system can move almost anywhere in the phase map. This effect is clearly highlighted in Fig. 4.13(b), where we plot the expansion of the system trajectory, for variations of the time-delay, for three different feedback rates $\kappa = 0, 2 \cdot 10^{-3}$ and $4 \cdot 10^{-3}$ in blue, black and red respectively. In addition, we show that a time-delay variation of the order of 10^{-3} is sufficient to inverse the system trajectory for increasing feedback rates - see the two trajectories for $\tau = 100.2$ in green and $\tau = 100.2015$ in yellow in Fig. 4.13(b) -, the system can therefore move from a switching to a non-switching dynamics just with this tiny change of the time-delay. With a photon lifetime of 2 ps and the parameters used, such small change would be equivalent to a $0.6 \mu\text{m}$ displacement of the external cavity mirror.

Considering the huge impact of the feedback phase on the GS-ES switching dynamics reported above, we expect the switching bubbles to dramatically shrink in size and potentially exhibit some kind of recurrence related to the frequencies of the two modes. To confirm these hypotheses, we perform new simulations including the contribution of the phase in the feedback terms for both the ground and excited states.

In Fig. 4.14, we plot the evolution of the switching scenario in the current versus time-delay plane for different values of the feedback rate. Here, it is important to remark that the scale for the time-delay variations is tiny (about 0.01), but is sufficient to observe multiple switchings between ground and excited state emissions. Although at first glance, the evolution with the time-delay is clearly recurrent - with a period that does not relate to GS or ES optical frequencies but lies in between -, some small defects indicate that the switching bubbles are in fact not repeating themselves periodically. For instance, a small break around $\tau \sim 100$ and $J \approx 5$ can be observed; hence suggesting that a more complex mechanism takes place.

In Fig. 4.14(a), we observe that the switching bubbles are asymmetric, and for increasing feedback rates (e.g. in (d)) we can identify two distinct regimes: 1/ The switching bubble in itself e.g. around $\tau = 100$: the ground state emission is quickly destabilized,

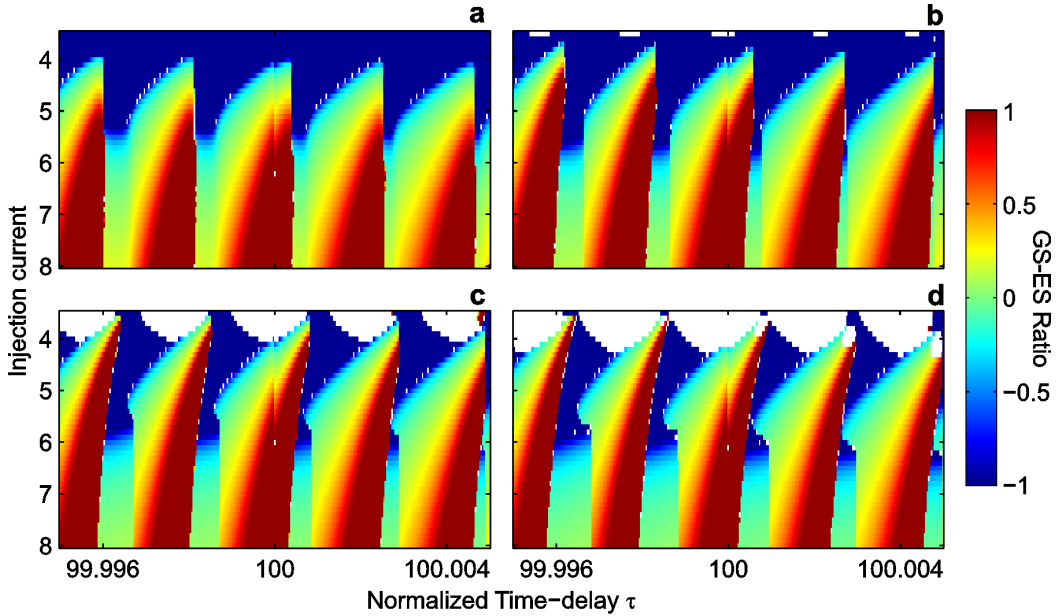


Figure 4.14 – **Evolution of the switching behavior when taking into account the feedback phase term.** We plot the steady-state evolution of the system in the current versus time-delay plane for four different feedback rates: (a) $\kappa = 0.004$, (b) $\kappa = 0.006$, (c) $\kappa = 0.008$ and (d) $\kappa = 0.010$. The color code is similar to other plots: GS (ES) emission is shown in blue (red) and intermediate colors show the ratio between GS and ES contribution for simultaneous emission. White areas indicate dynamical behaviors.

for increasing currents or increasing feedback rates, toward simultaneous emission or self-pulsing dynamics. In Fig. 4.14, we can see that this regime evolves for increasing feedback rates, from a curvy to a sharper half-arrow shape for increasing time-delays. 2/ a regime with enhanced stability of the GS steady-state: increasing the feedback rate leads to an enhanced stability of the GS emission. In the solitary laser, the GS emission, stable at threshold, will be destabilized for currents of about $J \approx 4.5$ while in Fig. 4.14(d), e.g. for $\tau \approx 99.996$, currents of $J > 6$ are required to destabilize the GS emission steady-state. Although the separation between the two regimes is largely influenced by increasing feedback rates - for a given value of the time-delay, the system might go from one regime to the other -, the stability range of the second regime with respect to the time-delay seems to be enlarged for stronger feedbacks, especially at high injection currents. The stability range of the first regime is therefore reduced, suggesting once again that the GS emission is indeed favored by the optical feedback.

Finally, for small injection currents $J < 4.3$, we observe that for large feedback rates $\kappa \geq 0.008$ the GS steady-state is destabilized and a period-1 self-pulsing dynamics emerges: see the white (dynamical) region replacing the blue GS emission steady-state

in Fig. 4.14(c-d). This self-pulsing dynamics only takes place on the GS emission - the ES mode is extinct - and the oscillation frequency does not relate to the time-delay. Similarly, at low injection current in Fig. 4.14(d), the simultaneous emission steady-state also get destabilized for some values of the time-delays ($\tau > 100$) and an antiphase period-1 dynamics appears. In both cases, the period of the self-pulsations does not clearly relate to the external cavity frequency nor to the relaxation oscillation frequency obtained using the approximated expression developed in [116].

To sum up, we investigated the impact of the external cavity length on the switching dynamics uncovered in the previous section. We report a strong dependence of the dynamics with the feedback phase: the GS-ES switching dynamics repeats itself when varying the external cavity length, with a period close to the averaged wavelength of the laser, i.e. neither the GS nor the ES wavelengths but in between. In practice, we therefore expect the dynamics to evolve roughly at the scale of the optical wavelength of the laser with respect to the external cavity round-trip length.

4.5.2 *Impact of the electron escape rate*

Finally, we investigate the impact of the electron escape rate on the dynamics of the laser subject to optical feedback. In section 4.3, we already showed that a change of the electron escape rate could greatly modify the behavior of the solitary device. In particular, with all other parameters being constant, we reported that increasing the electron escape rate would lead the laser to emit from the excited state directly at threshold - instead of exhibiting a transition from GS to ES emission through simultaneous GS-ES emission. Here, we analyze the effect of such change on the GS-ES switching dynamics reported.

In Fig. 4.15 and 4.16, we plot the steady-state evolution of the system in the current versus time-delay plane for electron escape rates of $C_e = 1.5$ and $C_e = 3$ respectively. As described in section 4.3, for $C_e = 1.5$ the solitary laser still starts emitting from the GS at threshold, but the ES emission quickly appears for $J > 4$ and the GS emission vanishes for $J > 5$. On the other hand, for $C_e = 3$, the solitary laser directly emits from the ES at threshold and no GS emission appears.

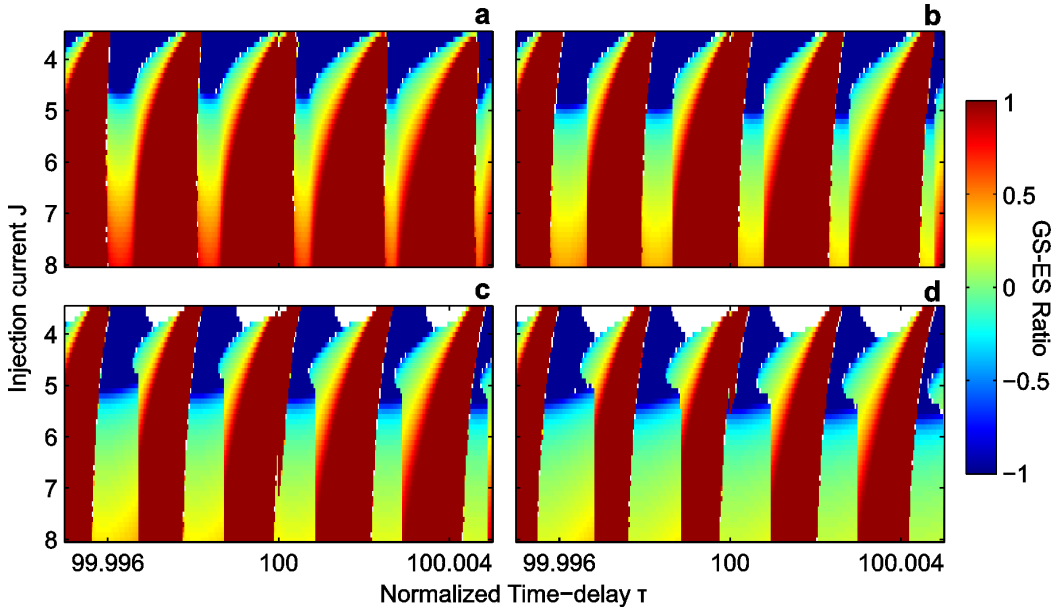


Figure 4.15 – Evolution of the switching behavior for $C_e = 1.5$. The color code and feedback rate are identical to those of Fig. 4.16.

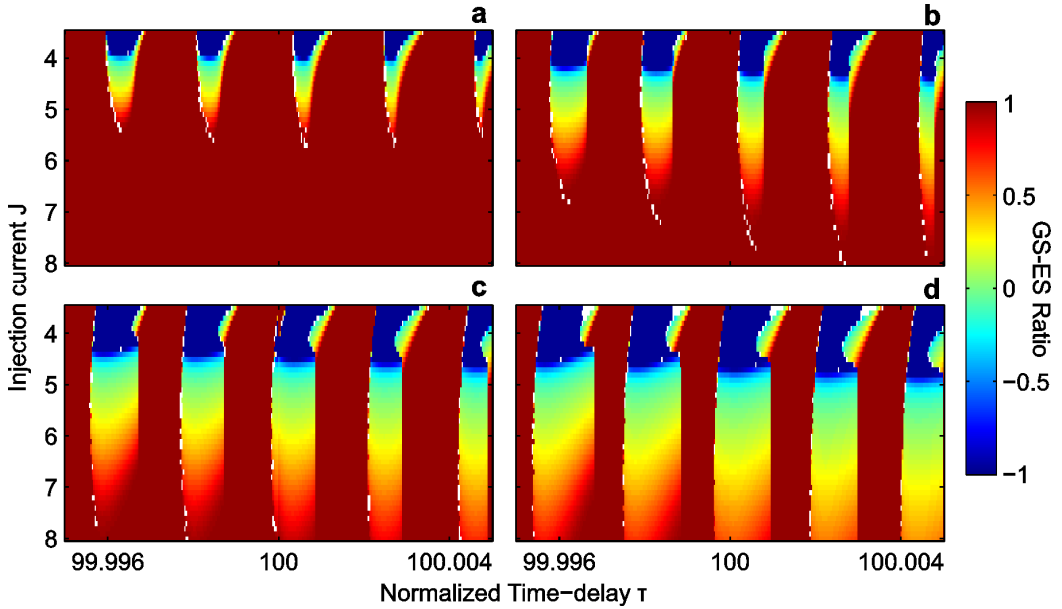


Figure 4.16 – Evolution of the switching behavior for $C_e = 3$. We plot the steady-state evolution of the system in the current versus time-delay plane for four different feedback rates: (a) $\kappa = 0.004$, (b) $\kappa = 0.006$, (c) $\kappa = 0.008$ and (d) $\kappa = 0.010$. The color code is similar to other plots: GS (ES) emission is shown in blue (red) and intermediate colors show the ratio between GS and ES contribution for simultaneous emission. White areas indicate dynamical behaviors.

As could be expected, the ES emission takes over for all ranges of current. This is however better seen in Fig. 4.16(a) in which the laser only emits from the ES for currents above $J > 6$. Despite this change, the switching dynamics reported previously remains mostly similar: we still observe the two regimes described in the previous section and a roughly periodic evolution, with a scaling between GS and ES optical frequencies. Again we observe that for increasing feedback rates the GS emission is favored. In particular at medium current values around $J = 5$, we clearly observe that the stability region of the ES steady-state with respect to the time-delay is severely reduced. Interestingly, the most handy switching dynamics between GS and ES emissions seems to take place for $C_e = 3$. In this case, comparing the different panels of Fig. 4.16, we see that the extinction of the ES emission could be tuned by controlling the injection current while the width of the ES and GS stability range with respect to the time-delay might be controlled by the feedback rate. In addition, the switching between GS and ES emission appears to be more sudden for variations of the time-delay. For instance, in Fig. 4.16(c) for $J \approx 5 - 6$ no transition can be found between the two regimes: the laser goes directly from simultaneous GS-ES emission to ES emission.

Finally, we observe that, at low injection currents, the period-1 dynamics destabilizing the steady-state emission disappears when increasing the electron escape rate. Indeed, a similar dynamics can still be observed in Fig. 4.15(c-d) for $C_e = 1.5$, but in Fig. 4.16(c-d) for $C_e = 3$ it has been completely suppressed.

To conclude, the switching dynamics reported in the previous section dramatically depends on the optical feedback time-delay - i.e. the external cavity length - and appears to be recurrent, with a periodicity scaling to the averaged optical wavelength. Nevertheless, the switching dynamics seems to be relatively robust with respect to the electron escape rate and therefore to the solitary laser behavior: we easily reproduce a behavior similar to the one uncovered previously in the case of a laser emitting only from the ES in free-running configuration.

4.6 EXPERIMENTAL OBSERVATION OF SWITCHING FOR VARYING TIME-DELAYS

In this section, we present the experimental study performed in order to confirm the theoretical predictions made so far. At the time I am writing these lines, these experimental investigations are still in progress; the results presented here will therefore be completed and expanded in future works.

The work described in this section has been performed in collaboration with Stefan Breuer from the Institute of Applied Physics, Technische Universität Darmstadt. I therefore gladly acknowledge his support for this work. I also take this opportunity to acknowledge the fruitful participation of Lukas Drzewietzki and the support of Prof. Wolfgang Elsässer, both from the same University.

4.6.1 *Experimental setup*

The QD laser investigated here was grown by Molecular Beam Epitaxy and contains 5 layers of Stranski-Krastanov self-assembled and undoped InAs quantum dots separated by GaAs barriers. The device is a two-section laser with a total length of 1 mm and a shorter section of 0.1 mm. The width of the waveguide is 4 μm and the facets are cleaved. It is important at this point to note that the two sections of the laser are biased homogeneously and that we do not exploit any property of the device related to this two-section structure. The QD laser emits from the ES at room temperature ($\lambda_{\text{ES}} \approx 1.17 \mu\text{m}$), but simultaneous GS-ES emission (with the GS emitting at $\lambda_{\text{GS}} \approx 1.25 \mu\text{m}$) slowly appears when the temperature is decreased sufficiently, typically down to about 4°C. To avoid damaging the device because of the condensation, the temperature is set at 8°C so that the laser is close to its simultaneous GS-ES emission point. The complete experimental setup used in this work is described in Fig. 4.17.

The external cavity is formed by a mirror placed at about 20 cm from the laser diode. In between, we put a variable neutral density filter in order to control the feedback strength and a 90/10 beamsplitter for measurements. As shown in Fig. 4.17, we use in total four different measurement branches: 1 & 2 are used all the time while 3 & 4 - delimited by the dashed line - were only used to confirm the steady-state behavior of the system. Branches 1, 3 & 4 are placed after an optical isolator to avoid undesired reflections from the fiber front facets.

- Branch 1: after coupling the beam into a monomode fiber, we split the signal in two using a 2x2 90/10 fiber coupler that we direct to: a) a power meter (Coherent Fieldmaster, LM-2 IR, 0.8-1.55 μm) to estimate the total output power of the laser and b)

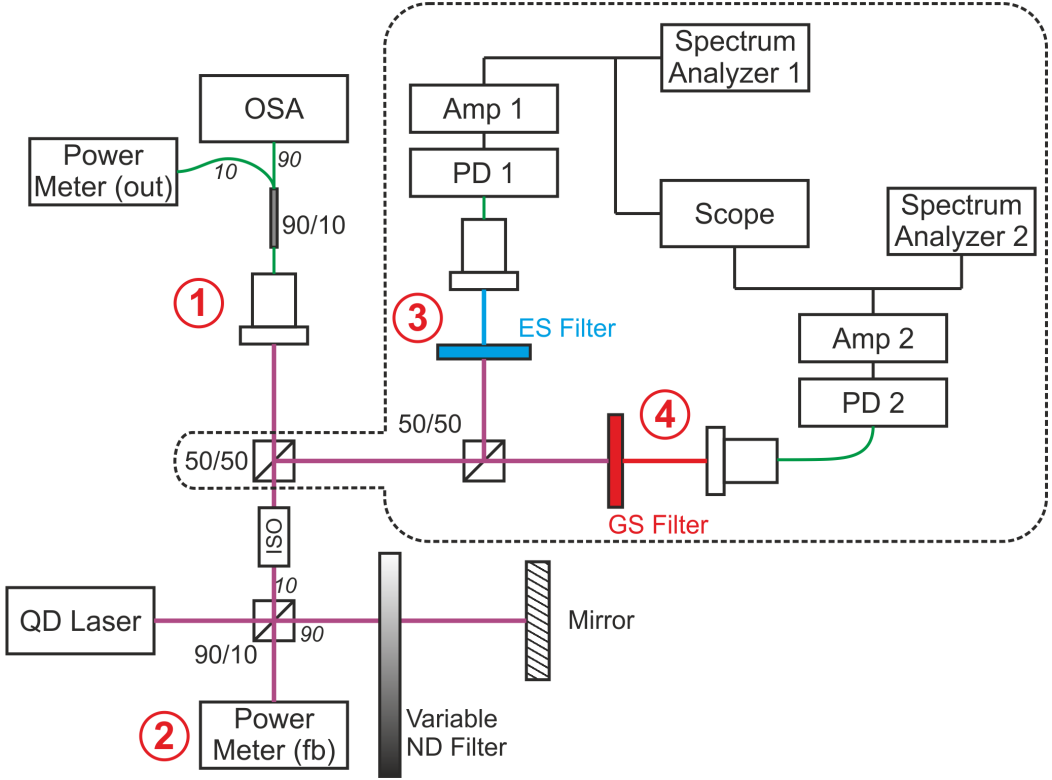


Figure 4.17 – **Experimental setup for the analysis of GS-ES switching in QD laser with feedback.** The intensity of the optical feedback is controlled with a variable neutral density (ND) filter introduced between the mirror and the laser. In total we have four measurement branches: 1/ unfiltered branch where we measure the total output power (out) and the optical spectrum (OSA), 2/ a feedback branch to estimate the feedback strength (fb), and two filtered branches (3 & 4) measuring the dynamical evolution - i.e. radio-frequency spectrum and time-series - of the spectrally resolved ES and GS emission in branches 3 and 4 respectively. Branches 1, 3 and 4 are placed after an optical isolator to avoid undesired reflections from the fiber front facet. The part of the setup delimited by the dashed line has only been used to confirm the steady-state behavior of the laser.

an optical spectrum analyzer (OSA) (Anritsu MS9710C, 0.6-1.75 μm) to record the optical spectrum of the laser output.

- Branch 2: we use the same power meter as in branch 1, but in free-space, to estimate the power of the light being sent back toward the laser device. Of course, we do not know exactly what is the amount of light being effectively fed back to the laser cavity, but this measurement gives us a relative estimation.
- Branch 3: before coupling the beam into a monomode fiber, we filter it to keep the ES contribution only, and then send the optical signal to a fast photodetector combined with an electronic amplifier (NewFocus 1014, 40 GHz with 40 dB amplification across 0.1-10 GHz). The radio-frequency is recorded using a spectrum analyzer (Tektronix 6114A, 14 GHz) and the time-series are recorded using an oscilloscope (Tektronix TDS 6154C, 15 GHz, 40 GS/s).
- Branch 4: is similar to branch 3 except that we filter the laser beam to keep the GS contribution. Otherwise, we send the optical signal to a fast photodetector with electronic amplification (Newport D8-IR, 50 GHz with 27 dB amplification across 0.01 - 45 GHz). The radio-frequency spectrum is recorded using a spectrum analyzer (Tektronix 2755AP, 21 GHz) and the time-series are recorded using the same scope as in branch 3.

To investigate the effect of the variations of the time-delay on the dynamics of the laser, the mirror is placed on a piezo-electric actuator with a displacement capability of about 200 nm/V with a precision of 0.1 V - i.e. about 20 nm. The piezo-actuator is controlled by an open-loop piezo-controller.

4.6.2 *Behavior of the solitary laser diode*

Without optical feedback and with a temperature fixed at 8°C, the laser only emits from the excited state. In Fig. 4.18, we present the LI-curve of the solitary laser diode with two optical spectra captured before and after the laser threshold. Before threshold, we clearly observe a peak corresponding to the GS emission whereas the ES emission is off. However the GS emission never reaches its threshold and instead the laser starts emitting from the excited state for $I > 47$ mA. Well above threshold - i.e. for $I = 55$ mA -, we observe that the GS peak of the optical spectrum does not change much, hence suggesting that the GS is already saturated for $I = 47$ mA but at this temperature the gain

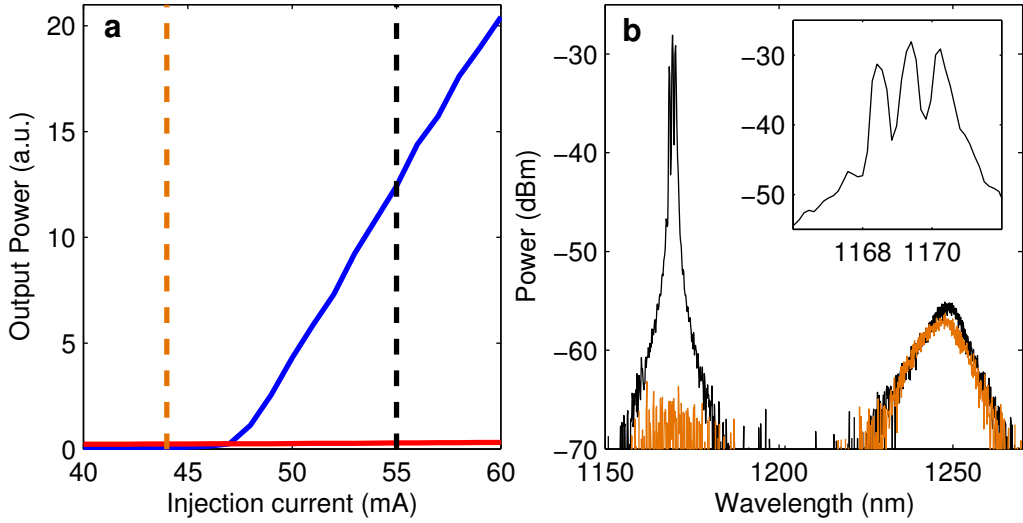


Figure 4.18 – **Behavior of the solitary two section QD laser.** (a) LI-curve of the laser with GS (ES) emission in red (blue). The black and orange vertical dashed curves shows where the corresponding optical spectra have been recorded. (b) Optical spectra taken before threshold at $I = 44$ mA in orange and after threshold at $I = 55$ mA in black. The inset shows the detail of the ES peak at $I = 55$ mA.

is never sufficient to overcome the losses. Finally, as shown in the inset of Fig. 4.18(b) where several peaks appear in the ES emission spectrum, we highlight that the excited state emission is multimode. Considering the length of the laser cavity (1 mm), the separation between longitudinal modes would be slightly over 200 pm. In Fig. 4.18(b), the peaks are more separated - we measure a separation slightly below 1 nm -, which appear to be consistent with the separation that could be expected from higher-order transverse modes considering the 4 μm width of the waveguide. The presence of these additional modes complicate the lasing process and the effects of the optical feedback, and therefore suggest that a more complex model, compared to the one used earlier, might be required to reproduce some specific features.

4.6.3 Impact of the optical feedback: experimental observations

When the laser is subject to optical feedback, we immediately observe that, as described in [110], it triggers the ground state emission in the QD laser. For weak feedbacks, the laser still emits from the ES at threshold, but the GS emission appears at larger injection currents. Even though we did not observe such behavior in theory with the rate equation model and the set of parameters used in the previous section, we suppose how-

ever that this phenomenon might be explained by direct capture of carriers from the wetting layer to the ground state [117, 192]. In Fig. 4.19, we plot the evolution of the GS and ES threshold for increasing reflectivities of the external mirror. As can be expected from the optical feedback scheme, the threshold of the GS emission decreases for increasing feedback strengths: from 60 to less than 40 mA. In contrast, the threshold of the ES emission remains almost constant around 46 mA. Thus, for an external mirror reflectivity of about 3.5% the two modes have a similar threshold, and for stronger feedbacks the GS emission appears before the ES emission.

As a result, we already confirm that an optical feedback can trigger ground state emission in a quantum dot laser emitting only from the excited state in solitary configuration. Moreover, the lack of threshold reduction on the excited state emission obviously suggests that the optical feedback specifically favors the ground state emission, hence supporting the theoretical observations described previously.

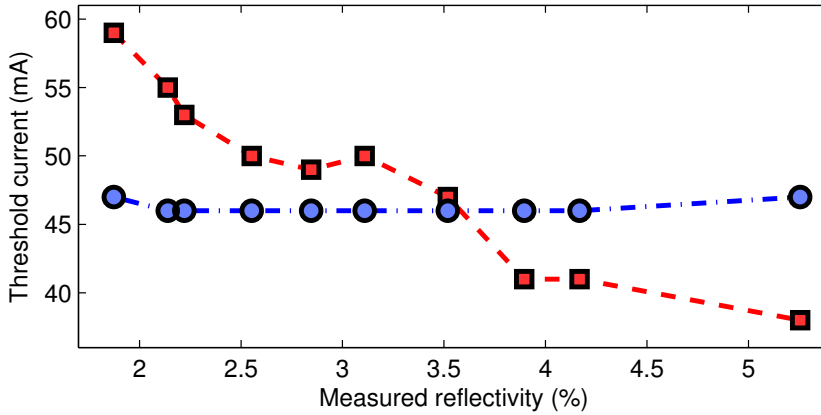


Figure 4.19 – **Evolution of the GS and ES emission threshold versus mirror reflectivity.** The threshold of the GS (ES) emission is plotted in red (blue). The markers indicate the measurement points and the dashed (dash-dotted) line only connects them.

Next, we investigate the impact of time-delay variations on the laser dynamics, i.e. variations of the external cavity length. We set the injection current at $J = 50$ mA and then carefully increase the external mirror reflectivity until the ground state emission is close to its threshold. We then move the mirror using a piezo-electric actuator as explained above.

We obtain the results displayed in Fig. 4.20(a): when changing the external cavity length, anti-correlated evolution of the GS and ES output power appears. The laser exhibits switching between ES emission and simultaneous GS-ES emission steady-states. The oscillations are somewhat irregular but appear roughly each half optical wavelength (about

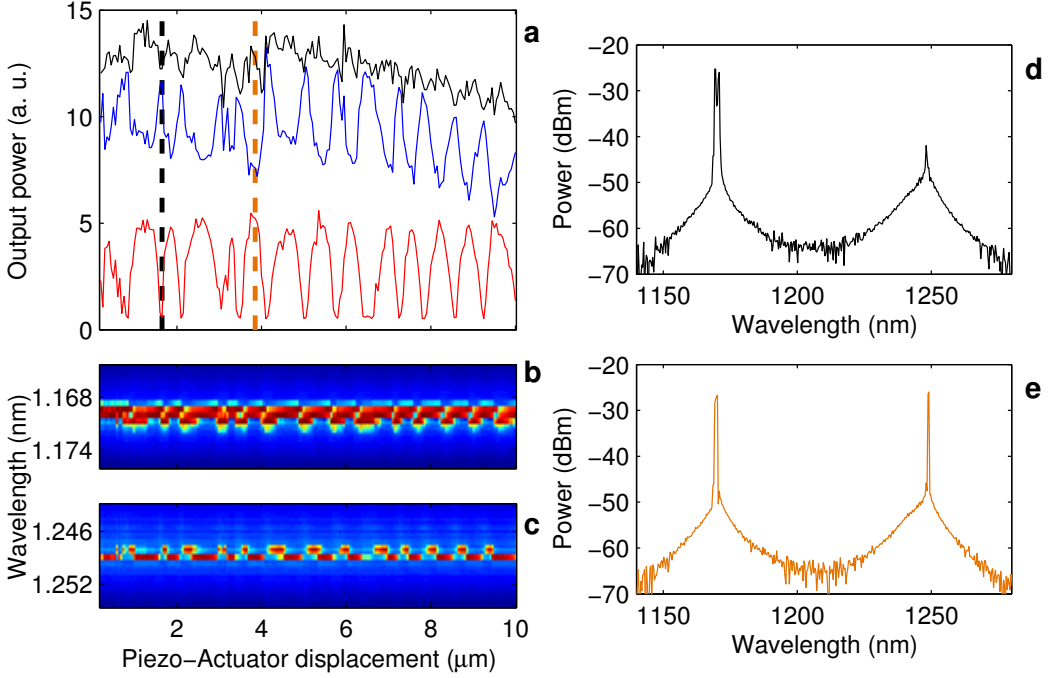


Figure 4.20 – **Anti-correlated evolution of the GS and ES emission for varying external cavity length.** Experimental observations of incomplete switching for a current of $J = 50$ mA and a external mirror reflectivity of about 3%. (a) Output power evolution: the GS (ES) emission is plotted in red (blue) respectively, while the total emission power is shown in black. The two vertical dashed lines indicates where the two spectra plotted in panels (d, in black) and (e, in orange) have been captured respectively. (b) and (c) evolution of the optical frequency for the ES and GS emission respectively. (d) and (e) shows the optical spectra for two different positions of the mirror with the GS emission on and off respectively.

0.6 μm), i.e. at the optical wavelength scale for the total external round-trip length. In Fig. 4.20(d–e), we show two spectra corresponding to the ES emission and simultaneous GS-ES emission, respectively. In Fig. 4.20(d), the ground state is switched off, but we can clearly see that the mode is really close to threshold as the optical spectrum still exhibits a small peak. In both cases, the ES emission appears to be multimode as in the case of the solitary laser. However, when the GS emission is turned on as in Fig. 4.20(e), the ES peak width becomes smaller while the sharp peak of the GS emission clearly shows that it is single-mode.

Finally, in Fig. 4.20(b,c), we show the evolution of the optical spectra for the ES and GS emission respectively. For both modes, we observe a slight shift of the frequency between the ES emission only and the simultaneous GS-ES emission - toward larger wavelengths for the ES and toward shorter wavelengths for GS emission. We therefore show that the

switching between the two steady-states also include a slight variation of the optical frequency for both modes. At this point, it should be noted that, for the external cavity length considered ($L \approx 20$ cm), the separation between external cavity modes induced by the optical feedback would be about few picometers and therefore cannot be resolved here. Therefore, the frequency shifts reported here are not the result of switching between different external cavity modes.

The reported anti-correlated oscillations of the GS and the ES output powers occur at the scale of the optical wavelength with respect to the total external round-trip length. This result therefore confirms the impact of the feedback phase as described theoretically in the previous section. Although incomplete switchings for external cavity length variations has been theoretically predicted - for instance in Fig. 4.16(a) for a current around $J \approx 4 - 5$ -, experimentally we were not able to achieve a complete switching between the GS and the ES emissions as could have been expected from theoretical results. Nevertheless, as already mentioned, the incomplete switching dynamics is accompanied by slight changes of the frequency for the emissions from both the GS and the ES, as shown in Fig. 4.20(b,c). Considering that the device investigated here is multimode, such peculiar evolution of the frequency suggests that the GS-ES switching are accompanied by switchings between different modes of the GS and the ES. As a result, we observe switching between ES emission and simultaneous GS-ES emission, but probably also between different transverse modes of both the GS and the ES emissions. Considering the strong feedback phase sensitivity highlighted in the theoretical part, a small frequency difference could potentially largely impact the evolution of the laser when varying the external cavity length. In particular, the switchings between GS and ES emissions would not necessarily take place at the same mirror positions. Which means that even if one mode of the ES emission could be switched off by the optical feedback at a given position of the mirror, the others would not be necessarily switched off as well for the same mirror position. Thus, for any configuration one of the ES mode would always be on, hence the ES emission would never be totally switched off by the sole effect of the optical feedback. The same reasoning can of course be applied to the GS emission. This approach could therefore explain the discrepancy between experimental and theoretical results, i.e. the inability to reach a complete extinction of the ES emission experimentally.

In the previous sections, we used a simple model for both GS and ES emission in which only a single-mode emission was taken into account for each energy level. We therefore cannot reach the same level of complexity as observed in the experimental results. Yet, as mentioned earlier, we were also able to find some parameter configuration where incomplete switching dynamics between the ES emission and simultaneous GS-ES emission could be observed. In Fig. 4.21, we show simulated results of the laser steady-

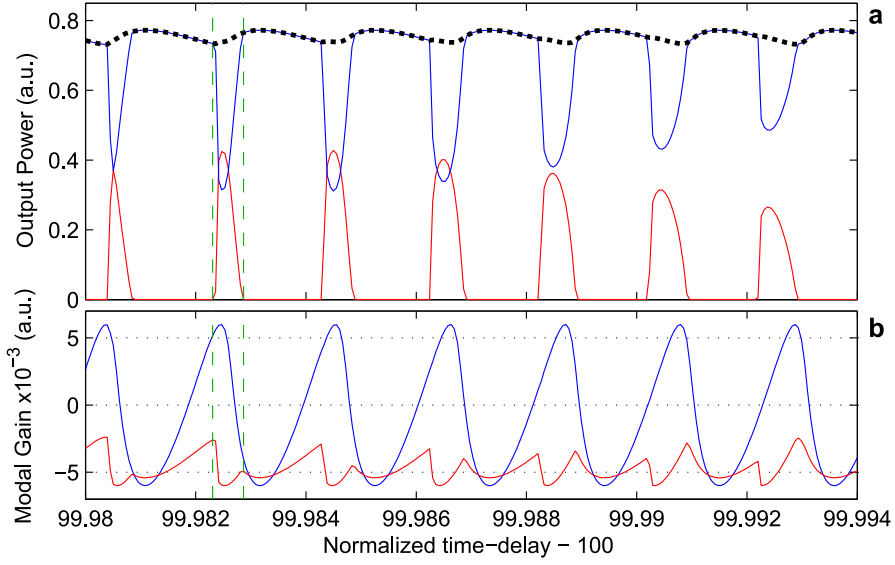


Figure 4.21 – **Simulation of the steady-state evolution of the laser when varying the feedback time-delay.** The feedback rate is fixed at $\kappa = 0.003$ and the time-delay is varied around $\tau = 99.99$. The injection current is set at $J = 4$ and the electron escape rate is $C_e = 3$. (a) Evolution of the GS and ES output power in red and blue respectively while the dotted black curve gives the total output power. (b) Plot of the modal gain in the laser cavity for the GS and the ES in red and blue respectively. The two green vertical dashed lines simply indicate two time-delay values where the GS mode is turned on/off and are reported in the modal gain plot.

state showing such incomplete switching dynamics showing a good agreement with the experimental observations described above. We use parameters that qualitatively reproduce the experimental situation. With an electron escape rate of $C_e = 3$ the laser only emits from the ES without optical feedback, the injection current is set at $J = 4$ about 1.2 times the laser threshold and we use a weak feedback with a feedback rate set at $\kappa = 0.003$. In addition, we set the emission frequency of the ground and the excited state to $\omega_g = 3015.9$ and $\omega_e = 3222.1$. The time-delay τ is varied between 99.98 and 99.994, which corresponds to a complete variation of about $8 \mu\text{m}$ of the cavity length for a photon lifetime of 2 ps.

As a result, we successfully reproduce an evolution that shows a good agreement with the reported experimental features. The incomplete switchings are recurrent and appear with a periodicity related to the averaged optical frequency. We also plot the evolution of the modal gain for GS and ES emission: $G_{e,g} = g_{e,g}(n_{e,g}^e + n_{e,g}^h - 1) - 1$. In free-running configuration - i.e. without feedback $\kappa = 0$ - the laser only emits from the ES and we have $G_e = 0$. With optical feedback however, we obtain an almost periodic evolution between positive and negative values of the ES emission gain when varying the

time-delay: depending on the time-delay the feedback favors (thus, a lower gain < 0 is sufficient) or impede the ES emission (and a higher gain > 0 is therefore required). The same behavior would obviously be expected for a lasing ground state. Thus, in Fig. 4.21(b), we observe that simultaneous GS-ES emission only appears when two conditions are combined: 1/ $G_e \geq 0$, i.e. the ES emission is disfavored and 2/ $G_g \approx -5 \cdot 10^{-3}$, i.e. GS emission is largely favored by the optical feedback. For a given time-delay, when these two features are combined, simultaneous GS-ES emission appears, and the laser exhibits an incomplete switching from ES to GS emission. Furthermore, because of the large difference between the optical frequencies of the two modes, the oscillations of the two gains are not synchronized. As a result, the two conditions described above are not fulfilled identically for different mirror positions, hence leading to unsteady switching ratios for different values of the time-delay as can be seen in Fig. 4.21(a).

In summary, we presented new experimental results for a quantum dot laser subject to optical feedback. The solitary laser does not emit simultaneously from the ground and the excited state for the temperature considered, but we confirmed again that GS emission can be easily triggered by optical feedback. Furthermore, we showed that the optical feedback has little to no impact on the ES emission threshold while it strongly decreases the one of the GS emission. We also report incomplete switchings between ES emission and simultaneous GS-ES steady-states when the external cavity length is varied. The switching typically occurs at the optical wavelength scale for the total external round-trip. These first results match qualitatively the conclusions of our theoretical findings described in the previous section.

4.7 SUMMARY AND PERSPECTIVES

To conclude, we make an in-depth theoretical investigation of the optical feedback impact on the dynamics of a quantum dot laser emitting simultaneously from the ground and the excited states.

Based on the relatively simple theoretical model of Viktorov *et al.* [115], we describe analytically the three steady-states of the system - GS emission, ES emission and simultaneous GS-ES emission - and provide some additional insight on their stability. Then, we investigate the behavior of the solitary QD laser diode: we identify the bifurcations connecting the three steady-states of the system and show that the laser behavior strongly depends on the carrier escape rates.

Next, we analyze the QD laser diode dynamics when subject to time-delayed optical feedback. First, we unveil a GS to ES switching for an increasing feedback strength, and second, we uncover a relatively large bistability between the fundamental ES emission branch and the first GS external cavity mode. Moreover, we highlight an hysteresis cycle connecting the two states, and therefore show that the control of the feedback strength can be sufficient to switch from GS to ES emission with a complete extinction of the other mode. For stronger feedback levels, we report a bifurcation scenario toward antiphase self-pulsing dynamics showing a dominant GS-emission and with a frequency close to the time-delay. From a different viewpoint, we also highlight that the optical feedback, overall, favors GS emission. Indeed independently of the free-running laser behavior, a sufficiently strong feedback always trigger the GS emission and might lead to a dominant ground state emission.

Investigating the influence of the feedback parameters, we report a major impact of the external cavity length. In fact, we link the effects of external cavity length variations to the frequency-shifts induced by the optical feedback, and, in particular, to the respective frequency-shifts for the GS and ES emissions. Since these shifts are strongly related to the feedback phase, these findings clearly indicate that the latter, although neglected before, must be considered. With a more comprehensive model, we find that the switching dynamics is deeply impacted by small variations of the time-delay: we report a roughly periodical evolution at the scale of the optical wavelength, with respect to the total external round-trip length. Furthermore, we investigate the impact of the electron escape rate on the switching dynamics uncovered. Because changing the electron escape rate modifies the emission properties of the solitary QD laser, we were able to theoretically confirm that similar GS-ES switching dynamics take place in devices emitting only from the ES in solitary configuration.

Finally, we present the first experimental results obtained in collaboration with the Technische Universität Darmstadt in a two-section quantum dot laser, biased homogeneously, and subject to optical feedback. Although the solitary laser only emits from the excited state, the device temperature is set so that it is close to simultaneous GS-ES emission. In this context, we report a strong decrease of the GS emission threshold for increasing feedback strengths, while the ES emission threshold is almost not impacted. These results support our theoretical observations that optical feedback favors ground state emission. In addition, we successfully uncover an incomplete GS-ES switching for variations of the external cavity length: the laser switches between an excited state emission and a simultaneous GS-ES emission. The switchings take place at the optical wavelength scale (about $1.2\text{ }\mu\text{m}$) with respect to the total external round-trip and show a good qualitative agreement with our theoretical observations.

These results are of course intended to be completed with future work, especially on the experimental side. At this point, I believe that the perspectives for future investigations are at least three-fold:

- The theoretical and experimental work presented here motivates further in-depth experimental investigations. We theoretically show that because of the large frequency separation between the GS and the ES emissions, the impact of the feedback phase is largely increased. Combined with the complexity of the carrier dynamics between the two levels, QD lasers cannot be treated as common multimode devices. Therefore additional investigations are required to fully understand the effects of optical feedback on these devices. In particular, our work so far raises some questions such as: is it possible to achieve a complete GS-ES switching in contrast with the incomplete switching uncovered here? Does the bistability between the fundamental ES emission and the first GS external cavity mode exist? and if yes, can it really be exploited in practice?
- Additional theoretical work would also be required to fully understand the impact of the multimode emission from the GS and the ES emissions. Indeed we experimentally show that different modes of the ground and excited state emissions appear when the GS emission is on or off. As a result, a crucial point would be to verify if this multimode emission is preventing a complete GS-ES switching as opposed to the incomplete switching observed.

- Finally, our work also brings new light into potential applications of QD laser diodes emitting simultaneously from the ground and the excited states. First, terahertz generation that would benefit from additional controls of the laser output. Secondly, the effects of the optical feedback might be of interest for all-optical processing applications or optical memories.

5

CONCLUSION AND PERSPECTIVES

*If you thought that science was certain
- well, that is just an error on your part.*

— Richard P. Feynman

This final chapter aims at concluding this thesis by reminding the essential points and achievements described in this manuscript. I will also highlight the main perspectives for future investigations motivated by our work.

This chapter is therefore organized as follows: in section 5.1, we briefly summarize the results presented in each chapter and emphasize the main achievements described in this thesis. Then, in section 5.2, we describe the main perspectives motivated by the work and results highlighted in this dissertation.

5.1 MAIN ACHIEVEMENTS

For the sake of clarity, I will not strictly follow the same progression as in the thesis but the limited overlap between the different chapters allows me to separate the results described in each of them.

In chapter 2, we studied the polarization instabilities and the resulting dynamics in quantum dot vertical-cavity surface-emitting lasers.

- First, we demonstrated that the peculiar mode-hopping dynamics between elliptically polarized states reported in [54] is, in fact, a deterministic chaos. In section 2.3, based on the spin-flip model (SFM), we reproduced a bifurcation scenario that matches the experimental observations, including all the experimentally uncovered statistical features. We unambiguously identified the dynamics as a deterministic chaos using several algorithms, such as Wolf's or Grassberger-Procaccia's algorithm as shown in section 2.4. In contrast to the commonly accepted thought that laser diodes behave as damped oscillators, we made the first demonstration of a temporal chaotic dynamics in a free-running single-mode laser diode without the need for any external perturbation or forcing.
- Second, we demonstrated that the frequency of the dynamics induced by polarization instabilities in VCSELs is not simply determined by one of the characteristic frequencies of the system. As discussed in section 2.2, depending on the model parameters the frequency can be close to the relaxation oscillation frequency or the birefringence frequency, but is foremost defined by a bifurcation problem and can therefore take a large range of different values. Reciprocally, this result shows that the birefringence of the laser cavity cannot be measured through dynamical measurements.
- Next, in section 2.5, we uncovered a new dynamical behavior in a QD VCSEL: a bistability between two limit cycles oscillating around two non-orthogonal elliptically polarized states symmetric with respect to the linear polarization at threshold. The two cycles exhibit different amplitudes and frequencies hence providing a definitive proof that the two orientations are not equivalent. We then demonstrated that to reproduce this behavior in the spin-flip model (SFM) framework a slight misalignment between the phase and amplitude anisotropies is required. Hence, we provided the first experimental evidence of the existence of such anisotropy misalignment in VCSELs.

- Last but not least, we confirmed the validity of the SFM as a unifying framework to describe the polarization dynamics of VCSELs. We showed that all experimental observations reported so far can be accurately reproduced within the SFM framework including the limit cycle bistability reported in section 2.5 and the polarization chaos in a free-running VCSEL as shown in section 2.3.

Part of the work presented in this chapter has been published in [123–129].

Then, in chapter 3, we studied the feasibility of an optical random bit generator based on polarization chaos from a free-running laser diode:

- We successfully made a proof-of-concept for a competitive and highly simplified - i.e. without the need for optical injection or feedback - random bit generator scheme based on polarization chaos. We generated random bit sequences at competitive bitrates (> 100 Gbps) without complex and/or unconventional post-processing methods. All the obtained sequences passed the standard statistical tests of randomness. Using more demanding high-order derivative techniques, we successfully generated sequences that passed the statistical tests for bitrates up to 560 Gbps. In addition, due to its enhanced simplicity and the use of small bandwidth electronic equipment, the proposed scheme shows a great potential for parallelization and integration.
- By providing a clear counter example, we demonstrated that the commonly accepted requirements on the dynamics for chaos-based random bit generation at high-speed - typically large and flat radio-frequency bandwidth and fast autocorrelation decay - are biased and cannot be generalized to all systems. Indeed, despite not ideal dynamical features - in particular a small radio-frequency bandwidth -, we successfully achieved competitive performances, comparable or even higher than those of some other systems showing a much better match to the accepted requirements.
- We theoretically linked the achieved performances to the intrinsic features of polarization chaos dynamics. By analyzing the entropy growth of the system, we highlighted the crucial role played by the low-pass filtering induced by the limited bandwidth of the acquisition electronics. We showed that the randomness of the dynamics mostly appears in the slower mode-hopping dynamics, i.e. the jumps between the two wings of the attractor. Filtering the fast correlated oscillations - i.e. the oscillations on the wings of the attractor around an unstable elliptically polarized state - therefore allows us to keep only the most random part of the dynamics. Thus, combined with a large value of the largest Lyapunov exponent, extremely

short memory times could be achieved in our system resulting in the fast random bit generation.

Part of the work presented in this chapter has been published in [142, 143].

Finally, in chapter 4, we investigated the impact of a time-delayed optical feedback on the nonlinear dynamics of quantum dot lasers emitting simultaneously from the ground (GS) and the excited states (ES):

- First, we theoretically showed that the optical feedback can be exploited to select the laser output, between GS or ES emission. We uncovered a bistability, between a GS and an ES emission steady-states with similar output powers, connected through an hysteresis cycle for varying feedback rates. As a result, the control of the feedback rate alone appeared to be potentially sufficient to control the laser output. In addition, we reported that, overall, the optical feedback favored the ground state emission. As a result, independently of the free-running behavior of the laser, a sufficiently strong feedback always triggered the GS emission, and eventually led to complete extinction of the ES mode.
- Secondly, we reported a strong impact of the feedback phase on the uncovered GS-ES switching dynamics. We demonstrated that the switching dynamics is strongly related to the respective frequency shifts of the GS and ES modes induced by the optical feedback. Because of the large frequency separation between GS and ES emission, the evolution of these frequency shifts, which directly relate to the feedback phase, was dramatically different. As a result, for varying time-delays, we observed a periodic recurrence of switchings between GS and ES emissions at a period related to the optical wavelength of the laser.
- Finally, we unveiled preliminary experimental evidence supporting our theoretical findings. Despite that the investigated laser emitted only from the ES, we found that the optical feedback could easily trigger the GS emission. We reported a strong decrease of the GS emission threshold for increasing feedback strengths, while the ES emission threshold was almost left unchanged. Last, we observed incomplete switchings between GS and ES emission for variations of the external cavity round-trip length at the scale of the optical wavelength. All these results are in good agreement with the conclusions of our theoretical work.

Part of the work presented in this chapter has been published in [183–185].

5.2 PERSPECTIVES FOR FUTURE WORK

Based on the work described in this thesis along with the main achievements summarized above, we can draw some interesting perspectives for future work.

Regarding the nonlinear polarization dynamics in vertical-cavity surface-emitting lasers, the discovery of polarization chaos, generated in a free-running device, of course motivates further investigations.

The most straightforward perspective is obviously a detailed experimental and theoretical investigation of this new dynamics. In particular, it would be of interest to analyze the impact of the cavity anisotropies on the dynamics uncovered (polarization chaos, limit cycle bistability): theoretically, considering both the phase and amplitude anisotropy with an eventual misalignment, and experimentally, by putting additional strains on the device as described in [38, 39]. Furthermore, several predictions have been made using optical feedback or optical injection in the SFM framework [193, 194]; these predictions can now be tested experimentally.

Next, considering the simplicity of generating an optical chaos directly from a free-running device, another clear perspective is the exploitation of this dynamics for chaos-based applications. In chapter 3, we successfully demonstrated random bit generation at high-speed based on polarization chaos. Similarly, we obviously could think of using polarization chaos in secured chaos-based communication schemes, but some security issues (related to the low dimension of the dynamics or finite-time Lyapunov exponents) might need to be considered.

Finally, the discovery of a new dynamics combined with the validation of the SFM motivates the search for other dynamics that have been predicted theoretically but have never been observed experimentally. In particular, a cascade of three Hopf bifurcations and a bistability between linear and elliptical polarizations have been predicted in [75], but these behaviors have never been reported in an experiment.

Regarding the successful demonstration of a polarization chaos-based random bit generator, we can easily see two complementary directions for future work.

First, although good performances have been obtained, we believe that the dynamics and the scheme itself could be optimized to obtain a faster and more reliable random bit generator. Theoretically, we showed that the low-pass filtering of the acquisition electronics played a significant role for the randomness generation, and we linked this effect to the dynamical features of the chaotic attractor. Additional investigations are however still required to optimize both the filtering of the time-series and the random bit extraction process.

Secondly, the simplicity of the suggested scheme clearly paves the way toward its integration and heavy parallelization. A medium-term perspective would therefore be a feasibility study and eventually the development of integrated random bit generator prototypes. Obviously many questions need to be answered and hurdles to be overcome before, but such opportunity would definitely be of interest.

Finally, regarding the impact of optical feedback on the dynamics of quantum dot lasers emitting simultaneously from the ground and the excited states, at this point, the main perspectives are, to my point of view, two-fold.

On one hand, we obtained encouraging preliminary experimental results that motivate further in-depth experimental investigations and analysis of the laser dynamics. In particular, it would be of interest to check whether the other features reported theoretically such as the bistability between GS and ES emission steady-states can be obtained experimentally as well. Moreover many other configurations such as filtered optical feedback or feedback with different time-delays for the two modes remain to be investigated as they could provide additional insight and control of the system dynamics.

On the other hand, although the experimental observations support the main theoretical results, some details cannot be explained in the framework of the model used so far. Additional theoretical works are therefore required to explain these features. In particular, the model would need to be completed to take into account the multimode behavior of the laser to match the experimental features, but probably also the direct injection of carriers from the wetting layer to the ground state.



RÉSUMÉ EN FRANÇAIS

C'est totalement absurde les rappels.

Enfin, écoutez, dans la vie normale, dans la vie courante, quand un type a fini son boulot, qu'est-ce qu'il fait ? Il dit au revoir, et il s'en va. Voilà. Il ne revient pas : enfin, on n' imagine pas un plombier, par exemple, re-sonnant à la porte, après avoir réparé une fuite, juste pour refiler un petit coup de clé de douze.

— Pierre Desproges

Le travail décrit dans ce manuscrit a été réalisé dans le cadre d'une cotutelle de thèse entre Supelec en France et la Vrije Universiteit Brussel en Belgique. L'anglais a naturellement été la langue de travail ainsi que la langue utilisée pour la rédaction et la défense de cette thèse de doctorat.

Par conséquent, ce chapitre a pour but de résumer, en français, la démarche et les résultats du travail effectué et décrit précédemment en anglais. Ce résumé sera donc organisé comme suit. Une brève introduction décrivant le contexte et les objectifs des travaux réalisés est donnée en section A.1. En section A.2, nous présentons l'étude de la dynamique induite par la compétition de différents modes de polarisation dans une diode laser nanostructurée de type VCSEL en configuration "free-running", c'est-à-dire sans perturbation externe. Nous décrivons notamment une nouvelle dynamique chaotique, découvrant ainsi le premier chaos temporel déterministe dans une diode laser monomode et isolée. Nous démontrons ensuite en section A.3 que cette dynamique peut être exploitée pour générer à grande vitesse des séquences de nombres aléatoires. Après cela, nous abordons un autre système en section A.4 et étudions l'impact d'une rétroaction optique sur une diode laser nanostructurée émettant simultanément depuis l'état fondamental et le premier état excité. Finalement, nous résumons les principales avancées de ces travaux et concluons en section A.5.

A.1 INTRODUCTION

Les lasers sont au coeur des systèmes photoniques et sont ainsi utilisés pour des applications diverses et variées comme la chirurgie, les identifications médico-légales, l'imagerie 3D ou encore des applications de métrologie ou militaire. Cependant le domaine des télécommunications est probablement celui où les lasers ont eu l'impact le plus grand sur notre vie de tous les jours. En effet, combinés avec les fibres optiques, ils nous ont permis de mettre en place des systèmes d'échange de données ultra rapides et efficaces sur de longues distances. Les performances des systèmes optiques sont si bonnes, que les systèmes électroniques ne sont maintenus que pour des raisons de coût sur des distances relativement courtes - par exemple les réseaux locaux ou métropolitains -, même si la photonique est aussi en train de prendre le pas pour les très courtes distances. Ainsi au niveau des interconnexions informatiques, l'électronique représente maintenant une limitation, par exemple pour les "data-centers", particulièrement en terme de chaleur dégagée et d'efficacité énergétique, alors que les nouveaux concepts d'interconnexions introduits par la photonique sur silicium montrent d'excellentes performances. Le point commun de tous ces systèmes est finalement qu'un laser est requis pour produire le faisceau lumineux qui transportera l'information. Considérant les fortes contraintes des applications citées ci-dessus - en taille, coût et efficacité - les lasers à semiconducteurs (ou diodes lasers) sont rapidement apparus comme le choix le plus pertinent: ils sont de petite taille, alimentés électriquement, très efficaces et relativement peu chers. Néanmoins, la forte croissance de la quantité de données échangées sur internet pousse l'ensemble des sous-systèmes à la limite de leurs performances, motivant ainsi l'amélioration de tous les composants utilisés. Cela inclus évidemment les diodes lasers pour lesquels une attention tout particulière est nécessaire compte tenu de leur comportement dynamique complexe.

Au premier abord, les lasers peuvent ressembler à des ampoules un peu particulières, mais le principe physique sur lequel ils reposent - c'est-à-dire l'émission stimulée de radiations - en fait intrinsèquement des composants dynamiques. Généralement on s'attend à ce que les lasers à semiconducteurs réagissent comme des oscillateurs nonlinéaires amortis: lorsqu'ils sont soumis à un échelon de courant, ils vont osciller vers un point fixe stable, c'est-à-dire vers un état d'émission stationnaire. Cependant, lorsqu'ils sont soumis à des perturbations, comme une modulation du courant d'injection, une injection optique ou une rétroaction à délai, les diodes lasers peuvent rapidement être déstabilisées et manifester un comportement dynamique, incluant notamment des comportements auto-pulsés ou chaotiques. La spécificité de ces comportements nécessite une approche différente du problème, orientée vers la dynamique nonlinéaire.

Le domaine de la dynamique nonlinéaire - c'est-à-dire l'étude des systèmes dynamiques nonlinéaires - a débuté avec l'observation du comportement de certains systèmes dynamiques (oscillateurs, pendules) ainsi que des objets astronomiques (mouvement des planètes), et a ainsi attiré l'attention de nombreux scientifiques comme Henri Poincaré au début du XX^{ème} siècle. Ce domaine a cependant été dramatiquement changé lorsqu'en 1963, Edward Lorenz mis en évidence un comportement apériodique et déterministe d'un système nonlinéaire lié à une extrême dépendance aux conditions initiales. La théorie du chaos a alors bouleversé l'approche des systèmes dynamiques complexes, et ainsi a largement contribué à améliorer notre compréhension et notre capacité à prédire et contrôler ces systèmes, incluant notamment les arythmies cardiaques ou les réseaux de neurones. En effet, puisque les concepts tels que le chaos ou les bifurcations sont généraux, la dynamique nonlinéaire est un domaine extrêmement interdisciplinaire avec de larges implications dans quasiment tous les domaines scientifiques.

Dans ce contexte, l'intérêt pour l'étude de la dynamique des lasers à semiconducteurs est triple: 1/ La compréhension des mécanismes nonlinéaires contrôlant la dynamique des diodes lasers permet d'identifier les propriétés essentielles et les limitations intrinsèques de ces composants. Considérant les relations largement nonlinéaires entre le comportement du laser et ses paramètres intrinsèques, les améliorations pratiques - comme par exemple l'augmentation de la bande passante en modulation - sont principalement des compromis entre différentes propriétés. Cela nécessite bien entendu des analyses poussées et une compréhension fine du système afin de pouvoir l'optimiser au mieux. 2/ L'étude de tels composants permet de découvrir des nouveaux comportements, et donne ainsi la possibilité de développer de nouvelles applications, par exemple les communications sécurisées par chaos optique ou la génération de nombres aléatoires. Tout particulièrement, de nombreuses analogies peuvent être faites et des applications peuvent être transposées, bénéficiant ainsi de la rapidité des lasers. 3/ Comme mentionné précédemment, les concepts de la dynamique nonlinéaire étant génériques, les systèmes lasers peuvent être vus comme un bac à sable nonlinéaire facile à utiliser et à analyser comparé à d'autres systèmes. Par exemple, l'étude de dynamiques particulières comme l'excitabilité - une propriété liée au comportement des neurones - est beaucoup plus facile à étudier dans les lasers plutôt qu'en utilisant des vrais neurones. L'étude de la dynamique nonlinéaire des lasers à semiconducteurs peut ainsi fournir des indications essentielles et interdisciplinaires sur les mécanismes dynamiques concernés.

Depuis la démonstration de la première diode laser en 1962, les lasers à semiconducteurs ont connu d'important changements et de nombreuses améliorations. Une des plus importantes a été l'introduction de puits quantiques - c'est-à-dire une couche de matériel semiconducteur suffisamment fine pour confiner les porteurs de charges dans son plan - en tant que milieu à gain. Cette innovation a permis d'obtenir des composants avec un

plus grand rendement, un gain plus large, un seuil plus faible et un élargissement de bande réduit. Il est alors assez naturel de s'attendre à ce qu'un confinement sur plusieurs dimensions conduise à des performances encore meilleures; c'est d'ailleurs ce qui a motivé la recherche de diodes lasers ultra-performantes utilisant des boîtes quantiques (ou quantum dots QDs) - c'est-à-dire des nanostructures de semiconducteurs dans lesquels les porteurs de charges sont confinés dans les 3 dimensions de l'espace. En théorie, les lasers à boîtes quantiques devaient montrer des performances proches du laser parfait. Mais, en pratique, les nombreuses difficultés de production et la complexité accrue des nanostructures réelles ont fortement ralenti leur développement. Aujourd'hui, la plupart de ces difficultés ont été surmontées et des performances prometteuses ont été obtenues. Toutefois, à cause de la complexité des boîtes quantiques font que beaucoup de spécificités de ces lasers restent à étudier pour bénéficier au maximum de ces composants innovants.

Dans cette thèse, nous étudions deux systèmes de diodes lasers nanostructurées dans lesquels on observe une compétition entre deux modes: 1/ un laser à cavité vertical émettant par la surface (vertical-cavity surface-emitting laser, VCSEL) dans lequel deux modes de polarisation peuvent entrer en compétition, 2/ un laser à boîte quantique émettant simultanément depuis l'état fondamental (ground state, GS) et le premier état excité (excited state, ES) soumis à une rétroaction optique à délai.

D'un côté, les lasers de type VCSEL sont connus pour souffrir d'instabilités en polarisation: à cause de leur géométrie circulaire, la sélection de la direction de polarisation se fait uniquement à partir des anisotropies de la cavité laser, mais ces dernières ne sont pas assez fortes pour fixer complètement la polarisation du faisceau laser. Ainsi, de nombreuses instabilités de polarisation ont été rapportées, éventuellement accompagnées par des dynamiques auto-pulsées. Récemment, un comportement surprenant a été observé dans un laser VCSEL à boîtes quantiques: l'évolution de la dynamique ne ressemble à aucun des comportements déjà observés et certaines propriétés semblent même être incompatibles avec celles-ci. En particulier un saut de mode apparemment aléatoire entre deux modes de polarisation elliptiques non-orthogonaux a été observé. Statistiquement, l'évolution de cette dynamique est de plus opposée à celle observée jusqu'à maintenant dans le cas de VCSEL à puits quantiques. Ce comportement surprenant motive évidemment une analyse en profondeur du système afin de mettre en lumière les mécanismes sous-jacents et le potentiel de cette nouvelle dynamique.

D'un autre côté, dans un laser à boîtes quantiques, plusieurs niveaux d'énergies peuvent être confinés, ainsi dans des conditions adéquates, le laser peut émettre non seulement depuis l'état fondamental, mais aussi depuis un ou plusieurs états excités. Cette situation conduit typiquement le laser à émettre simultanément à deux fréquences distinctes et largement séparées. Cette propriété spécifique est intéressante, notamment pour la

génération de fréquences terahertz ou pour le traitement tout optique de signaux. Malheureusement le contrôle de cette émission à deux modes est difficile, et plusieurs études ont été menées avec des lasers à deux sections ou une injection optique. Alternativement, et malgré des résultats prometteurs, peu d'études se sont concentrés sur le potentiel d'une rétroaction optique à délai: aucune analyse en profondeur de l'impact d'une telle rétroaction sur ces lasers à deux modes n'a été effectuée. Des travaux supplémentaires sont donc requis pour clarifier cet impact et préciser les possibilités ouvertes par cette solution.

Pour résumer, cette thèse se concentre sur l'étude de la compétition entre deux modes dans les lasers à boîtes quantiques. Parce que ces comportements peuvent altérer les performances des composants de manière dramatique s'ils ne sont pas évités, mais aussi parce qu'ils peuvent potentiellement être exploités pour des nouvelles applications révolutionnaires, la dynamique nonlinéaire des lasers est un domaine d'étude essentiel pour s'assurer du bon fonctionnement des systèmes actuels et pour apporter de nouvelles innovations.

A.2 CHAOS EN POLARISATION DANS UN LASER VCSEL À BOITE QUANTIQUE

Dans cette première section, nous étudions le comportement d'un laser de type VCSEL dans lequel une compétition entre deux modes de polarisation conduit à l'émergence d'instabilités dynamiques. Les résultats de ces travaux ont été présentés en partie dans les publications suivantes: [123–129].

Typiquement, un VCSEL au seuil va émettre de la lumière polarisée linéairement, toutefois un changement de température ou de courant d'injection peut déstabiliser cet état. Le laser va alors commuter, après éventuellement diverses transitions dynamiques, vers un état où la lumière sera polarisée orthogonalement par rapport à la direction de polarisation au seuil: ce phénomène est appelé "polarization switching" (PS). Une récente description de l'état de l'art concernant ces comportements peut être trouvée dans la référence suivante: [30].

A cause de la biréfringence de la cavité laser, ces deux modes de polarisation n'ont pas exactement la même fréquence, on peut donc les identifier comme le mode basse fréquence (Low Frequency, LF) et haute fréquence (High Frequency, HF). Les PSs peuvent être classés en deux catégories [31] 1/ Type I: le laser commute de HF vers LF, 2/ Type II: le laser commute de LF vers HF. Cette classification est importante car les deux types de PS n'ont pas les mêmes caractéristiques. Le PS de type I a tendance à

être soudain: le laser change brusquement de mode de polarisation. Près de ce point de commutation, il est possible d'observer une région de bistabilité dans laquelle le bruit d'émission spontanée est suffisant pour faire sauter aléatoirement le laser d'un mode à l'autre. Cette dynamique stochastique a été identifiée comme étant similaire à celle d'une particule entre deux puits de potentiel séparés par une barrière de potentiel: c'est-à-dire un saut de mode de Kramers [47]. En particulier, le temps de résidence sur chaque mode - c'est-à-dire le temps entre deux sauts successifs - croît exponentiellement avec le courant d'injection. Dans le cas du PS de type II, la commutation entre les deux modes de polarisation n'est généralement pas soudaine mais accompagnée par une transition dynamique incluant notamment des états de polarisation elliptiques ainsi que des oscillations auto-pulsées à la fréquence de la biréfringence [51, 52].

Chaos en polarisation déterministe

Récemment, Olejniczak *et al.* ont mis en évidence un comportement surprenant dans un VCSEL à boîte quantique [53, 54]. Malgré certaines similitudes avec un PS de type II, notamment l'apparition d'états elliptiques et de dynamiques auto-pulsées, les auteurs ont mis en évidence plusieurs caractéristiques qui nécessitent une approche plus en profondeur. Outre le fait que les oscillations auto-pulsées apparaissent à la fréquence des oscillations de relaxation (au lieu de la fréquence de biréfringence), et que le laser n'atteint jamais l'état de polarisation orthogonale pour les courants les plus forts, les auteurs rapportent l'apparition d'un saut de mode aléatoire entre deux polarisations elliptiques particulièrement intrigant. Non seulement les deux états de polarisation sont non-orthogonaux et symétriques par rapport à la direction de polarisation au seuil (indiquant qu'il ne s'agit donc pas des deux modes LF et HF dégénérés), mais en plus, le temps de résidence moyen sur chaque état décroît exponentiellement lorsque le courant d'injection est augmenté - avec une échelle de temps de quelques secondes jusqu'à quelques nanosecondes. Cette évolution, opposée à celle d'un saut de mode stochastique - pour lequel la dynamique est uniquement induite par le bruit - et combinée à l'ensemble des indices décrits, justifie la recherche d'une interprétation alternative.

A partir du modèle spin-flip (SFM) considérant les processus de relaxation du spin des électrons dans la cavité laser [61, 70], nous avons mis en évidence un scénario de bifurcation montrant un bon accord avec les observations expérimentales, mais basé sur une interprétation purement déterministe de la dynamique, c'est-à-dire sans intervention du bruit. Dans le cadre du modèle spin-flip présenté en section 2.1 et avec les paramètres indiqués, le laser émet une lumière polarisée linéairement lorsqu'il est au seuil. Une augmentation du courant d'injection μ va cependant déstabiliser cet état stationnaire

par le biais d'une bifurcation de type pitchfork et créer deux états elliptiques représentés en Fig. A.1(a). On observe alors le scénario de bifurcation suivant: les deux états elliptiques sont déstabilisés par des bifurcations de Hopf qui créent deux cycles limites, voir Fig. A.1(b) - c'est-à-dire des solutions périodiques - qui vont osciller autour des deux états stationnaires maintenant instables. Une cascade de doublements de période va alors transformer chacun deux cycles en un attracteur chaotique, comme on peut le voir en Fig. A.1(c); attracteurs dont la taille augmente avec le courant d'injection. Par conséquent, au delà d'une valeur critique du courant, les deux attracteurs fusionnent et forment un unique attracteur à double enroulement qui ressemble au fameux attracteur de Lorenz [12]. En Fig. A.1(e) et (f), on montre les traces temporelles correspondant à cette dynamique - moyennées pour reproduire les effets d'une bande passante limitée comme pour les observations expérimentales - après projection sur l'axe de polarisation au seuil (0°), sur l'axe orthogonal (90°), ainsi que sur les projections à $\pm 45^\circ$ de la direction de polarisation au seuil. On observe alors que la dynamique du laser peut être vue comme un saut de mode entre deux états elliptiques symétriques par rapport à la direction de polarisation au seuil. De plus, nous avons aussi pu vérifier que les propriétés statistiques de cette dynamique, et notamment l'évolution du temps de résidence lorsque le courant augmente, sont en adéquation avec l'expérience. En simulation, nous avons ainsi pu obtenir une évolution décroissante du temps de résidence moyen allant de la microseconde à la nanoseconde.

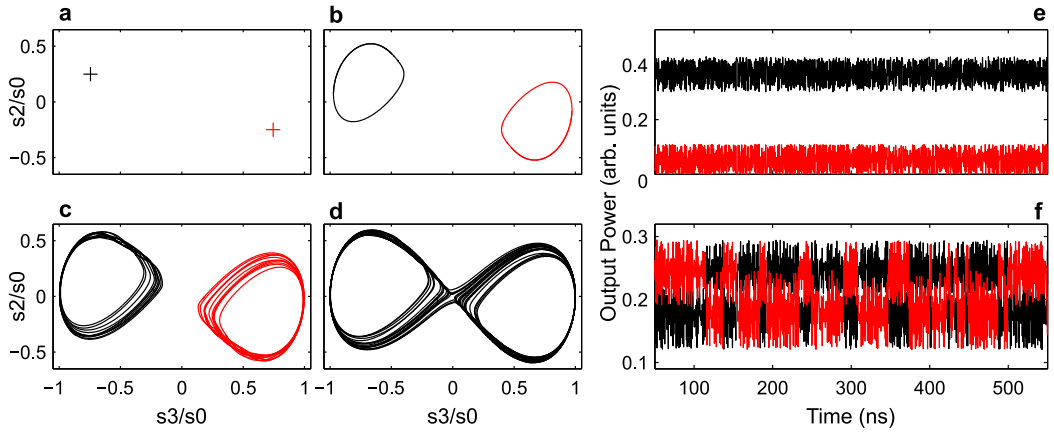


Figure A.1 – **Scénario conduisant au chaos en polarisation dans le modèle SFM.** Simulation de la trajectoire du système dans l'espace des paramètres de Stokes ($s_2/s_0, s_3/s_0$) lorsque le courant d'injection μ augmente. Pour les panneaux (a-d), les courants d'injections sont les suivants: (a) $\mu = 1.34$, (b) $\mu = 1.39$, (c) $\mu = 1.41$, et (d) $\mu = 1.425$. (e, f) Traces temporelles de la puissance de sortie du laser après projection sur un axe de polarisation: à 0° (noir) et 90° (rouge) pour (e), et à 45° (noir) et -45° (rouge) pour (f).

Nous avons donc théoriquement mis en évidence une dynamique chaotique montrant les mêmes caractéristiques que le saut de mode entre deux polarisations elliptiques et non-orthogonales découvert expérimentalement: aussi bien le scénario de bifurcation que l'évolution statistique sont en parfait accord avec les observations. Cependant, l'interprétation purement chaotique et déterministe présentée, est en contradiction avec le comportement typiquement attendu pour une diode laser, c'est-à-dire celui d'un oscillateur nonlinéaire amorti, ne pouvant pas devenir chaotique sans perturbation extérieure. Pour confirmer l'accord entre l'expérience et notre interprétation théorique, il est donc indispensable de démontrer expérimentalement que la dynamique observée est bien chaotique.

Identification expérimentale de la dynamique chaotique

Par définition, le chaos est une dynamique déterministe, apériodique et montrant une hyper-sensibilité aux conditions initiales du système: deux systèmes débutant avec des conditions initiales légèrement différentes (potentiellement indiscernables l'une de l'autre) vont, après un certain temps, montrer une évolution complètement différente. La divergence causée par la différence des conditions initiales est typiquement quantifiée par les exposants de Lyapunov, qui, s'ils sont de valeurs positives, caractérisent les systèmes chaotiques.

Pour démontrer qu'une dynamique est chaotique, il suffit donc potentiellement de prouver que le système a un exposant de Lyapunov positif. En pratique, même si l'on ne peut pas contrôler les conditions initiales du système, il est possible d'exploiter de longues traces temporelles afin d'estimer le plus grand exposant de Lyapunov. Ainsi, en utilisant l'algorithme de Wolf [131] décrit en section 2.4, on obtient un exposant positif avec une valeur de $\lambda_{\max} \approx 2 \text{ ns}^{-1}$.

Pour compléter ces résultats, nous avons aussi déterminé la valeur de l'entropie- K_2 ou entropie de Kolmogorov. Pour une dynamique organisée (périodique ou quasi-périodique) $K_2 = 0$, alors que pour une dynamique purement stochastique on obtient $K_2 = \infty$. Pour une dynamique chaotique, l'entropie- K_2 prend une valeur finie positive. Cette estimation peut être obtenue en utilisant l'algorithme de Grassberger-Procaccia (GP) qui dans le même temps, pour les dynamiques effectivement chaotiques, donne une estimation de la dimension de corrélation D_2 de l'attracteur chaotique. Les détails de l'algorithme sont fournis en section 2.4. En résumé, on calcule d'abord l'intégrale de corrélation $C_D(r)$ d'une trace temporelle X , c'est-à-dire le nombre moyen de vecteurs de taille D séparés par une distance inférieure à r . Pour un attracteur chaotique, on peut alors observer que

$C_D(r) \approx r^\nu \exp(-\tau D \kappa)$ avec τ le pas temporel de la trace, ν la dimension de corrélation et κ l'entropie de Kolmogorov. En pratique, en traçant l'évolution de l'intégrale de corrélation en fonction de r en échelle logarithmique ainsi que la pente de cette courbe on observe que pour un système chaotique la pente de l'intégrale de corrélation converge et nous donne ainsi une estimation de la dimension de corrélation D_2 .

Nous utilisons cette approche afin de confirmer la nature chaotique de la dynamique observée expérimentalement. Le montage expérimental est décrit en détail en section 2.4, et les composants utilisés sont des lasers VCSELs à boîtes quantiques similaire à ceux utilisé dans [54]. En Fig. A.2, on trace l'évolution de l'intégrale de corrélation ainsi que sa pente pour le chaos de Lorenz, le chaos en polarisation simulé à partir du modèle SFM et enfin pour les traces expérimentales. Dans les trois cas, on remarque une nette convergence de l'algorithme avec la formation d'un plateau indiqué par une ligne rouge en pointillé. Pour l'entropie- K_2 , on obtient les valeurs suivantes: $K_2 \approx 1.65$ pour le chaos de Lorenz, $K_2 \approx 2.5 \text{ ns}^{-1}$ pour le chaos en polarisation simulé et $K_2 \approx 7.1 \text{ ns}^{-1}$ pour les traces expérimentales. Enfin, on observe que dans les trois cas la dynamique obtenue est de faible dimension avec une dimension de corrélation proche de 2.

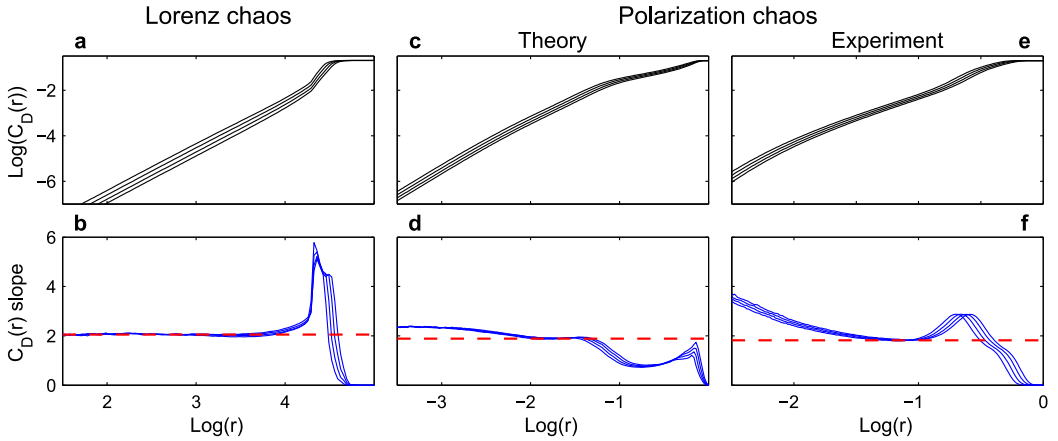


Figure A.2 – **Identification du comportement chaotique en utilisant l'algorithme de Grassberger-Procaccia.** Résultats de l'algorithme GP pour le chaos de Lorenz (a,b), les traces temporelles simulées du chaos en polarisation (c, d) et pour les données expérimentales (e,f). En haut, c'est-à-dire pour les panneaux (a), (c) et (e), on trace l'évolution de l'intégrale de corrélation $C_D(r)$ en fonction du rayon de la sphère r . En bas, pour (b), (d) et (f), on trace l'évolution de la dérivée de $C_D(r)$ en fonction du rayon de la sphère. Tous les tracés sont en échelle logarithmique. Les lignes rouges, horizontales en pointillé, donnent une estimation de la dimension de corrélation pour chacun des trois cas: le chaos de Lorenz $D_2 \approx 2.05$, la simulation du chaos en polarisation $D_2 \approx 1.89$ et les données expérimentales $D_2 \approx 1.82$.

Finalement, l'interprétation chaotique (et donc déterministe) de la dynamique de saut de mode entre deux états elliptiques non-orthogonaux est confirmée par l'ensemble des tests réalisés. Ces résultats soutiennent le très bon accord qualitatif obtenue entre la dynamique simulée et les observations expérimentales. Nous pouvons donc conclure avec un bon niveau de confiance, que pour la première fois, nous avons observé un chaos temporel produit par une diode laser isolée (c'est-à-dire sans perturbations externes) et avec un seul mode longitudinal.

Bistabilité de cycle limite

Avec les mêmes composants, juste avant l'émergence de la dynamique chaotique, nous avons aussi observé l'apparition d'une bistabilité entre deux cycles limites. L'originalité de cette dynamique étant accentuée par le fait que ces deux solutions périodiques oscillent autour de deux états elliptiques non-orthogonaux et ont donc des orientations de polarisation différentes comme indiqué en Fig. A.3(a). En observant cette bistabilité plus en détail, on remarque qu'en plus des différentes polarisations les deux cycles ont aussi des amplitudes différentes (voir Fig. A.3(b), (c) et (d)) et des fréquences différentes (voir Fig. A.3(e) et (f)).

Ces observations sont importantes, notamment car elles prouvent que les deux états elliptiques observés ne sont pas symétriques. En effet, avec le modèle SFM utilisé précédemment et présenté en section 2.1, les deux états de polarisation elliptiques sont strictement identiques malgré une inversion des polarisations circulaires droite et gauche. En particulier, le même scénario de bifurcation apparaît pour les deux modes. Dans ce cadre, il n'est donc pas possible d'obtenir deux cycles limites avec des amplitudes et des fréquences différentes.

En section 2.5, on démontre qu'un comportement similaire peut-être obtenu en introduisant une asymétrie entre les deux états de polarisation elliptiques. En pratique, la symétrie de la cavité peut être rompue en considérant un désalignement entre l'anisotropie en phase et celle en amplitude. De cette manière, l'un des deux états de polarisation elliptique subira toujours des pertes plus importantes que l'autre. Dans la même section, on montre qu'avec un angle minime entre les deux anisotropies ($\theta = -0.023$), un très bon accord avec les observations expérimentales peut être atteint.

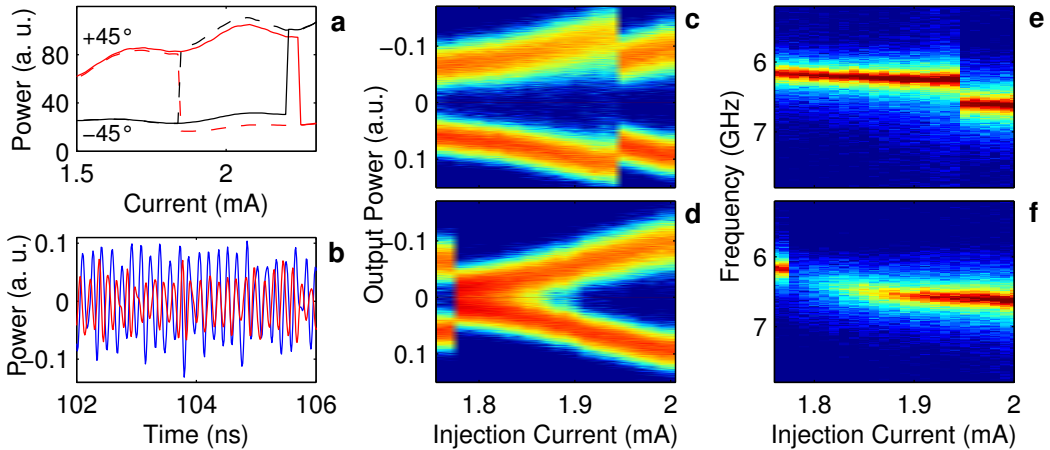


Figure A.3 – **Observation expérimentale de la bistabilité de cycles limites.** (a) Courbes PI résolues en polarisation à $+45^\circ$ et -45° par rapport à la polarisation linéaire au seuil: en rouge et noir pour les courants croissants (lignes continues) et décroissants (lignes en pointillés). (b) Traces temporelles mesurées expérimentalement pour un courant de 1.85 mA obtenues après augmentation (bleu) ou diminution (rouge) du courant. (c, d) Représentation des extrema des traces temporelles pour des courants croissants (haut, c) et décroissants (bas, d). (e, f) FFT des traces temporelles pour des courants croissants (haut, e) et décroissants (bas, f). Toutes les traces temporelles sont considérées après projection à 0° et après retrait de la composante continue du signal.

En résumé, nous avons montré qu'un laser de type VCSEL peut effectivement générer des fluctuations chaotiques grâce à la compétition des différents modes de polarisation. Cette nouvelle dynamique, avec l'observation d'une bistabilité originale entre deux cycles limites, nous a en outre permis de confirmer la validité du modèle SFM pour les lasers de type VCSEL.

A.3 GÉNÉRATION DE NOMBRES ALÉATOIRES À PARTIR DU CHAOS EN POLARISATION

La génération de nombres aléatoires est une étape cruciale pour un grand nombre d'applications, notamment pour les systèmes informatiques de sécurisation, d'authentification ou de cryptage. La rapidité et la qualité de ces séquences aléatoires est essentielle pour garantir la fiabilité de ces applications. D'un côté, la génération rapide de nombres aléatoires peut être réalisée à partir d'algorithmes informatiques. Les séquences obtenues ne sont cependant que pseudo-aléatoires et le déterminisme du système fait qu'elles peuvent être facilement reproduites si les paramètres sont découverts. D'un autre côté, la génération de séquences vraiment aléatoires (true random numbers) peut

être réalisée en utilisant des sources physiques d'entropie comme le bruit thermique d'une résistance. Bien que les séquences produites sont alors de très bonne qualité et ne peuvent absolument pas être reproduites, la vitesse de génération est généralement limitée à seulement quelques dizaines de Mbps (1 Mbps = 1 millions de bits par seconde). Récemment, l'exploitation de la dynamique de diodes lasers a été démontrée comme étant un moyen très efficace pour obtenir une grande vitesse de génération à partir d'une source physique d'entropie [11]. Bien entendu le chaos est un processus déterministe et non pas aléatoire, mais la dynamique peut amplifier les bruits intrinsèques du système chaotique permettant ainsi d'obtenir une source d'entropie rapide et fiable [166–168]. En profitant de la rapidité de la dynamique chaotique générée dans une diode laser, des vitesses de l'ordre de la dizaine de Gbps (1 Gbps = 1 milliards de bits par seconde) [158–160], et jusqu'à quelques centaine de Gbps ont été obtenues [157, 161–165]. Cependant, l'ensemble des systèmes proposés reposent sur l'utilisation de perturbations externes pour forcer la diode laser à générer un signal chaotique, c'est-à-dire sur des montages ou des designs relativement complexes impliquant des branches d'injection optique ou des boucles de rétroaction. La découverte du chaos en polarisation dans une diode laser solitaire, sans perturbation externe, pourrait donc permettre une large simplification de ces systèmes, et ainsi accélérer leurs développements.

Dans cette section, nous démontrons donc que le chaos en polarisation généré par une diode laser isolée, c'est-à-dire sans perturbation externe, est pertinente pour les applications exploitant le chaos optique; en particulier pour la génération de nombres aléatoires à grande vitesse.

Ces résultats ont déjà été publiés en partie dans les publications suivantes [142, 143].

Système physique, post-traitement et performances

Empiriquement, le lien entre certaines caractéristiques dynamiques et les performances d'un générateur de nombres aléatoires ont été mises en évidence. Ces besoins peuvent être résumés en 4 points:

- Un spectre radiofréquence (RF) large et plat pour obtenir une contribution fréquentielle proche d'un bruit blanc,
- Une décroissance rapide de l'autocorrélation,
- Une croissance rapide de l'entropie du système,
- De nombreux exposants de Lyapunov positifs en temps fini (finite-time Lyapunov exponents) afin d'assurer qu'à chaque instant il y ait toujours au moins un exposant de Lyapunov positif, c'est-à-dire que le système soit bien chaotique à chaque instant.

L'ensemble de ces exigences conduisent généralement à l'utilisation de dynamiques complexes à grande dimension et large bande-passante avec de nombreux exposants de Lyapunov positifs. En pratique, cela motive l'emploi de fortes rétroactions [172], qui conduisent typiquement à l'apparition d'hyper-chaos [135,179], c'est-à-dire une dynamique chaotique avec de nombreux exposants de Lyapunov positifs.

Malheureusement, comme détaillé en section 3.2, le chaos en polarisation généré dans une diode laser solitaire n'a pas toutes les qualités citées plus haut. En particulier, la dynamique est de dimension faible ($D_2 \approx 2$), donc un faible nombre d'exposants de Lyapunov, et une décroissance d'autocorrélation deux fois plus grande que celle mesurée dans d'autres systèmes (0.7 ns contre moins de 0.3 ns dans [11]). Cependant l'absence de rétroaction optique nous assure intrinsèquement qu'aucune corrélation n'existe au-delà d'une nanoseconde. A première vue, les propriétés de la dynamique chaotique décrite dans la section précédente ne semblent pas être optimales pour la génération de nombres aléatoires à grande vitesse.

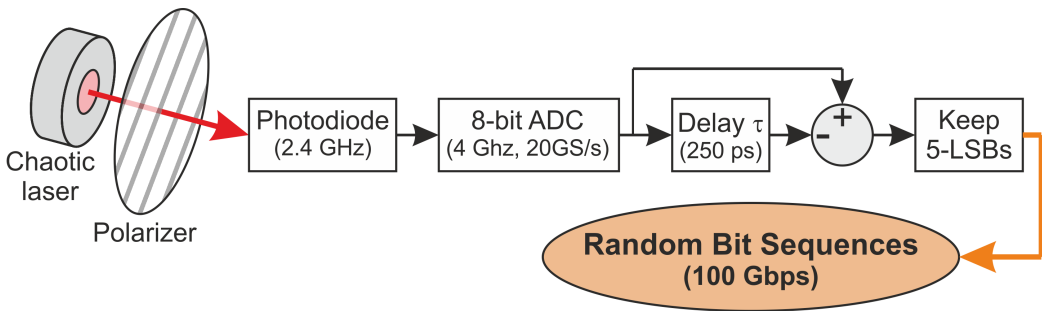


Figure A.4 – **Schéma du générateur de nombres aléatoires exploitant le chaos en polarisation.** Les fluctuations en polarisation du laser chaotique sont transformées en fluctuations d'intensité en utilisant un polariseur. On peut ensuite capturer l'évolution du signal avec une photodiode à petite bande-passante couplée à un convertisseur analogique-numérique de 8-bit. On compare alors la trace temporelle obtenue avec une version retardée d'elle-même. Enfin, les séquences de nombres aléatoires sont obtenues en ne gardant que les 5 bits les moins significatifs pour chaque point de la trace temporelle.

Afin de vérifier l'intérêt du chaos en polarisation pour les applications basées sur le chaos-optique et notamment pour la génération de nombres aléatoires, nous avons mis en place le montage expérimental décrit en Fig. A.4; le montage détaillé est présenté en section 3.2 et le post-traitement en section 3.3. Tout d'abord, les fluctuations chaotiques de polarisation sont converties en fluctuations d'intensité par le biais d'un polariseur orienté à 45° de la direction de polarisation au seuil. L'évolution de l'intensité est alors capté par une photodiode (2.4 GHz de bande passante) puis convertie en signal numérique codé sur 8 bit par l'ADC de l'oscilloscope (4 GHz de bande-passante, 20 GSamples/s).

En observant les traces temporelles obtenues et leurs histogrammes montrés en Fig. 3.2, il est clair que le signal chaotique ne peut pas être directement considéré comme étant aléatoire et ce malgré l'amplification des bruits intrinsèques du système. Une dernière étape de post-traitement est typiquement nécessaire afin d'éliminer tout biais et/ou corrélation résiduelle. Parmi les nombreuses méthodes utilisées par d'autres groupes, nous avons choisi d'effectuer une comparaison entre la trace temporelle et une version retardée d'elle-même, combinée avec une sélection des bits de poids faible pour chaque point de mesure [157, 160].

Pour vérifier si la séquence finale obtenue peut en effet être considérée comme aléatoire, nous utilisons deux batteries de tests standard: la NIST Statistical test suite [180] et la DieHard test suite [181]. A partir de ces deux batteries de tests, nous avons ainsi pu vérifier qu'avec un taux d'échantillonnage de 20 GS/s, un délai de $\tau = 250$ ps pour le post-traitement, nous pouvons garder les 5 bits de poids le plus faible pour chaque point de mesure, c'est-à-dire une vitesse de génération de $20 \text{ GS/s} \times 5 \text{ bits} = 100 \text{ Gbps}$. Les résultats des tests sont donnés en section 3.3 dans les tableaux 3.1 et 3.2.

De manière similaire, nous avons pu vérifier qu'en cascader plusieurs comparaisons de la trace temporelle chaotique obtenue, il était possible de garder plus de bits pour chaque point de mesure tout en passant avec succès les tests NIST et dieHard [160, 162]. Nous avons ainsi pu garder jusqu'à 28 bits en utilisant 23 comparaisons en cascade, obtenant ainsi une vitesse de génération jusqu'à 560 Gbps.

Evolution de l'entropie et impact du filtrage

Pour mieux comprendre l'origine de ces performances très compétitives, malgré des caractéristiques dynamiques apparemment peu optimales pour la génération de nombres aléatoires, nous nous intéressons théoriquement à la croissance de l'entropie du système pour le chaos en polarisation, de façon similaire au travail présenté dans [176]. On s'intéresse en particulier à l'impact du filtrage passe-bas du signal induit par la bande-passante limitée de la photodiode utilisée.

Dans cette section, on utilise à nouveau le modèle SFM, avec des paramètres qui permettent d'avoir une dynamique similaire à celle observée expérimentalement (avec un temps de résidence moyen et une fréquence des oscillations similaire). Les détails de la simulation et du calcul de l'entropie 1-bit sont donnés en section 3.4. En Fig. A.5(a), on trace l'évolution de l'entropie pour différents niveaux de bruit avec et sans filtrage passe-bas. En définissant le temps de mémoire du système comme étant la durée nécessaire pour que l'entropie du système atteigne 0.995, on observe clairement que le filtrage

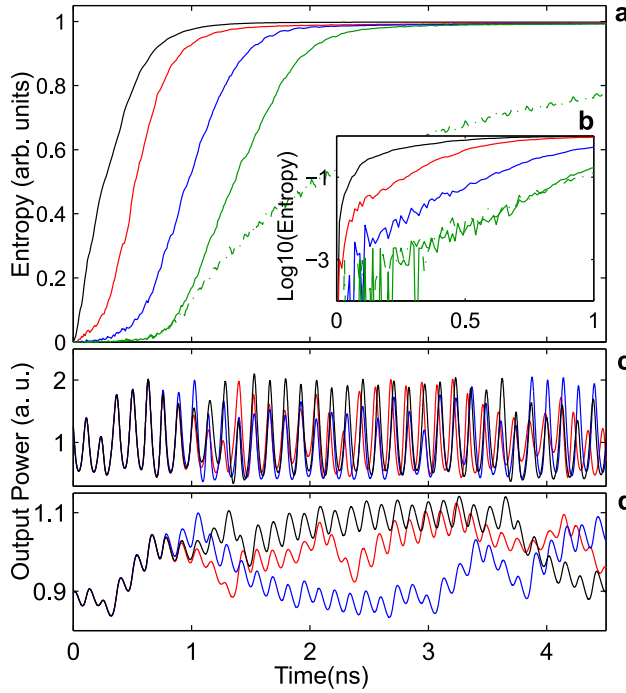


Figure A.5 – **Evolution de l'entropie du chaos en polarisation pour différents niveaux de bruit.** (a) Les lignes noires, rouges, bleues et vertes donnent l'évolution de l'entropie pour des niveaux de bruit de -30, -40, -50 et -60 dB respectivement. La courbe pleine et la courbe en pointillé montrent l'évolution pour le cas filtré et non filtré respectivement. (b) est identique à (a) mais avec une échelle logarithmique pour l'entropie. (c) et (d) montrent un exemple de séparation des traces temporelles pour 3 systèmes différents, avec un bruit de -60 dB, avec (c) et sans filtrage temporel (d).

réduit dramatiquement la mémoire du système: voir la différence de progression entre les deux courbes vertes en Fig. A.5. On remarque cependant que cet effet n'apparaît que lorsque l'entropie atteint des valeurs de l'ordre de 0.1. Comme on peut le voir sur la Fig. A.5(b) en échelle logarithmique, pour les faibles valeurs d'entropie, l'évolution est exponentielle avec un coefficient apparemment similaire quel que soit le niveau de bruit. En utilisant l'algorithme de Shimada pour déterminer la valeur du plus grand exposant de Lyapunov $\lambda_{\max} \approx 7 \text{ ns}^{-1}$, on s'aperçoit que cette valeur est très proche de la pente des courbes tracées en Fig. A.5(b). Finalement, on trace en Fig. A.5(c) et (d) l'évolution de trois systèmes, partant avec les mêmes conditions initiales, mais avec 3 séquences de bruit différent avant (c) et après filtrage passe-bas (d). Il est alors clair que le filtrage passe bas permet de s'affranchir des oscillations rapides de la dynamique (correspondant aux oscillations autour d'un des deux états elliptiques) qui sont fortement corrélées. Alors que sans filtrage l'évolution des trois systèmes semble être très corrélée

et relativement difficile à distinguer, après filtrage passe-bas, les trois traces temporelles sont parfaitement séparés et peuvent être aisément distingués les uns des autres. La suppression des oscillations rapides et fortement corrélées permet en somme d'avoir un premier niveau de post-traitement particulièrement efficace.

Finalement, en observant la croissance de l'entropie du système, nous avons pu mettre en évidence le lien intrinsèque entre le filtrage passe-bas induit par la bande-passante limitée de la photodiode utilisé et les performances obtenues dans la génération de signaux aléatoires. Ce filtrage apparaît donc comme une étape essentielle de notre système. Ce résultat va cependant à l'encontre des approches généralement considérés pour les autres systèmes, à savoir l'augmentation de la bande passant RF du signal obtenue.

Malgré les doutes liés aux caractéristiques potentiellement non-optimales du chaos en polarisation, notre travail confirme la pertinence de cette dynamique pour les applications basées sur le chaos optique et en particulier pour la génération de nombres aléatoires à grande vitesse. De plus, l'analyse théorique de l'évolution de l'entropie du système montre l'importance du filtrage passe-bas induit par la bande passante limitée (2.4 GHz) de la photodiode utilisée. Notre travail met donc en lumière une situation plus complexe que celle suggérée par les besoins observés empiriquement jusqu'à maintenant. Notre travail montre aussi l'importance de la structure de l'attracteur chaotique.

A.4 RÉTROACTION OPTIQUE SUR UN LASER À BOITE QUANTIQUE À DEUX COULEURS

Nous nous intéressons maintenant au second système considéré dans ce manuscrit : les lasers à boîtes quantiques à deux couleurs avec une rétroaction optique à délai. Dans une boîte quantique, plusieurs niveaux d'énergie excités (excited state, ES) peuvent être confinés en plus du niveau fondamental (ground state, GS). Ainsi, sous certaines conditions, le laser peut émettre des radiations simultanément depuis l'état fondamental et un (voire plusieurs) état excité [106]. Ces deux émissions ont des fréquences largement différentes, de l'ordre du terahertz, ce qui a suscité un large intérêt pour ces systèmes notamment dans le cadre de la génération de radiations aux fréquences terahertz [109–111], le verrouillage de mode à deux couleurs [112, 113], ou encore pour le traitement tout optique de l'information [120].

Cependant le contrôle de la puissance de sortie de chaque mode est un problème complexe. Ainsi plusieurs études ont montré qu'une rétroaction optique pouvait déclencher l'émission depuis le niveau d'énergie fondamentale [110], ou encore des fluctuations basses fréquences en antiphase [121]. Néanmoins, aucune analyse détaillée des bifurcations et des mécanismes sous-jacents n'a été effectuée jusqu'à maintenant.

Dans cette section, nous abordons donc cette problématique théoriquement et expérimentalement afin de mettre en lumière l'impact d'une rétroaction optique à délai sur les lasers à boîte quantique à deux modes.

Les résultats de cette étude ont déjà été en partie publiés dans [183–185].

Switching entre émission depuis l'état fondamental et depuis l'état excité

A partir du modèle théorique développé dans [115, 121], nous avons tout d'abord identifié et développé semi-analytiquement les expressions des quatre états stationnaires du système. Cela nous a permis de montrer que, lorsque le laser émet simultanément depuis les GS et ES, les états stationnaires sont connectés par le biais de bifurcations transcritiques; les détails sont donnés en sections 4.2 et 4.3. Ces résultats confirment et complètent les résultats obtenus par d'autres équipes [190, 191].

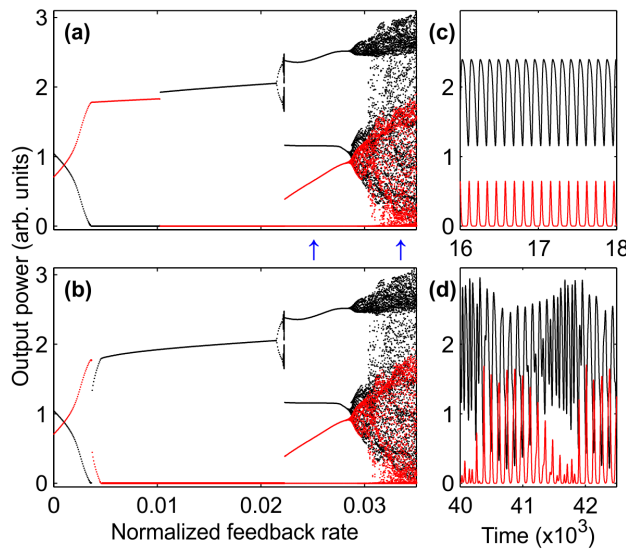


Figure A.6 – **Diagramme de bifurcation pour $J = 5$, obtenu par intégration numérique.** (a-b) Diagramme de bifurcation: extrema des traces temporelles en intensité pour un taux de feedback croissant (a) et décroissant (b), pour un courant d'injection de $J = 5$. Les points noirs (rouges) représentent l'émission de GS (ES). (c-d) Traces temporelles en intensité pour des taux de feedback de $\kappa = 0.025$ (c) et $\kappa = 0.033$ (d). Les deux flèches bleues indiquent la position de ces traces temporelles dans le diagramme de bifurcation.

Ensuite, nous avons montré qu'une rétroaction optique pouvait induire un switching entre GS et ES indépendamment de l'état d'émission du laser sans rétroaction: c'est-à-dire que si le laser émet depuis GS sans rétroaction, il est possible de le forcer à émettre uniquement depuis ES avec une rétroaction, et inversement. De plus, on observe dans certain cas, une bistabilité entre deux états d'émission depuis GS et ES avec une extinction complète de l'autre mode. En Fig. A.6, on trace le diagramme de bifurcation pour un taux de feedback croissant (a) et décroissant (b). On observe ainsi que sans rétroaction le laser émet simultanément depuis GS et ES, mais une augmentation du taux de rétroaction force le laser à émettre uniquement depuis ES à partir de $\kappa \approx 0.005$. Cependant, si le taux de rétroaction est augmenté au-delà de $\kappa > 0.01$, le laser commute soudainement vers une émission depuis GS uniquement. A partir de ce point, une diminution de la rétroaction dévoile une zone de bistabilité entre les deux modes d'émission. Il est à noter de plus que la puissance d'émission est similaire pour les deux fréquences. Enfin, pour des fortes rétroactions, le laser évolue vers des dynamiques anti-corrélées entre GS et ES, mais toujours avec une émission dominante de GS, comme on peut le voir en Fig. A.6(c) et (d).

Enfin, notre travail confirme aussi la tendance générale de la rétroaction optique à favoriser l'émission depuis l'état fondamental. En effet, indépendamment de l'état d'émission du laser, une forte rétroaction conduit globalement au déclenchement et à l'augmentation de la puissance d'émission depuis GS, et éventuellement jusqu'à l'extinction de l'émission depuis ES.

Impact de la phase de la rétroaction

Nous avons ensuite complété ces travaux, en s'intéressant à l'impact d'un changement du délai de la rétroaction optique. Nous avons ainsi pu mettre en évidence l'importance de la phase de la rétroaction: en effet les deux fréquences d'émission étant largement séparées, l'évolution de la phase de la rétroaction va être très différente pour chaque mode.

Par une analyse semi-analytique du système, nous avons pu montrer que la phase de la rétroaction est un facteur essentiel du comportement du laser. Ainsi, comme indiqué en Fig. A.7, le système va évoluer de manière plus ou moins répétitive avec une période proche de la longueur d'onde moyenne du système (entre les longueurs d'onde de GS et ES). La dynamique du système peut alors se résumer à deux régimes distincts en fonction du délai de la rétroaction: 1/ Dans le premier régime, par exemple autour de $\tau = 100$, l'émission depuis GS au seuil est rapidement déstabilisé par la rétroaction

optique. 2/ A l'inverse, dans le second cas par exemple autour de $\tau = 99.996$, l'émission depuis GS est favorisée. On remarque notamment que le seuil d'émission depuis ES augmente avec la force de la rétroaction optique. Avec la même approche, nous avons aussi pu constater qu'une évolution similaire apparaît dans des lasers émettant uniquement depuis ES directement au seuil sans rétroaction.

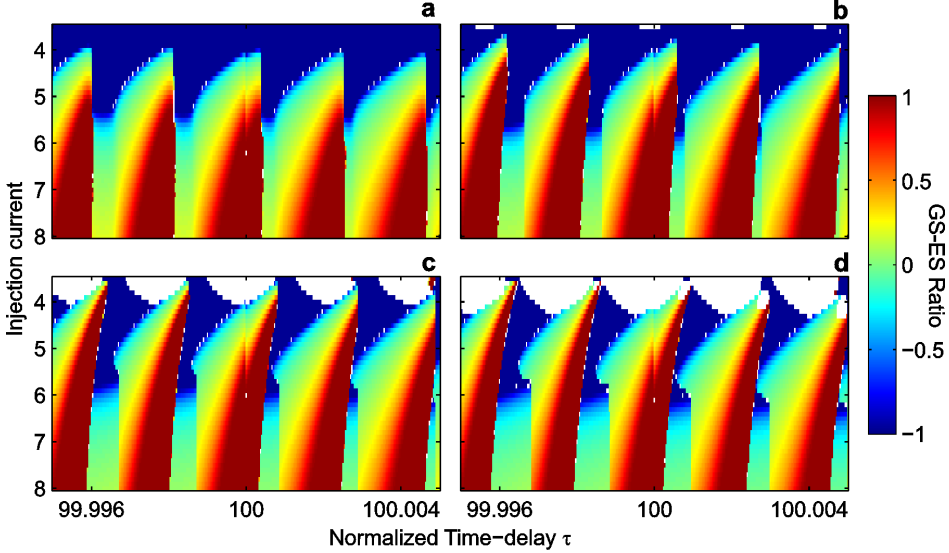


Figure A.7 – **Evolution du switching lorsque l'effet de la phase de la rétroaction est pris en compte.** On indique l'évolution des états stationnaires du système en fonction du délai pour 4 différentes valeurs du taux de feedback: (a) $\kappa = 0.004$, (b) $\kappa = 0.006$, (c) $\kappa = 0.008$ et (d) $\kappa = 0.010$. Le code couleur est le suivant: émission par GS (ES) est indiqué en bleu (rouge) et les couleurs intermédiaires donnent le ratio entre les puissances des deux modes en cas d'émission simultanée. Les zones blanches indiquent un comportement dynamique.

Observation expérimentales

Finalement, nous avons étudié expérimentalement l'impact d'une rétroaction optique sur un laser à boîte quantique à deux couleurs. Ce travail a été réalisé en collaboration avec Stefan Breuer de la Technische Universität Darmstadt où le montage expérimental a été réalisé. Nous avons ainsi pu observer l'impact d'une modification de la taille de la cavité externe, à l'échelle du micromètre, sur les propriétés d'émission d'un laser à deux couleurs avec une rétroaction optique. Les détails de l'expérience réalisée sont donnés en section 4.6.

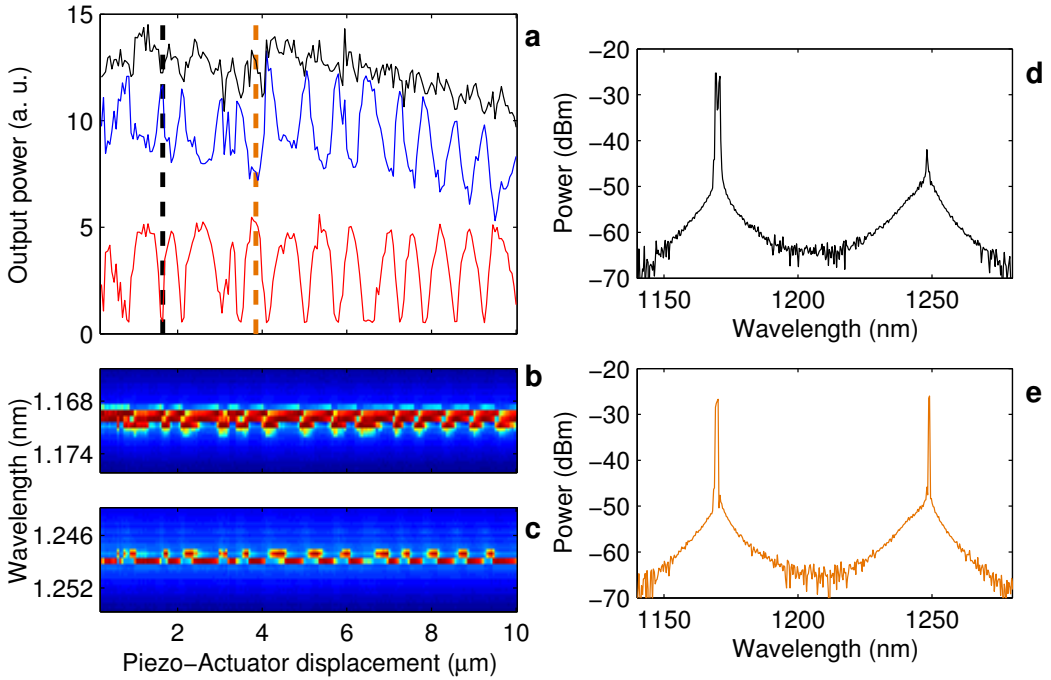


Figure A.8 – **Evolution anti-corrélée des émissions de l'état GS et ES lorsque la taille de la cavité externe est modifiée.** Observations expérimentales d'un switching incomplet pour un courant de $J = 50$ mA, et une réflectivité du miroir externe d'environ 3%. (a) L'évolution de la puissance d'émission de l'état GS (ES) est tracée en rouge (bleu), tandis que la puissance émise totale est tracée en noir. Les deux lignes verticales indiquent pour quel déplacement de l'actuateur piezo les deux spectres tracés dans les panneaux (d, noir) et (e, orange) ont été mesurés. (b) et (c) donnent l'évolution du spectre optique pour les émissions de l'état GS et ES respectivement. (d) et (e) montrent le spectre optique pour deux différentes positions du miroir externe avec et sans émission depuis l'état fondamental GS.

En Fig. A.8, nous montrons les résultats expérimentaux obtenus. Sur le panneau (a), on trace l'évolution de la puissance de sortie du laser pour GS (en rouge) et ES (en bleu) lorsque la taille de la cavité externe est modifiée. On observe ainsi l'apparition de commutations partielles entre une émission uniquement depuis ES, et une émission simultanée (GS-ES). Ces commutations incomplètes sont répétitives et apparaissent avec une période qui correspond grossièrement à la longueur d'onde des radiations ($\approx 1.2 \mu\text{m}$). L'évolution du spectre optique pour l'émission depuis ES et GS est donné sur les panneaux (b) et (c) respectivement. On peut alors remarquer que les commutations partielles entre les deux modes s'accompagnent d'une variation de la fréquence optique de ces deux modes. Enfin, deux spectres optiques sont tracés sur les panneaux (d) et (e) lorsque l'émission depuis le GS est éteinte et active respectivement.

Théoriquement, un comportement similaire avec des commutations partielles peut être reproduit par simulation en utilisant la même approche que celle utilisée dans la partie précédente. Même si certaines caractéristiques restent à détailler, il est cependant clair que ces observations expérimentales soutiennent les résultats théoriques décrits plus haut.

A.5 CONCLUSION

En résumé, ce travail de thèse a permis de mettre en évidence de nouveaux comportements des lasers à boîtes quantiques. Pour un laser de type VCSEL, nous avons démontré en particulier que, contrairement à ce qui peut être attendu d'une diode laser, ces composants peuvent générer des fluctuations chaotiques sans perturbation externe. Au delà de l'excellent accord observé entre les observations expérimentales et le scénario de bifurcation théorique, le caractère déterministe et chaotique du saut de mode entre deux modes elliptiques non-orthogonaux a été confirmé expérimentalement par différentes approches qui ont toutes donné des résultats positifs. Cette nouvelle dynamique nous a de plus permis de confirmer la validité et la pertinence du modèle spin-flip (SFM) pour modéliser le comportement des VCSELs; Résultats complétés par l'observation d'une bistabilité de cycle limite pouvant être efficacement reproduite en prenant en compte un désalignement des anisotropies de la cavité laser.

Ensuite, considérant le fort potentiel d'une telle dynamique chaotique, générée directement par une diode laser, pour les applications basées sur le chaos optique, nous avons assemblé un générateur de nombres aléatoires ultra-rapide. Malgré la faible complexité et la bande passante étroite du chaos en polarisation, nous avons réussi à générer des séquences de nombres aléatoires à des vitesses extrêmement compétitives (> 100 Gbps) sans post-traitement inhabituel ou particulièrement complexe. Ce résultat nous a ainsi permis de démontrer la pertinence du chaos en polarisation pour les applications de chaos optique.

Enfin, nos travaux sur les lasers à boîtes quantiques à deux couleurs et soumis à une rétroaction optique à délai ont permis de mettre en évidence plusieurs points essentiels. Nous avons montré qu'une rétroaction optique permet de contrôler l'état d'émission du laser, avec potentiellement une extinction complète de l'un ou l'autre mode uniquement par le biais de la rétroaction optique. Nous avons aussi souligné l'impact majeur de la phase de la rétroaction, c'est-à-dire de la longueur de la cavité externe. En effet, le comportement du laser est fortement impacté par un changement du délai de

la rétroaction, et on observe une évolution répétitive avec une période proche de la longueur d'onde moyenne du laser. Enfin, nous avons observé expérimentalement des commutations répétitives à l'échelle du micromètre. Ces observations sont cohérentes avec les résultats théoriques obtenus et supporte l'interprétation théorique décrite dans ce manuscrit.

Pour conclure, nos travaux ont mis en lumière de nombreuses dynamiques nouvelles et ouvert des perspectives intéressantes: notamment la possibilité de réaliser des générateurs de nombres aléatoires ultra-rapide sur puce ou des communications sécurisés par chaos à partir d'une simple diode laser. Notre étude de l'impact d'un laser à deux couleurs soumis à une rétroaction optique à délai a montré des résultats prometteurs qui motivent la poursuite de notre étude.

B

LINEARIZATION OF THE SFM

In this appendix, we give the detail of the linearization of the spin-flip model used in this thesis. The detail of the linearization around a stationnary solution is essential especially for the use of continuation techniques with the DDE-BIFTOOL toolbox [130] along with the derivation with respect to other parameters.

The SFM equations reduced to 5 real equations, as described in section 2.1, read as follows:

$$\frac{dR_+}{dt} = \kappa(N + n - 1)R_+ - (\gamma_a \cos(\Phi) + \gamma_p \sin(\Phi)) R_- \quad (B.1)$$

$$\frac{dR_-}{dt} = \kappa(N - n - 1)R_- - (\gamma_a \cos(\Phi) - \gamma_p \sin(\Phi)) R_+ \quad (B.2)$$

$$\frac{d\Phi}{dt} = 2\kappa\alpha n - \left(\frac{R_-}{R_+} - \frac{R_+}{R_-}\right) \gamma_p \cos(\Phi) + \left(\frac{R_-}{R_+} + \frac{R_+}{R_-}\right) \gamma_a \sin(\Phi) \quad (B.3)$$

$$\frac{dN}{dt} = -\gamma \left(N - \mu + (N + n)|E_+|^2 + (N - n)|E_-|^2 \right) \quad (B.4)$$

$$\frac{dn}{dt} = -\gamma_s n - \gamma \left((N + n)|E_+|^2 - (N - n)|E_-|^2 \right) \quad (B.5)$$

Considering a steady-state solution $X = (R_+, R_-, \Phi, N, n)$ of the SFM equations F and a tiny perturbation δX around X , the nonlinear equations can be developed to a first order taylor serie. Considering that X is a solution of the equation (hence $dX/dt = F(X) = 0$), we obtain the following equation:

$$\frac{d(\delta X)}{dt} = \left. \frac{dF}{dX} \right|_X \delta X \quad (B.6)$$

The eigenvalues of the linear system dF/dX can then provide the stability information of solution X . In practice, the linear equations can be calculated by concatenating the derivatives for each variable, i.e. each column of the matrix corresponds to the derivative of F with respect to one variable. For the SFM, those read as follows:

$$\frac{\partial F}{\partial R_+} = \begin{pmatrix} \kappa(N+n-1) \\ -\gamma_a \cos(\Phi) + \gamma_p \sin(\Phi) \\ \gamma_p \cos(\Phi) \left(\frac{R_-}{R_+^2} + \frac{1}{R_-} \right) + \gamma_a \sin(\Phi) \left(-\frac{R_-}{R_+^2} + \frac{1}{R_-} \right) \\ -2\gamma R_+(N+n) \\ -2\gamma R_+(N+n) \end{pmatrix} \quad (B.7)$$

$$\frac{\partial F}{\partial R_-} = \begin{pmatrix} -\gamma_a \cos(\Phi) - \gamma_p \sin(\Phi) \\ \kappa(N-n-1) \\ -\gamma_p \cos(\Phi) \left(\frac{1}{R_+} + \frac{R_+}{R_-^2} \right) + \gamma_a \sin(\Phi) \left(\frac{1}{R_+} - \frac{R_+}{R_-^2} \right) \\ -2\gamma R_-(N-n) \\ -2\gamma R_-(N-n) \end{pmatrix} \quad (B.8)$$

$$\frac{\partial F}{\partial \Phi} = \begin{pmatrix} \gamma_a R_- \sin(\Phi) - \gamma_p R_- \cos(\Phi) \\ \gamma_a R_+ \sin(\Phi) + \gamma_p R_+ \cos(\Phi) \\ \gamma_p \sin(\Phi) \left(\frac{R_-}{R_+} - \frac{R_+}{R_-} \right) + \gamma_a \cos(\Phi) \left(\frac{R_-}{R_+} + \frac{R_+}{R_-} \right) \\ 0 \\ 0 \end{pmatrix} \quad (B.9)$$

$$\frac{\partial F}{\partial N} = \begin{pmatrix} \kappa R_+ \\ \kappa R_- \\ 0 \\ -\gamma(1 + R_+^2 + R_-^2) \\ -\gamma(R_+^2 - R_-^2) \end{pmatrix} \quad \text{and} \quad \frac{\partial F}{\partial n} = \begin{pmatrix} \kappa R_+ \\ -\kappa R_- \\ 2\kappa\alpha \\ -\gamma(R_+^2 - R_-^2) \\ -\gamma_s - \gamma(R_+^2 + R_-^2) \end{pmatrix} \quad (B.10)$$

Finally, for continuation techniques it is also useful to describe the derivative of F with respect to the system parameters. Thus, we obtain the following results:

$$\frac{\partial F}{\partial \kappa} = \begin{pmatrix} (N+n-1)R_+ \\ (N-n-1)R_- \\ 2\alpha n \\ 0 \\ 0 \end{pmatrix} \quad \frac{\partial F}{\partial \alpha} = \begin{pmatrix} 0 \\ 0 \\ 2\kappa n \\ 0 \\ 0 \end{pmatrix} \quad \frac{\partial F}{\partial \mu} = \begin{pmatrix} 0 \\ 0 \\ 0 \\ \gamma \\ 0 \end{pmatrix} \quad (\text{B.11})$$

$$\frac{\partial F}{\partial \gamma_p} = \begin{pmatrix} -R_- \sin(\Phi) \\ R_+ \sin(\Phi) \\ -\cos(\Phi) \left(\frac{R_-}{R_+} - \frac{R_+}{R_-} \right) \\ 0 \\ 0 \end{pmatrix} \quad \frac{\partial F}{\partial \gamma_a} = \begin{pmatrix} -R_- \cos(\Phi) \\ -R_+ \cos(\Phi) \\ \sin(\Phi) \left(\frac{R_-}{R_+} + \frac{R_+}{R_-} \right) \\ 0 \\ 0 \end{pmatrix} \quad (\text{B.12})$$

$$\frac{\partial F}{\partial \gamma_s} = \begin{pmatrix} 0 \\ 0 \\ 0 \\ 0 \\ -n \end{pmatrix} \quad \frac{\partial F}{\partial \gamma} = \begin{pmatrix} 0 \\ 0 \\ 0 \\ -(N-\mu + (N+n)R_+^2 + (N-n)R_-^2) \\ -((N+n)R_+^2 - (N-n)R_-^2) \end{pmatrix} \quad (\text{B.13})$$

When considering a misalignment between the phase and amplitude anisotropies as in section 2.5, the SFM equations are slightly different and read as, with θ the angle between the axis of maximum frequency and the axis of maximum losses:

$$\frac{dR_+}{dt} = \kappa(N + n - 1)R_+ - \overline{\gamma}_a R_- \cos(\phi) - \overline{\gamma}_p^+ R_- \sin(\phi) \quad (\text{B.14})$$

$$\frac{dR_-}{dt} = \kappa(N - n - 1)R_- - \overline{\gamma}_a R_+ \cos(\phi) + \overline{\gamma}_p^- R_+ \sin(\phi) \quad (\text{B.15})$$

$$\frac{d\phi}{dt} = 2\kappa\alpha n + \overline{\gamma}_a \sin(\phi) \left(\frac{R_-}{R_+} + \frac{R_+}{R_-} \right) + \left(\overline{\gamma}_p^- \frac{R_+}{R_-} - \overline{\gamma}_p^+ \frac{R_-}{R_+} \right) \cos(\phi) \quad (\text{B.16})$$

With $\overline{\gamma}_p^\pm = \gamma_p \mp \sin(2\theta)\gamma_a$ and $\overline{\gamma}_a = \cos(2\theta)\gamma_a$, and the two equations for the carrier unchanged. As a result, we observe small changes in the linear system dF/dX , but with potentially dramatic consequences as already reported in section 2.5. The partial derivatives now read as follows:

$$\frac{\partial F}{\partial R_+} = \begin{pmatrix} \kappa(N + n - 1) \\ -\overline{\gamma}_a \cos(\Phi) + \overline{\gamma}_p^- \sin(\Phi) \\ \cos(\Phi) \left(\overline{\gamma}_p^+ \frac{R_-}{R_+^2} + \overline{\gamma}_p^- \frac{1}{R_-} \right) + \overline{\gamma}_a \sin(\Phi) \left(-\frac{R_-}{R_+^2} + \frac{1}{R_-} \right) \\ -2\gamma R_+(N + n) \\ -2\gamma R_+(N + n) \end{pmatrix} \quad (\text{B.17})$$

$$\frac{\partial F}{\partial R_-} = \begin{pmatrix} -\overline{\gamma}_a \cos(\Phi) - \overline{\gamma}_p^+ \sin(\Phi) \\ \kappa(N - n - 1) \\ -\cos(\Phi) \left(\overline{\gamma}_p^+ \frac{1}{R_+} + \overline{\gamma}_p^- \frac{R_+}{R_-^2} \right) + \overline{\gamma}_a \sin(\Phi) \left(\frac{1}{R_+} - \frac{R_+}{R_-^2} \right) \\ -2\gamma R_-(N - n) \\ -2\gamma R_-(N - n) \end{pmatrix} \quad (\text{B.18})$$

$$\frac{\partial F}{\partial \phi} = \begin{pmatrix} \overline{\gamma}_a R_- \sin(\Phi) - \overline{\gamma}_p^+ R_- \cos(\Phi) \\ \overline{\gamma}_a R_+ \sin(\Phi) + \overline{\gamma}_p^- R_+ \cos(\Phi) \\ \gamma_p \sin(\Phi) \left(\overline{\gamma}_p^+ \frac{R_-}{R_+} - \overline{\gamma}_p^- \frac{R_+}{R_-} \right) + \overline{\gamma}_a \cos(\Phi) \left(\frac{R_-}{R_+} + \frac{R_+}{R_-} \right) \\ 0 \\ 0 \end{pmatrix} \quad (\text{B.19})$$

The derivatives with respect to the carrier population variables are unchanged.

C

GRASSBERGER-PROCACCIA ALGORITHM IMPLEMENTATION

In this section, we give the implementation of the Grassberger-Procaccia (GP) algorithm as used in the work described in this thesis. The principle of the GP algorithm has been described in section 2.4 based on [132–134], and considering an additional re-embedding procedure based on singular-value analysis as described in [136, 137].

The script used is typically divided in 4 steps: 1/ loading of the time-series X , 2/ application of the re-embedding procedure, 3/ application of the Grassberger-Procaccia algorithm, and 4/ result plots in logarithmic scales. For simplicity, the re-embedding procedure and the direct application of the GP algorithm has been introduced as separated functions: “SVA_embedding.m” and “GP_algo.m”. In this section, we therefore give the detail of these two functions and present a simple example of the script we used.

Most of the work described in this dissertation has been performed using matlab for practical reason. However for speed issues, e.g. when considering large time-series, an implementation in C/C++ eventually using mex-files in matlab would be recommended.

A typical script for the application of the GP algorithm as described previously is as follows (details about the functions and their respective input and output can be find afterwards):

```

clear all, close all;
load Time_series X

%% Singular Value Analysis - re-embedding
window = 12; % size of the time-window
degree = 5; % number of principal components kept
P = SVA_embedding(X, window, degree);

%% Application GP Algorithm
D = [1 1 15]; % set up the vector size D which will be computed
R = [-6 400 0]; % set up the sphere radius step
[Cd r] = GP_algo(P, D, R, 15);

%% Result Plot
% plot of correlation integral
figure, subplot(211); plot(log(r), log(Cd), 'k');

% plot of the correlation integral slope
subplot(212);
for k = 1:size(Cd, 1)
    plot(log(r(2:end)),...
        (log(Cd(k, 2:end)) - log(Cd(k, 1:end-1)))./ ...
        (log(r(2:end)) - log(r(1:end-1))));
    hold on;
end

```

In this script, we used only basic matlab functions for simplicity and clarity, but, of course, *loglog*, *diff* or other functions can be used.

The Singular-Value-Analysis embedding is a short but necessary step to improve the performances of the GP algorithm. We implemented it as follows:

```

function P = SVA_embedding(X, M, degree)
% formation of the X-M vectors of size M
Y = zeros(M, length(X)-M+1);
for k = 1:M
    Y(k, :) = X(k:end-M+k);
end

% Toeplitz matrix and eigenvalues
Toep = (Y*Y')';
[V D] = eig(Toep);

% Projection and principal components selection
P = zeros(degree, length(X)-M+1);
for k = 1:degree
    E = V(:,end-k+1);
    P(k, :) = E'*Y;
end

```

INPUT:

- X: input time-series. 1D-vector typically of type double or single.
- M: size of the time-window in terms of number of points. Integer $M \geq 1$.
- degree: number of principal components selected. Integer $M \geq \text{degree} \geq 1$.

OUTPUT:

- P: re-embedded time-series. 1D vector of the same type as X.

Finally, we compute the correlation integral using the function GP_algo. This computation can be performed in several various ways, however we chose here to use the following approach:

```
function [Cd r] = GP_algo(X, var_d, var_r, tau)

% initialization
vect_d = var_d(1):var_d(2):var_d(3);
r = exp(linspace(var_r(1), var_r(3), var_r(2)));
Cd = zeros(length(vect_d), length(r));
N = size(X, 2);

for n = 1:N % scan of the time-series
    X_n = abs(X(:, 1:N-n) - X(:, n+1:N));
    for inc = 1:length(vect_d); % calculation for each value of D
        d = vect_d(inc);
        if(d < N-n) % if enough points left before the end of the sequence
            for m = tau:N-n-d % computation of correlation integral
                X_mod = reshape(X_n(:, m:m+(d-1)), 1, d*size(X_n, 1));
                Cd(inc, :) = Cd(inc, :) + (norm(X_mod, 2)<r);
            end % for-m
        end % if
    end % for-inc
end %for-n

% normalization
Cd = Cd./N^2; % correlation integral that goes down to 0
% Cd = Cd./N^2 + 1/N; % correlation integral limited to 1/N
```

INPUT:

- X: multi-variate double or single time-series, i.e. matrix of dimension $V \times N$ with V the number of different variables and N the length of the time-series. In practice, the different variables are the principal components selected after the re-embedding procedure.
- var_d: 3 element integer vector detailing for which values of D the correlation integral C_D will be computed. var_d(1) gives the starting point (≥ 1), var_d(2) indicates the step and var_d(3) gives the maximum value ($\geq \text{var_d}(1)$).

- `var_r` : 3 element vector detailing the range and number of points for the sphere radius r to compute the correlation integral $C_D(r)$. `var_r(1)` is a double or single value giving the minimal value of r in log-scale, `var_r(2)` is an integer indicating the number of points (typ. 200), and `var_r(3)` is a double or single value giving the maximal value of r in log-scale. In practice, the range of r will be set empirically as it strongly depends on the dynamics analyzed.
- `tau`: an integer indicating the number of points to discard to avoid time-correlation between near neighbors. When this function is used in combination with the re-embedding procedure, we need to use $\tau > M$ with M the time-window used for the singular-value analysis.

OUTPUT:

- `Cd`: double or single matrix containing the computed correlation integral. The size of `Cd` is $D \times R$, with $R = \text{var_r}(2)$.
- `r`: double 1D vector with the corresponding values of the sphere radius r , i.e. the X-axis for the plot of the correlation integral in log-scale.

D

DDE-BIFTOOL DETAILS FOR LASERS WITH FEEDBACK

In this section, we provide some additional necessary details for the efficient use of the DDE-BIFTOOL package [130] when studying laser systems with conventional optical feedback.

The equation for the electrical field for a laser subject to optical time-delayed feedback is typically similar to the one of the Lang and Kobayashi (LK) equation system as described in section 1.2 and in [25]:

$$\frac{dE}{dt} = (1 - i\alpha)NE + \kappa e^{-i\omega_0\tau}E(t - \tau) \quad (D.1)$$

With E the normalized electrical field, α the linewidth enhancement factor, κ the feedback rate, ω_0 the laser solitary frequency and τ the time-delay.

As explained in [188] and mentioned in section 4.2, one important feature of these equations is that they typically exhibit a rotational symmetry: if $E(t)$ is a solution, $E(t)e^{i\phi}$ with $\phi \in [0, 2\pi]$ is a solution as well. In particular, as explained in [188], this phase indeterminacy allows the emergence of external cavity modes (ECM), i.e. stationary states whose frequency is shifted by a multiple of the external cavity frequency. With the LK equations, ECMs appear as periodic solutions with a frequency corresponding to the frequency shift with respect to the laser solitary frequency. For direct numerical integration, this is not really an issue, but for continuation techniques it makes the access to the secondary bifurcations more challenging. Indeed, it is much easier to follow and analyze the bifurcations of a steady-state solution branch than that of a periodic solution.

To overcome this hurdle, we followed in section 4.2 the same approach as in [188] and introduced an additional frequency shift Δ to the equations. Making the following substitution: $E(t) = A(t)e^{i\Delta t}$, the field equation now reads:

$$\frac{dA}{dt} = (1 - i\alpha)NA - i\Delta A + \kappa e^{-i(\omega_0\tau + \Delta)}A(t - \tau) \quad (D.2)$$

and the additional frequency shift then allows us to force $A(t)$ to be real without any loss of generality. As described in [188], the ECMs can then be considered as steady-state solutions with different values of Δ , and secondary bifurcations can be easily identified.

In practice, forcing the $A(t)$ variable to be real is not necessarily straightforward with the DDE-BIFTOOL toolbox. Indeed, it is not possible to simply discard the imaginary part of the equations as it is required to compute correctly the eigenvalues of the system's solutions. Instead, we need to use the extra conditions described in the "sys_cond.m" file of DDE-BIFTOOL which reads as:

```
function [resi,deri]=sys_cond(point)

% initialisation of the deri output
deri(1) = p_axpy(0, point, []);

% the case of periodic solution has to be processed independently
if(strcmp(point.kind,'stst') || strcmp(point.kind,'fold') ...
|| strcmp(point.kind,'hopf'))
    resi(1) = point.x(3, 1);
    deri(1).x(3, 1) = 1;
elseif(strcmp(point.kind,'psol'))
    resi(1) = point.profile(3, 1);
    deri(1).profile(3, 1) = 1;
end

return;
```

Here the system defined in DDE-BIFTOOL is a conventional optical feedback system of three variables: $(N, \text{Real}(E), \text{Imag}(E))$. The imaginary part of the field is therefore the third variable.

INPUT:

- point: DDE-BIFTOOL point structure.

OUTPUT:

- resi: residual difference between the current point and the point corrected with the additional correction(s). Here, we want the imaginary part of the electrical field (i.e. the third variable) to be 0, so the residual is only $x(3,1)$.
- deri: partial derivative of the residual formula. Here, the residual is equal to the value of the imaginary part, so the corresponding derivative is 1.

In practice, having a variable systematically forced to 0 might be detrimental for the determination of the eigenvalues or for some other complex internal procedure as experienced with the set of equations used in chapter 4. This can however be easily avoided by setting a $\pi/4$ phase for A instead of a real value, i.e. force the real and imaginary part of the electrical field to be equal. The residual then becomes the difference between the real and imaginary part, and the derivative can easily be changed accordingly.

REFERENCES

- [1] T. H. Maiman, "Stimulated optical radiation in ruby," *Nature* **187**, 493 (1960). (Cited on page 7.)
- [2] R. N. Hall, G. E. Fenner, J. D. Kingsley, T. J. Soltys, and R. O. Carlson, "Coherent Light Emission from Ga-As Junctions," *Phys. Rev. Lett.* **9**, 366 (1962). (Cited on page 8.)
- [3] M. I. Nathan, W. P. Dumke, G. Burns, F. H. Dill, and G. Lasher, "Stimulated emission of radiation from GaAs p-n junctions," *Appl. Phys. Lett.* **1**, 62 (1962). (Cited on page 8.)
- [4] H. Kroemer, "A proposed class of hetero-junction injection lasers," *Proc. IEEE* **51**, 1782 (1963). (Cited on page 9.)
- [5] Z. I. Alferov, V. M. Andreev, D. Z. Garbuzov, Y. V. Zhilyaev, E. P. Morozov, E. L. Portnoi, and V. G. Trofim, "Investigation of the influence of the AlAs-GaAs heterostructure parameters on the laser threshold current and the realization of continuous emission at room," *Sov. Phys.-Semicond* **4**, 1573 (1971). (Cited on page 9.)
- [6] H. Kroemer, "Quasi-electric fields and band offsets: teaching electrons new tricks," Nobel Lecture, December 8 p. 449 (2000). (Cited on page 9.)
- [7] Z. I. Alferov, "Nobel Lecture: The double heterostructure concept and its applications in physics, electronics, and technology," *Rev. Mod. Phys.* **73**, 767 (2001). (Cited on page 9.)
- [8] D. M. Kane and K. A. Shore, *Unlocking dynamical diversity: optical feedback effects on semiconductor lasers* (John Wiley & Sons, 2005). (Cited on page 10.)
- [9] J. Ohtsubo, *Semiconductor lasers: Stability, Instability and Chaos* (Springer, 2013). (Cited on pages 10, 12, 14, 15, and 16.)
- [10] G. D. VanWiggeren and R. Roy, "Communication with Chaotic Lasers," *Science* **279**, 1198 (1998). (Cited on page 10.)
- [11] A. Uchida, K. Amano, M. Inoue, K. Hirano, S. Naito, H. Someya, I. Oowada, T. Kurashige, M. Shiki, S. Yoshimori, K. Yoshimura, and P. Davis, "Fast physical

- random bit generation with chaotic semiconductor lasers," *Nature Photon.* **2**, 728 (2008). (Cited on pages 10, 96, 97, 98, 102, 103, 176, and 177.)
- [12] E. N. Lorenz, "Deterministic Nonperiodic Flow," *J. Atmos. Sci.* **20**, 130 (1963). (Cited on pages 10, 64, 72, and 171.)
- [13] H. Haken, "Analogy between higher instabilities in fluids and lasers," *Phys. Lett. A* **53**, 77 (1975). (Cited on pages 11 and 74.)
- [14] F. T. Arecchi, R. Meucci, G. Puccioni, and J. Tredicce, "Experimental evidence of subharmonic bifurcations, multistability and turbulence in a Q-switched Gas Laser," *Phys. Rev. Lett.* **49**, 1217 (1982). (Cited on page 11.)
- [15] C. O. Weiss, A. Godone, and A. Olafsson, "Routes to chaotic emission in a cw He-Ne laser," *Phys. Rev. A* **28**, 892 (1983). (Cited on page 11.)
- [16] F. T. Arecchi, G. L. Lippi, G. P. Puccioni, and J. R. Tredicce, "Deterministic chaos in laser with injected signal," *Opt. Commun.* **51**, 308 (1984). (Cited on pages 11 and 12.)
- [17] T. Midavaine, D. Dangoisse, and P. Glorieux, "Observation of Chaos in a Frequency-Modulated CO₂ Laser," *Phys. Rev. Lett.* **55**, 1989 (1985). (Cited on page 11.)
- [18] C. O. Weiss and J. Brock, "Evidence for Lorenz-type chaos in a laser," *Phys. Rev. Lett.* **57**, 57 (1986). (Cited on page 11.)
- [19] C. O. Weiss, N. B. Abraham, and U. Hübner, "Homoclinic and Heteroclinic Chaos in a Single-Mode Laser," *Phys. Rev. Lett.* **61**, 1587 (1988). (Cited on page 11.)
- [20] T.-Y. Li and J. A. Yorke, "Period three implies chaos," *Amer. Math. Monthly* **82**, 985 (1975). (Cited on page 11.)
- [21] R. Broom, "Self modulation at gigahertz frequencies of a diode laser coupled to an external cavity," *Electron. Lett.* **5**, 571 (1969). (Cited on page 13.)
- [22] R. W. Tkach and A. R. Chraplyvy, "Regimes of feedback effects in 1.5- μ m distributed feedback lasers," *J. Lightwave Tech.* **4**, 1655 (1986). (Cited on pages 14 and 15.)
- [23] D. Lenstra, B. H. Verbeek, and A. J. Den Boef, "Coherence collapse in single-mode semiconductor lasers due to optical feedback," *IEEE J. Quantum Electron.* **21**, 674 (1985). (Cited on page 14.)
- [24] A. Tabaka, K. Panajotov, I. Veretennicoff, and M. Sciamanna, "Bifurcation study of regular pulse packages in laser diodes subject to optical feedback," *Phys. Rev. E* **70**, 036211 (2004). (Cited on page 15.)
- [25] R. Lang and K. Kobayashi, "External optical feedback effects on semiconductor injection laser properties," *IEEE J. Quantum Electron.* **16**, 347 (1980). (Cited on pages 16 and 197.)

- [26] E. A. Viktorov and P. Mandel, "Low frequency fluctuations in a multimode semiconductor laser with optical feedback." *Phys. Rev. Lett.* **85**, 3157 (2000). (Cited on pages 16 and 119.)
- [27] J. Helms and K. Petermann, "A simple analytic expression for the stable operation range of laser diodes with optical feedback," *IEEE J. Quantum Electron.* **26**, 833 (1990). (Cited on page 16.)
- [28] H. Soda, K.-i. Iga, C. Kitahara, and Y. Suematsu, "GaInAsP/InP surface emitting injection lasers," *Jap. J. Appl. Phys.* **18**, 2329 (1979). (Cited on page 17.)
- [29] Y. H. Lee, J. L. Jewell, A. Scherer, S. L. McCall, J. P. Harbison, and L. T. Florez, "Room-temperature continuous-wave vertical-cavity single-quantum-well microlaser diodes," *Electron. Lett.* **25**, 1377 (1989). (Cited on pages 17 and 27.)
- [30] K. Panajotov and F. Prati, "Polarization dynamics of vcsels," in "VCSELs," , R. Michalzik, ed. (Springer-Verlag, 2012), p. 181. (Cited on pages 18, 25, and 169.)
- [31] B. Ryvkin, K. Panajotov, A. Georgievski, J. Danckaert, M. Peeters, G. Verschaffelt, H. Thienpont, and I. Veretennicoff, "Effect of photon-energy-dependent loss and gain mechanisms on polarization switching in vertical-cavity surface-emitting lasers," *J. Opt. Soc. Am. B* **16**, 2106 (1999). (Cited on pages 19, 20, 21, 24, 38, and 169.)
- [32] K. D. Choquette, D. A. Richie, and R. E. Leibenguth, "Temperature dependence of gain-guided vertical-cavity surface emitting laser polarization," *Appl. Phys. Lett.* **64**, 2062 (1994). (Cited on pages 18, 21, and 24.)
- [33] C. J. Chang-Hasnain, J. P. Harbison, G. Hasnain, A. C. Von Lehmen, L. T. Florez, and N. G. Stoffel, "Characteristics of Vertical Cavity Surface Emitting Lasers," *IEEE J. Quantum Electron.* **27**, 1402 (1991). (Cited on page 18.)
- [34] K. D. Choquette and R. E. Leibenguth, "Control of vertical-cavity laser polarization with anisotropic transverse cavity geometries," *IEEE Photon. Technol. Lett.* **6**, 40 (1994). (Cited on pages 18 and 24.)
- [35] A. K. Jansen van Doorn, M. P. van Exter, and J. P. Woerdman, "Elasto-optic anisotropy and polarization orientation of vertical-cavity surface-emitting semiconductor lasers," *Appl. Phys. Lett.* **69**, 1041 (1996). (Cited on pages 18 and 20.)
- [36] A. K. Jansen van Doorn, M. P. van Exter, and J. P. Woerdman, "Tailoring the birefringence in a vertical-cavity semiconductor laser," *Appl. Phys. Lett.* **69**, 3635 (1996). (Cited on page 20.)
- [37] A. K. Jansen van Doorn, M. P. van Exter, A. M. van der Lee, and J. P. Woerdman, "Coupled-mode description for the polarization state of a vertical-cavity semiconductor laser," *Phys. Rev. A* **55**, 1473 (1997). (Cited on page 20.)

- [38] K. Panajotov, B. Nagler, G. Verschaffelt, A. Georgievski, H. Thienpont, J. Danckaert, and I. Veretennicoff, "Impact of in-plane anisotropic strain on the polarization behavior of vertical-cavity surface-emitting lasers," *Appl. Phys. Lett.* **77**, 1590 (2000). (Cited on pages 20, 22, and 163.)
- [39] K. Panajotov, J. Danckaert, G. Verschaffelt, M. Peeters, B. Nagler, J. Albert, B. Ryvkin, H. Thienpont, and I. Veretennicoff, "Polarization behavior of vertical-cavity surface-emitting lasers: Experiments, models and applications," *AIP Conference Proceedings* **560**, 403 (2001). (Cited on pages 20 and 163.)
- [40] M. Sondermann, M. Weinkath, T. Ackemann, J. Mulet, and S. Balle, "Two-frequency emission and polarization dynamics at lasing threshold in vertical-cavity surface-emitting lasers," *Phys. Rev. A* **68**, 033822 (2003). (Cited on pages 20, 21, 22, and 25.)
- [41] M. B. Willemsen, M. U. F. Khalid, M. P. van Exter, and J. P. Woerdman, "Polarization Switching of a Vertical-Cavity Semiconductor Laser as a Kramers Hopping Problem," *Phys. Rev. Lett.* **82**, 4815 (1999). (Cited on pages 21, 25, 66, and 73.)
- [42] K. D. Choquette, R. P. Schneider, K. L. Lear, and R. E. Leibenguth, "Gain-dependent polarization properties of vertical-cavity lasers," *IEEE J. Sel. Top. Quantum Electron.* **1**, 661 (1995). (Cited on page 21.)
- [43] K. Panajotov, B. Ryvkin, J. Danckaert, M. Peeters, H. Thienpont, and I. Veretennicoff, "Polarization switching in VCSEL's due to thermal lensing," *IEEE Photon. Technol. Lett.* **10**, 6 (1998). (Cited on pages 21 and 24.)
- [44] B. Nagler, M. Peeters, J. Albert, G. Verschaffelt, K. Panajotov, H. Thienpont, I. Veretennicoff, J. Danckaert, S. Barbay, G. Giacomelli, and F. Marin, "Polarization-mode hopping in single-mode vertical-cavity surface-emitting lasers: Theory and experiment," *Phys. Rev. A* **68**, 013813 (2003). (Cited on pages 21, 25, and 81.)
- [45] J. Danckaert, M. Peeters, C. R. Mirasso, M. San Miguel, G. Verschaffelt, J. Albert, B. Nagler, H. Unold, R. Michalzik, G. Giacomelli, and F. Marin, "Stochastic polarization switching dynamics in vertical-cavity surface-emitting lasers: theory and experiment," *IEEE J. Sel. Top. Quantum Electron.* **10**, 911 (2004). (Cited on pages 21 and 25.)
- [46] G. Giacomelli, F. Marin, M. Gabrysch, K. H. Gulden, and M. Moser, "Polarization competition and noise properties of VCSELs," *Opt. Commun.* **146**, 136 (1998). (Cited on page 21.)
- [47] M. B. Willemsen, M. P. van Exter, and J. P. Woerdman, "Anatomy of a Polarization Switch of a Vertical-Cavity Semiconductor Laser," *Phys. Rev. Lett.* **84**, 4337 (2000). (Cited on pages 21, 25, and 170.)

- [48] H. Kawaguchi, I. S. Hidayat, Y. Takahashi, and Y. Yamayoshi, "Pitchfork bifurcation polarization bistability in vertical-cavity surface-emitting lasers," *Electron. Lett.* **31**, 109 (1995). (Cited on page 21.)
- [49] H. Kawaguchi, "Bistable Laser Diodes and Their Applications : State of the Art," *IEEE J. Sel. Top. Quantum Electron.* **3**, 1254 (1997). (Cited on pages 22 and 25.)
- [50] M. Sondermann, M. Weinkath, and T. Ackemann, "Polarization Switching to the Gain Disfavored Mode in Vertical-Cavity Surface-Emitting Lasers," *IEEE J. Quantum Electron.* **40**, 97 (2004). (Cited on pages 22 and 25.)
- [51] M. Sondermann, T. Ackemann, S. Balle, J. Mulet, and K. Panajotov, "Experimental and theoretical investigations on elliptically polarized dynamical transition states in the polarization switching of vertical-cavity surface-emitting lasers," *Opt. Commun.* **235**, 421 (2004). (Cited on pages 22, 23, 25, 33, 46, 50, 52, 56, 57, 63, 64, and 170.)
- [52] T. Ackemann and M. Sondermann, "Characteristics of polarization switching from the low to the high frequency mode in vertical-cavity surface-emitting lasers," *Appl. Phys. Lett.* **78**, 3574 (2001). (Cited on pages 22, 23, 57, and 170.)
- [53] L. Olejniczak, M. Sciamanna, H. Thienpont, K. Panajotov, A. Mutig, F. Hopfer, and D. Bimberg, "Polarization switching in quantum-dot vertical-cavity surface-emitting lasers," *IEEE Photon. Technol. Lett.* **21**, 1008 (2009). (Cited on pages 23, 25, 33, 46, 58, 63, 64, 65, 66, 71, 92, and 170.)
- [54] L. Olejniczak, K. Panajotov, H. Thienpont, M. Sciamanna, A. Mutig, F. Hopfer, and D. Bimberg, "Polarization switching and polarization mode hopping in quantum dot vertical-cavity surface-emitting lasers." *Opt. Express* **19**, 2476 (2011). (Cited on pages 23, 33, 37, 46, 58, 61, 62, 63, 64, 65, 66, 68, 71, 72, 73, 74, 92, 100, 160, 170, and 173.)
- [55] A. Valle, J. Sarma, and K. A. Shore, "Dynamics of transverse mode competition in vertical cavity surface emitting laser diodes," *Opt. Commun.* **115**, 297 (1995). (Cited on page 24.)
- [56] A. Valle, L. Pesquera, and K. A. Shore, "Polarization behavior of birefringent multitransverse mode vertical-cavity surface-emitting lasers," *IEEE Photon. Technol. Lett.* **9**, 557 (1997). (Cited on page 24.)
- [57] G. Verschaffelt, J. Albert, I. Veretennicoff, J. Danckaert, S. Barbay, G. Giacomelli, and F. Marin, "Frequency response of current-driven polarization modulation in vertical-cavity surface-emitting lasers," *Appl. Phys. Lett.* **80**, 2248 (2002). (Cited on page 25.)
- [58] G. Verschaffelt, J. Albert, B. Nagler, M. Peeters, J. Danckaert, S. Barbay, G. Giacomelli, and F. Marin, "Frequency response of polarization switching in vertical-

- cavity surface-emitting lasers," *IEEE J. Quantum Electron.* **39**, 1177 (2003). (Cited on page 25.)
- [59] J. Martin-Regalado, J. L. A. Chilla, J. J. Rocca, and P. Brusenbach, "Polarization switching in vertical-cavity surface emitting lasers observed at constant active region temperature," *Appl. Phys. Lett.* **70**, 3350 (1997). (Cited on page 25.)
- [60] J. Albert, G. Van der Sande, B. Nagler, K. Panajotov, I. Veretennicoff, J. Danckaert, and T. Erneux, "The effects of nonlinear gain on the stability of semi-degenerate two-mode semiconductor lasers: a case study on VCSELs," *Opt. Commun.* **248**, 527 (2005). (Cited on page 25.)
- [61] M. San Miguel, Q. Feng, and J. V. Moloney, "Light-polarization dynamics in surface-emitting semiconductor lasers," *Phys. Rev. A* **52**, 1728 (1995). (Cited on pages 25, 38, and 170.)
- [62] M. P. Van Exter, R. F. M. Hendriks, and J. P. Woerdman, "Physical insight into the polarization dynamics of semiconductor vertical-cavity lasers," *Phys. Rev. A* **57**, 2080 (1998). (Cited on page 25.)
- [63] M. P. van Exter, A. Al-Remawi, and J. P. Woerdman, "Polarization Fluctuations Demonstrate Nonlinear Anisotropy of a Vertical-Cavity Semiconductor Laser," *Phys. Rev. Lett.* **80**, 4875 (1998). (Cited on page 25.)
- [64] M. P. van Exter, M. B. Willemsen, and J. P. Woerdman, "Polarization fluctuations in vertical-cavity semiconductor lasers," *Phys. Rev. A* **58**, 4191 (1998). (Cited on pages 25 and 70.)
- [65] A. Tackeuchi, O. Wada, and Y. Nishikawa, "Electron spin relaxation in InGaAs / InP multiple-quantum wells," *Appl. Phys. Lett.* **70**, 1131 (1997). (Cited on page 25.)
- [66] A. Tackeuchi, Y. Nishikawa, and O. Wada, "Roomtemperature electron spin dynamics in GaAs / AlGaAs quantum wells Room-temperature electron spin dynamics in GaAs / AlGaAs quantum wells," *Appl. Phys. Lett.* **68**, 797 (1996). (Cited on page 25.)
- [67] T. Adachi, Y. Ohno, R. Terauchi, F. Matsukura, and H. Ohno, "Mobility dependence of electron spin relaxation time in n-type InGaAs/InAlAs multiple quantum wells," *Physica E* **7**, 1015 (2000). (Cited on page 25.)
- [68] K. Jarasiunas, V. Gudelis, R. Aleksiejunas, M. Sudzius, S. Iwamoto, M. Nishioka, T. Shimura, K. Kuroda, and Y. Arakawa, "Picosecond dynamics of spin-related optical nonlinearities in In_xGa_(1-x)As multiple quantum wells at 1064 nm," *Appl. Phys. Lett.* **84**, 1043 (2004). (Cited on page 25.)
- [69] T. Erneux, J. Danckaert, K. Panajotov, and I. Veretennicoff, "Two-variable reduction of the San Miguel-Feng-Moloney model for vertical-cavity surface-emitting lasers," *Phys. Rev. A* **59**, 4660 (1999). (Cited on pages 25, 39, and 88.)

- [70] J. Martin-Regalado, F. Prati, M. San Miguel, and N. B. Abraham, "Polarization properties of vertical-cavity surface-emitting lasers," *IEEE J. Quantum Electron.* **33**, 765 (1997). (Cited on pages 25, 38, 39, 40, 41, 42, 44, and 170.)
- [71] M. Travagnin, M. P. van Exter, A. K. Jansen van Doorn, and J. P. Woerdman, "Role of optical anisotropies in the polarization properties of surface-emitting semiconductor lasers," *Phys. Rev. A* **54**, 1647 (1996). (Cited on pages 25 and 42.)
- [72] M. Travagnin, M. P. van Exter, A. K. Jansen van Doorn, and J. P. Woerdman, "Erratum: Role of optical anisotropies in the polarization properties of surface-emitting semiconductor lasers," *Phys. Rev. A* **55**, 4641 (1997). (Cited on page 25.)
- [73] J. Martin-Regalado, M. San Miguel, N. B. Abraham, and F. Prati, "Polarization switching in quantum-well vertical-cavity surface-emitting lasers," *Opt. Lett.* **21**, 351 (1996). (Cited on page 25.)
- [74] F. Prati, P. Caccia, and F. Castelli, "Effects of gain saturation on polarization switching in vertical-cavity surface-emitting lasers," *Phys. Rev. A* **66**, 063811 (2002). (Cited on pages 25, 26, and 51.)
- [75] F. Prati, P. Caccia, M. Bache, and F. Castelli, "Analysis of elliptically polarized states in vertical-cavity-surface-emitting lasers," *Phys. Rev. A* **69**, 033810 (2004). (Cited on pages 26, 42, 50, 51, and 163.)
- [76] H. van der Lem and D. Lenstra, "Saturation-induced frequency shift in the noise spectrum of a birefringent vertical-cavity surface emitting laser," *Opt. Lett.* **22**, 1698 (1997). (Cited on page 26.)
- [77] M. Travagnin, "Linear anisotropies and polarization properties of vertical-cavity surface-emitting semiconductor lasers," *Phys. Rev. A* **56**, 4094 (1997). (Cited on pages 26 and 88.)
- [78] S. Balle, E. Tolkachova, M. San Miguel, J. R. Tredicce, J. Martin-Regalado, and A. Gahl, "Mechanisms of polarization switching in surface-emitting lasers : thermal shift and nonlinear semiconductor dynamics," *Opt. Lett.* **24**, 1121 (1999). (Cited on page 26.)
- [79] G. Van Der Sande, M. Peeters, I. Veretennicoff, J. Danckaert, G. Verschaffelt, and S. Balle, "The Effects of Stress, Temperature, and Spin Flips on Polarization Switching in Vertical-Cavity Surface-Emitting Lasers," *IEEE J. Quantum Electron.* **42**, 896 (2006). (Cited on page 26.)
- [80] C. Masoller and M. S. Torre, "Modeling thermal effects and polarization competition in lasers," *Opt. Express* **16**, 21282 (2008). (Cited on page 26.)
- [81] M. Asada, Y. Miyamoto, and Y. Suematsu, "Gain and the threshold of three-dimensional quantum-box lasers," *IEEE J. Quantum Electron.* **22**, 1915 (1986). (Cited on page 28.)

- [82] D. Bimberg, "Quantum dot based nanophotonics and nanoelectronics," *Electron. Lett.* **44**, 168 (2008). (Cited on page 28.)
- [83] D. Bimberg, M. Grundmann, N. N. Ledentsov *et al.*, *Quantum dot heterostructures*, vol. 471973882 (John Wiley Chichester, 1999). (Cited on page 28.)
- [84] J. J. Coleman, J. D. Young, and A. Garg, "Semiconductor quantum dot lasers: a tutorial," *J. Lightwave Tech.* **29**, 499 (2011). (Cited on page 28.)
- [85] F. Hopfer, A. Mutig, M. Kuntz, G. Fiol, D. Bimberg, N. N. Ledentsov, V. A. Shchukin, S. S. Mikhlin, D. L. Livshits, I. L. Krestnikov, A. R. Kovsh, N. D. Zakharov, and P. Werner, "Single-mode submonolayer quantum-dot vertical-cavity surface-emitting lasers with high modulation bandwidth," *Appl. Phys. Lett.* **89**, 141106 (2006). (Cited on pages 28, 64, and 100.)
- [86] A. Persano, A. Cola, A. Taurino, M. Catalano, M. Lomascolo, A. Convertino, G. Leo, L. Cerri, A. Vasanelli, and L. Vasanelli, "Electronic structure of double stacked InAs-GaAs quantum dots: Experiment and theory," *J. Appl. Phys.* **102**, 094314 (2007). (Cited on page 28.)
- [87] P. G. Eliseev, H. Li, G. T. Liu, A. Stintz, T. C. Newell, L. F. Lester, and K. J. Malloy, "Ground-state emission and gain in ultralow-threshold InAs-InGaAs quantum-dot lasers," *IEEE J. Sel. Top. Quantum Electron.* **7**, 135 (2001). (Cited on page 28.)
- [88] P. Bhattacharya, S. Ghosh, S. Pradhan, J. Singh, Z.-K. Wu, J. Urayama, K. Kim, and T. B. Norris, "Carrier dynamics and high-speed modulation properties of tunnel injection InGaAs-GaAs quantum-dot lasers," *IEEE J. Quantum Electron.* **39**, 952 (2003). (Cited on page 28.)
- [89] S. M. Kim, Y. Wang, M. Keever, and J. S. Harris, "High-Frequency Modulation Characteristics of 1.3- μ m InGaAs Quantum Dot Lasers," *IEEE Photon. Technol. Lett.* **16**, 377 (2004). (Cited on page 28.)
- [90] K. Lüdge, M. J. P. Bormann, E. Malic, P. Hövel, M. Kuntz, D. Bimberg, A. Knorr, and E. Schöll, "Turn-on dynamics and modulation response in semiconductor quantum dot lasers," *Phys. Rev. B* **78**, 035316 (2008). (Cited on pages 29 and 30.)
- [91] K. Lüdge and E. Schöll, "Quantum-dot lasers—desynchronized nonlinear dynamics of electrons and holes," *IEEE J. Quantum Electron.* **45**, 1396 (2009). (Cited on page 29.)
- [92] C. Otto, B. Globisch, K. Lüdge, and E. Schöll, "Complex dynamics of semiconductor quantum dot lasers subject to delayed optical feedback," *Int. J. Bifurcation Chaos* **22**, 1250246 (2012). (Cited on page 29.)
- [93] M. Kuntz, N. N. Ledentsov, D. Bimberg, A. R. Kovsh, V. M. Ustinov, A. E. Zhukov, and Y. M. Shernyakov, "Spectrotemporal response of 1.3 μ m quantum-dot lasers," *Appl. Phys. Lett.* **81**, 3846 (2002). (Cited on page 29.)

- [94] T. Erneux, E. A. Viktorov, and P. Mandel, "Time scales and relaxation dynamics in quantum-dot lasers," *Phys. Rev. A* **76**, 023819 (2007). (Cited on page 29.)
- [95] T. Erneux, E. A. Viktorov, B. Kelleher, D. Goulding, S. P. Hegarty, and G. Huyet, "Optically injected quantum-dot lasers." *Opt. Lett.* **35**, 937 (2010). (Cited on page 29.)
- [96] B. Kelleher, C. Bonatto, G. Huyet, and S. P. Hegarty, "Excitability in optically injected semiconductor lasers: Contrasting quantum- well- and quantum-dot-based devices," *Phys. Rev. E* **83**, 026207 (2011). (Cited on page 29.)
- [97] T. C. Newell, D. J. Bossert, A. Stintz, B. Fuchs, K. J. Malloy, and L. F. Lester, "Gain and linewidth enhancement factor in InAs quantum-dot laser diodes," *IEEE Photon. Technol. Lett.* **11**, 1527 (1999). (Cited on page 29.)
- [98] Z. Xu, D. Birkedal, M. Juhl, and J. H. Hvam, "Submonolayer InGaAs-GaAs quantum-dot lasers with high modal gain and zero-linewidth enhancement factor," *Appl. Phys. Lett.* **85**, 3259 (2004). (Cited on page 29.)
- [99] B. Dagens, A. Markus, J. X. Chen, J. G. Provost, D. Make, O. Le Gouezigou, J. Landreau, A. Fiore, and B. Thedrez, "Giant linewidth enhancement factor and purely frequency modulated emission from quantum dot laser," *Electron. Lett.* **41**, 6 (2005). (Cited on pages 29 and 122.)
- [100] S. Melnik, G. Huyet, and A. V. Uskov, "The linewidth enhancement factor alpha of quantum dot semiconductor lasers." *Opt. Express* **14**, 2950 (2006). (Cited on page 29.)
- [101] C. F. Chuang, Y. H. Liao, C. H. Lin, S. Y. Chen, F. Grillot, and F.-Y. Lin, "Linewidth enhancement factor in semiconductor lasers subject to various external optical feedback conditions," *Opt. Express* **22**, 5651 (2014). (Cited on page 29.)
- [102] B. Lingnau, K. Lüdge, W. W. Chow, and E. Schöll, "Failure of the alpha-factor in describing dynamical instabilities and chaos in quantum-dot lasers," *Phys. Rev. E* **86**, 065201 (2012). (Cited on pages 29 and 122.)
- [103] D. O'Brien, S. P. Hegarty, G. Huyet, J. G. McInerney, T. Kettler, M. Laemmlin, D. Bimberg, V. M. Ustinov, A. E. Zhukov, S. S. Mikhlin, and A. R. Kovsh, "Feed-back sensitivity of 1.3 μm InAs/GaAs quantum dot lasers," *Electron. Lett.* **39**, 25 (2003). (Cited on pages 29 and 30.)
- [104] D. O'Brien, S. P. Hegarty, G. Huyet, and A. V. Uskov, "Sensitivity of quantum-dot semiconductor lasers to optical feedback." *Opt. Lett.* **29**, 1072 (2004). (Cited on pages 29 and 30.)
- [105] S. Azouigui, B. Dagens, F. Lelarge, J. G. Provost, D. Make, O. Le Gouezigou, A. Accard, A. Martinez, K. Merghem, F. Grillot, O. Dehaese, R. Piron, S. Loualiche,

- Q. Zou, and A. Ramdane, "Optical Feedback Tolerance of Quantum-Dot-and Quantum-Dash-Based Semiconductor Lasers Operating at 1.55 μm ," *IEEE J. Sel. Top. Quantum Electron.* **15**, 764 (2009). (Cited on page 29.)
- [106] A. Markus, J. X. Chen, C. Paranthoen, A. Fiore, C. Platz, and O. Gauthier-Lafaye, "Simultaneous two-state lasing in quantum-dot lasers," *Appl. Phys. Lett.* **82**, 1818 (2003). (Cited on pages 30, 31, 128, and 180.)
- [107] L. Olejniczak, K. Panajotov, H. Thienpont, and M. Sciamanna, "Self-pulsations and excitability in optically injected quantum-dot lasers: Impact of the excited states and spontaneous emission noise," *Phys. Rev. A* **82**, 023807 (2010). (Cited on pages 30, 32, and 129.)
- [108] A. Markus, J. X. Chen, O. Gauthier-Lafaye, J. G. Provost, C. Paranthoen, and A. Fiore, "Impact of intraband relaxation on the performance of a quantum-dot laser," *IEEE J. Sel. Top. Quantum Electron.* **9**, 1308 (2003). (Cited on page 30.)
- [109] S. Hoffmann and M. R. Hofmann, "Generation of Terahertz radiation with two color semiconductor lasers," *Laser Photon. Rev.* **1**, 44 (2007). (Cited on pages 30 and 180.)
- [110] N. A. Naderi, F. Grillot, K. Yang, J. B. Wright, A. Gin, and L. F. Lester, "Two-color multi-section quantum dot distributed feedback laser," *Opt. Express* **18**, 27028 (2010). (Cited on pages 30, 32, 118, 136, 149, and 180.)
- [111] F. Grillot, N. A. Naderi, J. B. Wright, R. Raghunathan, M. T. Crowley, and L. F. Lester, "A dual-mode quantum dot laser operating in the excited state," *Appl. Phys. Lett.* **99**, 231110 (2011). (Cited on pages 30, 118, and 180.)
- [112] M. A. Cataluna, D. I. Nikitichev, S. Mikroulis, H. Simos, C. Simos, C. Mesaritakis, D. Syvridis, I. Krestnikov, D. Livshits, and E. U. Rafailov, "Dual-wavelength mode-locked quantum-dot laser, via ground and excited state transitions: experimental and theoretical investigation," *Opt. Express* **18**, 12832 (2010). (Cited on pages 30 and 180.)
- [113] S. Breuer, M. Rossetti, L. Drzewietzki, P. Bardella, I. Montrosset, and W. Elsässer, "Joint experimental and theoretical investigations of two-state mode locking in a strongly chirped reverse-biased monolithic quantum dot laser," *IEEE J. Quantum Electron.* **47**, 1320 (2011). (Cited on pages 30, 140, and 180.)
- [114] L. Olejniczak, K. Panajotov, S. Wieczorek, H. Thienpont, and M. Sciamanna, "Intrinsic gain switching in optically injected quantum dot laser lasing simultaneously from the ground and excited state," *J. Opt. Soc. Am. B* **27**, 2416 (2010). (Cited on page 31.)

- [115] E. A. Viktorov and P. Mandel, "Electron-hole asymmetry and two-state lasing in quantum dot lasers," *Appl. Phys. Lett.* **87**, 053113 (2005). (Cited on pages 31, 120, 121, 128, 129, 155, and 181.)
- [116] M. Abusaa, J. Danckaert, E. A. Viktorov, and T. Erneux, "Intradot time scales strongly affect the relaxation dynamics in quantum dot lasers," *Phys. Rev. A* **87**, 063827 (2013). (Cited on pages 31, 122, and 143.)
- [117] M. Gioannini, "Ground-state power quenching in two-state lasing quantum dot lasers," *J. Appl. Phys.* **111**, 043108 (2012). (Cited on pages 31, 32, and 150.)
- [118] D.-C. Wu, L.-C. Su, Y.-C. Lin, M.-H. Mao, J.-S. Wang, G. Lin, and J.-Y. Chi, "Experiments and simulation of spectrally-resolved static and dynamic properties in quantum dot two-state lasing," *Jap. J. Appl. Phys.* **48**, 032101 (2009). (Cited on page 32.)
- [119] L. Drzewietzki, G. P. A. Thè, M. Gioannini, S. Breuer, I. Montrosset, W. Elsässer, M. Hopkinson, and M. Krakowski, "investigations of the temperature dependent continuous wave lasing characteristics and the switch-on dynamics of an InAs/In-GaAs quantum-dot semiconductor laser," *Opt. Commun.* **283**, 5092 (2010). (Cited on page 32.)
- [120] B. Tykalewicz, D. Goulding, S. P. Hegarty, G. Huyet, and B. Kelleher, "All-optical switching with a dual state quantum dot laser," *Proc. SPIE* **9134**, 91341B (2014). (Cited on pages 32 and 180.)
- [121] E. A. Viktorov, P. Mandel, I. O'Driscoll, O. Carroll, G. Huyet, J. Houlihan, and Y. Tanguy, "Low-frequency fluctuations in two-state quantum dot lasers." *Opt. Lett.* **31**, 2302 (2006). (Cited on pages 32, 119, 120, 121, 122, 134, 180, and 181.)
- [122] F. Grillot, C. Wang, N. A. Naderi, and J. Even, "Modulation properties of self-injected quantum dot semiconductor diode lasers," *IEEE J. Sel. Top. Quantum Electron.* **19**, 1900812 (2013). (Cited on pages 32 and 118.)
- [123] M. Virte, K. Panajotov, H. Thienpont, and M. Sciamanna, "Deterministic polarization chaos from a laser diode," *Nature Photon.* **7**, 60–65 (2013). (Cited on pages 37, 161, and 169.)
- [124] M. Virte, K. Panajotov, and M. Sciamanna, "Bifurcation to nonlinear polarization dynamics and chaos in vertical-cavity surface-emitting lasers," *Phys. Rev. A* **87**, 013834 (2013). (Cited on pages 37, 161, and 169.)
- [125] M. Virte, M. Sciamanna, E. Mercier, and K. Panajotov, "Bistability of time-periodic polarization dynamics in a free-running VCSEL," *Opt. Express* **22**, 6772 (2014). (Cited on pages 37, 161, and 169.)
- [126] M. Virte, K. Panajotov, and M. Sciamanna, "Dynamics accompanying polarization switching in vertical-cavity surface-emitting lasers," in "Proc. SPIE, Semiconduc-

- tor Laser and Laser Dynamics V, Eds K. Panajotov, M. Sciamanna, A. Valle and R. Michalzik," , vol. 8432 (2012), vol. 8432, p. 84321E. (Cited on pages 37, 161, and 169.)
- [127] M. Virte, M. Sciamanna, and K. Panajotov, "Bifurcation to chaotic polarization mode hopping in vertical-cavity surface-emitting lasers," in "Advanced Photonics Congress," (Optical Society of America, 2012), p. JTU5A.31. (Cited on pages 37, 161, and 169.)
- [128] M. Virte, K. Panajotov, H. Thienpont, and M. Sciamanna, "Polarization chaos from a free-running quantum dot laser diode," in "Lasers and Electro-Optics Europe (CLEO EUROPE/IQEC), 2013 Conference on and International Quantum Electronics Conference," (2013), p. 6800709. (Cited on pages 37, 161, and 169.)
- [129] M. Virte, M. Sciamanna, E. Mercier, and K. Panajotov, "Experimental and theoretical analysis of limit cycle bistability in a free-running vcsel," in "Proc. SPIE, Semiconductor Laser and Laser Dynamics VI, Eds K. Panajotov, M. Sciamanna, A. Valle and R. Michalzik," , vol. 9134 (2014), vol. 9134, p. 91340A. (Cited on pages 37, 161, and 169.)
- [130] K. Engelborghs, T. Luzyanina, and G. Samaey, "Dde-biftool v. 2.03: a matlab package for bifurcation analysis of delay-differential equations," Tech. rep., TW-330, Dept. of CS, K. U. Leuven, Belgium (2002). (Cited on pages 45, 125, 127, 187, and 197.)
- [131] A. Wolf, J. B. Swift, H. L. Swinney, and J. A. Vastano, "Determining Lyapunov exponents from a time series," *Physica D* **16**, 285 (1985). (Cited on pages 77 and 172.)
- [132] P. Grassberger and I. Procaccia, "Estimation of the Kolmogorov entropy from a chaotic signal," *Phys. Rev. A* **28**, 2591 (1983). (Cited on pages 78, 79, and 191.)
- [133] P. Grassberger and I. Procaccia, "Characterization of strange attractors," *Phys. Rev. Lett.* **50**, 346 (1983). (Cited on pages 78 and 191.)
- [134] P. Grassberger and I. Procaccia, "Measuring the strangeness of strange attractors," *Physica D* **9**, 189 (1983). (Cited on pages 78 and 191.)
- [135] I. Fischer, O. Hess, W. Elsässer, and E. Göbel, "High-Dimensional Chaotic Dynamics of an External Cavity Semiconductor Laser," *Phys. Rev. Lett.* **73**, 2188 (1994). (Cited on pages 79, 99, and 177.)
- [136] K. Fraedrich and R. Wang, "Estimating the correlation dimension of an attractor from noisy and small datasets based on re-embedding," *Physica D* **65**, 373 (1993). (Cited on pages 79 and 191.)
- [137] R. Vautard, P. Yiou, and M. Ghil, "Singular-spectrum analysis: A toolkit for short, noisy chaotic signals," *Physica D* **58**, 95 (1992). (Cited on pages 79 and 191.)

- [138] A. Provenzale, L. A. Smith, R. Vio, and G. Murante, "Distinguishing between low-dimensional dynamics and randomness in measured time series," *Physica D* **58**, 31 (1992). (Cited on pages 81, 83, and 84.)
- [139] C. Myers, A. Singer, F. Shin, and E. Church, "Modeling chaotic systems with hidden Markov models," *Proc. IEEE* **4**, 565 (1992). (Cited on page 81.)
- [140] I. Kanter, A. Frydman, and A. Ater, "Utilizing hidden Markov processes as a tool for experimental physics," *Europhys. Lett.* **69**, 798 (2005). (Cited on pages 81 and 82.)
- [141] L. R. Rabiner, "A tutorial on hidden Markov models and selected applications in speech recognition," *Proc. IEEE* **77**, 257 (1989). (Cited on page 82.)
- [142] M. Virte, E. Mercier, H. Thienpont, K. Panajotov, and M. Sciamanna, "Physical random bit generation from chaotic solitary laser diode," *Opt. Express* **22**, 17271–17280 (2014). (Cited on pages 95, 162, and 176.)
- [143] M. Virte, E. Mercier, H. Thienpont, K. Panajotov, and M. Sciamanna, "Random bit generation using polarization chaos from free-running laser diode," in "Proc. SPIE, Semiconductor Laser and Laser Dynamics VI, Eds K. Panajotov, M. Sciamanna, A. Valle and R. Michalzik," , vol. 9134 (2014), vol. 9134, p. 913426. (Cited on pages 95, 162, and 176.)
- [144] Wikipedia, "Applications of randomness — wikipedia, the free encyclopedia," http://en.wikipedia.org/w/index.php?title=Applications_of_randomness&oldid=594179493 (2014). [Online; accessed 6-April-2014]. (Cited on page 96.)
- [145] Wikipedia, "Comparison of hardware random number generators — wikipedia, the free encyclopedia," http://en.wikipedia.org/w/index.php?title=Comparison_of_hardware_random_number_generators&oldid=602090625 (2014). [Online; accessed 6-April-2014]. (Cited on page 96.)
- [146] IDquantique, "Quantis: True random number generator exploiting quantum physics," <http://www.idquantique.com/random-number-generators/products.html> (2014). [Online; accessed 6-April-2014]. (Cited on page 96.)
- [147] LETech, "Genuine random number generator," http://www.letech.jp/rng/grang_24ch_e.html (2014). [Online; accessed 6-April-2014]. (Cited on page 96.)
- [148] S. Pironio, A. Acín, S. Massar, A. Boyer de la Giroday, D. N. Matsukevich, P. Maunz, S. Olmschenk, D. Hayes, L. Luo, T. A. Manning, and C. Monroe, "Random numbers certified by Bell's theorem," *Nature* **464**, 1021 (2010). (Cited on page 96.)
- [149] T. Symul, S. M. Assad, and P. K. Lam, "Real time demonstration of high bitrate quantum random number generation with coherent laser light," *Appl. Phys. Lett.* **98**, 231103 (2011). (Cited on page 96.)

- [150] C. Gabriel, C. Wittman, D. Sych, R. Dong, W. Mauerner, U. L. Andersen, C. Marquardt, and G. Leuchs, "A generator for unique quantum random numbers based on vacuum states," *Nature Photon.* **4**, 711 (2010). (Cited on page 96.)
- [151] T. Durt, C. Belmonte, L. P. Lamoureaux, K. Panajotov, F. Van den Berghe, and H. Thienpont, "Fast quantum-optical random-number generators," *Phys. Rev. A* **87**, 022339 (2013). (Cited on page 96.)
- [152] M. Jofre, M. Curty, F. Steinlechner, G. Anzolin, J. P. Torres, M. W. Mitchell, and V. Pruneri, "True random numbers from amplified quantum vacuum," *Opt. Express* **19**, 271 (2011). (Cited on page 96.)
- [153] D. P. Rosin, D. Rontani, and D. J. Gauthier, "Ultrafast physical generation of random numbers using hybrid Boolean networks," *Phys. Rev. E* **87**, 040902 (2013). (Cited on page 96.)
- [154] W. Li, I. Reidler, Y. Aviad, Y. Huang, H. Song, Y. Zhang, M. Rosenbluh, and I. Kanter, "Fast Physical Random-Number Generation Based on Room-Temperature Chaotic Oscillations in Weakly Coupled Superlattices," *Phys. Rev. Lett.* **111**, 044102 (2013). (Cited on page 96.)
- [155] Y. Liu, M.-Y. Zhu, B. Luo, J.-W. Zhang, and H. Guo, "Implementation of 1.6 Tb s⁻¹ truly random number generation based on a super-luminescent emitting diode," *Laser Phys. Lett.* **10**, 045001 (2013). (Cited on page 96.)
- [156] C. R. S. Williams, J. C. Salevan, X. Li, R. Roy, and T. E. Murphy, "Fast physical random number generator using amplified spontaneous emission." *Opt. Express* **18**, 23584 (2010). (Cited on page 96.)
- [157] T. Yamazaki and A. Uchida, "Performance of Random Number Generators Using Noise-based Super-Luminescent Diode and Chaos-based Semiconductor Lasers," *IEEE J. Sel. Top. Quantum Electron.* **19**, 0600309 (2013). (Cited on pages 96, 97, 103, 176, and 178.)
- [158] X.-Z. Li and S.-C. Chan, "Random bit generation using an optically injected semiconductor laser in chaos with oversampling." *Opt. Lett.* **37**, 2163 (2012). (Cited on pages 96, 97, and 176.)
- [159] R. M. Nguimdo, G. Verschaffelt, J. Danckaert, X. Leijtens, J. Bolk, and G. Van Der Sande, "Fast random bits generation based on a single chaotic semiconductor ring laser," *Opt. Express* **20**, 28603 (2012). (Cited on pages 96 and 176.)
- [160] I. Reidler, Y. Aviad, M. Rosenbluh, and I. Kanter, "Ultrahigh-Speed Random Number Generation Based on a Chaotic Semiconductor Laser," *Phys. Rev. Lett.* **103**, 024102 (2009). (Cited on pages 96, 97, 99, 103, 104, 105, 176, and 178.)

- [161] A. Argyris, S. Deligiannidis, E. Pikasis, A. Bogris, and D. Syvridis, "Implementation of 140 Gb/s true random bit generator based on a chaotic photonic integrated circuit," *Opt. Express* **18**, 18763 (2010). (Cited on pages 96, 97, and 176.)
- [162] I. Kanter, Y. Aviad, I. Reidler, E. Cohen, and M. Rosenbluh, "An optical ultrafast random bit generator," *Nature Photon.* **4**, 58 (2009). (Cited on pages 96, 97, 104, 105, 176, and 178.)
- [163] X.-Z. Li and S.-C. Chan, "Heterodyne Random Bit Generation Using an Optically Injected Semiconductor Laser in Chaos," *IEEE J. Quantum Electron.* **49**, 829 (2013). (Cited on pages 96, 97, and 176.)
- [164] N. Oliver, M. C. Soriano, D. W. Sukow, and I. Fischer, "Fast random bit generation using a chaotic laser: approaching the information theoretic limit," *IEEE J. Quantum Electron.* **49**, 910 (2013). (Cited on pages 96, 97, 98, 102, 104, 105, and 176.)
- [165] N. Li, B. Kim, V. N. Chizhevsky, A. Locquet, M. Bloch, D. S. Citrin, and W. Pan, "Two approaches for ultrafast random bit generation based on the chaotic dynamics of a semiconductor laser," *Opt. Express* **22**, 6634 (2014). (Cited on pages 96, 105, and 176.)
- [166] R. F. Fox and J. E. Keizer, "Effect of molecular fluctuations on the description of chaos by macrovariable equations," *Phys. Rev. Lett.* **64**, 249 (1990). (Cited on pages 96 and 176.)
- [167] R. F. Fox and J. E. Keizer, "Amplification of intrinsic fluctuations by chaotic dynamics in physical systems," *Phys. Rev. A* **43**, 1709 (1991). (Cited on pages 96 and 176.)
- [168] C. Bracikowski, R. F. Fox, and R. Roy, "Amplification of intrinsic noise in a chaotic multimode laser system," *Phys. Rev. A* **45**, 403 (1992). (Cited on pages 96 and 176.)
- [169] T. Stojanovski and L. Kocarev, "Chaos-based random number generators-part I: analysis," *IEEE Trans. Circuits Syst. I, Reg. Papers* **48**, 281 (2001). (Cited on page 96.)
- [170] T. Stojanovski, J. Pihl, and L. Kocarev, "Chaos-based random number generators. Part II: practical realization," *IEEE Trans. Circuits Syst. I, Reg. Papers* **48**, 382 (2001). (Cited on page 96.)
- [171] M. E. Yalcin, J. A. K. Suykens, and J. Vandewalle, "True random bit generation from a double-scroll attractor," *IEEE Trans. Circuits Syst. I, Reg. Papers* **51**, 1395 (2004). (Cited on page 96.)
- [172] N. Oliver, M. C. Soriano, D. W. Sukow, and I. Fischer, "Dynamics of a semiconductor laser with polarization-rotated feedback and its utilization for random bit generation," *Opt. Lett.* **36**, 4632 (2011). (Cited on pages 97, 98, 99, 103, and 177.)

- [173] T. Harayama, S. Sunada, K. Yoshimura, J. Muramatsu, K.-I. Arai, A. Uchida, and P. Davis, "Theory of fast nondeterministic physical random-bit generation with chaotic lasers," *Phys. Rev. E* **85**, 046215 (2012). (Cited on pages 97, 98, 99, and 113.)
- [174] S. Sunada, T. Harayama, P. Davis, K. Tsuzuki, K.-I. Arai, K. Yoshimura, and A. Uchida, "Noise amplification by chaotic dynamics in a delayed feedback laser system and its application to nondeterministic random bit generation." *Chaos* **22**, 047513 (2012). (Cited on pages 97, 98, 99, and 110.)
- [175] X. Fang, B. Wetzal, J. M. Merolla, J. M. Dudley, L. Larger, C. Guyeux, and J. M. Bahi, "Noise and chaos contributions in fast random bit sequence generated from broadband optoelectronic entropy sources," *IEEE Trans. Circuits Syst. I, Reg. Papers* **61**, 888 (2014). (Cited on pages 97 and 104.)
- [176] T. Mikami, K. Kanno, K. Aoyama, A. Uchida, T. Ikeguchi, T. Harayama, S. Sunada, K.-I. Arai, K. Yoshimura, and P. Davis, "Estimation of entropy rate in a fast physical random-bit generator using a chaotic semiconductor laser with intrinsic noise," *Phys. Rev. E* **85**, 016211 (2012). (Cited on pages 98, 99, 110, 111, 113, and 178.)
- [177] K. Hirano, K. Amano, A. Uchida, S. Naito, M. Inoue, S. Yoshimori, K. Yoshimura, and P. Davis, "Characteristics of fast physical random bit generation using chaotic semiconductor lasers," *IEEE J. Quantum Electron.* **45**, 1367 (2009). (Cited on page 98.)
- [178] K. Hirano, T. Yamazaki, S. Morikatsu, H. Okumura, H. Aida, A. Uchida, S. Yoshimori, K. Yoshimura, T. Harayama, and P. Davis, "Fast random bit generation with bandwidth-enhanced chaos in semiconductor lasers," *Opt. Express* **18**, 1367 (2010). (Cited on page 98.)
- [179] R. Vicente, J. Dauden, P. Colet, and R. Toral, "Analysis and characterization of the hyperchaos generated by a semiconductor laser subject to a delayed feedback loop," *IEEE J. Quantum Electron.* **41**, 541 (2005). (Cited on pages 99 and 177.)
- [180] A. Rukhin, J. Soto, J. Nechvatal, M. Smid, E. Barker, S. Leigh, M. Levenson, M. Vangel, D. Banks, A. Heckert, J. Dray, and S. Vo, "A Statistical Test Suite for Random and Pseudorandom Number Generators for Cryptographic Applications - Special Publication 800-22 Rev1a," Tech. Rep. April, National Institute of Standards and Technology (2010). (Cited on pages 103, 107, and 178.)
- [181] G. Marsaglia, "DieHard: a battery of tests of randomness," Tech. rep., Florida State University (1996). (Cited on pages 103 and 178.)
- [182] I. Shimada and T. Nagashima, "A Numerical Approach to Ergodic Problem of Dissipative Dynamical Systems," *Prog. Theor. Phys.* **61**, 1605 (1979). (Cited on page 113.)

- [183] M. Virte, K. Panajotov, and M. Sciamanna, "Mode Competition Induced by Optical Feedback in Two-Color Quantum Dot Lasers," *IEEE J. Quantum Electron.* **49**, 578–585 (2013). (Cited on pages 117, 162, and 181.)
- [184] M. Virte, K. Panajotov, and M. Sciamanna, "Corrections to "mode competition induced by optical feedback in two-color quantum dot lasers " [jul 13 578-585]," *Quantum Electronics, IEEE Journal of* **50**, 174–174 (2014). (Cited on pages 117, 162, and 181.)
- [185] M. Virte, K. Panajotov, and M. Sciamanna, "Impact of optical feedback on a quantum dot laser emitting simultaneously from the ground and excited states," in "Lasers and Electro-Optics Europe (CLEO EUROPE/IQEC), 2013 Conference on and International Quantum Electronics Conference," (2013), p. 6801840. (Cited on pages 117, 162, and 181.)
- [186] F. Rogister, M. Sciamanna, O. Deparis, P. Mégret, and M. Blondel, "Low-frequency fluctuation regime in a multimode semiconductor laser subject to a mode-selective optical feedback," *Phys. Rev. A* **65**, 015602 (2001). (Cited on page 119.)
- [187] C. Mesaritakis, C. Simos, H. Simos, S. Mikroulis, I. Krestnikov, E. Roditi, and D. Syvridis, "Effect of optical feedback to the ground and excited state emission of a passively mode locked quantum dot laser," *Appl. Phys. Lett.* **97**, 061114 (2010). (Cited on page 119.)
- [188] B. Haegeman, K. Engelborghs, D. Roose, D. Pieroux, and T. Erneux, "Stability and rupture of bifurcation bridges in semiconductor lasers subject to optical feedback," *Phys. Rev. E* **66**, 046216 (2002). (Cited on pages 123, 197, and 198.)
- [189] A. Markus, M. Rossetti, V. Calligari, D. Chek-Al-Kar, J. X. Chen, A. Fiore, and R. Scollo, "Two-state switching and dynamics in quantum dot two-section lasers," *J. Appl. Phys.* **100**, 113104 (2006). (Cited on page 128.)
- [190] V. V. Korenev, A. V. Savelyev, A. E. Zhukov, A. V. Omelchenko, M. V. Maximov, and Y. M. Shernyakov, "Simultaneous multi-state stimulated emission in quantum dot lasers: experiment and analytical approach," *Proc. SPIE* **8432**, 84321L (2012). (Cited on pages 128 and 181.)
- [191] V. Korenev, A. Savelyev, and A. Zhukov, "Effect of carrier dynamics and temperature on two-state lasing in semiconductor quantum dot lasers," *Semicond.* **47**, 1406 (2013). (Cited on pages 128 and 181.)
- [192] Y. Wu and L. V. Asryan, "Direct and indirect capture of carriers into the lasing ground state and the light-current characteristic of quantum dot lasers," *J. Appl. Phys.* **115**, 103105 (2014). (Cited on page 150.)
- [193] M. Sciamanna and K. Panajotov, "Two-mode injection locking in vertical-cavity surface-emitting lasers." *Opt. Lett.* **30**, 2903–5 (2005). (Cited on page 163.)

- [194] M. Sciamanna and K. Panajotov, "Route to polarization switching induced by optical injection in vertical-cavity surface-emitting lasers," *Phys. Rev. A* **73**, 023811 (2006). (Cited on page 163.)

LIST OF ACRONYMS

In this section, we provide a list and a short description of the acronyms used throughout this dissertation:

ADC	A nalog to D igital C onverter.
DBR	D istributed B ragg R eflector.
ECM	E xternal C avity M ode. In a laser subjected to optical feedback, an ECM designate the modes created when the laser resonates with the outside cavity. In particular, the optical frequency is shifted by an integer multiple of the external cavity frequency.
EEL	E dge- E mitting L aser.
EP	E lliptical P olarization. In this manuscript an EP designates an elliptically polarized steady-state of a VCSEL.
ES	E xcited S tate. First excited energy level for the carriers in a quantum dot laser.
FFT	F ast F ourier T ransform.
GS	G round S tate. Fundamental energy level for the carriers in a quantum dot laser.
Gbps	G iga- B its P er S econd. Unit of bitrate measure: 1 Gbps = one billion bits generated per second.
HF	H igh F requency. A VCSEL generally have two preferred linear and orthogonal polarization state with slightly different optical frequency; HF designates the one of these two states which shows the highest frequency.
HMM	H idden M arkov M odels. Statistical modeling approach assuming that the modeled process is Markovian but with unobserved (hidden) states.
LASER	L ight A mplification by S timulated E mission of R adiation.

LF	Low Frequency. A VCSEL generally have two preferred linear and orthogonal polarization state with slightly different optical frequency; LF designates the one of these two states which shows the lowest frequency.
LP	Linear Polarization.
LSB	Least Significant Bit. For data encoded on multiple bits (e.g. 8 or 16 bits), the LSB is the bit giving the less information; it is the binary equivalent of taking the least significant digit of a number.
Mbps	Mega-Bits Per Second. Unit of bitrate measure: 1 Mbps = one million bits generated per second.
PS	Polarization Switching. Considering the polarization instabilities in a VCSEL, a PS designates the event when the laser switches from one linear polarization to the orthogonal linear polarization.
QD	Quantum Dot. Nanocrystal of semiconductor material small enough to confine the electrons in 3 dimension.
QW	Quantum Well. Thin layer of semiconductor material thin enough to confine the electrons in its 2 dimensional plane.
RBG	Random Bit Generator.
RF	Radio Frequency. Designate the 3 kHz - 300 GHz range of frequency which, in particular, is used to carry radio signals.
RNG	Random Number Generator. Equivalent to the random bit generator considering that <i>numbers</i> are formed by several bits.
RO	Relaxation Oscillation. Designate the undamped oscillations of an under-damped oscillator when it is subject to e.g. a current step.
SFM	Spin-Flip Model. Rate equation model used in this dissertation to model the behavior of VCSELs.
VCSEL	Vertical-Cavity Surface-Emitting Laser.

CURRICULUM VITAE

Martin Virte was born in 1987 in Nancy, France. In 2011, he received the master of engineering with a major in Photonics from the french *Grande Ecole* Supelec (now Centrale-Supelec). The same year, he received the master of science with a specialization in physics and photonics from the *Université de Lorraine*. He then started to work toward the PhD degree in a joint program between the OPTEL research group of Supelec (Metz, France) and the Brussels Photonics Team (B-phot) of the Vrije Universiteit Brussel (Brussels, Belgium). In this framework, he is studying the nonlinear dynamics and polarization properties of quantum dot lasers: in particular his research focus on two-mode dynamics that can induced by mode competition in quantum dot VCSELs or two-color quantum dot lasers.

Contact Information

Martin Virte
Brussels Photonics Team (B-Phot)
Department of Applied Physics and Photonics (TONA)
Vrije Universiteit Brussel,
Pleinlaan 2, 1050 Elsene
BELGIUM

Phone: +32 (0) 629 36 62
E-mail: mvirte@b-phot.org, or mvirte@vub.ac.be

Professional Experience

- OCT. 2011 – OCT. 2014): **Research assistant** and **PhD candidate** in a joint PhD program between **Supelec** (Metz, France) and the **Vrije Universiteit Brussel**(Brussels, Belgium).
- APR. – SEPT. 2011: **Research assistant** at **Supelec** (Metz, France). Theoretical study of the nonlinear dynamics of a laser diode subject to a phase-conjugate feedback.
- JUN. 2009 – AUG. 2010: Internship as a **Junior development engineer** at **Sagem, Safran group** (Massy, France) in collaboration with the **ONERA** (Toulouse, France). Development and demonstration of a multi-spectral imaging system for target detection and classification.

Awards

- 2011: **Mention d'honneur** awarded by **Supélec** (Ecole supérieure d'électricité, France) in recognition of brilliant results obtained at Supélec.
- 2014: IEEE Photonics Society Graduate Student Fellowship **Award** which is awarded to ten graduate students worldwide for the quality of their research work during their graduate studies. The prize has been awarded on october 13th 2014 during the IEEE Photonics Society annual meeting held in San Diego, USA.

Professional Activities

- Research assistant, PhD Thesis focusing on experimental and theoretical investigations of two-mode dynamics and switching in quantum dot lasers.
- Supervision of lab studies on “Electro-optic modulation” and “Processing and conversion of electrical energy” for master and bachelor level-student at Supelec.
- Exercise session on “numerical methods” for bachelor level students at Supelec.
- Co-promotor of the final 5-month internship at the VUB of Emeric Mercier to obtain the master of engineering degree from Supelec: “Experimental study of the polarization properties and nonlinear dynamics of SFM-like quantum dot VCSELs”, 2013.
- Co-promotor of the final 5-month internship at the VUB of Elodie Mirisola to obtain the master of engineering degree from Supelec: “Impact of phase and amplitude anisotropy misalignment on the nonlinear dynamics of VCSELs”, 2014.
- Reviewer for international journals including Optics Express, Journal of Lightwave Technology, IEEE Journal of Quantum Electronics and Optics Communication.

Education

- OCT. 2014: **PhD in engineering** from the Vrije Universiteit Brussel (Belgium), and **PhD in physics** from Supelec (France).
- SEPT. 2011: **Master in engineering** from Supelec (France) with major in *Photonics and Communication System (SPC)*. **Master of science** from Supelec and the Université de Lorraine (France) with a specialization in *Physics, Plasma and Photonics*.
- SEPT. 2005 - SEPT. 2007: Classe Préparatoire (Nancy, France). Two-year intensive program in advanced mathematics and physics in preparation for the nationwide competitive examination for the french *Grandes Ecoles* for studies in science.
- JUN. 2005: **Baccalauréat S serie** obtained with honors. French secondary school diploma with a major in science.

List of Publications

Publications in Peer-reviewed journals:

1. M. Virte, A. Karsaklian Dal Bosco, D. Wolfersberger, and M. Sciamanna, "Chaos crisis and bistability of self-pulsing dynamics in a laser diode with phase-conjugate feedback", *Phys. Rev. A* **84**, 043836 (2011).
2. M. Sciamanna, M. Virte, C. Masoller, and A. Gavrielides, "Hopf bifurcation to square-wave switching in mutually coupled semiconductor lasers," *Phys. Rev. E*, **86**, 016218 (2012).
3. M. Virte, K. Panajotov, H. Thienpont, and M. Sciamanna, "Deterministic polarization chaos from a laser diode," *Nature Photon.* **7**, 60-65 (2013).
4. M. Virte, K. Panajotov, and M. Sciamanna, "Bifurcation to nonlinear polarization dynamics and chaos in vertical-cavity surface-emitting lasers," *Phys. Rev. A* **87**, 013834 (2013).
5. M. Virte, K. Panajotov, and M. Sciamanna, "Mode competition induced by optical feedback in two-color quantum dot lasers," *IEEE J. Quantum Electron.* **49**, 578 (2013).
6. M. Virte, M. Sciamanna, E. Mercier, and K. Panajotov, "Bistability of time-periodic polarization dynamics in a free-running VCSEL," *Opt. Express* **22**, 6772 (2014).
7. M. Virte, K. Panajotov, and M. Sciamanna, "Corrections to "mode competition induced by optical feedback in two-color quantum dot lasers" [jul 13 578-585], " *IEEE J. Quantum Electron.* **50**, 174 (2014).
8. M. Virte, E. Mercier, H. Thienpont, K. Panajotov and M. Sciamanna, "Physical random bit generation from chaotic solitary laser diode," *Opt. Express* **22**, 17271 (2014).

9. M. Virte, S. Breuer, M. Sciamanna and K. Panajotov, "Switching between ground and excited states by optical feedback in a quantum dot laser diode", *Appl. Phys. Lett.* **105**, 121109 (2014).

Publication in indexed international conference proceedings:

1. M. Virte, K. Panajotov, and M. Sciamanna, "Dynamics accompanying polarization switching in vertical-cavity surface-emitting lasers," in "Proc. SPIE," , vol. 8432 (2012), vol. 8432, pp. 84321E–84321E–9.
2. M. Virte, M. Sciamanna, and K. Panajotov, "Bifurcation to chaotic polarization mode hopping in vertical-cavity surface-emitting lasers," in "Advanced Photonics Congress," (Optical Society of America, 2012), p. JTu5A.31.
3. M. Virte, K. Panajotov, and M. Sciamanna, "Impact of optical feedback on a quantum dot laser emitting simultaneously from the ground and excited states," in "Lasers and Electro-Optics Europe (CLEO EUROPE/IQEC), 2013 Conference on and International Quantum Electronics Conference," (2013), pp. 1–1.
4. M. Virte, K. Panajotov, H. Thienpont, and M. Sciamanna, "Polarization chaos from a free-running quantum dot laser diode," in "Lasers and Electro-Optics Europe (CLEO EUROPE/IQEC), 2013 Conference on and International Quantum Electronics Conference," (2013), pp. 1–1.
5. M. Virte, M. Sciamanna, E. Mercier, and K. Panajotov, "Experimental and theoretical analysis of limit cycle bistability in a free-running vcsel," in "Proc. SPIE," , vol. 9134 (2014), vol. 9134, pp. 91340A–91340A–6.
6. M. Virte, E. Mercier, H. Thienpont, K. Panajotov, and M. Sciamanna, "Random bit generation using polarization chaos from free-running laser diode," in "Proc. SPIE," , vol. 9134 (2014), vol. 9134, pp. 913426–913426–6.

Publication in non-indexed international conference proceedings:

1. M. Sciamanna, M. Virte, H. Thienpont, and K. Panajotov, "Deterministic polarization chaos from a laser diode," in proceedings of the International Symposium on Nonlinear Theory and its Applications, NOLTA 2012, Spain (2012).
2. M. Virte, K. Panajotov, H. Thienpont, M. Sciamanna, "From mode competition to polarization chaos in free-running VCSELs," in proceedings of the 33rd edition of Dynamics Days Europe, XXXIII Dynamics Days Europe 2013, Spain (2013).
3. E. Mercier, M. Virte, K. Panajotov, and M. Sciamanna, "Bistability of limit cycles in a free-running VCSEL," in proceedings of the International Symposium on Physics and Applications of Laser Dynamics, IS-PALD 2013, France (2013).

4. M. Virte, K. Panajotov, and M. Sciamanna, "Optical feedback induces bistability between ground and excited states in quantum dot lasers, " in proceedings of the International Symposium on Physics and Applications of Laser Dynamics, IS-PALD 2013, France (2013).
5. K. Panajotov, M. Virte, H. Thienpont, and M. Sciamanna, "Two-mode Dynamics of Vertical-Cavity Surface-Emitting Lasers," in Proceedings of the Australian and New Zealand Conference on Optics and Photonics, ANZCOP 2013, Australia (2013).

Contribution to workshops and national conferences:

1. M. Virte, A. Karsaklian Dal Bosco, D. Woflersberger, and M. Sciamanna, "Chaos crisis and multistability of self-pulsing dynamics in a laser diode with phase-conjugate feedback", 15th Annual IEEE Photonics Society Workshop, Belgique (2012).
2. A. Karsaklian Dal Bosco, M. Virte, D. Wolfersberger, and M. Sciamanna, "Nonlinear dynamics in laser diode with phase-conjugate optical feedback," FRISNO 11 - 10th European/French Israeli Symposium on Nonlinear and Quantum Optics, France (2011).
3. M. Virte, M. Sciamanna and K. Panajotov, "Nonlinear dynamics induced by polarization modes competition in vertical-cavity surface-emitting laser," International traveling summer school (ITSS 2012), Czech Republic (2012).
4. M. Sciamanna, M. Virte, H. Thienpont, and K. Panajotov, "Polarization switching, nonlinear dynamics and chaos in quantum dot VCSELs," PAMO-JSM, France (2012).
5. M. Sciamanna, M. Virte, H. Thienpont, and K. Panajotov, " Polarization switching, nonlinear dynamics and chaos in quantum dot VCSELs," WIAS workshop on Nonlinear Dynamics of semiconductor lasers, Germany, 2012.
6. M. Virte, K. Panajotov, and M. Sciamanna, "Bifurcation and switching in two lasing state quantum dot lasers with optical feedback," WIAS workshop on Nonlinear Dynamics of semiconductor lasers, Germany, 2012.

COLOPHON

This document was typeset using the typographical look-and-feel classicthesis developed by André Miede. The style was inspired by Robert Bringhurst's seminal book on typography *"The Elements of Typographic Style"*. classicthesis is available for both L^AT_EX and L^yX:

<http://code.google.com/p/classicthesis/>

Happy users of classicthesis usually send a real postcard to the author, a collection of postcards received so far is featured here:

<http://postcards.miede.de/>

Final version— October 22, 2014.